



Chair of Process Technology and Environmental  
Protection

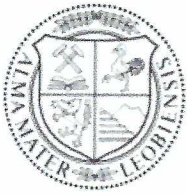
Dissertation



Methanation of CO/CO<sub>2</sub> mixtures

Dipl.-Ing. Andreas Krammer

Juni 2024



**AFFIDAVIT**

I declare on oath that I wrote this thesis independently, did not use any sources and aids other than those specified, have fully and truthfully reported the use of generative methods and models of artificial intelligence, and did not otherwise use any other unauthorized aids.

I declare that I have read, understood and complied with the "Good Scientific Practice" of the Montanuniversität Leoben.

Furthermore, I declare that the electronic and printed versions of the submitted thesis are identical in form and content.

Date 26.07.2024

Signature Author  
Andreas Harald Krammer



## Danksagung

Zuallererst gilt mein herzlicher Dank Prof. Markus Lehner für seine gelassene und kompetente Art, mit der er mich bereits einige Jahre begleitet und nach wie vor immer unterstützt. Danke, auf der einen Seite für den großen Freiraum, eigene Ideen umsetzen zu können, und gleichzeitig für die immer offene Tür und den oft entscheidenden Ratschlag. Danke für das entgegengebrachte Vertrauen und für Ihren permanenten Einsatz mit dem nötigen Fingerspitzengefühl für jede und jeden Einzelnen auf unserem Lehrstuhl.

Vielen Dank an meine KollegInnen am Lehrstuhl für Verfahrenstechnik, insbesondere an Mark und Fritz aus unserem Technikum und das famose „Team CH<sub>4</sub>“. Ohne so manche technische und nicht-technische Weisheit und eure Unterstützung vor Ort wäre das meiste gar nicht erst möglich gewesen. Bedanken möchte ich mich auch bei unseren Bachelor-, Master-Studenten und studentischen Mitarbeitern, für das fleißige Modellieren und die Hilfe bei Versuchen und Umbauten.

Zu Dank verpflichtet bin ich auch meiner „Alma Mater Leobensis“ und ihren vielen motivierten Menschen, die jeden Tag versuchen einen positiven Beitrag zu leisten. Ich bin sehr dankbar für viele prägende Begegnungen und tiefe Freundschaften, die während meiner Zeit an der Montanuniversität entstanden sind. Allen voran die „Meet&Eat-Schwammerl-Gruppe“ war vom Beginn des Studiums nicht nur für den Faktor Spaß, sondern auch die Diskussionen abseits des Studiums für mich ein enorm wichtiger Teil dieses Lebensabschnitts.

Ganz besonderer Dank gilt meiner Frau Ina, die mich vom Moment der Entscheidung das Studium in Leoben zu beginnen und trotz so manchen spätnächtlich vorangetriebenen Neben-Projekten parallel zur Dissertation immer nur bestärkt und unterstützt hat. Danke, dass es mit dir möglich ist, neben unserer Familie, die mir das Allerwichtigste ist, auch noch so manchen eignen (Um-)Weg gehen zu können, auch wenn das die Familienorganisation nicht unbedingt vereinfacht. Ohne unsere Gespräche, die vielen schönen und witzigen Momente mit dir wären die Herausforderungen der letzten Jahre und diese Arbeit nicht möglich gewesen. Ich bin sehr dankbar für dein Vertrauen, die Entspannung, die du ausstrahlst und deine unfassbare Kraft, die in dir schlummert und wie eine Superkraft immer dann besonders zum Vorschein kommt, wenn es wirklich wichtig ist. Diese Eigenschaften sind durchaus hilfreich, vor allem wenn zu zwei Dissertationen, noch zwei großartige Kinder dazukommen. Vielen Dank an meine Kinder Josefine und Louis für die riesengroße Freude, die sie mir jeden Tag bereiten.

Ein gigantisches Danke geht an meine Eltern, Regina und Gerald. Eure bedingungslos liebevolle Fürsorge, euer tiefes Vertrauen von Anfang an und eure tagtägliche Tatkraft ist mir nicht nur Vorbild, sondern die entscheidende Ausgangsbasis, für alles, was ich in meinem bisher Leben schaffen durfte. Danke an meine Geschwister Caro, Luki, Lisi und Belli für eure Freundschaft und das Fundament Familie, das für mich besonders in den letzten Jahren so unendlich wertvoll war und nach wie vor ist.

## **Abstract**

### **Methanation of CO/CO<sub>2</sub> mixtures**

Methanation of CO/CO<sub>2</sub> can be used to store renewable electric energy in the form of the well-known transportable gaseous energy carrier methane, which makes it a crucial technology to transform our existing fossil-based energy infrastructure. Methanation plants suitable for industrial-scale capacity at low complexity are necessary to produce cheap renewable synthetic natural gas (SNG) from fossil or biogenic carbon sources. To achieve highly optimized methanation reactors for CO/CO<sub>2</sub> feed, such as from high temperature Co-electrolysis (Co-SOEC), the limiting mechanisms of existing reactor systems were identified. Several reactors with different dimensions, natural air-cooling or thermal-oil cooling and under variation of process conditions including pressure and catalyst load were experimentally investigated. A 1D plug-flow reactor model in MATLAB and a 2D CFD reactor model in COMSOL Multiphysics were developed and used to verify experimental findings and deepen the understanding of the methanation process. Based on a combined modelling and experimental approach tuning parameters were derived to overcome process limitations and a strategy to design high performance methanation reactors was elaborated. Thermodynamic and kinetic limitations along the reactor axis could be identified and significantly reduced by optimizing the axial temperature curve based on appropriate reactor dimensions and operation parameters. The 1D model works as a reactor optimization and design tool for CO/CO<sub>2</sub> mixtures and other feed gases, such as biogas or CO<sub>2</sub>. Reactor and process design examples for single-stage Co-SOEC syngas methanation, high-capacity methanation at 100.000 h<sup>-1</sup> GHSV (gas hourly space velocity) and energy efficient dual-pressure stage methanation are presented. The findings and proposals formulated in this thesis significantly improved the process of CO/CO<sub>2</sub> methanation with the aim to contribute to a liveable future for upcoming generations on our planet.

## Kurzfassung

### Methanisierung von CO/CO<sub>2</sub>-Mischungen

Durch die Methanisierung von CO/CO<sub>2</sub>-Mischungen kann erneuerbare elektrische Energie in den leicht transportierbaren, gasförmigen Energieträger Methan umgewandelt und gespeichert werden. Dadurch ist die Methanisierung eine Schlüsseltechnologie für die Transformation unseres fossilen Energiesystems. Effiziente, einfach skalierbare und kostengünstige Methanisierungsprozesse sind erforderlich, um konkurrenzfähiges synthetisches Erdgas (SNG) aus CO<sub>2</sub> aus fossilen oder biogenen Quellen erzeugen zu können. Um optimierte Reaktorsysteme für CO/CO<sub>2</sub> Mischungen, beispielsweise aus einer Hochtemperatur-Co-Elektrolyse (Co-SOEC), auslegen zu können, müssen zunächst die limitierenden Mechanismen in bestehenden Reaktoren identifiziert werden. Dazu wurden verschiedene Reaktoren mit unterschiedlichen Dimensionen unter Variation von Prozessbedingungen Druck und Katalysatorbelastung mit natürlicher Luftkühlung oder mit Thermalölkühlung unter realen industrienahen Bedingungen in einer Versuchsanlage experimentell untersucht. Ein 1D Pfropfenströmungsmodell in MATLAB und ein 2D CFD-Modell in COMSOL Multiphysics wurden zur Verifizierung der experimentellen Ergebnisse herangezogen, um ein vertieftes Verständnis für den Methanisierungsprozess zu erlangen. Aus der Kombination aus verifizierter Modellierung und Experimenten konnten prozesslimitierende Einflüsse abgeleitet und eine Strategie zur Reaktorauslegung ausgearbeitet werden. Thermodynamische und kinetische Limitierungen entlang der Reaktorachse konnten durch die Auswahl der richtigen Reaktor- und Prozessparameter identifiziert und signifikant reduziert werden. Das 1D Modell dient als Design- und Optimierungstool von Reaktoren für die Methanisierung von CO/CO<sub>2</sub>-Mischungen, aber auch anderen Feedgasen wie Biogas oder reinem CO<sub>2</sub>. Beispiele für Reaktorauslegung für Co-SOEC-Synthesegas in einer Reaktorstufe sowie für sehr hohe Reaktorbelastung von 100.000 h<sup>-1</sup> GHSV (gas hourly space velocity) in zwei Reaktorstufen und eine effiziente Prozessverschaltung mit zwei Druckstufen wurden in dieser Arbeit dargelegt. Mit den Ergebnissen dieser Arbeit wurden wertvolle Vorschläge für die effiziente Methanisierung von CO/CO<sub>2</sub>-Mischung erarbeitet, womit auch ein positiver Beitrag zum Erhalt unserer Lebengrundlage auch für zukünftige Generationen geleistet werden konnte.

## Table of contents

	<b>Page</b>
<b>1 INTRODUCTION.....</b>	<b>3</b>
1.1 Motivation .....	3
1.2 Problem formulation.....	4
1.3 State of the art .....	5
1.4 Research gap .....	6
1.5 Research questions .....	7
1.6 Methodology .....	7
1.7 Framework of the thesis.....	8
1.7.1 Book chapter – Co-SOEC and methanation.....	9
1.7.2 Paper I – 2D heterogeneous model of a polytropic methanation reactor .....	9
1.7.3 Paper II – High-capacity CO/CO <sub>2</sub> methanation reactor design strategy based on 1D PFR modelling and experimental investigation .....	9
1.7.4 Paper III – Dual Pressure Level Methanation of Co-SOEC Syngas.....	10
<b>2 FUNDAMENTALS .....</b>	<b>11</b>
2.1 Book chapter - Co-SOEC and methanation .....	11
2.2 Modelling of catalytic fixed bed reactors .....	38
2.2.1 Conservation laws.....	38
2.2.2 General transport phenomena .....	39
2.2.3 Transport phenomena in fixed beds.....	40
2.2.4 Mass transport in fixed beds .....	40
2.2.5 Heat transport in fixed bed reactors .....	41
2.2.6 Radial heat transport in fixed beds.....	41
2.2.7 Mass transport limitation .....	44
2.2.7.1 Catalyst efficiency via Thiele-modulus.....	46
2.2.8 Fixed bed characteristics .....	47
<b>3 RESEARCH.....</b>	<b>48</b>
3.1 Experimental and modelling investigation of Co-SOEC syngas methanation in a high diameter ratio polytropic reactor .....	48
3.2 Experimental and modelling investigation of Co-SOEC syngas methanation in low diameter ratio cooled and uncooled reactors.....	66
3.3 Plant level optimization concept for the methanation of Co-SOEC syngas for higher overall efficiency .....	88

---

<b>4</b>	<b>SUMMARY AND DISCUSSION.....</b>	<b>101</b>
4.1	Answer to research question 1: What are the limiting factors of fixed bed methanation of CO/CO <sub>2</sub> feed gas and what are the relevant design and operation parameters to reduce these limiting effects?.....	101
4.2	Answer to research question 2: Is the CO/CO <sub>2</sub> methanation limited by thermodynamics or kinetics and what is the influence of reactor cooling? ..	110
4.3	Answer to research question 3: What is the dependency of heat and mass transfer from operational and design parameters and what is the sensitivity to enhance methanation performance? .....	114
4.4	Answer to research question 4: What process and design strategies can be derived to overcome limiting effects and achieve maximum methanation performance?.....	119
4.5	Answer to research question 5: What are potential efficiency enhancements of a combined Co-SOEC and methanation plant? .....	123
<b>5</b>	<b>CONCLUSION .....</b>	<b>125</b>
<b>6</b>	<b>REFERENCES.....</b>	<b>128</b>
	<b>NOMENCLATURE .....</b>	<b>134</b>
	<b>FIGURES.....</b>	<b>138</b>
	<b>TABLES .....</b>	<b>141</b>
	<b>PUBLICATIONS.....</b>	<b>142</b>

# 1 Introduction

## 1.1 Motivation

The increasing consumption of fossil energy threatens all living conditions on our planet. Due to man-made greenhouse gas emissions the global temperature already rose by 1.2 °C between 1850 and 2021, as illustrated in Figure 1. Only 400 gigatons of CO<sub>2</sub> can be emitted starting from 2020 to prevent global warming to rise beyond 1.5 °C at a 67 % chance. At the current rate of emission this CO<sub>2</sub> budget will be used before 2030. By 2100 (my kids would turn 77 and 79 by then) the IPCC estimates a global warming of 3.2 °C including devastating consequences. [1]

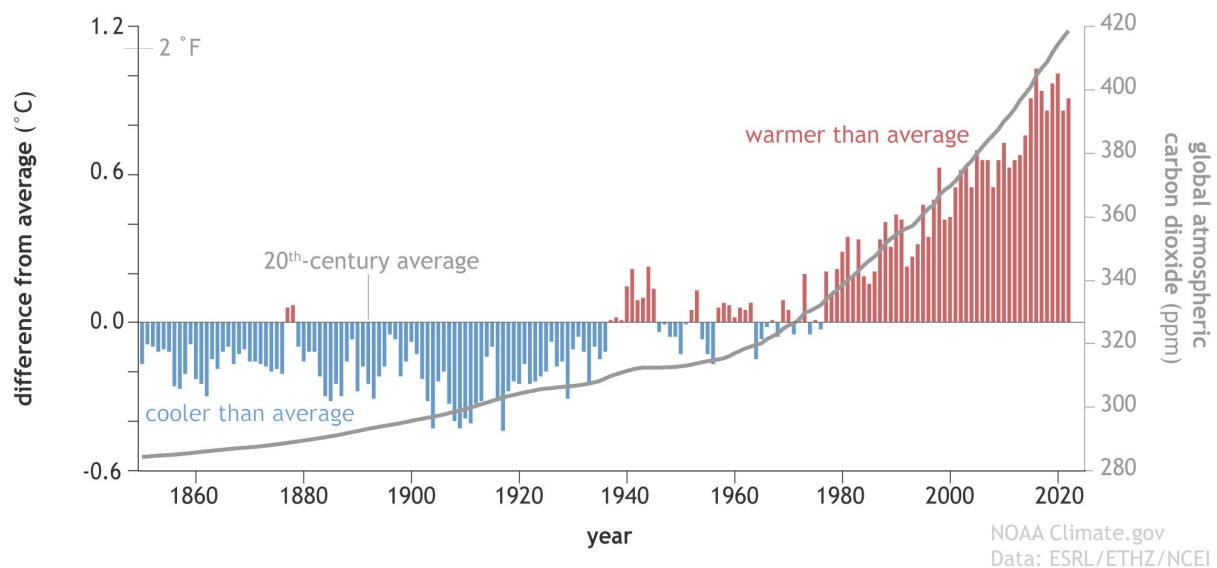


Figure 1: Yearly global surface temperature (bars) and atmospheric carbon dioxide (grey line) (1850-2022) [2]

The secretary-general of the United Nations António Guterres summed up the current situation of the climate crisis. [3]

*“Half of humanity is in the danger zone, from floods, droughts, extreme storms and wildfires. No nation is immune. Yet we continue to feed our fossil fuel addiction. [...] We have a choice. Collective action or collective suicide. It is in our hands.”*

*(Secretary-general of the United Nations António Guterres, 18<sup>th</sup> of July 2022)*

[3]

The technical solution to this problem is to prevent CO<sub>2</sub> emissions. This requires an extremely rapid transfer of our energy system from a linear consumption of fossil fuels to renewable energy sources and carbon recycling or disposal strategies. While many industrial processes can in principle be directly switched to renewable energy input, some CO<sub>2</sub> sources from hard-to-abate industries such as biogas plants, waste incineration plants or cement plants simply cannot be substituted. Furthermore, carbonaceous species will remain a valuable feedstock for the chemical industry. High-temperature heat for processes such as cement, glass or steel

production today rely to a large extent on high-temperature heat from incineration of mostly natural gas. Methanation in combination with an electrolyzer unit can be used to convert renewable energy into the molecule  $\text{CH}_4$ , which is the main component of natural gas. For such a renewable synthetic natural gas (SNG) a complete energy infrastructure already exists, including long-term energy storage in natural gas reservoirs and a dense global distribution network. As a result, power-to-gas as a combination of electrolysis and methanation will play a key role to reduce industrial  $\text{CO}_2$  emissions and contribute to prevent ecological collapse.

This work aims to contribute to a power-to-gas technology in particular a combination of high-temperature Co-electrolysis (Co-Solid oxide electrolyser cell - Co-SOEC) and catalytic methanation. The Co-SOEC uses renewable electric energy to produce syngas consisting of hydrogen, carbon monoxide and carbon dioxide at high energy efficiency from water and  $\text{CO}_2$ . In the second step the Co-SOEC syngas will be transformed in catalytic fixed bed reactors to synthetic natural gas (SNG). This SNG product meets all the requirements for direct injection into the natural gas grid. The combination of Co-SOEC and methanation enables global distribution and long-time storage of renewable electric energy. The focus of this work lies in the development of the catalytic methanation reactor system and its interplay with the Co-SOEC system. This thesis aims to contribute to cost-effective, high-capacity and industrially applicable CO/ $\text{CO}_2$  methanation plants.

## 1.2 Problem formulation

Capital expenditure and renewable electric energy consumption are the two main cost-driving factors of SNG production made from a combined Co-SOEC and methanation plant. [4] In order to achieve competitive SNG prices low plant complexity, high energy efficiency at excellent plant performance and process stability are essential.

The methanation reactor needs to be designed as simple and cost-effective as possible to reduce the total capital expenditure. At the same time all performance requirements in terms of product quality and process stability have to be met. The specific SNG costs of industrial scale methanation systems are directly linked to the reactor size and therefore to the volume specific capacity of a methanation reactor.

Furthermore, the energy efficiency of combined Co-SOEC and methanation power-to-gas plants needs to be optimized. This can be achieved by coherent interplay of all plant components. The excess heat of the methanation reaction can be used to preheat the Co-SOEC feed. A suitable actively cooled methanation reactor is required to enable internal heat recycling. This cooling system is also necessary to control the maximum catalyst bed temperature and the process performance. If available, external thermal energy sources can be used to reduce the primary electric energy demand in the high-temperature Co-SOEC. The pressure loss in high-capacity reactors may also play a crucial role for the overall plant efficiency. In addition, reactors with low or moderate operation pressure perfectly match with electrolyzers operating at low pressures and thus significantly reduce the gas compression effort. To find an optimum reactor design with highest overall efficiencies all influences of operation and design parameters not only on the methanation reaction behaviour but also on the down- and upstream process units have to be considered.



To achieve a cost effective green SNG product, the limiting factors and essential mechanisms of the catalytic reaction need to be fully understood and depicted. Subsequently, it is essential to derive the optimum design and process parameters for a high-capacity CO/CO<sub>2</sub> methanation reactor, while also incorporating an efficient cooling method.

### 1.3 State of the art

The catalytic methanation of syngas to form SNG has been investigated since its discovery by Sabatier and Senderens in 1902. [5] In the 1970s efforts for methanation of syngas from coal gasification for SNG production intensified as a consequence of the oil crisis. The first commercial syngas methanation plant, the Great Plains Synfuels Plant, was completed in 1984 in North Dakota with a daily output of 4.8 Mio m<sup>3</sup> SNG. [6] Since then, several industrial and pilot scale applications were developed and realized for methanation of syngas from coal and biomass gasification, of which only some reached the commercial stage. All industrial scale plants are based on at least one or several adiabatic reactors using gas recycling or excess steam addition for temperature moderation. Adiabatic reactors were used for the “Lurgi process”, the “TREMP process” established by the company Haldor Topsøe, the “Conoco/BGC process”, the “RMP process” and the “ICI/Koppers”. The HICOM process does not characterize its process as adiabatic but uses steam injection and gas recycling for temperature control. The “Vesta” process from Clariant and Foster Wheeler uses three fixed bed reactors with steam injection for temperature control. [6] A combination of isothermal and adiabatic reactors was considered for methanation in a process by the company Linde, which was not brought into commercial application for methanation, but for methanol synthesis. [6,7] According to Rönsch [7] several commercial CO methanation applications based on TREMP, HICOM and Lurgi were realized mainly in China for coal gasification. Syngas methanation based on adiabatic reactor systems can be considered TRL 9. [6] However, several drawbacks result from adiabatic reactors, steam injection and gas recycling. Adiabatic reactors are generally limited in capacity and can easily suffer from temperature hotspots, especially for CO/CO<sub>2</sub> methanation. [8] Product gas recycling requires additional recycling equipment such as recycle compressors and prior steam removal. Excess steam can lead to catalyst degradation for certain catalysts [9–11]. Foremost, both temperature control strategies lead to more necessary catalyst volume and additional cost driving process equipment. [12]

Methanation of syngas from biomass or waste gasification in pilot scale was conducted in honeycomb reactors in the DemoSNG project [13] and via fluidized bed methanation in Güssing, Austria [14] and in the project GAYA [15]. Fluidized bed reactors profit from high heat transfer rates, but lack high capacity due to limiting kinetics in the almost isothermal system and require higher operational effort. [7] Honeycomb reactors allow for less pressure drop over the reactor length. [7] Although heat transfer within the monolithic structure is higher compared to a fixed bed of bulk catalyst, the gap between reactor wall and the honeycomb structure significantly reduces overall radial heat transport of honeycomb reactors. [16,17] As a result, low-complexity fixed bed reactor process concepts with direct bed temperature control, which is essential for cost-effective operation of the highly reactive process, are neither in pilot nor in commercial scale available.

Methanation of CO<sub>2</sub>, biogas and syngas was intensively addressed in research papers in the last decades to establish new process and reactor strategies especially for CO<sub>2</sub> [18–25] and biogas [26]. Besides fixed bed reactors [19–21,23,24,27], also trickle-bed reactors [26], fluidized bed reactors [28–30], heat pipe reactors [31–33], heat exchanger reactors [18,22] or micro reactors [25,34] were investigated based on experiments and models. Furthermore, the development of new catalysts in terms of active material and support [35,36] has been intensively studied.

The methanation of CO-containing feed gas, such as Co-SOEC syngas, is especially challenging because of higher reaction enthalpy and extremely high reaction rates. In the field of CO methanation, CO/CO<sub>2</sub> methanation or syngas methanation a lot of research on catalyst development [37–39] and reaction mechanism [40,41] is available. Meyer experimentally investigated the transient behaviour of CO/CO<sub>2</sub> methanation with a 4.5 mm diameter reactor and <200 µm catalyst particles. [42] Gómez used a 6.8 mm sorption-enhanced reactor for CO/CO<sub>2</sub> methanation on Ru catalyst. [43] No literature could be found addressing industrially applicable fixed bed reactors with active cooling for CO/CO<sub>2</sub> methanation on commercially available Ni/Al<sub>2</sub>O<sub>3</sub> catalyst. The TRL for Co-SOEC syngas methanation could be increased to 5-6 within the research project HydroMetha. [44] The project HydroMetha funded by the Austrian “Klima- und Energiefonds” and the AVL List GmbH (grant no. 864578) was a main funding source for this work.

## 1.4 Research gap

The main technical challenges of the methanation process have been accurately summarized by Neubert [45] as the “trilemma of methanation” as shown in Figure 2. This analysis is especially true for Co-SOEC syngas methanation, as high reaction rates are most decisive for CO methanation design.

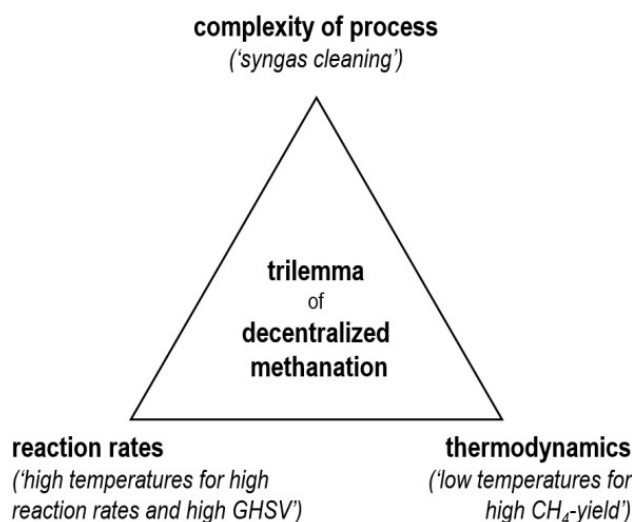


Figure 2: Trilemma of decentralized methanation by Neubert [45]

The methanation process is characterized by contrary dependencies in terms of temperature. Lower temperature at the reactor outlet is necessary to achieve high product concentrations due to the thermodynamic nature of the reactions. In contrast, higher temperatures within the

catalyst bed favour high reaction rates according to Arrhenius law, which leads to less necessary reaction volume and therefore higher reactor capacities. Those two important factors lead to a third, the complexity of the methanation system. The methanation system should be designed in a way to achieve all performance goals at lowest possible complexity. Sophisticated cooling methods such as product gas recycling or costly gas cleaning steps lead to more plant complexity, less energy efficiency and are contradictory to a cost-effective system.

As a result, the research gap on the way to effective fixed bed CO/CO<sub>2</sub> methanation systems lies in the design of a simple reactor, the understanding of its current system limitations, and strategies to overcome these. The dependencies of all operational and design parameters need to be derived in detail, which is necessary to achieve high capacity, avoid problematic hot-spots and reach sufficient educt conversion. Furthermore, an adequate cooling method is not only essential for the reactor operation but can also contribute to the overall plant efficiency by heat recycling, e.g. to the Co-SOEC system. Balanced thermo-management of the catalytic fixed bed is necessary to steer the reactor temperature between all given boundary conditions, including kinetics, thermodynamics and catalyst degradation. The methanation of CO/CO<sub>2</sub> should facilitate sufficient conversion rates for the SNG product to be directly injected into the natural gas grid. Austrian natural gas grid requires full conversion of CO and <2.5 vol.-% of CO<sub>2</sub> left in the product gas [46]. A reactor design capable of producing injection quality would save additional gas upgrading steps, and has not been resolved prior to this work for the methanation of Co-SOEC syngas.

## 1.5 Research questions

Based on the presented status quo and research gap the research questions were formulated. These questions refer to methanation in catalytic fixed beds in general, but with a main focus of Co-SOEC syngas as a feed gas. The answers to these questions are aimed to be derived from the research results compiled in chapter 3.

1. What are the limiting factors of fixed bed methanation of CO/CO<sub>2</sub> feed gas and what are the relevant design and operation parameters to reduce these limiting effects?
2. Is CO/CO<sub>2</sub> methanation limited by thermodynamics or kinetics and what is the influence of reactor cooling?
3. What is the dependency of heat and mass transfer from operational and design parameters and what is the sensitivity to enhance methanation performance?
4. What reactor and process design strategies can be derived to overcome limiting effects and achieve maximum methanation performance?
5. What are potential efficiency enhancements of a combined Co-SOEC and methanation plant?

## 1.6 Methodology

The investigation of Co-SOEC syngas methanation was conducted by experiments with a laboratory test plant combined with 1D and 2D reactor models. Each of these two methodical approaches have drawbacks and advantages, but combined they complement one another.

Experiments in a real test setup allow to measure hard and reliable data and understand the systems behaviour under realistic conditions. The drawbacks of experimental investigation encompass not only measurement errors and the potential influence of the measurement procedure on the process, but also the limitation in the quantity of punctual measurements. Temperature data collection within the reactor is limited to the number of inserted thermocouples. The more thermocouples, the more space is occupied by thermocouple wire affecting the fixed bed. Gas concentration and pressure measurement is restricted to one value at the input and output of the reactor.

These drawbacks can be balanced with proper reactor modelling. In a digital twin created to represent the real reactor, any corner of the fixed bed is covered and almost any necessary physical property can be derived from mathematical relations. However, a model is based on simplifications, since no mathematical equation is able to fully represent the complexity of reality, nor would there be enough computation power available if it was. Therefore, the simplified model must be verified by hard data from experiments to ensure its accuracy. In conclusion, by combination of the two methodical approaches, experiment and model, a complete and realistic picture of the investigated methanation process could be drawn.

The existing lab-scale methanation test plant was modified several times along the research progress, to improve its performance and process condition measurement quality. The 2D CFD and the 1D plug-flow reactor models were established in the course of this work. The lab-scale test plant was numerous times adapted and improved in cooperation with my PhD-colleges. Test plant and models are described in detail in the research papers presented in chapter 3 and referenced work.

## 1.7 Framework of the thesis

The cumulative dissertation includes three accepted peer-reviewed scientific articles as first author and one published book chapter. The book chapter is included in the fundamentals section. The three extensive papers form the research section of this thesis. In Table 1 an overview of the structure of the thesis is presented.

Table 1: Structure of the thesis including all publications

Introduction	<ul style="list-style-type: none"> <li>• Motivation</li> <li>• Problem formulation</li> <li>• State of the art</li> <li>• Research gap</li> <li>• Research questions</li> <li>• Methodology</li> <li>• Framework</li> </ul>	Written chapter
Fundamentals	Fundamentals of Co-SOEC syngas methanation	Book chapter
	Fundamentals of fixed bed reactor modelling	Written chapter
Research activity	Methanation reactor development	Paper I
		Paper II
	PtG process development	Paper III
Conclusive part	Summary and discussion	Written chapter
	Conclusion and outlook	Written chapter

### 1.7.1 Book chapter – Co-SOEC and methanation

A book chapter containing the fundamentals of methanation of Co-SOEC syngas was published in the book “High Temperature Electrolysis – From fundamentals to applications” edited by Sitte and Merkle [47]. This book chapter outlines the basic theory of the investigated methanation reactions including thermodynamics, kinetics, catalysts, reactor types, carbon deposition, energy efficiency and socio economic impact.

### 1.7.2 Paper I – 2D heterogeneous model of a polytropic methanation reactor

In the first presented paper the results of the combined experimental and modelling investigation of a 80 mm fixed bed methanation reactor are presented. Thorough experiments were the basis to understand the reactors behaviour under different operation conditions regarding pressure and volume flow. In addition, a 2D CFD model was established in COMSOL Multiphysics and validated with the experimental results. The model allowed deriving process limitations and proposing improvements in terms of reactor dimensioning and cooling. These results were the basis for paper II.

### 1.7.3 Paper II – High-capacity CO/CO<sub>2</sub> methanation reactor design strategy based on 1D PFR modelling and experimental investigation

The second paper builds on the results and proposals of the first paper. A new reactor design with and without active cooling with thermal oil was assessed. Again, extensive experiments were conducted accompanied by appropriate modelling effort. A 1D PFR approach was

developed, working accurately, a lot faster and more flexible than the 2D COMSOL model. With the new reactor many of the identified limitations could be overcome or reduced leading to much better reactor performance. The model revealed very good accuracy. Based on these results a reactor design strategy for high-capacity methanation of Co-SOEC syngas was proposed.

#### **1.7.4 Paper III – Dual Pressure Level Methanation of Co-SOEC Syngas**

The third paper addresses the overall Co-SOEC and methanation process and suggests an operation strategy to improve the total plant efficiency. Based on experiments and mass- and energy balance calculations a dual-step methanation was proposed, leading to a significant reduction in necessary compression power compared to the base case process variant.

## 2 Fundamentals

### 2.1 Book chapter - Co-SOEC and methanation

The book chapter in "High-Temperature Electrolysis – From Fundamentals to Applications" [47] provides a comprehensive summary of the current knowledge on Co-SOEC syngas methanation, similar in depth and scope to an extensive review paper. The combination of Co-SOEC and methanation enables to transform CO<sub>2</sub> in SNG at high efficiencies by reuse exothermic waste heat from the methanation process to reduce the primary energy demand of the electrolysis. The book chapter highlights the core principles of syngas methanation including reactor concepts, methanation catalysts and fundamentals of kinetics. In addition, the thermodynamic limitations regarding carbon deposition and equilibrium composition as a function of pressure and temperature for typical Co-SOEC syngas feed gas are addressed. Based on the discussed fundamentals, the necessary requirements for the successful application of Co-SOEC syngas methanation are examined. Finally, the possible energy efficiency and the socioeconomic impact of this valuable PtG approach are presented.

#### **Contribution statement:**

Andreas Krammer: Conceptualization, Data curation, Formal analysis, Investigation, Methodology, Software, Validation, Visualization, Writing – original draft, Writing – review & editing.

Markus Lehner: Conceptualization, Funding acquisition, Project administration, Resources, Supervision, Writing – review & editing.



# Chapter 15

## Co-solid oxide electrolysis and methanation

**Andreas Krammer and Markus Lehner**

A reduction in industrial CO<sub>2</sub> emissions can be achieved by recycling it back into the energy system using renewable energy sources. Using a combined co-solid oxide electrolysis cell (SOEC) and methanation power-to-gas (PtG) plant, it is possible to transform CO<sub>2</sub> into a valuable substitute natural gas for long-term energy storage. This chapter presents the requirements for the successful methanation of co-SOEC syngas at the catalyst, reactor, and plant levels. Reaction kinetics and thermodynamics define the baseline for well-balanced reaction conditions. The catalytically active materials, carrier materials, and catalyst forms used for chemical methanation need to be considered to maximize performance. Several reactor designs for co-SOEC syngas methanation are available, which differ in their combinations of phases, cooling characteristics, and complexity. Heat integration strategies and reactor arrangements substantially influence the methanation performance and the overall system efficiency. The economic viability of this combined co-SOEC and methanation system depends on an optimally tuned design at all system levels.

### **15.1 Power-to-Gas as an option for chemical storage of renewable energy**

The decarbonization of our existing energy systems will be based on an enormous increase in sustainable but also fluctuating power sources, such as wind and solar energy. PtG is an efficient strategy for transforming surplus electric energy into valuable gaseous energy carriers suitable for long-term storage [1–3]. The key element of a PtG plant is the electrolysis unit. The electrolyzer uses electric energy to reduce water to hydrogen. As an option, when co-electrolysis is used, carbon dioxide can also be fed together with water to produce a syngas product. Either way, a subsequent methanation reactor can transform both hydrogen and carbon oxides (CO, CO<sub>2</sub>) into methane. Figure 15.1 shows a schematic process diagram of a PtG system consisting of co-electrolysis and methanation.

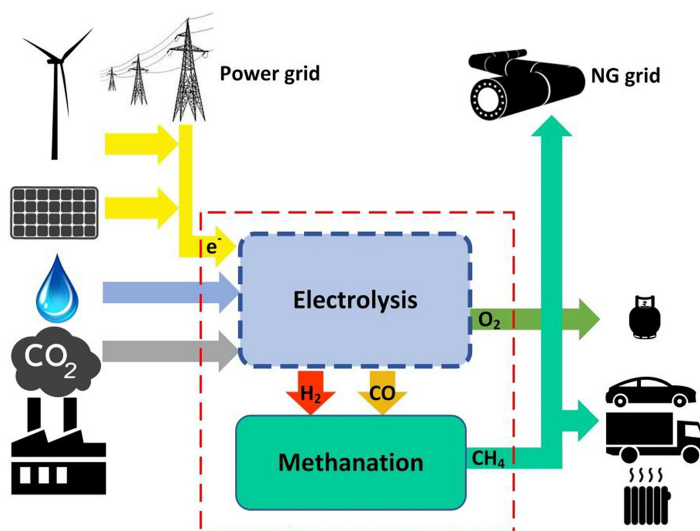
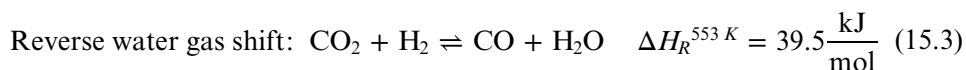
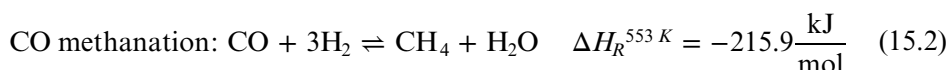
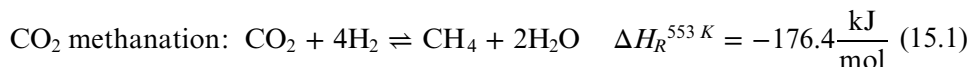


Figure 15.1. Schematic illustration of a PtG system that includes co-electrolysis and methanation.

A PtG unit allows electric energy to be stored in the form of highly calorific gases (at the terawatt-hour scale) for an almost unlimited time period in former natural gas reservoirs, for example. Hydrogen, as well as methane, can be transformed back to electric energy when needed, used directly in industrial processes, or used for heating or transport. While the production of methane requires an additional production step that leads to higher transformation losses, it benefits from important technical advantages. Existing infrastructure for the storage, distribution, and utilization of methane is already available in the form of the existing natural gas grid. Furthermore, CO<sub>2</sub> from industrial sources can be reused by methanation, thus recycling carbon back to the energy system. While some industrial CO<sub>2</sub> sources will certainly be replaced, e.g. by direct electrification, certain processes cannot be fully decarbonized. The carbonates in mineral raw materials, such as the limestone used for cement production, some sorts of iron ore used for steel production, or those used in the course of refractory material production, release CO<sub>2</sub>-based materials due to calcination. Furthermore, waste incineration and biogas production are, if not indispensable, very valuable technologies which cause CO<sub>2</sub> emissions. Therefore, it is necessary to establish solutions that can handle unavoidable CO<sub>2</sub> emissions efficiently. CO<sub>2</sub> can be captured post-combustion (e.g. by amine scrubbing), transformed into CH<sub>4</sub>, e.g. by a combined electrolysis and methanation system, and then injected into the natural gas grid as a substitute for primary natural gas. As a result, methanation will play a substantial role in the energy transformation from fossil fuels to renewables. Several different methanation process designs are possible in terms of reactor type, catalyst form, and thermal management. However, the focus of this chapter is the field of catalytic methanation, whereas biological methanation in stirred tank reactors plays a minor role in direct combination with high-temperature co-electrolysis.

## 15.2 The fundamentals of catalytic methanation

The methanation process is based on the Sabatier reactions first discovered by Sabatier and Senderens in 1902 [4]. These two Sabatier reactions, the CO<sub>2</sub> methanation reaction (equation (15.1)) and the CO methanation reaction (equation (15.2)), are always accompanied by a third, the reverse water gas shift reaction (equation (15.3)). The reverse water gas shift reaction links the two methanation reactions by linear combination.



The Boudouard reaction is an adverse side reaction that, among other side reactions, leads to carbon deposition [5]. It is favored at low pressures and low H<sub>2</sub>/CO or H<sub>2</sub>/CO<sub>2</sub> ratios in the methanation feed, which are addressed in greater detail in section 15.3.



The methanation process can be performed in several reactor types that differ in their operational methods and reactor cooling. Reactor performances can be compared using the resulting gas product quality, the conversion rate of carbon oxides, and temperature conditions. For comparability between reactor systems, the gas hourly space velocity (GHSV) must be considered, which represents the catalytic load and is always expressed under standard conditions as shown in equation (15.5).

$$\text{GHSV}_{\text{STP}} = \frac{\dot{V}_{\text{in}}}{V_{\text{catalyst}}} \frac{T_{\text{in}}}{T_{\text{STP}}} \frac{p_{\text{STP}}}{p_{\text{in}}} \quad (15.5)$$

### 15.2.1 Methanation reactors

In the most prevalent and mature packed-bed reactors, the catalyst is mostly applied in the form of a spherical or cylindrical bulk material that fills a tubular system. For adiabatic packed-bed reactors without direct cooling, intermediate cooling of the process gas can be used between several serial reactors. Further temperature control strategies for adiabatic reactor systems are product gas recycling, staged feed injection, or steam injection, which have the disadvantages of higher operational costs and lower CO<sub>2</sub>/CO conversion. However, adiabatic systems are easily exposed to hot spots, lower space-time yields, and generally lower CO/CO<sub>2</sub> conversions. Due to highly active catalysts, the limiting factor of packed-bed methanation is heat removal from the catalyst bed (and to a lesser extent reaction kinetics), especially for high GHSV

and CO-containing feed gases, such as co-SOEC syngas. Therefore, direct temperature control of packed-bed reactors is essential [2, 6]. Packed-bed systems with direct cooling can be realized in the form of tube-bundle reactors. Low-diameter reactor pipes are important in order to reduce the high radial heat gradients within the catalyst bed [7] and enhance radial heat transfer [6]. As an alternative to bulk catalysts, catalytically active materials can also be applied on ceramic or metallic honeycombs. These structured monolithic catalysts promise even higher radial heat transfer (by two or three orders of magnitude) and less pressure loss [2]. Microstructured reactor systems aim to achieve highly intensified heat transfer for improved temperature control. Although the maturity level of this reactor design is lower, plate reactors for intensified heat transfer are already commercially available for small-scale applications [8]. Furthermore, fluidized catalytic beds have been developed for enhanced heat and mass transfer. However, those reactors place a high demand on the attrition resistance of the catalyst. An additional reactor type is the three-phase bubble column reactor, which benefits from enhanced heat transfer but also results in additional mass transfer resistance between the reactants and the catalyst due to the required transfer from the gas to the liquid phase [9].

Trickle-bed or continuously stirred tank reactors are used for biological methanation, which makes use of microorganisms to catalyze the methanation reaction within the liquid phase. Biological methanation is conducted at moderate temperatures (30 °C–70 °C) and benefits from high resistance to catalyst poisons (such as sulfur components) compared to catalytic methanation. Figure 15.2 gives an overview of reactor and plant types, including technical readiness levels.

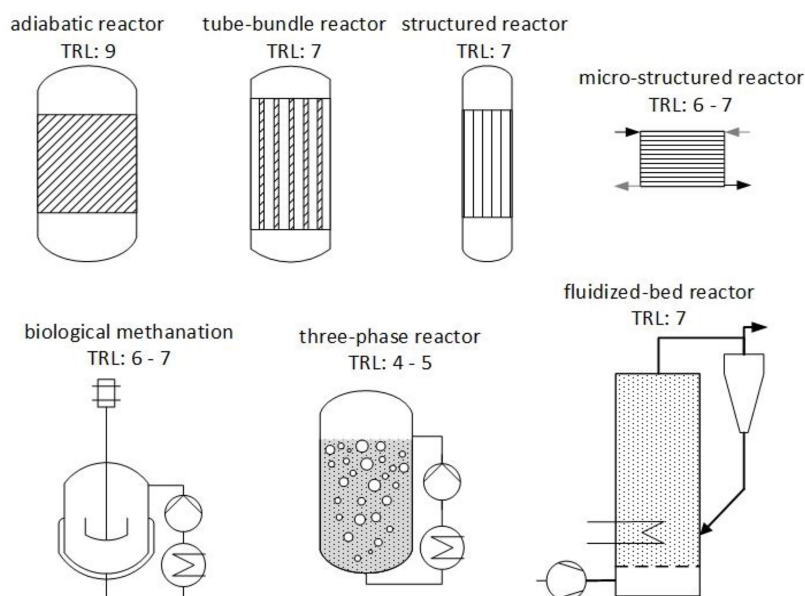


**Figure 15.2.** Overview of methanation reactor types including technology readiness levels (TRLs) based on [2, 10, 11].

### 15.2.2 Methanation catalysts

Active materials for catalytic methanation can be found in the VIII to X groups of metals. Although several metals have been investigated in terms of activity ( $\text{Ru} > \text{Fe} > \text{Ni} > \text{Co} > \text{Rh} > \text{Pd} > \text{Pt} > \text{Ir}$ ), nickel remains the most important active material for methanation due to its high activity and high selectivity at low material cost [2, 12]. Mills and Steffgen [13] published a list of most relevant methanation catalysts:

Activity:  $\text{Ru} > \text{Fe} > \text{Ni} > \text{Co} > \text{Mo}$

Selectivity:  $\text{Ni} > \text{Co} > \text{Fe} > \text{Ru}$ .

The most active catalyst material is ruthenium, but as a result of its immense costs, its use is infeasible for commercial applications. Although iron is also very active, its tendency to form higher hydrocarbons is highly adverse. Since cobalt is more expensive, less active, and less selective towards methane, it also fails to compete with nickel. Molybdenum has the highest reported sulfur stability in comparison to all the substances mentioned above. On the other hand, molybdenum is less active and less selective than nickel. As a result, nickel remains by far the most important catalyst for industrial methanation applications, providing great performance at low cost. Most commonly, the active substance is applied to metal oxide supports that usually consist of  $\text{Al}_2\text{O}_3$ ,  $\text{SiO}_2$ , or  $\text{TiO}_2$ . As the main goal of the catalyst support material is to provide a high surface area for the application of active sites, the support material significantly influences the catalytic activity. Certain catalyst properties can be tuned by substances that provide enhancements.  $\text{Ni}/\text{Al}_2\text{O}_3$  catalysts can be enhanced by  $\text{MgO}$ , which improves their carbon resistance [14] and thermal stability [15], whereas  $\text{La}_2\text{O}_3$  enhances catalytic activity [16], and  $\text{CeO}_2$  leads to higher reducibility and long-term stability [17]. The thermal stability, activity, and coke resistance of nickel catalysts can be improved by  $\text{V}_2\text{O}_3$  [2, 18].

Industrial off-gases that serve as  $\text{CO}_2$  sources for PtG plants often contain catalyst poisons such as sulfur compounds, heavy metals, tars, dust, chlorine compounds, ammonia, or alkalis. While dust or tar can deactivate the catalyst by mechanically blocking its active sites, other compounds such as sulfur can react with nickel to form irreversible inactivating bonds. In addition, high temperatures (especially in adiabatic reactors) can lead to thermal degradation by causing sintering effects. Furthermore, the carbon deposition caused by undesired side reactions that depend on the C–H–O ratio, temperature, and pressure can result in the loss of active sites. Countermeasures against the formation of carbon can be taken at the reactor and process design levels, as discussed in sections 15.3 and 15.4.

The exact methanation reaction mechanism on catalytic nickel or noble metal sites is still object of research. There appears to be a consensus among authors that a Langmuir–Hinshelwood–Hougen–Watson (LHHW) approach is the basis of the methanation mechanism. The LHHW mechanism assumes that both reaction partners first need to be adsorbed at the active sites to reach an activated state before they can form covalent bonds with each other. Nevertheless, the exact reaction mechanism and whether or not differences between  $\text{CO}_2$  and  $\text{CO}$  methanation occur are not yet clear. However, two main reaction mechanisms are

**Table 15.1.** Two methanation mechanisms on nickel or noble metal catalysts discussed in the literature; '\*' indicates adsorption sites [7, 19–23].

Intermediate surface carbon mechanism	Hydrogen-assisted mechanism
1: $\text{CO}_2 + 2^* \leftrightarrow \text{CO}^* + \text{O}^*$	1: $\text{CO}_2 + 2^* \leftrightarrow \text{CO}^* + \text{O}^*$
2: $\text{H}_2 + 2^* \leftrightarrow 2 \text{H}^* +$	2: $\text{H}_2 + 2^* \leftrightarrow 2 \text{H}^* +$
3: $\text{CO}^* + ^* \leftrightarrow \text{C}^* + \text{O}^*$	3: $\text{CO}^* + \text{H}^* \leftrightarrow \text{CHO}^* + ^*$
4: $\text{C}^* + \text{H}^* \leftrightarrow \text{CH}^* + ^*$	4: $\text{CHO}^* + ^* \leftrightarrow \text{CH}^* + \text{O}^*$
5: $\text{O}^* + \text{H}^* \leftrightarrow \text{OH}^* + ^*$	5: $\text{CH}^* + 3\text{H}^* \leftrightarrow \text{CH}_4^* + 3^*$
6: $\text{OH}^* + \text{H}^* \leftrightarrow \text{H}_2\text{O}^* + ^*$	6: $\text{CH}_4^* \leftrightarrow \text{CH}_4 + ^*$
7: $\text{H}_2\text{O}^* \leftrightarrow \text{H}_2\text{O} + ^*$	7: $\text{O}^* + \text{H}^* \leftrightarrow \text{OH}^* + ^*$
8: $\text{CH}^* + 3\text{H}^* \leftrightarrow \text{CH}_4^* + 3^*$	8: $\text{OH}^* + \text{H}^* \leftrightarrow \text{H}_2\text{O}^* + ^*$
9: $\text{CH}_4^* \leftrightarrow \text{CH}_4 + ^*$	9: $\text{H}_2\text{O}^* \leftrightarrow \text{H}_2\text{O} + ^*$

currently discussed among researchers: the ‘intermediate surface carbon mechanism’ and the ‘hydrogen-assisted mechanism.’ The rate-determining step (RDS) of the reaction mechanism, namely the formation of  $\text{COH}^*$  or CO dissociation, is under ongoing discussion as well. The derivation of a formal kinetic expression is based on the RDS of the reaction mechanism [7] (table 15.1).

### 15.2.3 Methanation kinetics

The kinetic expressions represent the reaction rates of the underlying reactions. In general, in accordance with Arrhenius’ law, the reaction rates increase at higher temperatures. However, the methanation reactions are characterized by an ignition temperature (225 °C–285 °C according to [24–26]) that depends on gas concentration and pressure. Below the ignition temperature, the reaction rate tends to zero. Therefore, the reactor temperature needs to be kept above this temperature level to keep the chemical reaction going. At the upper boundary of the temperature window, the reaction kinetics decelerates when thermodynamic equilibrium is approached at the particular pressure and temperature. The reaction rate is expressed by the formal kinetic equations as a function of temperature, pressure, and gas concentration. As the exact elementary reactions of the methanation mechanism are not yet fully understood, formal kinetic expressions can only be experimentally measured and derived. Formal kinetic formulations represent the reactions kinetics using a mathematical correlation to the observed experimental results. Although the mathematical structure of the kinetic law (LHHW or power law) is maintained, its physical parameters, such as the activation energy or the reaction order, serve only as adjustable values to limit the deviation between the experimental findings and the mathematical representation. Nevertheless, the form of the formal kinetic expression is influenced by the RDS of the reaction mechanism. Since the RDS is still part of the scientific discussion, as mentioned above, different forms of expression have been proposed. A number of power-law and LHHW kinetic approaches have been suggested for methanation in the literature, which differed in their measuring procedures (integral reactor or

differential reactor), catalyst forms (powder, pellets), catalyst materials (nickel, ruthenium) as well as pressure and temperature ranges. Furthermore, the kinetics can be formulated as single-step kinetics representing only one reaction (generally CO<sub>2</sub> methanation) (equation (15.1)), or as multistep kinetics that includes two or three of the methanation reactions (equations (15.1)–(15.3)).

In principle, in a power-law approach, the reaction rate depends on the rate coefficient, the partial pressures of the contributing species, and the ‘driving force’ of a reaction. The ‘driving force’ represents the deviation from thermodynamic equilibrium and takes on a value between zero and one. The driving force and therefore the reaction kinetics tend to zero if the species concentrations reach the thermodynamic equilibrium. The principal power-law expression for the CO<sub>2</sub> methanation reaction rate is shown in equation (15.6) [26].

$$r_j = k_j \cdot p_{\text{CO}_2}^a \cdot p_{\text{H}_2}^b \cdot \left( 1 - \frac{p_{\text{CH}_4} \cdot p_{\text{H}_2\text{O}}^2}{p_{\text{CO}_2} \cdot p_{\text{H}_2}^4 \cdot K_{p, \text{CO}_2\text{-Meth}}} \right) [\text{mol kg}_{\text{cat}}^{-1} \text{s}^{-1}] \quad (15.6)$$

For the LHHW kinetic expression, the power-law expression is complemented by the ‘adsorption term,’ which reflects the suppressing effects of the molecular adsorption of reactants or the desorption of products such as methane or water. The exponent of the adsorption expression corresponds to the number of active sites taking part in the reaction [26, 27]. Equation (15.7) represents the principal LHHW reaction rate of the CO<sub>2</sub> methanation reaction.

$$r_j = \frac{k_j \cdot p_{\text{CO}_2}^a \cdot p_{\text{H}_2}^b \cdot \left( 1 - \frac{p_{\text{CH}_4} \cdot p_{\text{H}_2\text{O}}^2}{p_{\text{CO}_2} \cdot p_{\text{H}_2}^4 \cdot K_{p, \text{CO}_2\text{-Meth}}} \right)}{\left( 1 - K_{\text{CO}_2} \cdot p_{\text{CO}_2}^c + K_{\text{H}_2} \cdot p_{\text{H}_2}^d + K_{\text{CH}_4} \cdot p_{\text{CH}_4}^e + \dots \right)^2} [\text{mol kg}_{\text{cat}}^{-1} \text{s}^{-1}] \quad (15.7)$$

The kinetic factors are calculated based on the Arrhenius-type relation (equation (15.8)) and the adsorption factors by the van ‘t Hoff-type (equation (15.9)) relation. As already mentioned, the parameters of these equations ( $E_{A, j}$ ,  $k_j^0$ ,  $\Delta H_{\text{ads}, i}$ ,  $K_i^0$ ) lose their physical purposes and serve as fitting parameters to achieve best correlation between the formal kinetic function and the experimental results.

$$k_j = k_j^0 \cdot \exp\left(-\frac{E_{A, j}}{RT}\right) \quad (15.8)$$

$$K_i = K_i^0 \cdot \exp\left(-\frac{\Delta H_{\text{ads}, i}}{RT}\right) \quad (15.9)$$

As early as 1950, the first LHHW kinetics for methanation was published by Binder and White [28]. Numerous kinetic formulations have been published since then, most often using the LHHW approach in recent publications [7, 20]. Gruber [26] presented a list of detailed kinetic approaches for nickel catalysts with varying nickel loads (5 w% to >55 w%), temperature ranges, and pressure ranges, which can be regarded as the most important recent kinetic formulations in the literature (table 15.2).



**Table 15.2.** Overview of detailed methanation kinetic expressions taken from Gruber [26].

No.	Author	Ni content	$T$ in °C	$p$ in bar	Type
1	Martinez Molina [29]	54 w%	150–260	atmos.	Single-step power law
2	Schollenberger [30]	unknown	200–300	2–17	Single-step power law
3	Weatherbee [31]	3 w%	227–327	1.4–1.75	Single-step LHHW
4	Koschany [20]	58 w%	180–340	1–15	Single-step LHHW
5	Yang Lim [32]	12 w%	180–210	up to 20	Single-step LHHW
6	HELMETH kinetic [26, 33]	>55 w%	250–350	15–25	Single-step LHHW
7	Xu & Froment [34]	15.2 w%	300–400	3–10	Multistep LHHW
8	Kopyscinski [21]	50 w%	280–360	up to 2	Multistep LHHW
9	Ducamp [35]	14–17 w%	280–400	1–10	Multistep LHHW
10	Rönsch [19]	18/50 w%	275–360	1–5	Multistep LHHW

For packed-bed methanation reactor modeling, the kinetic approach described by Xu and Froment [34] was often used directly or in an adapted version [2]. The three-step kinetics used by Xu and Froment was later adapted by Parlikkad *et al* [36], Kang and Lee [37], Klose and Baerns [38], and Zhang *et al* [39] [2]. Rönsch *et al* [19] again recommended and adapted the latter two Xu and Froment adaptations. Kopyscinski [21] modified findings by Weatherbee and Bartholomew [31] for CO methanation. The authors' kinetic expression was established for highly isothermal conditions and is therefore especially suitable for fluidized-bed methanation. Furthermore, in the recent work by Koschany *et al* [20], a single-step LHHW kinetics for CO<sub>2</sub> methanation was elaborated. Based on 200 data points within a temperature range between 180 °C and 340 °C and pressures of up to 15 bar, the authors found the best experiment-model fit for a hydrogen-assisted reaction mechanism assumption. Comprehensive overviews and comparisons of methanation reaction kinetic expressions are given by Kopyscinski *et al* [21], Rönsch [19], Younas *et al* [12], Gruber [26], and Neubert [7].

The kinetic expressions discussed above represent intrinsic kinetics without any form of mass transfer limitation. For packed-bed reactors filled with industrially applicable catalyst particles, mass transfer limitations must often be taken into account [6, 24, 25, 35, 40–42]. Therefore, not only can the intrinsic kinetics be applied, but also external factors limiting the chemical reaction rate. It is necessary to consider mass transfer limitation due to diffusion from the gas bulk to the catalyst surface, as well as the intraparticle diffusion limitation. Gruber [40], Sun and Simakov [41], Kiewidt [6], and Kreitz [42] used catalytic effectiveness factors calculated based on a Thiele-modulus approach within their packed-bed methanation models to consider mass transfer limitations. Ducamp *et al* [35], Try *et al* [25], and Schlereth and Hinrichsen [24] included a particle model to take mass transfer limitations into account.

### 15.3 Thermodynamics of catalytic methanation

Figure 15.3 gives the thermodynamic equilibrium compositions at varying temperatures and pressures, based on assumed co-SOEC product concentrations of

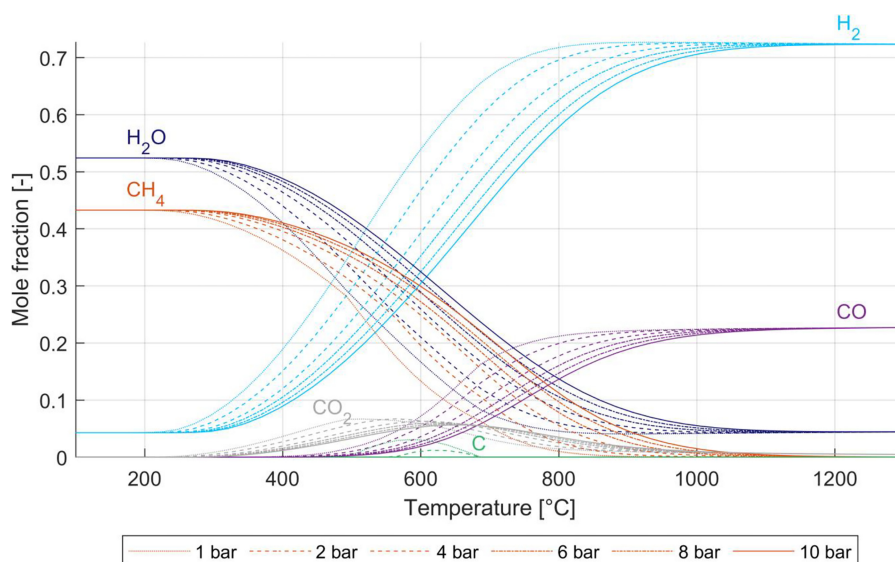


**Figure 15.3.** Dependence of the equilibrium composition of co-SOEC syngas on temperature and pressure based on a co-SOEC syngas composition with a 3% hydrogen excess (76.8 vol% H<sub>2</sub>, 18.3 vol% CO, and 4.9 vol% CO<sub>2</sub>) [43].

76.8 vol% H<sub>2</sub>, 18.3 vol% CO, and 4.9 vol% CO<sub>2</sub>. This composition contains hydrogen at more than 3% above the stoichiometric concentration according to equations (15.1) and (15.2) and is highly suitable for methanation purposes.

According to figure 15.3, moderate temperatures below 320 °C are necessary to achieve full conversion at maximum CH<sub>4</sub> concentration. In any event, temperatures below 400 °C are necessary to achieve sufficiently high methane concentrations, even at increased pressures above 4 bar. The beneficial effect of increased pressures between 1 and up to 10 bar is illustrated in figure 15.3 through different line styles. Increased pressures of 4 bar and higher not only lead to higher equilibrium methane concentrations but also reduce the tendency toward carbon formation between 500 °C and 700 °C.

In terms of the practical implications of the reactor temperature for reactor performance, contrary effects must be expected based on thermodynamics and kinetics. Starting from the ignition temperature (225 °C–285 °C [24–26]), the reaction rate increases with rising temperature until the temperature approaches the thermodynamic equilibrium value. On the other hand, based on thermodynamic equilibrium, the highest methane concentration can be expected at moderate temperatures, as already discussed according to figure 15.3. This antagonistic interplay between thermodynamics and kinetics makes temperature control in methanation systems highly important. A trade-off between high reaction rates at higher temperatures and high equilibrium product concentrations at lower temperatures is necessary to achieve optimum heat management and therefore reactor performance. Neubert [7] aptly called this crucial interaction between plant complexity, thermodynamics, and kinetics the ‘trilemma of methanation.’ The issue of optimum reactor temperature profiles is further addressed in section 15.4.

The Boudouard reaction (equation (15.4)) or the decomposition reactions of methane or higher hydrocarbons lead to the formation of solid carbon, which is deposited on the active catalyst sites. Different forms of carbon can be formed, such as graphitic carbon, amorphous carbon, vermicular carbon, bulk  $\text{Ni}_3\text{C}$ , or adsorbed carbon species. The tendency toward carbon formation is influenced by the C–H–O ratio and the temperature and the pressure of the process gas. High proportions of H and O reduce the risk of carbon formation. In consequence, the higher the over-stoichiometric excess of hydrogen, the lower the carbon formation risk. In addition, the injection of water into the methanation feed is an option that reduces the carbon formation tendency at the cost of hindering kinetic effects [26] and reducing equilibrium concentrations. [5]

In figure 15.4, the ternary C–H–O diagram is shown, which describes the risk of graphitic carbon formation. For each temperature-pressure pair, this diagram can be divided by an equilibrium curve into an upper section, in which carbon formation is thermodynamically possible, and a lower one, where it is not. Depending on the process gas’s C–O–H ratio, the alignment within this diagram gives a good indication of whether or not carbon formation is likely to happen. With an increasing excess of hydrogen based on the same  $\text{CO}/\text{CO}_2$  ratio, the tendency

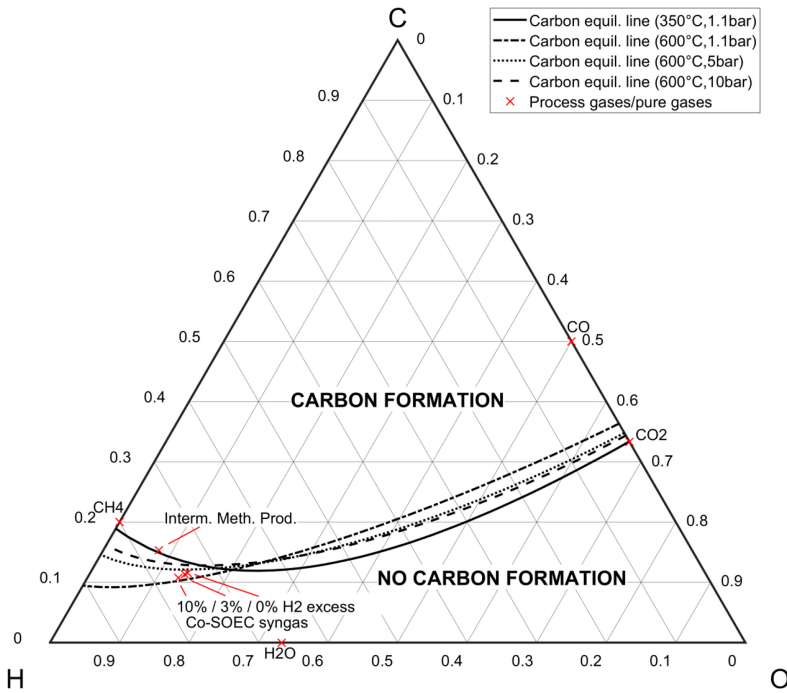


**Figure 15.4.** Ternary C–O–H diagram with pure gases and process gases (red ‘x’-markings) including co-SOEC syngas with 0%, 3%, and 10% of excess  $\text{H}_2$  and an intermediate methanation product after water removal. Graphitic carbon formation equilibrium lines for four temperature-pressure pairs (350 °C/1.1 bar; 600 °C/1.1 bar; 600 °C/5 bar; 600 °C/10 bar) divide the areas of thermodynamically possible carbon deposition. Figure adapted from Krammer *et al* [43].

toward carbon formation can be reduced, although even high proportions of hydrogen do not completely eliminate the risk. In fact, the pressure has to be kept elevated for typical co-SOEC compositions to prevent carbon deposition at any temperature. The increased potential for the formation of carbon at around 600 °C and 1.1 bar pressure in figure 15.4 is in alignment with stable equilibrium shares at low pressures and similar temperatures in figure 15.3.

## 15.4 Requirements for the successful methanation of co-SOEC syngas

The coordinated interplay between co-SOECs and methanation determines the success of a combined PtG plant. The syngas concentration influences not only the preferred reactor design, including the catalyst and the cooling method, but also the necessary pressure and resulting temperature profile that avoid carbon deposition and produce high-quality synthetic natural gas (SNG). This section discusses the requirements for co-SOEC syngas, based on the fundamentals of thermodynamics and kinetics elaborated in sections 15.2 and 15.3. Furthermore, a feasible reactor concept and promising operating conditions are derived.

The syngas generated by a co-SOEC without further process gas treatment other than water removal mainly consists of hydrogen and carbon monoxide, depending on the electrolyzer's feed concentration and recycling ratio. Small amounts of carbon dioxide downstream from the electrolyzer are the unproblematic result of incomplete CO<sub>2</sub> reduction [44]. A feed gas mixture for methanation purposes needs to follow certain criteria regarding minimum hydrogen content according to the methanation reactions. The H<sub>2</sub>-CO ratio needs to be greater than three and the remaining hydrogen should result in a H<sub>2</sub>-CO<sub>2</sub> ratio of more than four to guarantee an over-stoichiometric hydrogen concentration. As discussed in section 15.3 and illustrated in figure 15.4, the tendency for the reaction to form solid carbon can be reduced by increasing the hydrogen in the methanation feed to a level greater than the stoichiometric level. In addition, higher hydrogen contents lead to higher conversions of CO/CO<sub>2</sub>. On the other hand, the higher the excess of hydrogen in the syngas, the more unconverted hydrogen remains in the SNG product downstream from the methanation, even at full CO/CO<sub>2</sub> conversion. Due to a reduction in the total process gas volume flow within the methanation reactor (a consequence of the mole-decreasing reactions and the subsequent removal of formed water), the relative volumetric proportion of hydrogen in the product is even higher than in the syngas. For example, a share of 10 vol% excess hydrogen in the co-SOEC syngas serving as the methanation feed would result in about 23 vol% of H<sub>2</sub> in the dry SNG, assuming complete methanation and full water removal. The option of hydrogen recycling from the SNG product back to the feed is suboptimal, since it requires gas separation equipment such as polymer membranes [45], which increase plant complexity and decrease efficiency. Therefore, it is most feasible to omit recycle lines and employ direct injection into the natural gas grid in one run, while allowing the excess hydrogen to remain in the SNG. According to a joint report by the European Network of Transmission System Operators for Gas (ENTSOG),

Hydrogen Europe, and Gas Infrastructure Europe, moderate proportions of 10 vol% of hydrogen are technically already feasible for natural gas grids in most areas of Europe with no or little adaption [46, 47]. In Austria, 10 vol% of hydrogen is tolerated since 2021, according to recent legislation [48]. In Germany, up to 10 vol% of hydrogen, and, based on a recently released technical code starting in fall 2021, even higher concentrations are tolerated, depending on local grid requirements [49]. In this regard, the aim should be a trade-off between reducing the carbon deposition tendency and high conversion versus acceptable hydrogen proportions in the SNG product. To give a concrete example, a typical co-SOEC concentration of 76.8 vol% H<sub>2</sub>, 18.3 vol% CO, and 4.9 vol% CO<sub>2</sub> was tested in experiments and by modeling [43]. Based on this input concentration at full methanation, almost 90 vol% of methane and 10 vol% of hydrogen could be generated after a final drying step, which represents an attractive SNG product for direct grid injection. As a consequence, for this suggested co-SOEC composition, a hydrogen excess of 3% in the methanation feed results in a moderate hydrogen content of 10 vol% in the SNG product. However, an elevated pressure of at least 4 bar should be considered to prevent carbon deposition (figure 15.3).

The temperature profile within a catalytic two-phase reactor is an essential performance parameter that determines the reaction kinetics, catalyst degradation, and thermodynamic outlet concentration. The CO methanation reaction is accompanied by a higher exothermal reaction enthalpy compared to that of CO<sub>2</sub> methanation (compare equations (15.1) and (15.2)), which makes heat removal in co-SOEC syngas methanation even more relevant. As already discussed in section 15.2, the proven temperature-control concepts of adiabatic fixed beds are based on intermediate heat removal, staged heat injection, product recycling, or steam injection [2, 7]. However, the overall plant efficiency is higher and the required catalyst mass and reactor volume are lower if the reaction heat is directly removed from the catalyst in actively cooled polytropic reactors. Therefore, direct reactor cooling in fixed-bed, structured, or microstructured systems is a promising approach for cost-effective and high-capacity methanation. Recent research progress into temperature control strategies for catalytic methanation is addressed in the following section.

Reaction temperature control is an important area of recent research into catalytic methanation. For two-phase catalytic methanation, two main tasks can be accomplished by reactor cooling, as shown in figure 15.5. The first is to prevent the maximum temperature of the catalyst from being exceeded, thereby preventing sintering. The second is to guarantee a high thermodynamic equilibrium concentration of methane at the reactor outlet [7].

Kiewidt and Thöming [6] determined an optimal temperature profile based on a Semenov number-optimization method for single-stage methanation systems. The space-time yield could be increased twofold by temperature profile optimization based on the Semenov number, which can be tuned via the reactor diameter and gas load. The authors emphasized the importance of heat transfer to a cooling medium. Enhanced heat removal can also be realized with structured and microstructured reactors at the expense of higher investment costs. Using 1D modeling, El-Sibai *et al* [50]

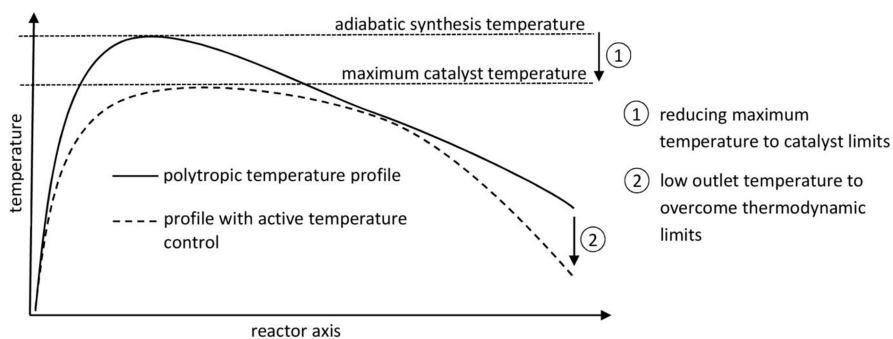


**Figure 15.5.** Schematic illustration of the two main purposes of active reactor cooling for methanation systems. Reproduced based on a figure by Neubert [7].

found that the most cost efficient number of cooled fixed-bed reactors in a cascade with intermediate water removal is two, whereas three reactors leads to a maximum space–time yield. In addition, the authors found that a minimization of reactor diameter is beneficial, since it enhances heat transfer to the cooling medium and increases the area-to-volume ratio. Although research activity for microstructured reactors is still high, plate reactors for small-scale applications are already commercially available with a GHSV of  $31\,500\text{ h}^{-1}$  for  $\text{CO}_2$  methanation. The catalyst is placed in microbeds stacked sequentially between cooling foils, ensuring that the surfaces have very high heat transfer capabilities [8]. In contrast to two-phase reactors, three-phase methanation allows for almost isothermal conditions at the expense of lower gas/liquid mass transfer rates. As a result, three-phase systems are not limited by heat transfer, but by mass transfer—to an extent that makes them inferior in terms of space-time yield. A comparison of fixed-bed tube bundle reactor and slurry bubble column reactor methanation revealed that a much higher GHSV is possible for fixed-bed reactors. However, for transient conditions, the slurry bubble column reactor is far more temperature stable, as the fixed-bed temperature fluctuations are immense [9, 51]. In summary, tube-bundle reactors are an attractive technology for large-scale PtG plants, as they allow for efficient heat removal at moderate costs. Nevertheless, promising research progress in the field of heat-transfer-optimized structured and microstructured systems might outweigh their complexity drawbacks in future.

In terms of operational pressure, higher pressure is beneficial for both thermodynamics (figure 15.3) and kinetics. The more the operational pressure is increased, the more the methane concentration and the  $\text{CO}/\text{CO}_2$  conversion downstream from a catalytic methanation reactor converting co-SOEC syngas become higher [43]. However, higher pressures require more compression power, which influences the overall PtG efficiency. As a result, the pressure level should be held as low as possible to provide sufficient methanation performance. In addition, carbon deposition should be taken into account, which can be reduced by increased pressures. In addition, the downstream process, e.g. the gas grid



pressure level, should be considered in this regard. The compression of process gas can be conducted at different stages within the process configuration. In section 15.5, the influence of compressor alignment on process efficiency is elaborated.

## 15.5 Energetic efficiency and the socioeconomic impact of co-SOEC syngas methanation

The successful implementation of a PtG technology depends on its economic feasibility in an existing energy market. The balance of the costs and revenues of a PtG system needs to compete with conventional energy provision technologies, such as fossil fuels, which have profited from decades of technical development. The current economic situation and the future outlook for a combined co-SOEC and methanation PtG plant was described by Böhm *et al* [52]. The authors considered learning and scaling effects on capital expenditure (CAPEX) to evaluate the systems competitiveness of renewable SNG in comparison to conventional natural gas. For a 10 MW plant in 2030, Böhm *et al* predict SNG costs of 8.5 c€/kWh, compared to an average natural gas price of ~3.03 c€/kWh for non-household consumers in the first half of 2021 for the EU-27 [53]. The most relevant ordering of the SNG production costs is (in chronological order of contribution): electrical energy price > CAPEX > OPEX > CO<sub>2</sub> supply costs. The revenue generated by the electrolysis-side product, oxygen, which can be directly used in the combined industrial processes, has a beneficial cost effect. The savings in terms of CO<sub>2</sub> certificates reduce the SNG production costs further, but to a lesser extent than the oxygen. Higher CO<sub>2</sub> certificate prices of at least 330 €/t<sub>CO2</sub> would be necessary to achieve cost parity, even in the long run. Based on a sensitivity analysis, the authors investigated the influence of cost parameters on the SNG production costs. As electrical energy costs are dominant, enhancing the energetic system efficiency results in the highest positive impact on the SNG costs. A 10% improvement in efficiency results in about a 10% reduction in SNG production costs. The second most sensitive influence parameter is the system lifetime, which only leads to a single-digit percentage cost reduction for a 25% lifetime increase [52].

Therefore, the overall energetic efficiency of SNG production in a combined co-SOEC and methanation plant that uses electric energy is critical to its economic success. As the chemical equations show, the methanation process releases significant quantities of reaction heat (equation (15.1) and equation (15.2)). This thermal energy can be used to preheat and evaporate water before it is fed to the co-SOEC system. Since the temperature range of the co-SOEC (600 °C–850 °C [54]) exceeds the maximum methanation cooling temperature (300 °C [9]), only preheating and evaporation of the co-SOEC feed water is possible. However, the excess methanation heat can be used to cover part of the co-SOEC energy demand. Posdziech *et al* found efficiencies for a SOEC system based on a lower heating value (LHV) of 60.5% with a steam generator and compression, 72% if no steam generator was necessary due to waste steam integration, and 84.5% without a steam generator or a compressor. Based on the higher heating value (HHV) the



authors found 84.4% system efficiency with heat integration [55]. In agreement with these results, Ancona *et al* reported efficiencies of between 80% and 85% for a combined co-SOEC and methanation system based on the HHV [54]. Wang *et al* targeted realistic HHV efficiencies for SOEC-based power-to-methane plants of between 70% and 75% [56].

The beneficial synergy effect of a combined co-SOEC and methanation system can be concretely demonstrated using efficiency calculations. Equation (15.10) gives the principal system efficiency of a combined co-SOEC and methanation PtG plant.

$$\begin{aligned}
 \eta_{\text{PtG}} &= \eta_{\text{co-SOEC}} \cdot \eta_{\text{compression}} \cdot \eta_{\text{methanation}} \\
 &= \frac{P_{l, \text{syngas}}}{P_{\text{el, co-SOEC}}} \cdot \frac{P_{l, \text{syngas}}}{P_{l, \text{syngas}} + P_{\text{el, compr.}}} \cdot \frac{P_{l, \text{SNG}}}{P_{l, \text{syngas}}} \\
 &= \frac{H_{l, \text{syngas}} \dot{m}_{\text{syngas}}}{P_{\text{el, co-SOEC}}} \cdot \frac{H_{l, \text{syngas}} \dot{m}_{\text{syngas}}}{H_{l, \text{syngas}} \dot{m}_{\text{syngas}} + P_{\text{el, compr.}}} \cdot \frac{H_{l, \text{SNG}} \dot{m}_{\text{SNG}}}{H_{l, \text{syngas}} \dot{m}_{\text{syngas}}} \quad (15.10)
 \end{aligned}$$

For an example case of a 10 MW PtG unit, we now calculate the resulting LHV system efficiency and SNG output with and without heat integration of a combined co-SOEC and methanation plant in detail. The unit capacity is based on the co-SOEC input power, which can be a combination of electric and thermal energy. Losses from electricity conversion or CO<sub>2</sub> removal from off-gases are not considered. Table 15.3 gives the nomenclature of all the calculation variables. Following the published efficiency values mentioned above for SOEC systems, a co-SOEC efficiency of 73% (which does not include waste heat integration or compression) was considered in the calculations. As a result, 975.8 kg/h syngas can be produced from 10 MW of power input, as demonstrated by equation (15.11), providing a syngas concentration of 76.8 vol% of H<sub>2</sub>, 18.3 vol% of CO, and 4.9 vol% of CO<sub>2</sub> on a dry basis.

$$\begin{aligned}
 \dot{m}_{\text{syngas}} &= \frac{\eta_{\text{co-SOEC}} P_{\text{in, co-SOEC}}}{H_{l, \text{syngas}}} = \frac{\eta_{\text{co-SOEC}} P_{\text{in, co-SOEC}}}{\frac{1}{M_{\text{mix, syngas}}} \left( H_{l, \text{H}_2} y_{\text{H}_2} M_{\text{H}_2} + H_{l, \text{CO}} y_{\text{CO}} M_{\text{CO}} \right)} \\
 &= \frac{0.73 \cdot 10 \cdot 10^6 [\text{W}]}{\frac{1}{8.83 \left[ \frac{\text{g}}{\text{mol}} \right]} \left( 119972 \left[ \frac{\text{J}}{\text{g}} \right] \cdot 0.768 \cdot 2.02 \left[ \frac{\text{g}}{\text{mol}} \right] + 10103 \left[ \frac{\text{J}}{\text{g}} \right] \cdot 0.183 \cdot 28.01 \left[ \frac{\text{g}}{\text{mol}} \right] \right)} \\
 &= 0.271 \left[ \frac{\text{kg}}{\text{s}} \right] = 975,8 \left[ \frac{\text{kg}}{\text{h}} \right] \quad (15.11)
 \end{aligned}$$

Before it arrives at the methanation unit, the syngas needs to be compressed. For a given pressure increase and gas mass flow, the electrical power consumption of the compressor can be determined. The resulting temperature of isentropic compression due to the pressure increase from 1.1 bar to 10 bar is demonstrated in equation (15.12).

**Table 15.3.** Nomenclature.

$E_{a,j}$	$\text{J mol}^{-1}$	Activation energy of reaction j
$c_{p,\text{mix}}$	$\text{J K}^{-1} \text{mol}^{-1}$	Heat capacity of the syngas mixture
$GHSV_{\text{STP}}$	$\text{h}^{-1}$	Gas hourly space velocity
$H_{1,\text{CO}}$	$\text{kJ kg}^{-1}$	Lower heating value of CO at stp
$H_{1,\text{H}_2}$	$\text{kJ kg}^{-1}$	Lower heating value of H <sub>2</sub> at stp
$H_{1,\text{SNG}}$	$\text{kJ kg}^{-1}$	Lower heating value of SNG at stp
$H_{1,\text{syngas}}$	$\text{kJ kg}^{-1}$	Lower heating value of syngas at stp
$K_i$	$\text{bar}^{-a,b,c}$	Adsorption constant for gas species i
$K_{i,0}$	$\text{bar}^{-a,b,c}$	Pre-exponential factor of adsorption
$k_j$	varying unit	Reaction rate coefficient of reaction j
$k_{j,0}$	varying unit	Pre-exponential factor of reaction rate coefficient
$K_{p,\text{CO}_2\text{-Meth}}$	$\text{bar}^{-2}$	Equilibrium constant
$M_{\text{CO}}$	$\text{g mol}^{-1}$	Molar mass of CO
$M_{\text{H}_2}$	$\text{g mol}^{-1}$	Molar mass of H <sub>2</sub>
$M_{\text{mix,syngas}}$	$\text{g mol}^{-1}$	Molar mass of syngas mixture
$\dot{m}_{\text{SNG}}$	$\text{kg s}^{-1}$	Mass flow of SNG
$\dot{m}_{\text{syngas}}$	$\text{kg s}^{-1}$	Mass flow of syngas
$\dot{n}_{\text{CO}}$	$\text{mol s}^{-1}$	Mole flow of CO
$\dot{n}_{\text{CO}_2}$	$\text{mol s}^{-1}$	Mole flow of CO <sub>2</sub>
$P_{\text{el,compr}}$	W	Electric power consumed by compressor
$P_{\text{el,Co-SOEC}}$	W	Electric power consumed by Co-SOEC
$p_i$	bar	Partial pressure of gas species i
$p_{\text{in}}$	bar	Low pressure level at compressor input
$P_{\text{isentr.}}$	W	Power consumption for isentropic compress.
$P_{1,\text{syngas}}$	W	Calorific power of syngas based on lower heating value
$P_{1,\text{SNG}}$	W	Calorific power of SNG based on lower heating value
$p_{\text{out}}$	bar	High pressure level at compressor output
$P_{\text{reaction heat}}$	W	Thermal power by methanation reaction heat
$p_{\text{STP}}$	bar	Standard pressure
$R$	$\text{J K}^{-1} \text{mol}^{-1}$	Ideal gas constant
$r_j$	$\text{mol kg}^{-1} \text{s}^{-1}$	Reaction rate of reaction j
$T$	K	Temperature
$T_{\text{in}}$	K	Temperature at compressor input
$T_{\text{out,isentr.}}$	K	Temperature at compressor output for isentropic compression
$T_{\text{STP}}$	K	Standard temperature
$U_{\text{CO}}$		CO conversion
$U_{\text{CO}_2}$		CO <sub>2</sub> conversion
$V_{\text{catalyst}}$	$\text{m}^3$	Catalyst bed volume
$\dot{V}_{\text{in}}$	$\text{m}^3 \text{h}^{-1}$	Input operating volume flow
$y_{\text{CO}}$		Mole fraction of CO in syngas
$y_{\text{H}_2}$		Mole fraction of H <sub>2</sub> in syngas
$\Delta H_{\text{ads},i}$	$\text{J mol}^{-1}$	Enthalpy of adsorption for gas species i
$\Delta H_{\text{r,COM}}^0$	$\text{J mol}^{-1}$	Reaction enthalpy of CO methanation (STP)

$\Delta H_{r,CO_2M}^0$	$J \text{ mol}^{-1}$	Reaction enthalpy of $CO_2$ methanation (STP)
$\eta_{\text{compression}}$		Efficiency of compression
$\eta_{\text{co-SOEC}}$		Efficiency of co-SOEC
$\eta_{\text{heat transf.}}$		Efficiency of heat transfer from methanation to co-SOEC
$\eta_{\text{isentr. compr.}}$		Efficiency of isentropic compression of gas
$\eta_{\text{methanation}}$		Efficiency of methanation system
$\eta_{\text{PtG}}$		Efficiency of power to gas system

For a mass flow of  $975.8 \text{ kg h}^{-1}$  of process gas, the isentropic compression power is calculated using equation (15.13). The electrical power consumed by the compressor, assuming an isentropic compression efficiency of 65% (not to be confused with the compression efficiency of the PtG system), can be expressed as shown in equation (15.14). Equation (15.15) can be used to determine the contribution of the compression efficiency to the overall PtG efficiency (as used in equation (15.10)).

$$\begin{aligned}
 T_{\text{out, isentr.}} &= T_{\text{in}} \cdot \exp\left(\frac{R}{c_{p, \text{mix}}} \cdot \ln\left(\frac{p_{\text{out}}}{p_{\text{in}}}\right)\right) \\
 &= 298.15[\text{K}] \cdot \exp\left(\frac{8.314\left[\frac{\text{J}}{\text{K mol}}\right]}{29.3\left[\frac{\text{J}}{\text{K mol}}\right]} \cdot \ln\left(\frac{10[\text{bar}]}{1.1[\text{bar}]}\right)\right) = 556.3[\text{K}]
 \end{aligned} \tag{15.12}$$

$$\begin{aligned}
 P_{\text{isentr.}} &= \frac{\dot{m}_{\text{syngas}}}{M_{\text{mix, syngas}}} c_{p, \text{mix}} (T_{\text{out, isentr.}} - T_{\text{in}}) \\
 &= \frac{0.271\left[\frac{\text{kg}}{\text{s}}\right]}{8.83 \cdot 10^{-3}\left[\frac{\text{kg}}{\text{mol}}\right]} 29.4\left[\frac{\text{J}}{\text{K mol}}\right] (556.3[\text{K}] - 298.15[\text{K}]) \\
 &= 233.1 [\text{kW}]
 \end{aligned} \tag{15.13}$$

$$P_{\text{el. compr.}} = \frac{P_{\text{isentr.}}}{\eta_{\text{isentr. compr.}}} = \frac{233.1 [\text{kW}]}{0.65} = 358.6[\text{kW}] \tag{15.14}$$

$$\begin{aligned}
 \eta_{\text{compression}} &= \frac{H_{l, \text{syngas}} \dot{m}_{\text{syngas}}}{H_{l, \text{syngas}} \dot{m}_{\text{syngas}} + P_{\text{el. compr.}}} \\
 &= \frac{26932\left[\frac{\text{kJ}}{\text{kg}}\right] \cdot 0.271\left[\frac{\text{kg}}{\text{s}}\right]}{26932\left[\frac{\text{kJ}}{\text{kg}}\right] \cdot 0.271\left[\frac{\text{kg}}{\text{s}}\right] + 358.6 [\text{kW}]} = 0.953
 \end{aligned} \tag{15.15}$$

The loss of exergy in the methanation process is based on the exothermic heat released by the chemical reaction, which needs to be removed from the reactor system. At full conversion, the maximum possible amount of exothermic heat is produced. For full stoichiometric CO methanation, the thermodynamically determined efficiency based on the lower heating value is 80%; for stoichiometric CO<sub>2</sub> methanation, it is 83% [7]. The efficiency of co-SOEC syngas methanation is calculated as shown in equation (15.16).

$$\begin{aligned}
 \eta_{\text{methanation}} &= \frac{H_{l, \text{SNG}} \dot{m}_{\text{SNG}}}{H_{l, \text{syngas}} \dot{m}_{\text{syngas}}} = \frac{H_{l, \text{syngas}} \dot{m}_{\text{syngas}} - P_{\text{reaction heat}}}{H_{l, \text{syngas}} \dot{m}_{\text{syngas}}} \\
 &= \frac{H_{l, \text{syngas}} \dot{m}_{\text{syngas}} - \dot{n}_{\text{CO}} \Delta H_{r, \text{COM}}^0 U_{\text{CO}} - \dot{n}_{\text{CO}_2} \Delta H_{r, \text{CO}_2\text{M}}^0 U_{\text{CO}_2}}{H_{l, \text{syngas}} \dot{m}_{\text{syngas}}} \\
 &= \frac{H_{l, \text{syngas}} \dot{m}_{\text{syngas}} - \frac{\dot{m}_{\text{syngas}}}{M_{\text{mix, syngas}}} \left( y_{\text{CO}} \Delta H_{r, \text{COM}}^0 U_{\text{CO}} + y_{\text{CO}_2} \Delta H_{r, \text{CO}_2\text{M}}^0 U_{\text{CO}_2} \right)}{H_{l, \text{syngas}} \dot{m}_{\text{syngas}}} \\
 &= \frac{26932 \left[ \frac{\text{kJ}}{\text{kg}} \right] \cdot 0.271 \left[ \frac{\text{kg}}{\text{s}} \right] - \frac{0.271 \left[ \frac{\text{kg}}{\text{s}} \right]}{8.83 \cdot 10^{-3} \left[ \frac{\text{kg}}{\text{mol}} \right]} \left( 0.183 \cdot 206 \left[ \frac{\text{kJ}}{\text{mol}} \right] \cdot 1 + 0.049 \cdot 164 \left[ \frac{\text{kJ}}{\text{mol}} \right] \cdot 1 \right)}{26932 \left[ \frac{\text{kJ}}{\text{kg}} \right] \cdot 0.271 \left[ \frac{\text{kg}}{\text{s}} \right]} \\
 &= 0.8078 \tag{15.16}
 \end{aligned}$$

The efficiency values of co-SOEC, compression, and methanation without heat integration add up to an overall PtG efficiency of 56.2% according to equation (15.17).

$$\begin{aligned}
 \eta_{\text{PtG}} &= \eta_{\text{co-SOEC}} \cdot \eta_{\text{compression}} \cdot \eta_{\text{methanation}} \\
 &= 0.73 \cdot 0.953 \cdot 0.808 = 0.562 \tag{15.17}
 \end{aligned}$$

For heat-integrated PtG systems, the excess heat generated by the methanation system can be used to reduce the electrical energy input and produce the same amount of SNG. With heat integration, the system efficiency changes to equation (15.18).

$$\begin{aligned}
 \eta_{\text{PtG, integr}} &= \eta_{\text{co-SOEC, integr}} \cdot \eta_{\text{compression}} \cdot \eta_{\text{methanation}} \\
 &= \frac{H_{l, \text{syngas}} \dot{m}_{\text{syngas}}}{P_{\text{in, co-SOEC}} - P_{\text{reaction heat}}} \cdot \eta_{\text{compression}} \cdot \eta_{\text{methanation}} \\
 &= \frac{7.3 \cdot 10^6 [\text{W}]}{10 \cdot 10^6 [\text{W}] - 1.4033 \cdot 10^6 [\text{W}]} \cdot 0.952 \cdot 0.808 = 0.849 \cdot 0.952 \cdot 0.808 \\
 &= 0.654 \tag{15.18}
 \end{aligned}$$

An efficiency of 65.4% would therefore be possible for a co-SOEC and methanation PtG plant with heat integration, according to the assumptions used

above; this efficiency is 9.2 percentage points higher than without heat integration. 1.4 MW of heat would be recycled back to the co-SOEC system, reducing the total electric energy demand for the electrolysis from 10 MW to 8.6 MW. The system efficiency could be increased even further if more waste heat from secondary industrial processes were integrated into the co-SOEC. According to Sapountzi *et al* [57], HHV efficiencies close to 100% are possible for SOECs with thermal integration.

As Böhm *et al* [52] found, system efficiency plays an essential role in reducing SNG costs. Accordingly, a sensitivity analysis was carried out to investigate the most important parameters that enhance the efficiency of PtG systems.

As shown in figure 15.6, heat integration plays a fundamental role in enhancing the efficiency of combined co-SOEC and methanation. The integration of 50% more heat, starting from a base value of the methanation reaction heat, leads to an increase of about six percentage points of system efficiency. Based on process flowcharts, the recycling of methanation reaction heat to the co-SOEC input is further explained in section 15.6. A reduction in CO/CO<sub>2</sub> methanation conversion or an increase in H<sub>2</sub> excess also improves the system efficiency, since more H<sub>2</sub> is simply passed through the methanation. However, the gas quality regulations for SNG grid injection require high methane and low hydrogen concentrations and therefore high conversion rates and moderate H<sub>2</sub> excesses. Furthermore, a reduction in compressor power leads to higher efficiencies, which is a promising approach for PtG enhancement. The compression energy can be reduced by the ‘dual-pressure-level

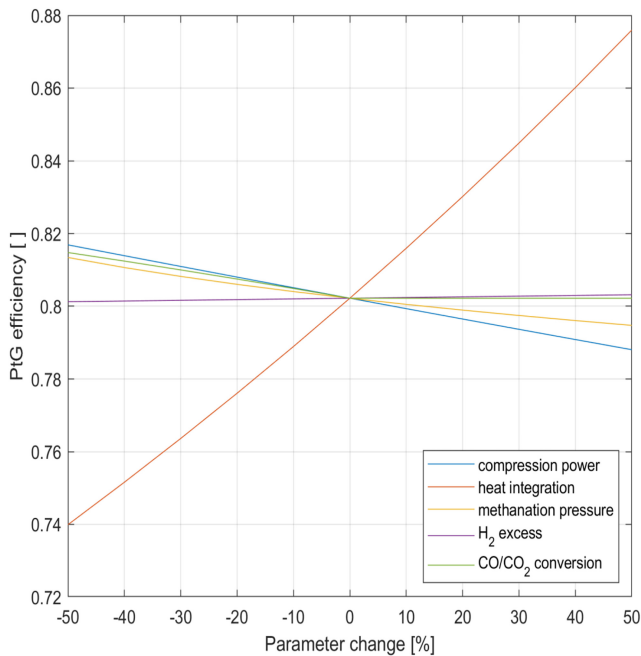


Figure 15.6. Sensitivity analysis of the overall co-SOEC and methanation PtG system.

methanation' concept further discussed in section 15.6. A reduction in methanation pressure by 40% from 10 bar to 6 bar led to an increase in overall efficiency of only one percentage point. Various other impacts such as methanation conversion and carbon deposition have to be considered with pressure changes.

## 15.6 Promising plant designs for efficient SNG production

The main technical benefit of combining endothermic co-SOEC with exothermic methanation lies in the possibility of transferring excess heat between these two process steps and therefore increasing the overall energy efficiency of the combined system. Using thermal integration, a combined co-SOEC and methanation system can convert 'green' electrical energy into methane at high LHV efficiencies of around 74%, based on the assumptions presented in section 15.5.

Figure 15.7 shows a possible plant design for a heat-integrated PtG system that includes co-SOEC and methanation. In addition to water, CO<sub>2</sub> from industrial sources is fed to the co-SOEC, producing a syngas mixture suitable for subsequent methanation. The water of the wet syngas needs to be condensed before it reaches the compressor. In order to reach a reactor pressure suitable for effective methanation at a low carbon deposition potential, the syngas is compressed to at least 4 bar, but usually up to 20 bar or higher. The methanation pressure level can be coordinated with the subsequent drying step and in particular with the necessary natural gas grid injection pressure. This PtG process design includes thermal integration, which is achieved by transferring methanation reaction heat to the co-SOEC water input. Thermal oil, pressurized boiling water, or molten salt can be used as cooling media in combination with a tube-bundle methanation reactor.

The compression of hydrogen and carbon monoxide requires gastight equipment that complies with increased safety standards. Furthermore, the position of the compressor significantly influences its compression capacity and, as a result, the overall plant efficiency. The compression of a higher volume flow of syngas at

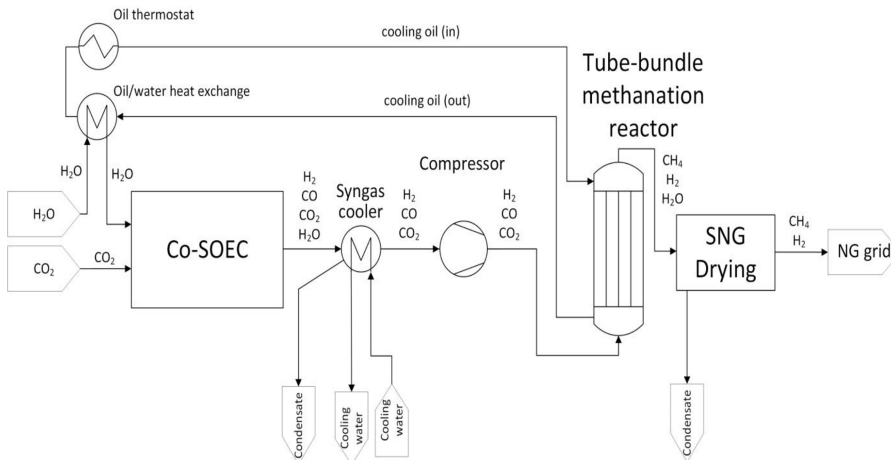


Figure 15.7. Possible plant design for a combined co-SOEC methanation PtG plant.

the co-SOEC outlet consumes a higher amount of electrical energy compared to other positions within the plant. Two alternative plant designs that result in reduced compression energy consumption are introduced below.

The ‘dual-pressure-level methanation’ concept is based on two sequential methanation reactors with intermediate water removal, as shown in figure 15.8. The compressor is placed between the first and the second reactor. As a result of a partial reaction in Reactor 1, less process gas needs to be compressed due to the volume-consuming reaction in the first reactor and intermediate water removal prior to compression. The use of intermediate compression can reduce the required compression capacity by up to 42% [43].

However, the carbon deposition risk within the second reactor is highly increased due to the removal of water. The tendency of the intermediate process gas to form solid carbon is shown in the ternary diagram of figure 15.4. Even at 10 bar of pressure, carbon deposition must be expected at certain temperatures. Higher pressures, higher hydrogen excesses, or excellent temperature control strategies would be necessary to reduce the carbon formation risk [43].

As an alternative to intermediate compression,  $\text{CO}_2$  and  $\text{H}_2\text{O}$  can be fed at already increased pressures to the methanation system, as shown in figure 15.9. The benefit of this design for the overall process is reduced energy consumption and the technically simple and safe compression of liquid water and  $\text{CO}_2$  compared to  $\text{H}_2$ - and  $\text{CO}$ -containing syngas. On the other hand, the co-SOEC needs to be operated under pressure. Brabandt and Poszdiech [58] overcame the mechanical problems of pressurized SOEC operation and successfully operated at 15 bar of pressure. The authors emphasized the efficiency benefits of the direct injection of pressurized steam from industrial processes and the combination with high-pressure downstream processes. Five percent to seven percent of the electrical energy demand

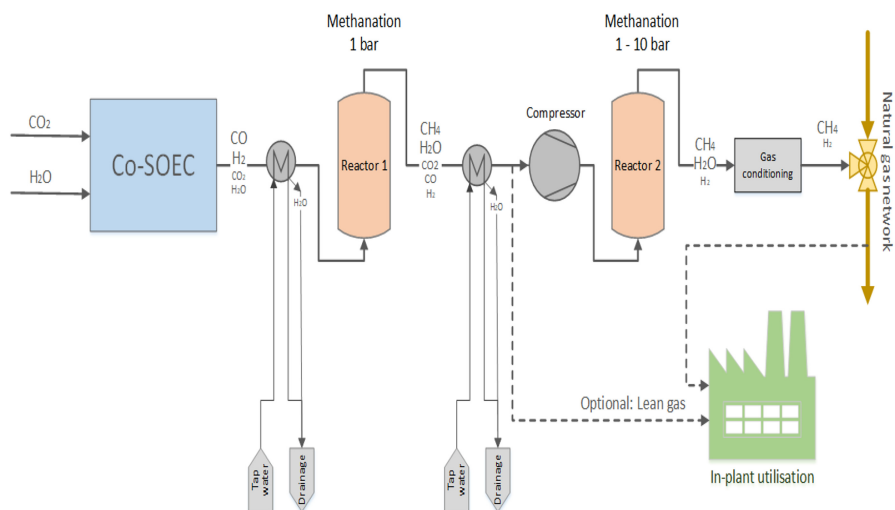


**Figure 15.8.** PtG plant design with dual-pressure-level methanation, including intermediate compression [43].

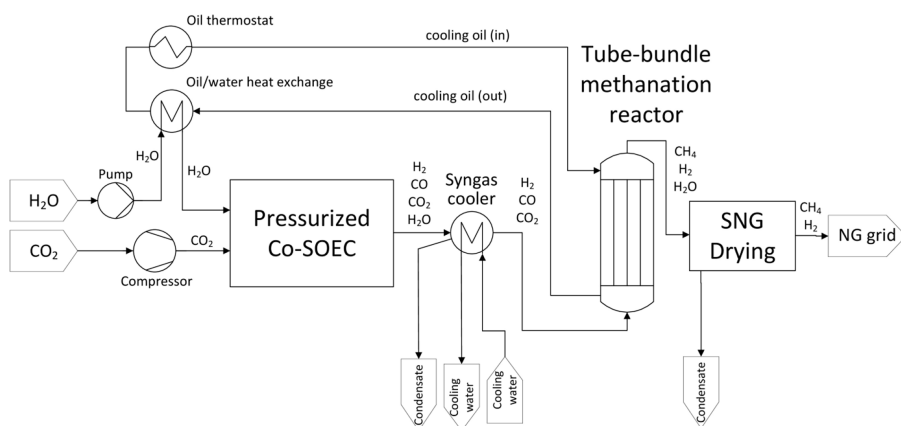


Figure 15.9. PtG process design including a pressurized co-SOEC.

can be saved by the direct provision of high-pressure steam instead of downstream hydrogen compression [58]. On the other hand, high-pressure (co-)SOEC is more complex due to the higher sealing effort required and suffers from increased cross permeation, higher temperatures, and a higher necessary operational voltage [58, 59].

In a fully integrated PtG plant, the direct integration of cooling water with the co-SOEC feed leads to the minimization of heat losses. Gruber *et al* [60] tried to directly couple a SOEC with a methanation system using steam from cooling water cycle as an SOEC feed. Unfortunately, it was not possible to control the steam mass flow to the extent necessary for full-load operation. However, the authors emphasized the positive effect on the overall efficiency. The use of water as a cooling medium would require pressures of more than 75 bar to guarantee a liquid cooling medium. Otherwise, the cooling water would evaporate, leading to a significant loss of heat transfer.

Although the main application scenarios of catalytic methanation will certainly be found in the area of industrial-scale energy provision, with the aim of preserving the living conditions on our globe, some potential purposes of this technology may go beyond the boundaries of planet Earth. An additional interesting aspect of the methanation process is its potential for long-term manned space missions. Hydrogen, a by-product of  $O_2$  production by the electrolysis of water in order to provide air for breathing, can be used with exhaled  $CO_2$  or  $CO_2$  from Mars' atmosphere to produce methane and water by methanation. Water can then again be used for  $O_2$  production and liquid methane can be used as propellant. As a result, closed-loop oxygen and water recycling is possible in space using methanation [61]. In 2011, a methanation system was installed at the International Space Station [62]. In 2012, a methanation system was demonstrated which was designed to produce methane on Mars from eighteen times lighter (and therefore cheaper) transportable hydrogen together with  $CO_2$  harvested from Mars' atmosphere, leading to a significant reduction in transport expenses [63].



## 15.7 Concluding remarks

The combination of co-SOEC and methanation enables carbon dioxide to be recycled into a valuable natural gas substitute powered by renewable electrical energy. Co-SOEC syngas methanation benefits from reactor designs with intensified heat removal, such as tube-bundle reactors or microstructured reactors. Nickel catalysts offer high activity and high selectivity at a low price, whereas promoting agents, carrier materials, and form play substantial roles in the overall process. Both kinetic and thermodynamic considerations must be kept in mind not only to achieve the highest conversion rates, but also to prevent carbon deposition or catalyst sintering. Therefore, reactor temperature control is important for achieving low outlet temperatures which reduce the thermodynamic limitation and keep the maximum temperature just below the catalyst's limits, thus allowing high reaction rates. Furthermore, for the feed gas composition used for methanation, a moderate hydrogen excess should be considered to prevent carbon deposition and ensure high conversions. Additionally, SNG is produced at a sufficient output quality for direct grid injection in line with legal requirements and requires only a modest gas conditioning effort. Since the electric energy price has a dominant effect on the resulting SNG price, the overall system energy efficiency needs to be maximized. Heat integration from exothermal methanation or external industrial sources into the co-SOEC feed needs to be substantial to achieve high efficiencies. The reduction of compression power by dual-pressure-level methanation can contribute to economic competition against conventional energy carriers. In conclusion, for the successful realization of a combined co-SOEC and methanation facility, all system levels (catalyst, reactor, and plant design) should be optimized.

## References

- [1] Hashimoto K *et al* 1999 Global CO<sub>2</sub> recycling—novel materials and prospect for prevention of global warming and abundant energy supply *Mater. Sci. Eng. A* **267** 200–6
- [2] Rönsch S, Schneider J, Matthischke S, Schlüter M, Götz M, Lefebvre J, Prabhakaran P and Bajohr S 2016 Review on methanation – from fundamentals to current projects *Fuel* **166** 276–96
- [3] Lehner M, Tichler R, Steinmüller H and Koppe M (ed) 2014 *Power-to-Gas: Technology and Business Models SpringerBriefs in Energy* (Cham: Springer International Publishing)
- [4] Sabatier P and Senderens J B 1902 New methane synthesis *J. Chem. Soc.* **82** 333
- [5] Bartholomew C H 1982 Carbon deposition in steam reforming and methanation *Catalysis Reviews* **24** 67–112
- [6] Kiewidt L and Thöming J 2015 Predicting optimal temperature profiles in single-stage fixed-bed reactors for CO<sub>2</sub>-methanation *Chem. Eng. Sci.* **132** 59–71
- [7] Neubert M 2019 *Catalytic Methanation for Small- and Mid-scale SNG Production* Friedrich-Alexander-Universität Erlangen-Nürnberg (FAU) <https://opus4.kobv.de/opus4-fau/frontdoor/index/index/year/2020/docId/13118>
- [8] Guilera J, Boeltken T, Timm F, Mallol I, Alarcón A and Andreu T 2020 Pushing the limits of SNG process intensification: high GHSV operation at pilot scale *ACS Sustain. Chem. Eng.* **8** 8409–18

- [9] Lefebvre J, Bajohr S and Kolb T 2020 Modeling of the transient behavior of a slurry bubble column reactor for CO<sub>2</sub> methanation, and comparison with a tube bundle reactor *Renew. Energy* **151** 118–36
- [10] Schlautmann R, Böhm H, Zauner A, Mörs F, Tichler R, Graf F and Kolb T 2021 Renewable power-to-gas: a technical and economic evaluation of three demo sites within the STORE&GO project *Chem. Ing. Tech.* **93** 568–79
- [11] Wulf C, Linßen J and Zapp P 2018 Review of power-to-gas projects in europe *Energy Proc.* **155** 367–78
- [12] Younas M, Loong Kong L, Bashir M J K, Nadeem H, Shehzad A and Sethupathi S 2016 Recent advancements, fundamental challenges, and opportunities in catalytic methanation of CO<sub>2</sub> *Energy Fuels* **30** 8815–31
- [13] Mills G A and Steffgen F W 1974 Catalytic methanation *Catal. Rev.* **8** 159–210
- [14] Hu D, Gao J, Ping Y, Jia L, Gunawan P, Zhong Z, Xu G, Gu F and Su F 2012 Enhanced investigation of CO methanation over Ni/Al<sub>2</sub>O<sub>3</sub> catalysts for synthetic natural gas production *Ind. Eng. Chem. Res.* **51** 4875–86
- [15] Fan M-T, Miao K-P, Lin J-D, Zhang H-B and Liao D-W 2014 Mg–Al oxide supported Ni catalysts with enhanced stability for efficient synthetic natural gas from syngas *Appl. Surf. Sci.* **307** 682–8
- [16] Qin H, Guo C, Wu Y and Zhang J 2014 Effect of La<sub>2</sub>O<sub>3</sub> promoter on NiO/Al<sub>2</sub>O<sub>3</sub> catalyst in CO methanation *Korean J. Chem. Eng.* **31** 1168–73
- [17] Liu H, Zou X, Wang X, Lu X and Ding W 2012 Effect of CeO<sub>2</sub> addition on Ni/Al<sub>2</sub>O<sub>3</sub> catalysts for methanation of carbon dioxide with hydrogen *J. Nat. Gas Chem.* **21** 703–7
- [18] Liu Q, Gu F, Lu X, Liu Y, Li H, Zhong Z, Xu G and Su F 2014 Enhanced catalytic performances of Ni/Al<sub>2</sub>O<sub>3</sub> catalyst via addition of V<sub>2</sub>O<sub>3</sub> for CO methanation *Appl. Catal., A* **488** 37–47
- [19] Rönsch S, Köchermann J, Schneider J and Matthischke S 2016 Global reaction kinetics of CO and CO<sub>2</sub> methanation for dynamic process modeling *Chem. Eng. Technol.* **39** 208–18
- [20] Koschany F, Schlereth D and Hinrichsen O 2016 On the kinetics of the methanation of carbon dioxide on coprecipitated NiAl(O)<sub>x</sub> *Appl. Catalysis B* **181** 504–16
- [21] Kopyscinski J, Schildhauer T J, Vogel F, Biollaz S M and Wokaun A 2010 Applying spatially resolved concentration and temperature measurements in a catalytic plate reactor for the kinetic study of CO methanation *J. Catal.* **271** 262–79
- [22] Coenen J, van Nesselrooy P, Croon M, de, van Dooren P and van Meerten R 1986 The dynamics of methanation of carbon monoxide on nickel catalysts *Applied Catalysis* **25** 1–8
- [23] Ayers K E, Anderson E B, Capuano C, Carter B, Dalton L, Hanlon G, Manco J and Niedzwiecki M 2010 Research advances towards low cost, high efficiency PEM electrolysis *ECS Trans.* **33** 3–15
- [24] Schlereth D and Hinrichsen O 2014 A fixed-bed reactor modeling study on the methanation of CO<sub>2</sub> *Chem. Eng. Res. Des.* **92** 702–12
- [25] Try R, Bengaouer A, Baurens P and Jallut C 2018 Dynamic modeling and simulations of the behavior of a fixed-bed reactor-exchanger used for CO<sub>2</sub> methanation *AIChE J* **64** 468–80
- [26] Gruber M 2020 Detaillierte Untersuchung des Wärme- und Stofftransports in einem Festbett-Methanisierungsreaktor für Power-to-Gas Anwendungen Dissertation Karlsruher Institut für Technologie (KIT) <https://doi.org/10.5445/IR/1000105268>
- [27] Krier C, Hackel M, Hägele C, Urtel H, Querner C and Haas A 2013 Improving the methanation process *Chemie-Ingenieur-Technik* **85** 523–8
- [28] Kai T, Takahashi T and Furusaki S 1988 Kinetics of the methanation of carbon dioxide over a supported Ni–La<sub>2</sub>O<sub>3</sub> catalyst *Can. J. Chem. Eng.* **66** 343–7

- [29] Martinez Molina M, Kern C and Jess A 2016 Catalytic hydrogenation of carbon dioxide to methane in wall-cooled fixed-bed reactors *Chem. Eng. Technol.* **39** 2404–15
- [30] Schollenberger D, Bajohr S, Gruber M, Reimert R and Kolb T 2018 Scale-up of innovative honeycomb reactors for power-to-gas applications – The Project Store&Go *Chem. Ing. Tech.* **90** 696–702
- [31] Weatherbee G and Barthomolew C 1982 Hydrogenation of CO<sub>2</sub> on group VIII metals II. kinetics and mechanism of CO<sub>2</sub> hydrogenation on nickel *J. Catal.* **77** 460–72
- [32] Yang Lim J, McGregor J, Sederman A J and Dennis J S 2016 Kinetic studies of CO<sub>2</sub> methanation over a Ni/ $\gamma$ -Al<sub>2</sub>O<sub>3</sub> catalyst using a batch reactor *Chem. Eng. Sci.* **141** 28–45
- [33] Giglio E, Deorsola F A, Gruber M, Harth S R, Morosanu E A, Trimis D, Bensaid S and Pirone R 2018 Power-to-gas through high temperature electrolysis and carbon dioxide methanation: reactor design and process modeling *Ind. Eng. Chem. Res.* **57** 4007–18
- [34] Xu J and Froment G F 1989 Methane steam reforming, methanation and water-gas shift: I. Intrinsic kinetics *AIChE J* **35** 88–96
- [35] Ducamp J, Bengaouer A and Baurens P 2017 Modelling and experimental validation of a CO<sub>2</sub> methanation annular cooled fixed-bed reactor exchanger *Can. J. Chem. Eng.* **95** 241–52
- [36] Parlikkad N R, Chambrey S, Fongarland P, Fatah N, Khodakov A, Capela S and Guerrini O 2013 Modeling of fixed bed methanation reactor for syngas production: operating window and performance characteristics *Fuel* **107** 254–60
- [37] Kang W R and Lee K B 2013 Effect of operating parameters on methanation reaction for the production of synthetic natural gas *Korean J. Chem. Eng.* **30** 1386–94
- [38] Klose J 1984 Kinetics of the methanation of carbon monoxide on an alumina-supported nickel catalyst *J. Catal.* **85** 105–16
- [39] Zhang J, Fatah N, Capela S, Kara Y, Guerrini O and Khodakov A Y 2013 Kinetic investigation of carbon monoxide hydrogenation under realistic conditions of methanation of biomass derived syngas *Fuel* **111** 845–54
- [40] Gruber M, Wiedmann D, Haas M, Harth S, Loukou A and Trimis D 2021 Insights into the catalytic CO<sub>2</sub> methanation of a boiling water cooled fixed-bed reactor: simulation-based analysis *Chem. Eng. J.* **406** 126788
- [41] Sun D and Simakov D S 2017 Thermal management of a sabatier reactor for CO<sub>2</sub> conversion into CH<sub>4</sub>: simulation-based analysis *J. CO<sub>2</sub> Util.* **21** 368–82
- [42] Kreitz B, Wehinger G and Turek T 2019 Dynamic simulation of the CO<sub>2</sub> methanation in a micro-structured fixed-bed reactor *Chem. Eng. Sci.* **195** 541–52
- [43] Krammer A, Medved A, Peham M, Wolf-Zöllner P, Salbrechter K and Lehner M 2020 Dual pressure level methanation of Co-SOEC syngas *Energy Technol.* **9** 2000746
- [44] Kusnezoff M, Megel S, Rix C, Adam P, Reichelt E, Herz G, Jahn M, Trofimenko N and Michaelis A 2019 Co-electrolysis CFY-stack operation and integration for carbon capture and utilization *ECS Trans.* **91** 2579–87
- [45] Gantenbein A, Witte J, Biollaz S M, Kröcher O and Schildhauer T J 2021 Flexible application of biogas upgrading membranes for hydrogen recycle in power-to-methane processes *Chem. Eng. Sci.* **229** 116012
- [46] ENTSOG, Gas Infrastructure Europe and Hydrogen Europe How to Transport and Store Hydrogen – Facts and Figures (ENTSOG, Gas Infrastructure Europe and Hydrogen Europe)
- [47] GRTgaz, GRDF, elenegy, Geomethane, Teregea, REGAZ Bordaux, Stroengy and R-GDS 2019 Technical and economic conditions for injecting hydrogen into natural gas networks:

- Final report June 2019 (GRTgaz, GRDF, elenegy, Geomethane, Teregea, REGAZ Bordaux, Stroengy and R-GDS)
- [48] ÖVGW 2021 Richtlinie G B210: Gasbeschaffenheit 75.060
- [49] DVGW 2021 G 260 Arbeitsblatt 09/2021: Gasbeschaffenheit (310700)
- [50] El Sibai A, Rihko Struckmann L K and Sundmacher K 2017 Model-based optimal sabatier reactor design for power-to-gas applications *Energy Technol* **5** 911–21
- [51] Lefebvre J, Bajohr S and Kolb T 2019 A comparison of two-phase and three-phase CO<sub>2</sub> methanation reaction kinetics *Fuel* **239** 896–904
- [52] Böhm H, Lehner M and Kienberger T 2021 Techno-economic assessment of thermally integrated co-electrolysis and methanation for industrial closed carbon cycles *Front. Sustain* **2** 726332
- [53] Eurostat 2021 Natural gas price statistics: Natural gas prices for non-household consumers [https://ec.europa.eu/eurostat/statistics-explained/index.php?title=Natural\\_gas\\_price\\_statistics#Natural\\_gas\\_prices\\_for\\_non-household\\_consumers](https://ec.europa.eu/eurostat/statistics-explained/index.php?title=Natural_gas_price_statistics#Natural_gas_prices_for_non-household_consumers) (accessed 25 Oct 2021)
- [54] Ancona M A, Antonucci V, Branchini L, Catena F, Pascale A, de, Di Blasi A, Ferraro M, Italiano C, Melino F and Vita A 2019 Thermal integration of a high-temperature co-electrolyzer and experimental methanator for power-to-gas energy storage system *Energy Convers. Manage.* **186** 140–55
- [55] Posdziech O, Schwarze K and Brabandt J 2019 Efficient hydrogen production for industry and electricity storage via high-temperature electrolysis *Int. J. Hydrogen Energy* **44** 19089–101
- [56] Wang L, Pérez-Fortes M, Madi H, Diethelm S, van herle J and Maréchal F 2018 Optimal design of solid-oxide electrolyzer based power-to-methane systems: a comprehensive comparison between steam electrolysis and co-electrolysis *Appl. Energy* **211** 1060–79
- [57] Sapountzi F M, Gracia J M, Weststrate C J, Fredriksson H O and Niemantsverdriet J W 2017 Electrocatalysts for the generation of hydrogen, oxygen and synthesis gas *Prog. Energy Combust. Sci.* **58** 1–35
- [58] Brabandt J and Posdziech O 2017 System approach of a pressurized high-temperature electrolysis *ECS Trans.* **78** 2987–95
- [59] Buttler A and Spliethoff H 2018 Current status of water electrolysis for energy storage, grid balancing and sector coupling via power-to-gas and power-to-liquids: a review *Renew. Sustain. Energy Rev.* **82** 2440–54
- [60] Gruber M, Weinbrecht P, Biffar L, Harth S, Trimis D, Brabandt J, Posdziech O and Blumentritt R 2018 Power-to-gas through thermal integration of high-temperature steam electrolysis and carbon dioxide methanation – experimental results *Fuel Proc. Tech.* **181** 61–74
- [61] Vogt C, Monai M, Kramer G J and Weckhuysen B M 2019 The renaissance of the Sabatier reaction and its applications on Earth and in space *Nat. Catal.* **2** 188–97
- [62] NASA Content Administrator 2012 The Sabatier System: Producing Water on the Space Station (NASA) [https://www.nasa.gov/mission\\_pages/station/research/news/sabatier.html](https://www.nasa.gov/mission_pages/station/research/news/sabatier.html)
- [63] Muscatello A and Santiago-Maldonado E 2012 Mars In Situ Resource Utilization Technology Evaluation *Mars In Situ Resource Utilization Technology Evaluation 50th AIAA Aerospace Sciences Meeting including the New Horizons Forum and Aerospace Exposition (Nashville, Tennessee)* American Institute of Aeronautics and Astronautics (Reston, VA: American Institute of Aeronautics and Astronautics)

## 2.2 Modelling of catalytic fixed bed reactors

Mathematical modelling and simulation of chemical processes is a crucial tool to develop, optimize and scale technical apparatuses. The coupled balance equations enable to derive the process condition, which for chemical reactors is characterized by spatial and temporal distribution of temperature, concentration, velocity and pressure. [48]

Simplification of a real process aims to enable its description with much lower complexity at sufficient accuracy. Tubular reactors can be accurately represented if the axial and radial dimensions are taken into account due to rotational symmetry. In some cases, even a one-dimensional approach is sufficient if the radial component can be neglected, for example in thin pipes. The energy balance in most technical applications can often be reduced to a heat balance since only thermal forms of energy need to be considered. Furthermore, for stationary applications the time-dependency can be eliminated. [48]

Ideal reactor concepts are simplified model approaches for certain applications. For tubular systems the two-dimensional diffusion model and plug-flow reactor (PFR) model are common. In the two-dimensional diffusion model convection only takes place in axial direction. Backmixing and fixed bed heat conduction is considered via effective diffusion and conduction in radial and axial direction. The angular dimension is eliminated. [48]

The PFR is even more simplified, as this approach assumes the reactor can be divided in small fully mixed “plugs” flowing through the pipe without any gas mixing influence between one plug and another. Therefore, no temperature, concentration or velocity gradients occur in radial direction. Convection takes place solely in direction of the reactor axis, whereas in contrast to the two-dimensional diffusion model also axial conduction and diffusion is considered negligible. For pipes with high length-diameter ratios the PFR concept is more accurate. Laminar flow is characterized by a parabolic velocity profile and less axial backmixing. For turbulent flow radial velocity gradients are low, but also lead to higher axial mixing phenomena. Gas flow through fixed beds is typically approximated with plug-flow. However, deviations from the ideal state should not be disregarded and can be approximately assessed by common rule of thumbs (e.g.  $d_i/L > 10$ ) [49] or more thorough criteria [49–51] e.g. proposed by Mears [52], Gierman [53] and Sie [49]. Safe model robustness can be achieved by experimental verification.

In the following section the fundamental laws and equations for modelling of fixed beds in tubular reactors are presented.

### 2.2.1 Conservation laws

In any technical process the sum of mass, energy and momentum within its system boundaries must be constant. Therefore, this fundamental principle of conservation of mass, energy and momentum is the basis of each model. A general formulation of a balance equation is presented in Equation 1. The temporal derivative of a state variable equals the sum of input and output flow added by a source term as shown in Equation 2.

$$\frac{\partial \Gamma}{\partial t} = -\text{div } j + \dot{Q} \quad (\text{Equation 1})$$

$$\operatorname{div} j = \nabla \cdot j = \frac{\partial j_x}{\partial x} + \frac{\partial j_y}{\partial y} + \frac{\partial j_z}{\partial z} \quad (\text{Equation 2})$$

## 2.2.2 General transport phenomena

Transport of mass and heat within fluid systems such as most chemical reactors are described by convective or diffusive transport and radiation (Table 2).

Table 2: Overview of heat and mass transport phenomena in chemical reactors

	Convection	Diffusion	Radiation
Mass transport	Mass convection	(Mass) Diffusion	-
Heat transport	Thermal convection	Conduction	(Heat) radiation

Convective mass transport is the transport of mass by bulk motion (advection) superimposed by a mostly negligible mass diffusion influence. In chemical reactors (mass) convection is normally related to one fluid component. It can be presented as mole flow of a species  $i$  through a given cross-sectional area as in Equation 3.

$$j_{i,conv} = \frac{\dot{n}_{i,conv}}{A} = \frac{\dot{m}_{i,conv}}{M_i A} = \frac{\rho_i \dot{V}}{M_i A} = c_i \frac{\dot{V}}{A} = c_i w \left[ \frac{\text{mol}}{\text{m}^2 \text{s}} \right] \quad (\text{Equation 3})$$

Heat convection is analogously caused by combination of bulk motion and random molecular motion. It is formulated as an enthalpy flux normally referring to a temperature of 0 °C (Equation 4).

$$j_{i,heat\ conv} = \frac{\dot{Q}_{conv}}{A} = \frac{\dot{m} c_p T}{A} = \frac{\rho \dot{V} c_p T}{M_i A} = \rho w c_p T \left[ \frac{\text{W}}{\text{m}^2 \text{s}} \right] \quad (\text{Equation 4})$$

Mass diffusion and heat conduction is caused by concentration and temperature gradients within a fluid or a solid phase due to random molecular motion. The rate of diffusive transport is characterized by the substance-specific transport property, diffusion coefficient  $D_i$  and heat conductivity  $\lambda$ . Fick's law describes mass diffusion in Equation 5 again for each species  $i$ .

$$j_{i,diff} = \frac{\dot{n}_{i,diff}}{A} = -D_i \operatorname{grad} c_i \left[ \frac{\text{mol}}{\text{m}^2 \text{s}} \right] \quad (\text{Equation 5})$$

Analogously, in Fourier's law heat conduction is defined according to Equation 6.

$$j_{cond} = \frac{\dot{Q}_{cond}}{A} = -\lambda \operatorname{grad} T \left[ \frac{\text{W}}{\text{m}^2} \right] \quad (\text{Equation 6})$$

Heat and mass transfer also take place through a fluid-solid or fluid-fluid phase interface. Driving force for mass transfer from one phase to another is again the concentration difference multiplied with the mass transfer coefficient as shown in Equation 7.

$$j_{i,mt} = \frac{\dot{n}_{ht}}{A} = \beta (c_{i,1} - c_{i,2}) \left[ \frac{\text{mol}}{\text{m}^2 \text{s}} \right] \quad (\text{Equation 7})$$

Heat transfer is analogously defined by the heat transfer coefficient driven by the difference in temperature between the two phases (Equation 8).



$$j_{ht} = \frac{\dot{Q}_{ht}}{A} = \alpha(T_1 - T_2) \left[ \frac{W}{m^2} \right] \quad (\text{Equation 8})$$

### 2.2.3 Transport phenomena in fixed beds

The mass and heat transport in multiphase reactive flow such as in catalytic fixed beds with external cooling are manifold. Intra-pellet, inter-pellet, intra-bed and bed-wall transfer effects need to be considered as presented in an overview in Figure 3.

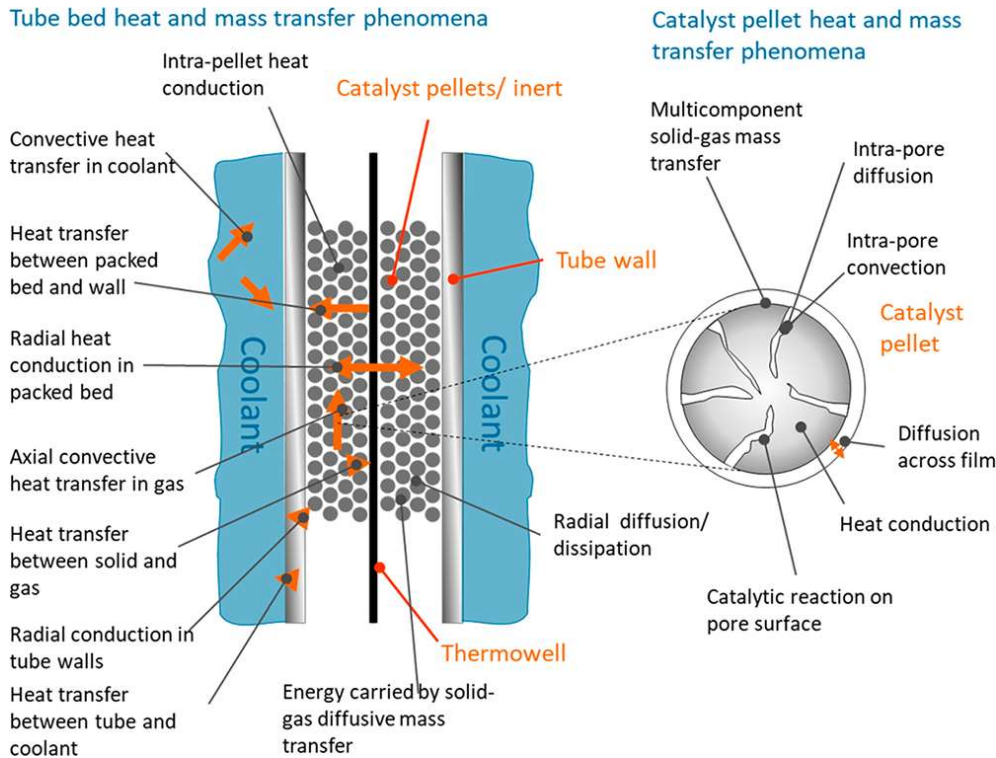


Figure 3: Heat and mass transfer phenomena in fixed beds taken from [54]

### 2.2.4 Mass transport in fixed beds

The general mass balance equation is necessary to calculate the concentration array within a reactor. The balance equation includes convection, diffusion and the reaction source term for a species  $i$  as given in Equation 9. The source term is defined by the reaction rate of each reaction  $j$  involved and the corresponding stoichiometry factor.

$$\frac{\partial c_i}{\partial t} = -\text{div}(c_i w - D_i \text{grad } c_i) + \sum_j \nu_{i,j} r_j \quad (\text{Equation 9})$$

Molecular diffusion has only subordinate influence. However, gas dispersion takes into account velocity maldistribution as a consequence of turbulence effects in fixed beds, which can be implemented via effective diffusion or dispersion coefficients in lateral and longitudinal direction. Longitudinal dispersion in fixed beds was empirically investigated by Edward and Richardson [29] (Equation 10) and lateral dispersion can be derived by the Gunn correlation [30] (Equation 11).

$$\frac{D_{i, \text{long}}}{D_{i, m}} = 0.73\varepsilon + 0.5 \left( 1 + \frac{9.49\varepsilon}{Re_p Sc} \right) Re_p Sc \quad (\text{Equation 10})$$

$$\frac{D_{i,lat}}{D_{i,m}} = \frac{\varepsilon}{1.91} + \frac{Re_p Sc}{11-4 \exp\left(-\frac{7}{Re_p}\right)} \quad (\text{Equation 11})$$

For cylindrical fixed beds the angular coordinate can be eliminated in assumption of rotational symmetry. The radial velocity component can be neglected, especially for high length-diameter-ratios. These assumptions lead to the two-dimensional diffusion model (also called dispersion model) for tubular (fixed bed) reactors according to Equation 12. [48]

$$\frac{\partial c_i}{\partial t} = -\frac{\partial(c_i w_z)}{\partial z'} + D_{i,r,eff} \left( \frac{\partial^2 c_i}{\partial r'^2} + \frac{1}{r'} \frac{\partial c_i}{\partial r'} \right) + D_{i,z,eff} \frac{\partial^2 c_i}{\partial z'^2} + \sum_j v_{i,j} r_j \quad (\text{Equation 12})$$

Under stationary conditions the time derivative of the concentration on the left side of the equation can be eliminated. Further simplifications can be made by assuming constant axial velocity, neglecting the radial component in a one-dimensional approach or by neglecting the dispersion influence. [48]

The mass balance for a PFR is presented in Equation 13 neglecting radial and axial dispersion.

$$\frac{\partial c_i}{\partial t} = -\frac{\partial(c_i w)}{\partial z'} + \sum_j v_{i,j} r_j \quad (\text{Equation 13})$$

### 2.2.5 Heat transport in fixed bed reactors

The heat balance is used to calculate the temperature of the reactor system and takes all relevant heat transport phenomena into account. The general heat balance is formulated in Equation 14.

$$\frac{\partial(\rho c_p T)}{\partial t} = -div(\rho w c_p T - \lambda grad T) + \sum_j r_j (-\Delta H_{Rj}) \quad (\text{Equation 14})$$

Heat and mass balance are coupled via the reaction rate, which is dependent on concentrations and temperature. Also thermodynamic properties such as  $c_p$  or transport properties such as  $\lambda$ ,  $D_{i,long}$  or  $D_{i,lat}$  cannot be calculated independently from the respective other balance equation. The same simplifications discussed for the mass balance also apply to the heat balance. The heat balance of the two-dimensional diffusion model is presented in Equation 15.

$$\frac{\partial(\rho c_p T)}{\partial t} = -\frac{\partial(\rho w_z c_p T)}{\partial z'} + \lambda_{r,eff} \left( \frac{\partial^2 T}{\partial r'^2} + \frac{1}{r'} \frac{\partial T}{\partial r'} \right) + \lambda_{z,eff} \frac{\partial^2 T}{\partial z'^2} + \sum_j r_j (-\Delta H_{Rj}) \quad (\text{Equation 15})$$

The ideal PFR can be calculated based on a simplified heat balance as given in Equation 16. In addition, heat loss by radiation to ambient air was included in Equation 16, as was conducted for the 1D model in paper II [55].

$$\frac{\partial(\rho c_p T)}{\partial t} = -\frac{\partial(\rho w c_p T)}{\partial z'} + \sum_j r_j (-\Delta H_{Rj}) - k \frac{4}{d_r} (T - T_c) - q_{radiation} \quad (\text{Equation 16})$$

### 2.2.6 Radial heat transport in fixed beds

For reactor modelling and design the radial heat transport is of utmost importance. Therefore, radial heat transport phenomena in fixed beds will be addressed here in greater detail.

#### Radial heat transport in 1D models



The heat transition coefficient  $k$  for the radial heat transition through a reactor pipe of an ideal PFR can be calculated from inner and outer heat transfer coefficients and the heat conductivity of the steel wall as shown in Equation 17 to Equation 19. [48]

$$\frac{1}{k A} = \frac{1}{\alpha_i A_i} + \frac{1}{\lambda_{steel} A_m} + \frac{1}{\alpha_o A_o} \quad (\text{Equation 17})$$

$$A_m = \frac{A_i - A_o}{\ln \frac{A_i}{A_o}} = \frac{d_i - d_o}{\ln \frac{d_i}{d_o}} \pi L \quad (\text{Equation 18})$$

$$k = \frac{1}{d_i} \left( \frac{1}{\alpha_i d_i} + \frac{1}{\lambda_{steel} \frac{d_i - d_o}{\ln \frac{d_i}{d_o}}} + \frac{1}{\alpha_o d_o} \right)^{-1} \quad (\text{Equation 19})$$

Numerous formulations for the inner bed-wall heat transfer coefficients for tubular fixed beds are compared by Winterberg [56]. For the 1D model presented in paper II [55] the formulation by Specchia [57] was used to calculate the bed-wall heat transfer coefficient (Equation 20).

$$\alpha_{bed-wall} = \frac{\lambda_{gas}}{d_p} \left( 0.0835 Re_{0,p}^{0.91} + 2 \varepsilon_{bed} + \frac{1 - \varepsilon_{bed}}{\frac{\lambda_{gas}}{\lambda_{solid}} + 1} \right) \quad (\text{Equation 20})$$

The outer heat transfer coefficient between the reactor wall and the coolant can be calculated according to Nusselt correlations, such as by Gnielinski for cooling by thermal oil or based on Equation 21 for natural air cooling.

$$\alpha_{o,wall-air} = 1.32^4 \sqrt{\frac{T_{wall} - T_{air}}{d_{r,o}}} \quad (\text{Equation 21})$$

In a 1D PFR model approach radial heat transport within the fixed bed is assumed to be very fast, therefore the radial temperature gradients within the fixed bed are considered as zero.

### Radial heat transport in packed beds in 2 dimensional models

For the two-dimensional approach and for better assessment of reactor design improvement in addition to heat transfer through the reactor wall the effective fixed bed conductivity is essential. Winterberg [56] thoroughly compared the two most common models to describe radial heat transport within a fixed bed, the  $\alpha_w$ -model and the  $\Lambda_r(R)$ -model. The well-known  $\alpha_w$ -model is based on the assumption that the effective bed heat conduction is constant due to constant velocity and porosity distribution over the bed radius (as shown in Equation 15). [58] The effective heat conduction for spherical fixed beds can be calculated by the model of Zehner, Bauer and Schlünder [59–61] as was done in the 2D reactor model in paper II [55]. According to the  $\alpha_w$ -model at the fixed bed-wall interface an immediate change in temperature occurs. This assumed temperature change is represented by the heat transfer coefficient  $\alpha_w$  (or  $\alpha_{bed-wall}$ ), which can be calculated based on Nusselt correlations such as from Specchia [57] as in paper II. The  $\alpha_w$ -heat transfer model was applied for the 2D reactor model in paper I, whereas it was additionally distinguished between the solid and gas phase via two heat balance equations.

In contrast, the  $\Lambda_r(r)$ -model assumes that there is no discontinuity at the interface between bed and wall, but rather the temperature of the fixed bed and of the wall at the interface is

equal (boundary condition:  $T_{wall} = T_{bed,(r=R)}$ ). In the  $\Lambda_r(r)$ -model the heat transfer between fixed bed and wall is described by the effective heat conductivity as a function of the reactor radius considering velocity and porosity distribution in radial direction. Within the boundary layer close to the reactor wall the effective bed conductivity significantly decreases. The  $\Lambda_r(r)$ -model is described in Equation 22-27. [58]

$$\Lambda_r(r) = \lambda_{bed}(r) + K_1 Pe_0 \frac{u_{0,c}}{u_0} f(R-r) \lambda_f \quad (\text{Equation 22})$$

$$0 < R-r \leq K_2 d \rightarrow f(R-r) = \left(\frac{R-r}{K_2 d}\right)^n \quad (\text{Equation 23})$$

$$K_2 d_{r,i} < R-r \leq R \rightarrow f(R-r) = 1 \quad (\text{Equation 24})$$

$$K_1 = 1/8 \quad (\text{Equation 25})$$

$$K_2 = 0.44 + 4 \exp\left(-\frac{Re_0}{70}\right) \quad (\text{Equation 26})$$

$$n = 2 \quad (\text{Equation 27})$$

### Diameter influence on radial heat transport

In Equation 28 a mean value over the radial distance for the effective fixed bed heat conductivity  $\Lambda_r(r)$  can be integrated which was conducted numerically in MATLAB.

$$\bar{\lambda}_{r,bed} = \frac{1}{d_i/2} \int_0^{d_i/2} \Lambda_r(r) dr \quad (\text{Equation 28})$$

This mean effective bed conductivity  $\bar{\lambda}_{r,bed}$  was used to study the effect of the reactor diameter on the radial heat transfer of catalytic fixed bed for methanation. As shown in Equation 29 an artificial heat transition coefficient  $k_{bed-oil}$  based on Gruber [62] can be formulated including the mean effective bed conductivity. This bed-to-oil heat transition coefficient includes all heat thermal resistances including the effective fixed bed heat conduction via a mean conductivity value, the bed-wall heat transfer via  $\alpha_i$ , the wall conductivity via  $\lambda_{steel}$  and the wall-oil heat transfer via  $\alpha_o$ . This artificial transition coefficient was not used in the 1D PFR and also not in the 2D model, but was used to derive the diameter dependency of the radial heat transition coefficient.

$$k_{bed-oil} = \frac{1}{d_i} \left( \frac{d_i}{8 \bar{\lambda}_{r,bed} d_i} + \frac{1}{\alpha_i d_i} + \frac{1}{\lambda_{steel} \frac{d_i - d_o}{\ln \frac{d_i}{d_o}}} + \frac{1}{\alpha_o d_o} \right)^{-1} \quad (\text{Equation 29})$$

To give a precise picture on how the reactor diameter affects overall radial heat transfer the radial heat flux under exclusion of the reactor-coolant temperature difference  $q'_r$  must be determined. Otherwise, the temperature difference profile along the reactor axis would interfere with the diameter effect on the heat transition coefficient (Equation 30 and 31). In Equation 30 and 31 this heat flux is presented based on the heat transition coefficient between wall and cooling oil  $k$  (Equation 19) neglecting fixed bed conductivity consistent with a 1D PFR assumption.

$$q_r = -k \frac{4}{d_r} (T - T_c) \quad [W m^{-3}] \quad (\text{Equation 30})$$

$$q'_r = \frac{q_r}{(T-T_c)} = -k \frac{4}{d_r} \quad [W m^{-3} K^{-1}] \quad (\text{Equation 31})$$

With the artificial heat transition coefficient  $k_{bed-o}$  an artificial heat flux  $q'_{r,bed-oil}$  taking the fixed bed heat conductivity into account can be calculated according to Equations 32 and 33.

$$q_{r,bed-oil} = -k_{bed-oil} \frac{4}{d_r} (T - T_c) \quad [W m^{-3}] \quad (\text{Equation 32})$$

$$q'_{r,bed-oil} = \frac{q_{r,bed-oil}}{(T-T_c)} = -k_{bed-o} \frac{4}{d_r} \quad [W m^{-3} K^{-1}] \quad (\text{Equation 33})$$

Equation 31 and Equation 33 were used to derive Figure 19.

### 2.2.7 Mass transport limitation

In heterogeneous gas catalysis the reaction takes place on the active sites exposed on the catalyst surface. Mass transfer from bulk gas to the catalyst surface and back are fundamental process steps of heterogeneous gas catalysis. The 7 steps of heterogeneous gas catalysis are illustrated in Figure 4 and include:

1. Diffusion of reactant from the bulk gas through the gas boundary layer
2. Diffusion of reactant through pores into the porous catalyst
3. Adsorption of the reactants on the active site
4. Reaction in an adsorbed state to form product species
5. Desorption of the product
6. Diffusion of the product out of the porous catalyst
7. Diffusion of the product through the gas boundary layer to the bulk gas

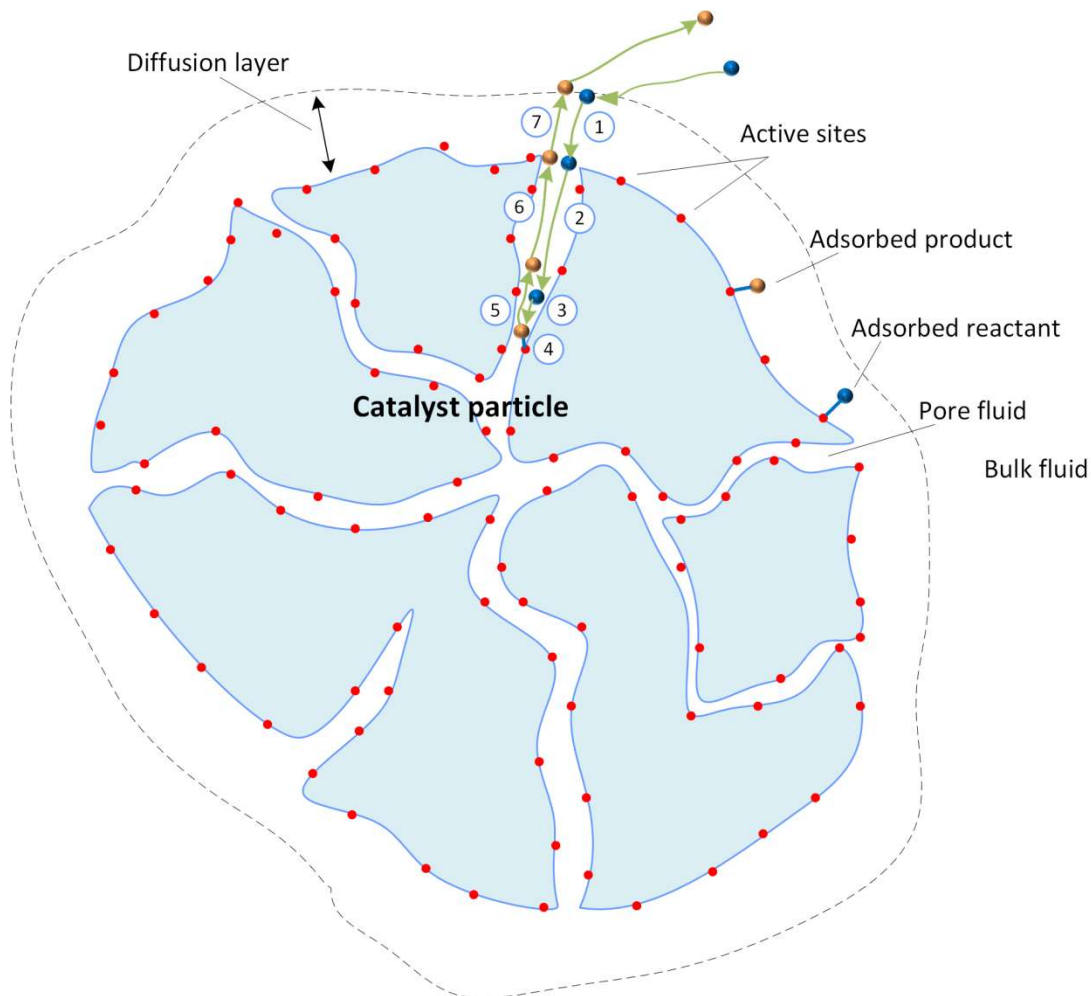


Figure 4: 7 steps of heterogeneous gas catalysis (reproduced based on [63])

For thorough research based on modelling of catalytic methanation it is important to take the rate determining step of the described steps of heterogeneous gas catalysis into account. The overall process may be determined by the intrinsic rate of reaction (step 4) in many cases. Empirically determined intrinsic kinetic models allow deriving the reaction rate without any other rate limiting influences. However, the mass transfer steps between bulk gas and active sites, which mainly are based on diffusion phenomena, can also be limiting under certain reactor conditions. The mass transfer between gas and catalyst depends on the gas flow and catalyst characteristics. The reaction rate is a function of partial pressures, temperature and catalyst activity. Therefore, the combination of these variables defines if mass transfer limitation occurs and in what intensity. As illustrated in Figure 5, any of the 7 steps of heterogeneous gas-catalysis can be rate determining, which influences the concentration profile between gas bulk and porous catalyst. The adsorption and desorption steps are included in Langmuir-Hinshelwood-Hougen-Watson kinetic models in adsorption terms as explained in detail in chapter 2.1.

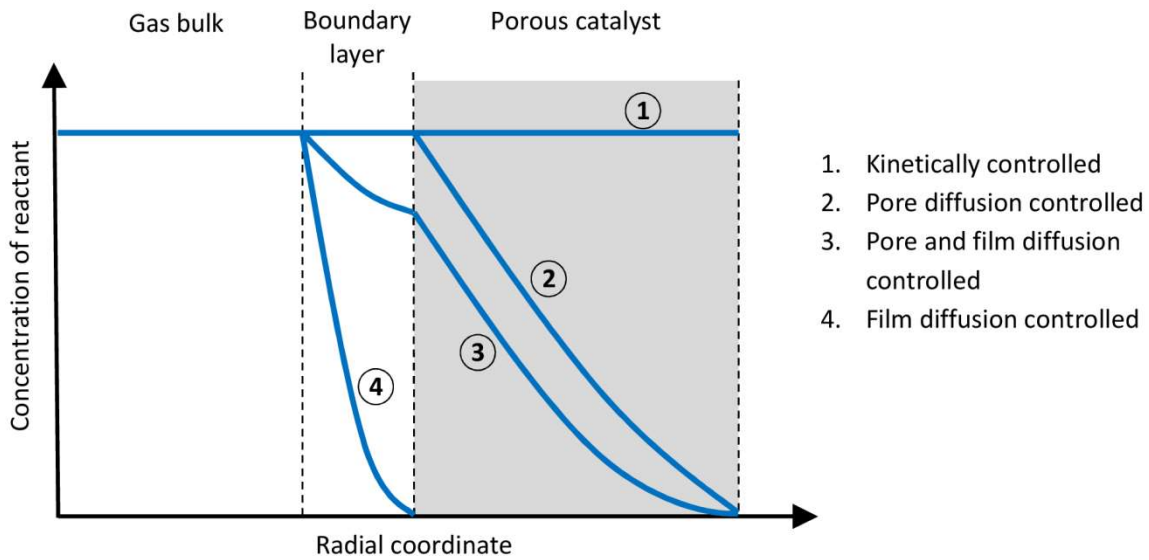


Figure 5: Reactant concentration profile as a consequence of rate determining phenomenon (reproduced based on [62])

Two approaches have been used in scientific publications to include mass transfer limitation in catalytic fixed bed reactors. The catalytic efficiency via the Thiele-modulus approach [19,22,24,25,62] was also used in this thesis. Another method is to integrate a separate particle model [20,21,23] into the main reactor model, which represents the mentioned diffusion phenomena.

### 2.2.7.1 Catalyst efficiency via Thiele-modulus

The catalytic efficiency takes the rate limiting transport effects to the catalyst surface and into the catalyst pores into account. It is based on the dimensionless Thiele-modulus. [19,51,62] The effective reaction rate of reaction  $j$  due to mass transfer limitation is calculated by multiplication of the intrinsic reaction rate with a catalytic efficiency factor as presented in Equation 34.

$$r_{j,eff} = r_{j,intr} \eta_{eff,j} \quad (\text{Equation 34})$$

The catalyst efficiency is calculated in consideration of external and pore diffusion, which are a function of the Thiele-modulus (Equation 35–Equation 37).

$$\eta_{eff,j} = \eta_{ext,j} \eta_{pore,j} \quad (\text{Equation 35})$$

$$\eta_{pore,j} = \frac{1}{\Phi_j} \left( \frac{1}{\tanh(3\Phi_j)} - \frac{1}{3\Phi_j} \right) \quad (\text{Equation 36})$$

$$\eta_{ext,j} = \frac{1}{1 + \frac{0.6}{Sh} \Phi_j \tanh(\Phi_j)} \quad (\text{Equation 37})$$

The Thiele-modulus for spherical particles is calculated according to Equation 38.

$$\Phi_j = \frac{d_p}{6} \sqrt{\frac{n_j+1}{2} \frac{k_{j,v} \rho_p c_{CO}^{n_j-1}}{D_{eff,CO}}} \quad (\text{Equation 38})$$

The volumetric reaction constant can be derived from the intrinsic kinetic model, although it is important to keep the correct unit in mind, which depends on the reaction stoichiometry of the reaction (Equation 39 and Equation 40).

$$k_{COM,V} = k_{COM,m} \frac{RT}{p^2} \quad \left[ \frac{m^3}{kg_{cat} s} \right] \quad (\text{Equation 39})$$

$$k_{WGS,V} = k_{WGS,m} RT \quad \left[ \frac{m^3}{kg_{cat} s} \right] \quad (\text{Equation 40})$$

Effective diffusion coefficient depends on catalyst tortuosity, porosity, molecular and Knudson diffusion (Equation 41 and Equation 42).

$$D_{eff,CO} = \frac{\varepsilon_{cat}}{\tau_{cat}} \frac{1}{\frac{1}{D_{CO}^m} + D_{knu,CO}} \quad (\text{Equation 41})$$

$$D_{knu,CO} = \frac{d_{pore}}{3} \sqrt{\frac{8RT}{\pi M_{CO}}} \quad (\text{Equation 42})$$

For high mass transfer limitation and therefore low catalyst efficiencies ( $\ll 10\%$ ) the basic Thiele modulus approach as presented above is not the most accurate. The calculation approach by Roberts and Satterfield [64] is more suitable for small values of the effective reaction rate, because it takes adsorption directly into account (Equation 43). If the concentration of educts tends to zero due to significant mass transfer limitation, as shown in Figure 5, adsorption effects are significant.

$$\eta_{eff\ thhw,j} = \frac{\sqrt{2}}{\Phi_j} \left( \frac{1+K p_{CO}}{K p_{CO}} \right) (K p_{CO} - \ln(1 + K p_{CO}))^{1/2} \quad (\text{Equation 43})$$

## 2.2.8 Fixed bed characteristics

The porosity of catalytic fixed beds is an important factor influencing the gas flow including gas dispersion, the distribution of catalytically active substance and the mass transfer limitation. Hence, it is very important for the design of well performing methanation reactors.

A fixed bed in a tubular system is characterized by porosity distribution caused by the reactor walls. The reactor wall disturbs the even distribution of a fixed bed and leads to higher porosity close to the wall. Higher porosities close to the reactor wall can result in near-wall gas channelling. [65–67]

In the appendix of paper II [55] the fixed bed characteristics of tubular reactors are thoroughly discussed. Conservative and more realistic rules of thumbs in terms of the  $d_{r,i}/d_p$  ratio for evenly distributed fixed beds according to Andrigo [68] and Sie [49] are assessed. Furthermore, radial distribution profiles of bed porosity for a 14 mm reactor were calculated and compared based on formulations by Giese [66] and De Klerk [67]. Finally, recent findings from Eppinger [65] based on a DEM method for the gas flow characteristics in low  $d_{r,i}/d_p$  ratio pipes were taken into account to evaluate the inhomogeneity of fixed bed porosity and its consequences for methanation performance.

## 3 Research

### 3.1 Experimental and modelling investigation of Co-SOEC syngas methanation in a high diameter ratio polytropic reactor

#### Scientific article I: “2D heterogeneous model of a polytropic methanation reactor”

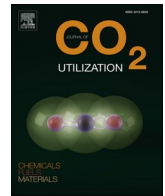
A. Krammer, M. Peham, M. Lehner, 2D heterogeneous model of a polytropic methanation reactor, Journal of CO<sub>2</sub> Utilization 62 (2022) 102059. <https://doi.org/10.1016/j.jcou.2022.102059>.

#### Contribution according to CRediT authorship contribution statement:

Andreas Krammer: Conceptualization, Methodology, Formal analysis, Investigation, Data curation, Validation, Writing – original draft.

Martin Peham: Conceptualization, Methodology.

Markus Lehner: Supervision, Conceptualization, Funding acquisition, Writing – review & editing.



## 2D heterogeneous model of a polytropic methanation reactor

Andreas Krammer<sup>\*</sup>, Martin Peham, Markus Lehner

Chair of Process Technology and Industrial Environmental Protection, Montanuniversität Leoben, Austria

### ARTICLE INFO

#### Keywords:

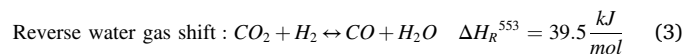
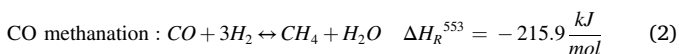
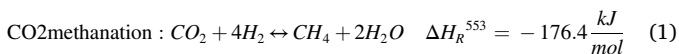
CO methanation  
Co-SOEC syngas methanation  
Uncooled methanation  
Effective reaction kinetics  
Mass transfer limitation

### ABSTRACT

The paper presents a heterogeneous 2D model of a polytropic fixed bed methanation reactor for Co-SOEC syngas. The reactor with 80 mm inner diameter is operated without active cooling. Lab-scale experiments were used for model validation under variation of gas hourly space velocity (GHSV) (2000 h<sup>-1</sup>, 4000 h<sup>-1</sup>, 6000 h<sup>-1</sup> and 8000 h<sup>-1</sup>) and pressure (1 bar, 2 bar, 4 bar, 6 bar, 8 bar, 10 bar). The conversion of Co-SOEC syngas containing a mixture of H<sub>2</sub>, CO and CO<sub>2</sub> was calculated based on a two-step methanation kinetic model. Effective methanation kinetics was implemented based on a novel approximation of two different reaction efficiency approaches. The catalytic efficiency approximation combines conventional power law related and a Langmuir-Hinshelwood type reaction efficiency correlation by Roberts and Satterfield. It was found that mass transfer limitation is substantial for highly temperature sensitive polytropic methanation reactor modelling. Despite high exothermic behaviour without active cooling, a stable model set-up was managed entirely without parameter fitting to experimental data for a naturally cooled methanation reactor with highly reactive and undiluted syngas feed. The modelled results of Co-SOEC syngas methanation agree well with the experiments over a wide variety of pressure and GHSV. The interaction and limiting factors of mass diffusion, reaction heat removal, kinetics and thermodynamics can be thoroughly analysed based on the established model, which is a key step for developing highly efficient methanation reactor systems in industrial scale.

### 1. Introduction

Successful decarbonisation of our energy sector is substantial to ensure stable development for all coming generations on this planet. To cover the continuously increasing demand for energy of this world and end the emission of greenhouse gases at the same time, renewable energy generation needs to be multiplied in a short period of time. As a result, efficient strategies to store volatile electric energy from renewable sources will be needed. [1] Under the term power to gas (PtG) all technologies aiming to transfer electric energy to gaseous energy carriers are summarized. The methanation of CO<sub>2</sub> with renewable hydrogen to methane is likely to play an important role in storing surplus electric energy. This catalytic process can be described by the Sabatier reactions (Eq. 1 and Eq. 2) and the reverse water gas shift reaction (Eq. 3), for which Nickel is the most common catalytic material. [2,3].



The methanation technology not only provides high potential for long term seasonal storage and future electric grid stabilization, it also benefits from the long-lasting experience, existing infrastructure and the continuing requirement for methane in the chemical industry. In the project “HydroMetha” a consortium of industrial and academic partners aim to develop and realize a coupled Co-SOEC and methanation plant to achieve the demonstration of an highly efficient PtG system. This work on reactor modelling intends to contribute to these methanation development tasks. [4].

Several recent publications addressing methanation reactor modelling can be found. In a substantial work by Gruber et al. [2,5] a 2D CO<sub>2</sub> methanation model including boiling water cooling of a 3 cm diameter packed bed reactor was realized. Based on a comprehensive numeric analysis of available intrinsic kinetic approaches the authors chose the single-step LHHW (Langmuir-Hinshelwood-Hougen-Watson) kinetic by Koschany [6] in an adapted version for the model implementation. In line with our experience, the author argues that an intrinsic kinetic alone is not sufficient to obtain functioning methanation models. Gruber therefore considered mass transport limitations through the

<sup>\*</sup> Correspondence to: Montanuniversität Leoben, Franz Josef-Straße 18, 8700 Leoben, Austria.  
E-mail address: [andreas.krammer@unileoben.ac.at](mailto:andreas.krammer@unileoben.ac.at) (A. Krammer).



Nomenclature	
<b>Abbreviations</b>	
0D, 1D, 2D, 3D	zero dimensional, one dimensional, two dimensional, three dimensional
CFD	Computational fluid dynamics
COx	Carbon oxides (carbon monoxide, carbon dioxide)
Co-SOEC	High-temperature co-electrolysis
GHSV	Gas hourly space velocity
LHHW	Langmuir-Hinshelwood-Hougen-Watson
NI	Standard litre
PtG	Power to Gas
wt	Weight
<b>Symbols</b>	
a	Reactor inlet cross-sectional area $m^2$
$A_{inlet}$	Reactor inlet cross-sectional area $m^2$
$A_{particle}$	Molar heat capacity $\frac{W}{mol \cdot K}$
$C_p$	Molar heat capacity $\frac{W}{mol \cdot K}$
$c_p$	Specific heat capacity $\frac{W}{kg \cdot K}$
$D_{ik}$	Particle diameter of catalyst/inert pellet $m$
$D_i^m$	Particle diameter of catalyst/inert pellet $m$
$D_{reactor}$	Particle diameter of catalyst/inert pellet $m$
$d_{particle}$	Particle diameter of catalyst/inert pellet $m$
$d_{reactor}$	Inside diameter of the reactor $m$
$h_{reactor}$	Molar mass $\frac{mol}{kg}$
$M$	Molar mass $\frac{mol}{kg}$
I	Identity vector $m^{-2}$
$J_i$	Diffusive flux of species $i$ $\frac{kg}{m^2 \cdot s}$
$K_{p,COM}$	Equilibrium constant (pressure based) CO methanation $Pa^{-2}$
$K_{p,rWGS}$	Equilibrium constant (pressure based) for reverse WGS-
$k_b$	Boltzmann constant $\frac{W}{m^2 \cdot K^4}$
$Nu$	Nusselt-number-
p	Prandtl-number-
Pr	Prandtl-number-
q	Heat flux (conduction) $\frac{W}{m^2}$
Q	Heat source $\frac{W}{m^3}$
$Ra_H$	Rayleigh-number-
$R_{gas}$	Temperature $K$
$R_i$	Temperature $K$
$T_j$	Temperature $K$
$S_v$	Temperature $K$
T	Temperature $K$
u	Collision integral-
$\dot{V}_{in}$	Collision integral-
$V_{particle}$	Collision integral-
$w_i$	Collision integral-
$x_i$	Collision integral-
$\alpha$	Collision integral-
$\Omega$	Collision integral-
$\varepsilon/k_b$	Potential energy minimum of the Lennard-Jones/Stockmeyer potential divided by the Ludwig-Boltzmann constant $K$
$\varepsilon_{bed}$	Bed porosity-
$\varepsilon_{rad}$	Emissivity-
$\eta$	Heat conductivity $\frac{W}{m \cdot K}$
$\kappa$	Heat conductivity $\frac{W}{m \cdot K}$
$\lambda$	Heat conductivity $\frac{W}{m \cdot K}$
$\mu$	Dipole moment $C \cdot m$
$\mu_D$	Dipole moment $C \cdot m$
$\nu$	Stoichiometric factor-
$\nu_{ij}$	Stoichiometric factor-
$\rho$	Characteristic length of the Lennard-Jones/Stockmeyer potential $m$
$\sigma$	Characteristic length of the Lennard-Jones/Stockmeyer potential $m$
<b>Subscripts and superscripts</b>	
cond	Conduction
conv	Convection
diff	Diffusion
ext	External
eff, Thiele	Effective conventional Thiele-based approach
gas	Gaseous phase
gas – wall	From gas to wall
i	Species i
j	Reaction j
k	Species k
lam	Laminar
rad	Radiation
reactor	Reactor
reaction	Reaction derived
RobSat	Method by Roberts and Satterfield
solid	Solid phase
solid – gas	From solid pellet bed material to gas
solid – wall	From solid to wall
sup	Superficial
turb	Turbulent
vis	Viscosity

implementation of an adapted Thiele modulus approach. After some numeric adjustments the model results were compared by Gruber to experimental findings and reveal good agreement.

In Table 1 recent methanation modelling publications are listed and compared by their reactor and model characteristics. It can be seen that all models are based on cooled reactor systems leading to a more stable modelling setting with lower risk of thermal runaway. In contrast, the underlying work aimed at modelling an uncooled, far more adiabatic reactor system with cooling only by natural convection. Uncooled methanation reactors are used in pilot and industrial scale in the TREMP® process by Haldor Topsoe A/S, which come to use for the methanation of gasified biomass within the project GoBiGas. [16,17] Furthermore, exclusively CO<sub>2</sub> methanation was investigated in the listed studies, most often in stoichiometric mixtures with H<sub>2</sub> in the feed.

Based on a comparison of recent publications on two-phase catalytic

methanation reactor modelling a research gap can be derived including following important aspects:

- Methanation of gas mixtures containing carbon monoxide
- Methanation of over-stoichiometric hydrogen shares
- Reactor systems with natural cooling at ambient air
- Reactor systems with diameters > 30 mm resulting in high radial gas velocity gradients

This works aim is to contribute in closing the above mentioned research gap in methanation modelling.

Most methanation modelling studies include effective methanation reaction kinetics by power law related Thiele modulus approach or through implementation of a particle model. Mass transfer limitation in methanation reaction models was considered via a catalytic efficiency

**Table 1**  
Overview of established methanation reactor models including model characteristics.

Author	Exp. verif./ Catalyst eff.	Model	Reactor (active catalyst mat.)	$d_{\text{Reactor}}$ $d_{\text{particle}}$ [mm]	GHSV [h <sup>-1</sup> ]	Feed gas	Pressure (abs.) [bar]	Kinetic approach
This work	Yes/Yes	2D stationary	Uncooled packed bed (Ni)	80 2.8–6.3	2000–8000	H <sub>2</sub> /CO/CO <sub>2</sub> ; 3% overstoich.	1–10	Rönsch[18] (LHHW)
Gruber[2,5] (2020)	Yes/Yes	0D/2D/3D stationary	Cooled packed bed (Ni)	30 5	7692–38462	H <sub>2</sub> /CO <sub>2</sub> ; 4/1	1–30	Koschany[6] (modified, LHHW)
Lefebvre[7] (2020)	No/Yes	1D stationary/ transient	Cooled packed bed tube bundle (Ni)	20 3	59683	H <sub>2</sub> /CO <sub>2</sub> / CH <sub>4</sub> ; 4/1/1	20	Lefebvre[8] (power law)
Vázquez[9] (2018)	Yes/No	1D/2D stationary	Heat exch. reactor (Ni)	2 wall coated	4400	H <sub>2</sub> /CO <sub>2</sub> ; 4/1; 6/1	atm.; 5	Xu and Froment[10] (adapted, LHHW)
Try[11] (2018)	Yes/Yes	2D stationary/ transient	Cooled packed bed (Ni)	6 0.34	15000	H <sub>2</sub> /CO <sub>2</sub> ; 4/1	2.5	Xu and Froment (LHHW)
Schlereth and Hinrichsen[12] (2014)	No/Yes	2D stationary	Cooled packed bed (Ni)	20 3	5000	H <sub>2</sub> /CO <sub>2</sub> ; 4/1	10	Xu and Froment (LHHW)
Sun and Simakov[13] (2017)	No/No	1D transient	Heat exch. reactor (Ni)	200 3	100–50000	H <sub>2</sub> /CO <sub>2</sub> ; 4/1	5	Xu and Froment (LHHW)
Ducamp[14] (2017)	Yes/Yes	2D stationary	Cooled packed bed (Ni)	20 1.5–6	15157 (excl. Ar)	H <sub>2</sub> /CO <sub>2</sub> /Ar; 4/1/10	4, 8	Xu and Froment (LHHW)
Kiewidt and Thöming [15] (2015)	Yes/Yes	1D stationary	Cooled packed bed (Ru)	25 3	6000, 15500	H <sub>2</sub> /CO <sub>2</sub> ; 4/1	1–20	Lunde and Kester[19] (Ruthenium)
Kreitz[20] (2019)	No/No	1D stationary/ transient	Cooled packed bed (Ni)	2 0.4	2000–5000	H <sub>2</sub> /CO <sub>2</sub> ; 0.25–8	8	Koschany (LHHW)[6]

factor in Schlereth and Hinrichsen [12], Kiewidt and Thöming [15] and Kreitz et al. [20]. Schlereth and Hinrichsen used a particle model based on an adapted dusty-gas approach by Skrzypek et al. [21] to calculate the catalytic efficiency factor. Schlereth and Hinrichsen [12] found values lower than 0.05 and up to 0.8 for a 20 mm reactor and 5 mm particles. Kiewidt and Thöming [15] calculated the effectiveness factor from the Thiele modulus for first-order reactions with CO<sub>2</sub> as the limiting species. The calculated effectiveness factor varies between 0.05 and 0.4 for a 25 mm reactor and 3 mm pellets. [15] Kreitz et al. modelled a 2 mm reactor with a particle size of 0.4 mm and found catalytic efficiencies between approximately 0.45 and above 0.95. The authors Kreitz et al. referenced the approach shown by Schlereth and Hinrichsen [12] and Ducamp et al. [14] for the calculation of the catalytic efficiency. Gruber et al. [2,5] found lowest values for catalyst efficiencies at temperature peaks of external catalyst efficiency to be around 0.35 and intra-particle catalyst efficiency of roughly 0.03. [2,5] Ducamp [14] reported catalyst efficiencies based on a pellet model below 0.2 over a wide range of reactor length and around 0.08 at the lowest point for both methanation reactions. The modelling and experimental trials were conducted at 4 bar and 25 Nl/min of stoichiometric CO<sub>2</sub>/H<sub>2</sub> mixture together with 50 Nl/min of argon to limit reactor temperature.

Furthermore, the modelled reactor in this work has a significantly wider diameter of 80 mm resulting in high gas velocity gradients in radial direction, compared to those 2D models in literature (2–30 mm). While some studies deal with wall coated catalysts [9,22] or very fine catalyst pellets [11], Gruber [2] (~5 mm), Schlereth and Hinrichsen [12] (3 mm), Lefebvre [7] (3 mm), Sun and Simakov [13] (3 mm) along with our working group (2.8–6.3 mm) focused on using larger catalyst pellets in a commercially available and industrial scale.

In the underlying work a large focus was placed on reaction efficiency investigation. As can be drawn from Eqs. 47–50 the catalytic efficiency is a function of the catalyst particle diameter and the Sherwood number, which again is a function of the Reynolds number and therefore the gas velocity. The lower the gas velocity and the larger the catalyst pellet the lower the catalytic efficiency. For the used setup with a relatively large reactor diameter of 80 mm and therefore low gas

velocities and large catalyst particles even lower catalytic efficiency than found in literature must be expected. The effective catalyst efficiency is calculated via a common n<sup>th</sup>-reaction order Thiele modulus approach for power law kinetics and a method proposed by Roberts and Satterfield [23] for LHHW kinetics. This expression was a key step to enable stable and accurate modelling of the uncooled methanation system.

## 2. Model design

For the simulation of a laboratory scale methanation reactor a 2D axisymmetric model was created with the simulation software Comsol Multiphysics®, which will be thoroughly described in the following chapter.

### 2.1. Model geometry and packed bed characteristics

The geometry of the model corresponds to the laboratory reactor design. The main dimensions, such as inner and outer diameter, catalyst bed height, inert bed heights and reactor wall thickness represent the original size. Furthermore, it is of particular importance to include gas inlet and gas outlet pipes in the original dimensions, because the high incoming gas velocity as a consequence of the small inlet diameter of 4 mm has a significant influence on the gas distribution within the catalyst bed and therefore the modelling results. Nevertheless, the exact flange design was not considered to be important, therefore, the reactor flanges were neglected in the model geometry. The simplified reactor geometry includes smoother transitions via relatively large transition radii between the small inlet and outlet diameter of 4 mm and the reactor diameter of 80 mm to enhance the stability of the model. In Fig. 1 and Fig. 2a schematic representation of the reactor model and the corresponding model geometry is shown.

As can be derived from Fig. 2 four domains are distinguished, representing the lower inert bed domain including the inlet pipe, the upper inert bed domain including the outlet pipe, the catalyst bed domain in the centre and the reactor wall domain. The spherical catalyst pellets have significant polydisperse character, leading to a decrease in bed

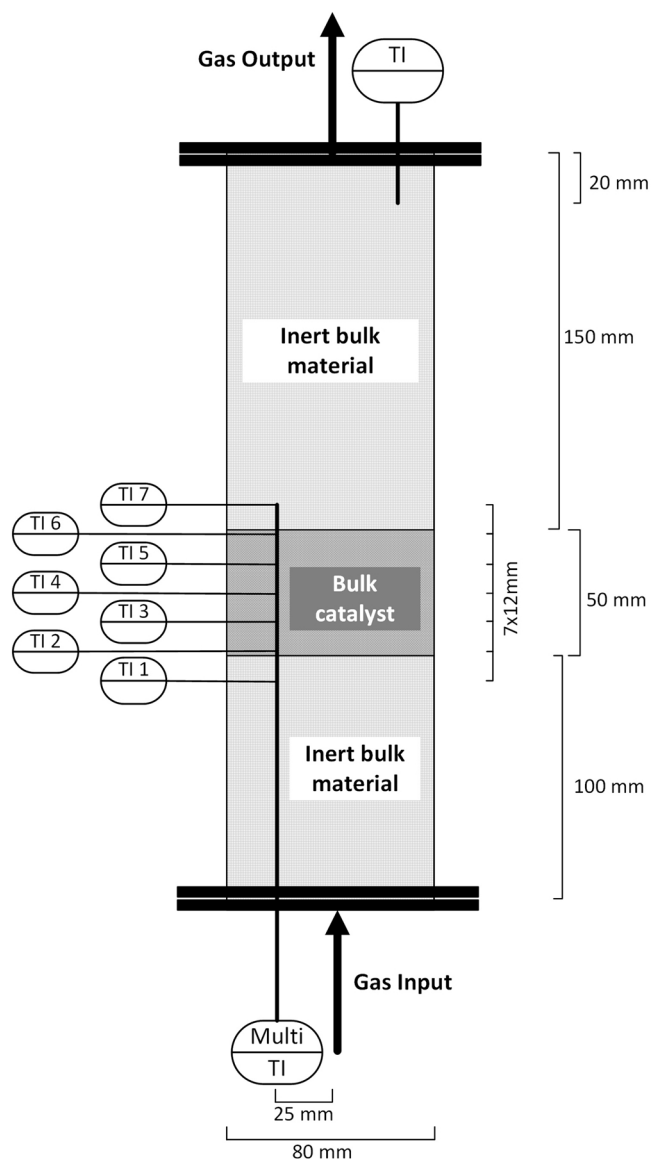


Fig. 1. Schematic drawing of the methanation reactor of the laboratory test plant including a multi-thermocouple with seven measurement points.

porosity. According to formulations by Tsotsas [24] for polydisperse spherical pellet beds a catalyst bed porosity of 0.389 was calculated including a manual measurement of the pellet size distribution of the catalyst spheres. Starting from this minimum value in the centre of the bed the radial increase of catalyst bed porosity towards the reactor wall was included by an approach presented by Winterberg et al. [25]. The intra-particle porosity of the catalyst particles is necessary to enable calculation of volume specific reaction rates and was experimentally determined to be 0.67 by weighing and dimension measurement. The size of the inert stoneware balls is with a diameter of about 9.5 mm larger compared to the catalyst spheres (2.8–6.3 mm) and its particle size distribution is less wide. A bed porosity of 0.37 was defined for the inert bed centre and its polydisperse character was neglected. The radial bed porosity distribution was considered analogously to the catalyst bed. Additionally, mixing of smaller catalyst pellets into the inert bed and vice versa likely occurred during reactor assembly at the bed interfaces. As a consequence, the boundary between inert and catalyst bed should not be expected to be as perfectly sharp in the experimental setup as in the model. The most important reactor and bed parameters are listed in Table 2.

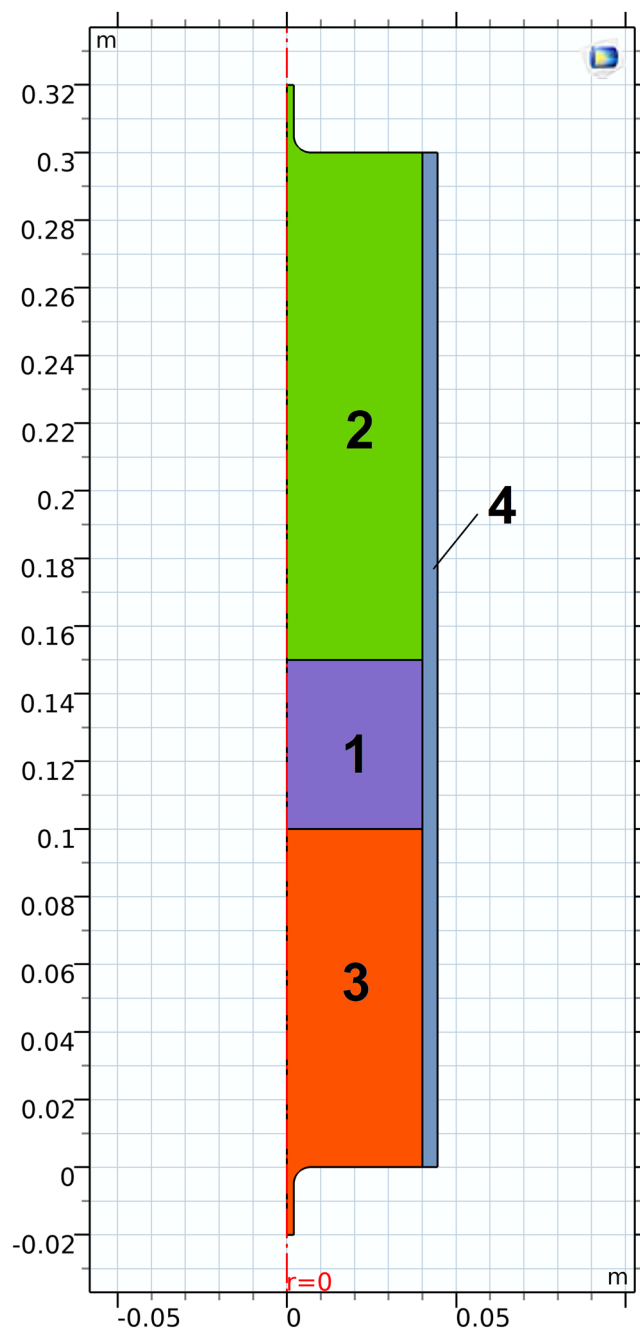


Fig. 2. Graphical representation of the methanation reactor system as the basis for a model in Comsol Multiphysics including 4 domains: Catalyst bed (1); Upper inert bed (2); Lower inert bed (3); Reactor wall (4).

## 2.2. Determination of pressure and velocity fields from mass and momentum equations

The transport of mass and momentum in porous media was calculated for each of the three bulk domains described above. The bulk domains were defined as porous, thus the Brinkman equations were chosen to compute the gas velocity and pressure fields in porous media. [26] The Brinkman equations are always solved as a combination of continuity equation and momentum equation and are given in the appendix for stationary flow of compressible Newtonian fluids excluding gravity and the Forchheimer drag.

The permeability  $\kappa$  of the packed bed is calculated by the Kozeny-Carman equation in Equation 4, whereby all particles are considered

**Table 2**  
Methanation reactor dimensions and packed bed parameters.

Inner reactor diameter	80 mm
Reactor wall thickness	4.45 mm
Catalyst bed height	50 mm
Catalyst pellet diameter	90% of catalyst mass between 2.8 mm and 6.3 mm
Catalyst bed porosity (centre)	0.389
Catalyst intra-particle porosity	0.67
Catalyst composition	Alumina (72.2 wt%), Calcium Oxide (5.6 wt%), Nickel (22.2 wt%)
Inert stoneware ball diameter	~9.5 mm
Inert bed porosity (centre)	0.37
Lower inert bed height	100 mm
Upper inert bed height	150 mm

as spheres.

$$\kappa = \frac{d_{particle} \epsilon_{bed}^3}{180(1 - \epsilon_{bed})^2} \quad (4)$$

The value  $d_{particle}$  corresponds to the mean particle diameter of the catalyst spheres respectively the inert stoneware balls of the upper and lower inert beds. The particle diameters were determined based on a representative manual size measurement [26–28].

The feed gas volume flow is defined in the model via the input gas velocity. For comparability of different reactor systems the volume flow can be transferred into the gas hourly space velocity (GHSV) according to Eq. 5 and Eq. 6 serving as plant capacity, respectively catalyst load. The GHSV is calculated as the quotient of input gas flow at standard pressure and temperature and total catalyst bed volume. Nevertheless, for the comparison of different reactor systems based on the GHSV (Eq. 5 and Eq. 6) further important performance influences, such as reactor pressure, active material load or catalyst density need to be taken into account.

$$\dot{V}_{in} = u_{in} \cdot A_{inlet} \quad (5)$$

$$GHSV = \frac{\dot{V}_{in}}{V_{reactor}} \frac{T_{in}}{T_N} \frac{p_N}{p_{reactor}} \quad (6)$$

### 2.3. Determination of species concentrations from mass transport phenomena

The mass balance was implemented according to Eq. 7 including convective mass transport and mass dispersion in the catalyst bed.

$$\nabla \cdot \mathbf{j}_i + \rho(\mathbf{u} \cdot \nabla)w_i = R_i \quad (7)$$

Longitudinal dispersion was implemented based on the Edward and Richardson correlation [29] (Eq. 8) and lateral dispersion by the Gunn correlation [30] (Eq. 9).

$$\frac{D_{i, long}}{D_{i, m}} = 0.73 \epsilon + 0.5 \left( 1 + \frac{9.49 \epsilon}{Re_{particle} Sc} \right) Re_{particle} Sc \quad (8)$$

$$\frac{D_{i, lat}}{D_{i, m}} = \frac{\epsilon}{1.91} + \frac{Re_{particle} Sc}{11 - 4 \exp\left(-\frac{7}{Re_{particle}}\right)} \quad (9)$$

The molecular diffusion was determined by a mixture-averaged approach. The binary diffusion coefficients  $D_{ik}$  for each species  $i$  in any other species  $k$  are calculated within the “Chemistry” interface of the program based on the kinetic gas theory (see also section “Determination of thermodynamic and transport properties”). [31,32] For this reactor model the thermal diffusion, the transport of mass driven by temperature gradients described as the Soret effect, is of irrelevant magnitude and therefore was neglected by setting all thermal diffusion constants  $D_i^T$  to zero. [33].

An important value for the methanation performance is the combined CO and CO<sub>2</sub> conversion, which will be called CO<sub>x</sub> conversion within this work. It is defined as the amount of transformed CO and CO<sub>2</sub> related to the amount of CO and CO<sub>2</sub> fed to the reactor system as shown in Eq. 10.

$$CO_x - conversion = \frac{(j_{CO,in} - j_{CO,out}) + (j_{CO_2,in} - j_{CO_2,out})}{j_{CO,in} + j_{CO_2,in}} \quad (10)$$

### 2.4. Determination of the temperature from heat balance equations

For the heat balance of each of the three bulk domains it has been distinguished between a fluid phase (Eq. 11) and a solid porous phase (Eq. 12). While for the mass balances a homogenous porous phase was considered, a heterogeneous bulk phase was used concerning heat transfer. Thus, two predefined software heat transfer interfaces, a “Heat Transfer in Fluids” interface for the gaseous phase and a “Heat Transfer in Solids” interface for the solid porous phase, were set up. This parallel heat balances approach for both continua enables to determine the temperature for the solid as well as for the gaseous phase.

$$\rho_{gas} c_{p,gas} \mathbf{u} \cdot \nabla T_{gas} + \nabla \cdot (\lambda_{gas} \nabla T_{gas}) = Q_{solid-gas} \quad (11)$$

$$\nabla \cdot (\lambda_{solid} \nabla T_{solid}) = -Q_{solid-gas} + Q_{Reaction} \quad (12)$$

Two temperature values, one for the gas and one for the solid phase, enables to estimate if heat transfer limitation between solid pellets and gaseous phase exists.

The reaction heat source  $Q_{Reaction}$  is introduced to the solid phase within the catalyst bed domain because the exothermal reaction takes place at the active sites of the solid catalyst. The reaction heat term does not exist for the inert bulk domains.

Also the heat transfer between gaseous and solid phase is implemented in the form of a heat source  $Q_{solid-gas}$  and is based on Nusselt-relations for the particle-fluid heat transfer by fluid flow in bulk material as described in Eqs. 13 to 22. [24].

$$Q_{solid-gas} = \alpha_{solid-gas} S_v (T_{gas} - T_{solid}) \quad (13)$$

$$\alpha_{solid-gas} = \frac{Nu_{solid-gas} \lambda_{gas}}{d_{particle}} \quad (14)$$

$$Nu_{solid-gas} = f_a \left( 2 + \sqrt{Nu_{sg,lam}^2 + Nu_{sg,turb}^2} \right) \quad (15)$$

$$Nu_{sg, lam} = 0.664 \sqrt{Re_{particle}} \sqrt[3]{Pr} \quad (16)$$

$$Nu_{sg, turb} = \frac{0.037 Re_e^{0.8} Pr}{1 + 2.443 Re_e^{-0.1} (Pr^{\frac{2}{3}} - 1)} \quad (17)$$

$$Re_{particle} = \frac{u_{sup} d_{particle}}{\nu \epsilon_{bed}} \quad (18)$$

$$Pr = \frac{\nu}{a} \quad (19)$$

$$f_a = 1 + 1.5 * (1 - \epsilon_{bed}) \quad (20)$$

$$S_v = (1 - \epsilon_{bed}) \frac{A_{particle}}{V_{particle}} \quad (21)$$

$$\alpha = \frac{\lambda_{gas}}{\rho c_p} \quad (22)$$

The heat transport within the solid phase of the catalyst bed was implemented by an effective heat conduction value for packed spherical beds  $\lambda_{solid}$  calculated based on the well-known model by Zehner, Bauer and Schlünder [34–37].

Furthermore, heat fluxes from the gaseous phase to the wall  $q_{gas-wall}$

(Eq. 23) as well as from the solid phase to the wall  $q_{solid-wall}$  (Eq. 24) are implemented.

$$q_{gas-wall} = \alpha_{gas-wall} (T_{fluid} - T_{wall}) \quad (23)$$

$$q_{solid-wall} = \alpha_{solid-wall} (T_{solid} - T_{wall}) \quad (24)$$

The required heat transfer coefficient between gas and wall  $\alpha_{gas-wall}$  was defined by the Nusselt-relation for heat transfer in cylindrical pipes with laminar flow as shown in Eq. 25 and Eq. 26. [24].

$$\alpha_{gas-wall} = \frac{Nu_{gw, lam} \lambda_{gas}}{d_{reactor}} \quad (25)$$

$$Nu_{gas-wall, lam} = 3.66 \quad (26)$$

For the description of the heat transfer between the packed pellet bed and reactor wall the solid-wall heat transfer coefficient  $\alpha_{solid-wall}$  is determined as given in Specchia et al. [38] (Eq. 27). For spherical particles the equation can be reduced to a less complex form. The implementation of the heat transfer approach by Specchia was crucial, since it is based on low gas turbulences, and therefore fits well to the flow characteristics in the modelled reactor.

$$\alpha_{solid-wall} = \frac{\lambda_{gas}}{d_{particle}} \left( 2 \varepsilon_{bed} + \frac{1 - \varepsilon_{bed}}{\frac{\lambda_{gas}}{\lambda_{solid}} + 1} \right) \quad (27)$$

Finally, the heat balance for the reactor wall solves as shown in Eq. 28.

$$\nabla \bullet (\lambda_{wall} \nabla T_{wall}) = 0 \quad (28)$$

The heat fluxes at the inner boundaries of the wall,  $q_{solid-wall}$  and  $q_{gas-wall}$ , were already described above and are implemented analogously to the heat balance of the wall domain only with an opposite sign up front. At the outside boundaries the heat flux from the reactor wall to the surrounding atmosphere by natural convection  $q_{ext conv}$  (Eq. 29 to Eq. 31) and external radiation  $q_{ext rad}$  (Eq. 32) read as

$$q_{ext conv} = \alpha_{ext conv} (T_{ext} - T_{wall}) \quad (29)$$

$$\alpha_{ext conv} = \frac{\lambda_{gas}}{h_{reactor}} \left( \frac{4}{3} \left( \frac{7 Ra_H Pr}{5(20 + 21 Pr)} \right)^{\frac{1}{4}} + \frac{4(272 + 315Pr)h_{reactor}}{35(64 + 63Pr)D_{reactor}} \right) \quad (30)$$

$$Ra_H = \frac{g \rho_{gas,ext} c_{p,gas,ext} |\rho_{gas,ext} - \rho_{wall}| h_{reactor}^3}{\lambda_{gas,ext} \mu_{gas,ext}} \quad (31)$$

$$q_{ext rad} = \varepsilon_{rad} k_b T_{wall}^4 \quad (32)$$

The emission coefficient  $\varepsilon_{rad}$  for the reactor material made of stainless steel was estimated at 0.55 [39].

## 2.5. Determination of reaction rates based on LHHW kinetic approach and catalyst efficiency

Some methanation models [5] rely on a one-step kinetic approach based on the CO<sub>2</sub> methanation reaction (Eq. 1), most use the three-step approach by Xu and Froment [10]. The intrinsic reaction kinetics for this work are based on a two-step kinetic approach by Rönch et al. [18] presented in the form given by Gruber [2] as given in Eq. 33 and Eq. 34. In this transparent form the 'Arrhenius term' ( $-k_1 K_C K_H^2 p_{CO}^{0.5} p_{H_2}$ ), 'driving force' ( $(1 - \frac{p_{CH_4} p_{H_2 O}}{p_{CO} p_{H_2}^3 K_{p,COM}})$ ) and 'adsorption term' ( $\frac{1}{(1 + K_C p_{CO}^{0.5} + K_H p_{H_2}^{0.5})^3}$ ) can be easily distinguished. The two-step methanation kinetics formally represents the CO methanation reaction (Eq. 2) and the reverse water gas shift reaction (Eq. 3). In combination, these two reactions represent the CO<sub>2</sub> methanation reaction path as well.

$$r_{COM, intr} = \frac{-k_1 K_C K_H^2 p_{CO}^{0.5} p_{H_2} (1 - \frac{p_{CH_4} p_{H_2 O}}{p_{CO} p_{H_2}^3 K_{p,COM}})}{(1 + K_C p_{CO}^{0.5} + K_H p_{H_2}^{0.5})^3} \left[ \frac{mol}{kg_{cat} s} \right] \quad (33)$$

$$r_{rWGS, intr} = \frac{\frac{k_2}{p_{H_2}} p_{CO} p_{H_2 O} (1 - \frac{p_{H_2} p_{CO}}{p_{CO} p_{H_2 O} K_{p,rWGS}})}{(1 + K_{CO} p_{CO} + K_{H_2} p_{H_2} + K_{CH_4} p_{CH_4} + K_{H_2 O} \frac{p_{H_2 O}}{p_{H_2}})^2} \left[ \frac{mol}{kg_{cat} s} \right] \quad (34)$$

For the underlying methanation model it is important to take heat and mass transfer limitations into account by using reaction efficiency factors, limiting the intrinsic reaction rate by a factor ranging between zero and one as given in Eqs. 35 and 36. Catalytic efficiencies above one would also be possible for highly exothermal reactions due to a decrease in inhibiting effects, e.g. by higher temperatures within the catalyst increasing the reaction kinetics compared to the pellet surface conditions, although this was not found in the present study. [40,41] Inhibition by diffusion limitation leading to catalyst efficiencies below one is in particular significant in methanation for highly active and undiluted feed gas, as was used in the underlying work.

$$r_{COM, eff} = r_{COM, intr} \bullet \eta_{eff,COM} \quad (35)$$

$$r_{rWGS, eff} = r_{rWGS, intr} \bullet \eta_{eff,rWGS} \quad (36)$$

An approximation of the catalytic efficiency between a power law type and a LHHW type approach was established. The catalyst efficiency is on the one hand described based on a Thiele modulus approach intended for power law kinetics as given in Eq. 37 to Eq. 44. [2,42] The catalyst efficiency for power law equations via a n<sup>th</sup>-order Thiele modulus as discussed in Jess and Wasserscheid [42] and Gruber [5] was found to be sufficiently exact in our model for efficiency values above 10%.

$$\eta_{eff,pl,j} = \eta_{ext,j} \bullet \eta_{pore,j} \quad (37)$$

$$\eta_{pore,j} = \frac{1}{\Phi_j} \left( \frac{1}{\tanh(3 \bullet \Phi_j)} - \frac{1}{3 \bullet \Phi_j} \right) \quad (38)$$

$$\eta_{ext,j} = \frac{1}{1 + \frac{0.6}{Sh} \Phi_j \tanh(\Phi_j)} \quad (39)$$

$$\Phi_j = \frac{d_{particle}}{6} \bullet \sqrt{\frac{n_j + 1}{2} \bullet \frac{k_{j,v} \rho_{particle} c_{CO}^{n_j - 1}}{D_{eff,CO}}} \quad (40)$$

$$k_{COM,v} = k_{COM,m} \bullet \frac{R \bullet T}{p^2} \left[ \frac{m^3}{kg_{cat} s} \right] \quad (41)$$

$$k_{WGS,v} = k_{WGS,m} \bullet R \bullet T \left[ \frac{m^3}{kg_{cat} s} \right] \quad (42)$$

$$D_{eff,CO} = \frac{\Psi_{cat}}{\tau_{cat}} \bullet \frac{1}{\frac{1}{D_{CO}^{pore}} + D_{knu,CO}} \quad (43)$$

$$D_{knu,CO} = \frac{d_{pore}}{3} \bullet \sqrt{\frac{8 R T}{\pi M_{CO}}} \quad (44)$$

On the other hand for catalytic efficiencies < 10% the approximated function tends towards a different approach by Roberts and Satterfield [23]. This formulation shown in Eq. 45 was established particularly for LHHW kinetic approaches and for small catalytic efficiencies. In the course of the model development this approach was found to be more accurate for low catalytic efficiencies.

$$\eta_{eff,lhw,j} = \frac{\sqrt{2}}{\Phi_j} \left( \frac{1 + K \frac{p_{CO}}{p_{CO}}}{K \frac{p_{CO}}{p_{CO}}} \right) (K \frac{p_{CO}}{p_{CO}} - \ln(1 + K \frac{p_{CO}}{p_{CO}}))^{1/2} \quad (45)$$

As Roberts and Satterfield [23] explained, if diffusional resistance



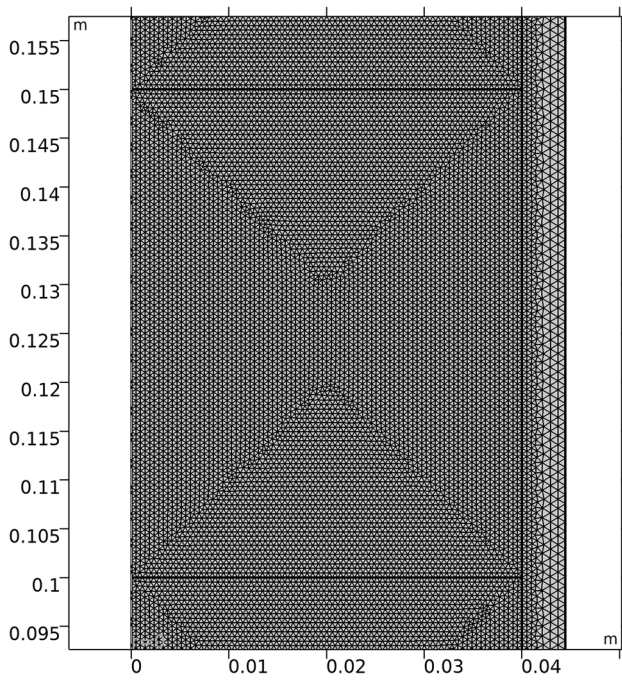


Fig. 3. Section of the mesh used for model computation showing the catalytic bed, lower and upper interface to inert bed and reactor wall.

within a particle is high (low catalytic efficiency) the reactant partial pressure might decrease from a higher value at the pellet surface to a value close to zero towards the pellet centre. As a result a wide range of concentrations occur within a catalyst pellet. The resistance of reaction rate by adsorption of educts onto or desorption of products from the active sites must be considered for the determination of catalyst efficiency. Roberts and Satterfield [23] considered adsorption effects for LHHW type of rate equations. Conventional power law type catalytic efficiency equations may approximate LHHW rate expressions well in a narrow range of concentrations within a catalyst pellet, but are less accurate for very low catalytic efficiencies. As a consequence, for high catalytic efficiencies (>10%) the power law based formulation was found to sufficiently accurate and the LHHW based expression was far off. At low catalytic efficiencies (<10%) the LHHW based expression delivered the best results, while too small and therefore not useful catalytic values were obtained with power law based efficiency equations. To find a practicable solution for the model the two strategies were merged via a hyperbolic tangent function to approximate the total catalytic efficiency as given in Eq. 46. The hyperbolic function is set up to be dominated by the power law approach above a threshold of 0.01, and on the other hand mostly be defined by the LHHW efficiency when approaching this threshold.

$$\eta_{eff,j} = \eta_{eff,pl,j}(\tanh(10 \cdot \eta_{cat,pl,j} - 0.01)) + \eta_{eff,lhhw,j} * (1 - \tanh(10 \cdot \eta_{eff,lhhw,j} - 0.01)) \quad (46)$$

As a consequence, at higher values above 10% the conventional method for power law kinetics is dominating the final efficiency, while for low values the method by Roberts and Satterfield designed for LHHW kinetics takes over. However, the exact threshold of 0.01 remains a result of arbitrary definition in the course of model development.

To obtain a volume related value the effective volume specific reaction rate  $r_{j,eff,v}$  can be calculated as given in Eq. 47 with the total bed density  $\rho_{bed}$  which considers the bed porosity  $\epsilon_{bed}$  as well as particle porosity  $\epsilon_{particle}$ .

$$r_{j,eff,v} = r_{j,eff} \cdot \rho_{bed} = r_{j,eff} \cdot \rho_{solid} (1 - \epsilon_{bed})(1 - \epsilon_{particle}) \quad (47)$$

The equilibrium constants  $K_{p,COM}$  and  $K_{p,rWGS}$  were calculated from correlations published by Elnashaie and Elshishini [43] described in Eq. 48 and Eq. 49, whereas for  $K_{p,COM}$  the unit [ $Pa^{-2}$ ] has to be considered.

$$K_{p,COM} = \frac{1}{1.026676 \cdot 10^{10}} \cdot \exp\left(\frac{26830 [K]}{T_{solid}} - 30.11\right) [Pa^{-2}] \quad (48)$$

$$K_{p,rWGS} = \frac{1}{\exp\left(\frac{4400 [K]}{T_{solid}} - 4.063\right)} [ - ] \quad (49)$$

Finally, with the reaction rate  $r_j$  of each reaction  $j$  the formation rate  $R_i$  of a species  $i$  can be determined as given in Eq. 50 and Eq. 51.

$$R_{ij} = \nu_{ij} r_j \quad (50)$$

$$R_i = \sum_j R_{ij} \quad (51)$$

## 2.6. Determination of thermodynamic and transport properties

In addition to the implementation of the kinetic expressions also the species related transport properties, such as the binary diffusion coefficients  $D_{i,k}$  (Eq. 52), the viscosities  $\mu_i$  (Eq. 53) and conductivities  $\lambda_i$  of the gas species (Eq. 54) are calculated within the model. The diffusion coefficients and the viscosity are determined based on the kinetic gas theory according to Brokaw [31] via the Collision integral  $\Omega$  given in Neufeld et al. [44] as predefined in the model software.

$$D_{i,k} = 2.628 \cdot 10^{-22} \frac{\sqrt{T^3(M_i + M_k)/(2 \cdot 10^3 M_i M_k)}}{p \sigma_i \sigma_k \Omega_{Diff}} \quad (52)$$

$$\mu_i = 2.669 \cdot 10^{-6} \frac{\sqrt{T} M_i \cdot 10^3}{\sigma_i^2 \Omega_{vis}} \quad (53)$$

The thermal conductivity  $\lambda_i$  is calculated via the Stiel-Thodos equation [45].

$$\lambda_i = \mu_i \cdot \frac{1.15 C_{p,i} + 0.88 R_{gas}}{M_i} = 2.669 \cdot 10^{-6} \frac{\sqrt{T} M_i \cdot 10^3}{\sigma_i^2 \Omega_{cond}} \cdot \frac{1.15 C_{p,i} + 0.88 R_{gas}}{M_i} \quad (54)$$

The three gas transport property values for each of the gas species, the Lennard-Jones/Stockmeyer potential  $\sigma$ , the potential energy minimum of the Lennard-Jones/Stockmeyer potential divided by the Boltzmann constant  $\epsilon/k_b$  (frequently listed form in literature) and the dipole moment  $\mu_D$  were taken from literature [39,46,47] and are listed in the Appendix.

The thermodynamic properties of each gas species such as the molar heat capacity  $C_{p,i}$ , the molar enthalpy  $h_i$  and the molar entropy  $s_i$  were calculated based on NASA polynomials as shown in Eq. 55 to Eq. 57. The corresponding polynomial constants are listed in the Appendix. [26,32,48].

$$C_{p,i} = R_{gas} (a_{1,i} + a_{2,i} \cdot T + a_{3,i} \cdot T^2 + a_{4,i} \cdot T^3 + a_{5,i} \cdot T^4) \quad (55)$$

$$h_i = R_{gas} (a_{1,i} T + a_{2,i} \cdot \frac{T^2}{2} + a_{3,i} \cdot \frac{T^3}{3} + a_{4,i} \cdot \frac{T^4}{4} + a_{5,i} \cdot \frac{T^5}{5} + a_{6,i}) \quad (56)$$

$$s_i = R_{gas} (a_{1,i} \ln \frac{T}{T_0} + a_{2,i} \cdot T + a_{3,i} \cdot \frac{T^2}{2} + a_{4,i} \cdot \frac{T^3}{3} + a_{5,i} \cdot \frac{T^4}{4} + a_{7,i}), T_0 = 1[K] \quad (57)$$

An extremely dense mesh was used for the model with a total number of 96731 elements of triangular shape. A central section of the used mesh is displayed in Fig. 3 including catalyst bed, lower and upper inert bed interface and reactor wall. The maximum size of a triangular

**Table 3**  
Composition of Co-SOEC syngas used as methanation feed gas.

Gas species /Process parameters	Co-SOEC syngas
H <sub>2</sub>	76.8 vol.-%
CO	18.3 vol.-%
CO <sub>2</sub>	4.9 vol.-%
GHSV [h <sup>-1</sup> ]	2000–8000
Pressure [bar]	1–10

element within the packed bed section is 0.3 mm and for the reactor wall 3.4 mm. A mesh test was conducted based on the temperature result in dependence of mesh density. The highly dense mesh was necessary since temperature peak within the first millimetres of the catalyst bed would slightly decrease at lower mesh density as Figure C.1 and Figure C.2 indicate.

### 3. Experimental

An existing lab-scale setup has been used to acquire reference data from experiments for extensive model validation. The modelled reactor equals the real setup in all relevant properties, an uncooled 80 mm diameter packed bed reactor filled with Nickel-based commercial catalyst spheres (Meth 134®). The nominal operating temperature is 260 °C and 510 °C, but it can withstand temperatures of 700 °C for short periods of time. The most important reactor parameters can be found in Fig. 1 and Table 2. For start-up and the catalyst activation procedure at elevated temperatures a reactor heater was installed. In operation the heaters can be flipped aside easily and then only cooling by natural convection of ambient air affects the polytropic reactor behaviour externally. The feed gas is mixed from gas bottles via mass-flow controllers. The feed gas composition (Table 3) equals Co-SOEC syngas and is based on experimental experiences from our partners of the

HydroMetha project. The syngas contains a hydrogen excess of 3% above stoichiometry, at full conversion of CO and CO<sub>2</sub> this would result in a product concentration of roughly 9 vol.-% unconverted hydrogen and 91 vol.-% methane. However, full conversion could not be reached with the modelled setup including only one reactor, but conversions above 99% were achieved with three serial reactors of this kind not reported in this paper. A small excess of hydrogen in the feed gas reduces the carbon formation tendency significantly, which was explained in greater detail by Krammer et al. [4]. A proportional valve downstream the reactor equipment controls the plant pressure. The product gas can be analysed by a gas analysing system (ABB Advanced Optima AO2000). The axial reactor temperature distribution is measured with a multi-thermocouple inside the reactor (Fig. 1) which is placed with a radial offset of 25 mm from the centre axis. Plant pressure is determined by a pressure transmitters just downstream the reactor. Finally, a torch enables controlled burning of all the process gases. In the work of Krammer et al. [4] and Medved et al. [49] a detailed description of the used lab-scale methanation test plant can be found, the latter including a detailed corresponding piping and instrumentation diagram of the setup.

The accuracy and quality of a model can be determined based on a thorough comparison to experimental results. Therefore, the model was compared to experiments under variation of GHSV, respectively input volume flow, and outlet pressures. For highly active Co-SOEC syngas feed modelling and experiments at GHSV values of 2000 h<sup>-1</sup>, 4000 h<sup>-1</sup>, 6000 h<sup>-1</sup> and 8000 h<sup>-1</sup> and pressures in the range of 1 bar, 2 bar, 4 bar, 6 bar, 8 bar and 10 bar were conducted.

### 4. Results and Discussion

Agreement of experimental and modelling results could be demonstrated based on comparison of reactor temperature, CO<sub>x</sub> conversion and output concentration to prove the good accuracy of the model. The

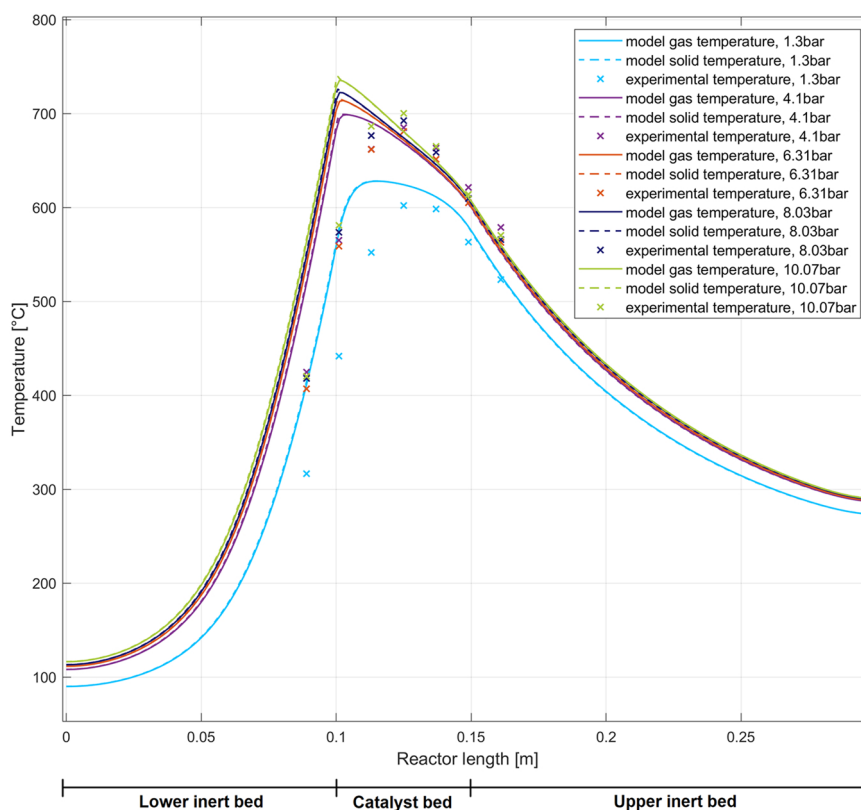


**Fig. 4.** Experiment-model-comparison of axial temperature profiles at a radial offset of 25 mm from the central reactor axis for a lab-scale packed bed methanation reactor at 4000 h<sup>-1</sup> GHSV and Co-SOEC syngas feed.

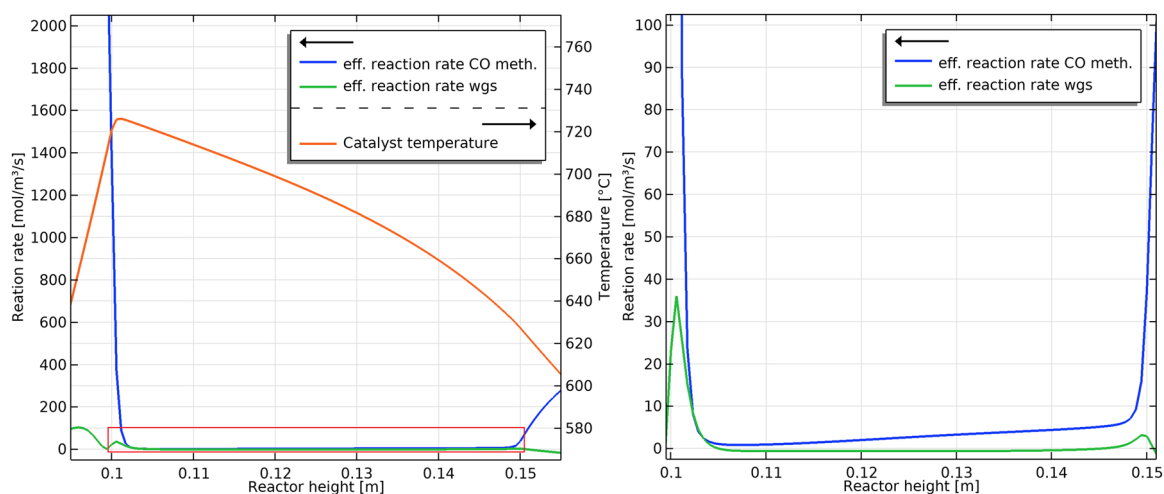


**Fig. 5.** Modelled effective reaction rate (left ordinate) of CO methanation and water gas shift (wgs) reaction along with catalyst temperature (right ordinate) at  $4000 \text{ h}^{-1}$  and 8 bar. For better visibility the area marked by a red box on the left side is presented at higher resolution on the right. (Reaction rate outside of catalyst zone is calculated but does not come into use in the model).

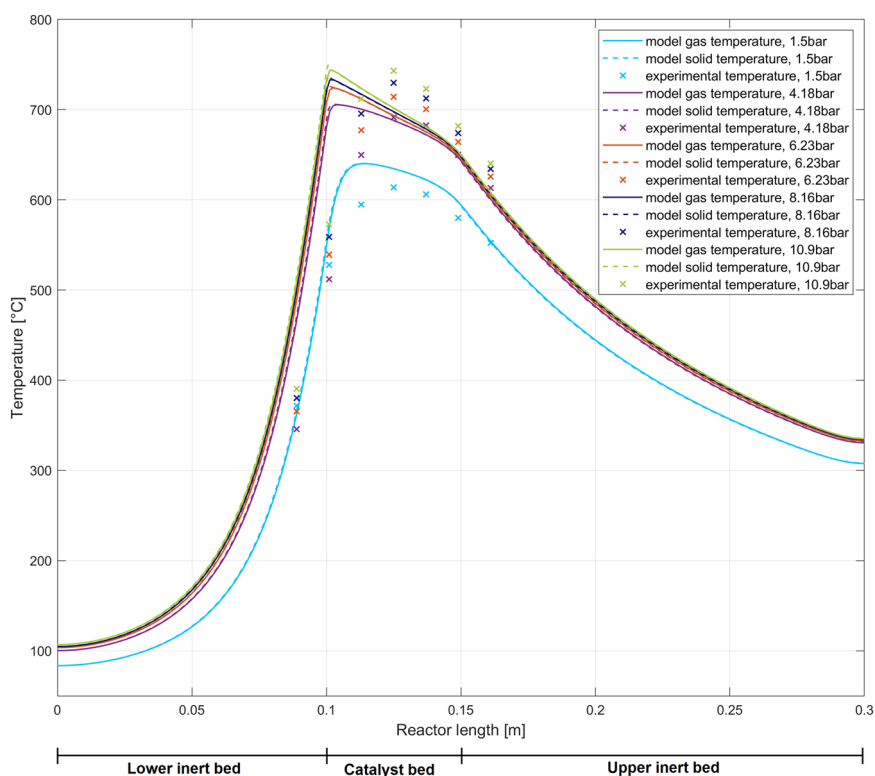


**Fig. 6.** Experiment-model-comparison of axial temperature profiles at a radial offset of 25 mm from the central reactor axis for a laboratory packed bed methanation reactor at  $6000 \text{ h}^{-1}$  GHSV and Co-SOEC syngas feed.

axial temperature profile with a radial offset of 25 mm from the central axis measured with the multi-thermocouple is compared to the modelled temperatures at the same position in Fig. 4, Fig. 6, Figure D.1 and Figure D.2. The characteristics of the axial temperature profiles can be thoroughly discussed based on the  $4000 \text{ h}^{-1}$  (equal to 16.7 NL/min) experimental results shown in Fig. 4. The experimental and modelled temperature curves at  $4000 \text{ h}^{-1}$  were determined at pressures of 1.3, 4.1, 6.3, 8.0 and 10.1 bar.

All profiles are characterized by a rapid temperature increase from approximately  $100 \text{ }^\circ\text{C}$  at the entrance of the lower inert bed (not inlet) to certainly above  $600 \text{ }^\circ\text{C}$  and up to  $735 \text{ }^\circ\text{C}$  in the initial catalyst zone as a

consequence of exothermic reaction heat release. The steep axial temperature curve close to the interface of lower inert and catalyst bed ( $<0.1 \text{ m}$ ) of approximately  $14 \text{ K/mm}$  clearly reflects the high initial reaction rate in the catalyst zone. By effective heat conduction and radiation within the catalyst bed, the released reaction heat spreads not only downstream and in radial direction but also upstream into the lower inert bed preheating the incoming gas flow. Downstream heat transport is further enhanced by convective heat transport including gas dispersion in the packed bed. The temperature profiles peak less than 1 mm at 10 bar and approximately 11 mm at 1.3 bar into the catalyst zone, followed by a continuous decrease of temperature further



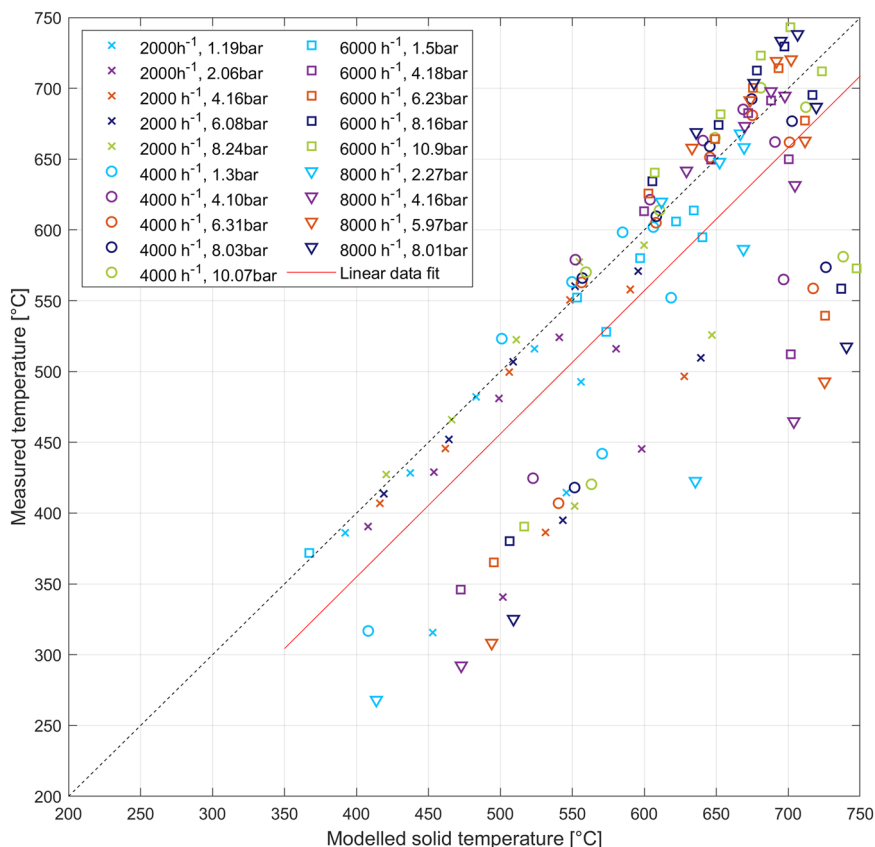


Fig. 7. Parity plot of modelled solid temperature and experimentally determined reactor temperature for Co-SOEC syngas feed at 2000 h<sup>-1</sup> to 8000 h<sup>-1</sup> GHSV and 1–10 bar pressure including a linear fit of the data.

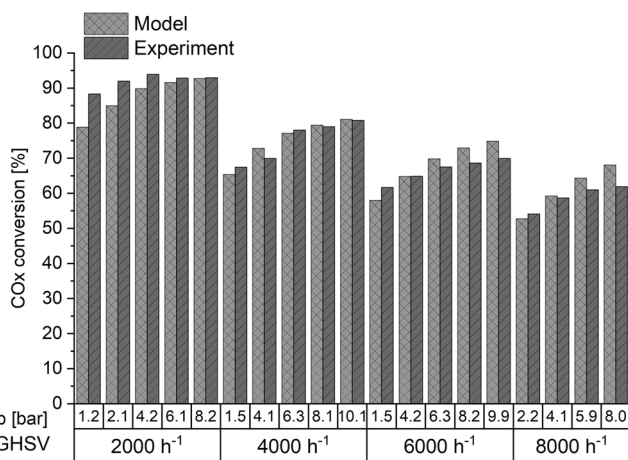


Fig. 8. Experiment-model-comparison based on CO<sub>x</sub> conversions at different pressures and GHSV values for Co-SOEC syngas feed.

downstream. The ascending temperature curve is characterized by a small deviation between gas and catalyst temperature. This can be explained by heat transport. Only effective heat conductivity and radiation within the solid particle bed transports heat upstream. Heat can only be transferred from hotter catalyst to the colder gas requiring higher temperature difference in this zone. Therefore, also the positions of gas and catalyst temperature peaks differ by a few millimetres. The initially high reaction rate at the catalyst entrance rapidly decreases at the temperature peak followed by a slow increase of the reaction rate at a low level, which is shown by the modelled reaction rate in Fig. 5.

The increase of reaction rates starting at the temperature peak and

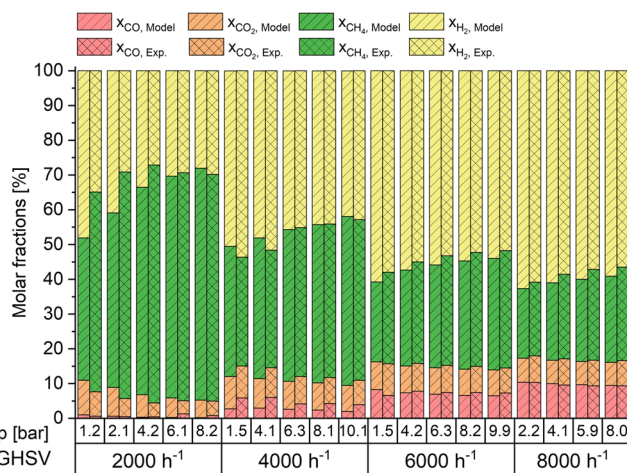


Fig. 9. Experiment-model-comparison based on molar fractions at different pressures and GHSV values for Co-SOEC syngas feed at dry basis.

continuing further downstream is caused by an increase of the ‘driving force’ term  $1 - \frac{p_{CH_4} p_{H_2 O}}{p_{CO} p_{H_2}^2 K_{p, CO M}}$  representing the deviation to thermodynamic equilibrium as can be seen in Eq. 33 and is illustrated in detail in Figure E.1. The deviation to the thermodynamic limit increases downstream the temperature peak as a result of temperature decrease.

As a consequence, the thermodynamic equilibrium is most likely reached in the point of maximum temperature. Downstream of the temperature peak the reaction takes place at a far lower rate, and is bound to the amount of heat being removed from the catalyst bed. Hence, the reactor performance bottleneck in most of the catalyst bed

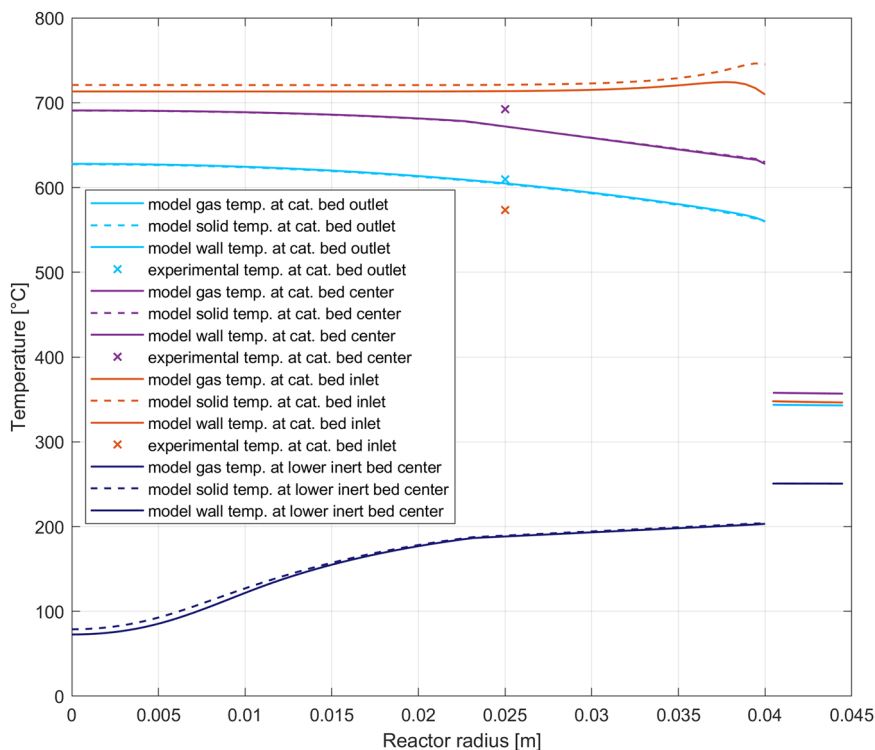


Fig. 10. Radial temperature profiles at the catalyst zone inlet (0.1 m reactor height), center (0.125 m reactor height) and outlet (0.15 m reactor height) of solid, gas and wall based on the 2D reactor model for a pressure of 8.03 bar and GHSV of 4000 h<sup>-1</sup>.

volume is the heat loss of the reactor system. In conclusion, only within the first Millimetres upstream of each temperature peak the reaction is determined by kinetics, whereas downstream it is limited by thermodynamics. It should also be noted that the axial position of the temperature peak can vary in radial direction. Although mostly thermodynamically limited, the whole reactor system was managed to be described correctly by the implemented kinetic expressions, which include termination terms.

With increasing pressure the temperature profiles are lifted to higher temperature values in an approximately parallel manner. This tendency can be found for the model as well as for the experimental findings and is in line with earlier findings [3]. The peak temperature of 618 °C is reached at 11 mm from the entrance of the catalyst bed at 1.3 bar pressure, and 738 °C is reached at after less than 1 mm of catalyst bed at 10 bar. In contrast, highest temperatures measured in the experiments were 602 °C at 1.3 bar and 687 °C at 10.1 bar 25 mm into the catalyst bed, hence a few Millimetres further downstream. The multi-thermocouple consists of 7 single thermocouples in a 6 mm steel encasement. Heat conduction within the multi-thermocouple may have dampened the maximum temperature values in the experiments. [2] Gruber [5] has taken the issue of heat conduction within a multi-thermocouple into account by including the heat conduction effect along a cylindrical steel encased multi-thermocouple, which was positioned in the centre of the reactor, to the model. Unfortunately, it was not possible to apply this method to our 2D model because of the radial offset of the instrument in our case. However, Gruber found the axial heat conduction of the multi-thermocouple to be less than 0.5 Wm<sup>-1</sup>K<sup>-1</sup>, decreasing the measured maximum temperature in the cooled reactor system by less than 20 K. Furthermore, the inert bed-catalyst bed interface is not characterized by a perfectly sharp transition due mixing of spherical particles. Mixing of single spherical particles may have led to a fuzzy inert-catalyst interface resulting in distortion of reaction heat release and lower temperatures in the experiments. Moreover, a reduction of catalytic performance in highly temperature stressed zones cannot be ruled out.

The temperature profile of the 6000 h<sup>-1</sup> experiments are likewise in good alignment with the model findings. The previously discussed qualitative profile shape is again well represented by the model. Strongly ascending temperature from the reactor input into the catalyst zone is given in both model and experiment followed by slowly decreasing temperature. The temperature peaks again differ in value and axial position between model and experiment, whereas gas-solid deviation is smaller at higher pressure. While at 10.9 bar pressure the highest temperature was modelled with 749 °C downstream less than 1 mm into the catalyst bed, the highest temperature measurement point showed 743 °C at 14 mm downstream of the catalyst bed interface. Again it appears the multi-thermocouple was not sensitive enough to replicate the extreme temperature gradients in the catalyst bed and is influenced by heat conduction and fuzzy or even incorrectly positioned inert-catalyst interface may have influenced the axial temperature profile. However, the pressure effect on the methanation reaction is well represented by the model with increasing temperatures at higher pressure.

The experimental and model results from a catalyst load of 2000 h<sup>-1</sup> and 8000 h<sup>-1</sup> are shown in Figure D.1 and Figure D.2 in the appendix. In analogy to the experiments with 4000 h<sup>-1</sup> and 6000 h<sup>-1</sup> the temperature profile characteristics determined by experiment and by model match well.

A parity plot in Fig. 7 gives the complete picture of the temperature deviation between model and experiment for all trials with Co-SOEC syngas feed into the first reactor.

While on the abscissa the modelled temperature is given, the ordinate shows the experimental temperature. Most values are accumulated around the diagonal line indicating good temperature alignment of model and experiment at the same axial position. However, a group of values accumulate at lower experimental temperature than predicted by the model. This group of values have a similar offset of approximately 150 K to their experimental counterpart. We assume that incorrect catalyst and inert bed heights in the experimental setup are the main reason for this offset.

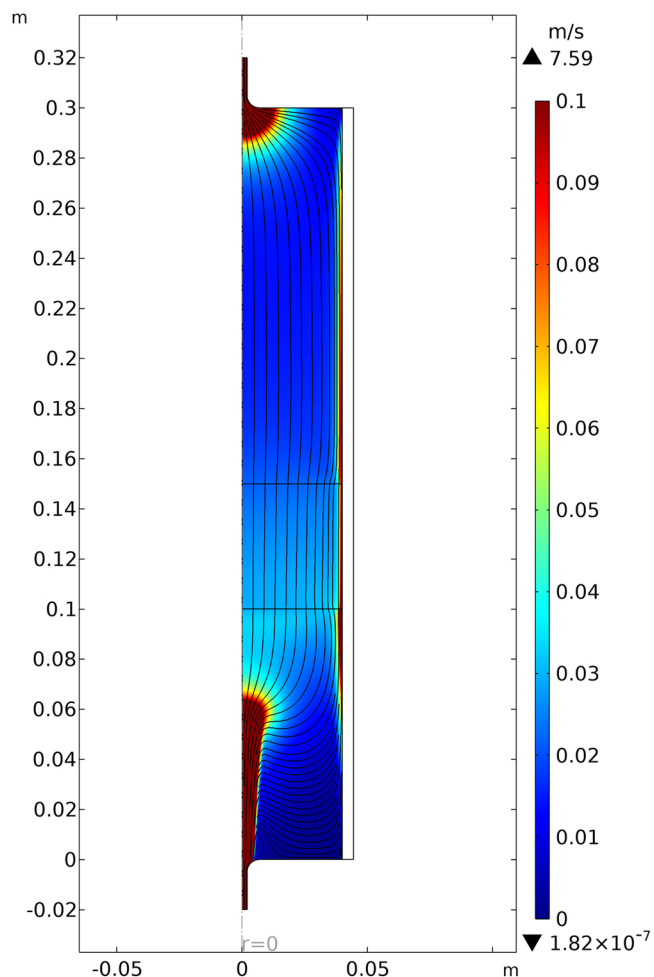


Fig. 11. 2D diagram of actual gas velocity (streamlines and color table) based on the 2D reactor model at 4.1 bar and 4000 h<sup>-1</sup>. (The maximum value in the color table is limited with 0.1 m/s for better readability of the diagram, therefore values higher than 0.1 m/s appear dark red.).

In addition to the temperature values discussed above, the experimentally determined CO<sub>x</sub> conversion and the concentrations of the species at the reactor exit is compared with the results of the model. In

Fig. 8 and Fig. 9 the CO<sub>x</sub> conversion and the output molar fractions from model and experiment are compared.

The CO<sub>x</sub> conversions evaluated with the model are in very good agreement to the experimental results, as can be derived from Fig. 8. As

Table A.1  
Thermodynamic properties for all gas species.

Polynomial factors for CH <sub>4</sub>	200K ≤ T < 1000	1000K ≤ T < 3500
<i>a</i> <sub>1,CH<sub>4</sub></sub>	5.15E+ 00	7.49E-02
<i>a</i> <sub>2,CH<sub>4</sub></sub>	-1.37E-02	1.34E-02
<i>a</i> <sub>3,CH<sub>4</sub></sub>	4.92E-05	-5.73E-06
<i>a</i> <sub>4,CH<sub>4</sub></sub>	-4.85E-08	1.22E-09
<i>a</i> <sub>5,CH<sub>4</sub></sub>	1.67E-11	-1.02E-13
<i>a</i> <sub>6,CH<sub>4</sub></sub>	-1.02E+ 04	-9.47E+ 03
<i>a</i> <sub>7,CH<sub>4</sub></sub>	-4.64E+ 00	1.84E+ 01
Polynomial factors for H <sub>2</sub> O	200K ≤ T < 1000	1000K ≤ T < 3500
<i>a</i> <sub>1,H<sub>2</sub>O</sub>	4.20E+ 00	3.03E+ 00
<i>a</i> <sub>2,H<sub>2</sub>O</sub>	-2.03E-03	2.18E-03
<i>a</i> <sub>3,H<sub>2</sub>O</sub>	6.52E-06	-1.64E-07
<i>a</i> <sub>4,H<sub>2</sub>O</sub>	-5.49E-09	-9.70E-11
<i>a</i> <sub>5,H<sub>2</sub>O</sub>	1.77E-12	1.68E-14
<i>a</i> <sub>6,H<sub>2</sub>O</sub>	-3.03E+ 04	-3.00E+ 04
<i>a</i> <sub>7,H<sub>2</sub>O</sub>	-8.49E-01	4.97E+ 00
Polynomial factors for CO	200K ≤ T < 1000	1000K ≤ T < 3500
<i>a</i> <sub>1,CO</sub>	3.58E+ 00	2.72E+ 00
<i>a</i> <sub>2,CO</sub>	-6.10E-04	2.06E-03
<i>a</i> <sub>3,CO</sub>	1.02E-06	-9.99E-07
<i>a</i> <sub>4,CO</sub>	9.07E-10	2.30E-10
<i>a</i> <sub>5,CO</sub>	-9.04E-13	1.68E-14
<i>a</i> <sub>6,CO</sub>	-1.43E+ 04	-1.42E+ 04
<i>a</i> <sub>7,CO</sub>	3.51E+ 00	7.82E+ 00
Polynomial factors for CO <sub>2</sub>	200K ≤ T < 1000	1000K ≤ T < 3500
<i>a</i> <sub>1,CO<sub>2</sub></sub>	2.34E+ 00	3.86E+ 00
<i>a</i> <sub>2,CO<sub>2</sub></sub>	8.98E-03	4.41E-03
<i>a</i> <sub>3,CO<sub>2</sub></sub>	-7.12E-06	-2.21E-06
<i>a</i> <sub>4,CO<sub>2</sub></sub>	2.46E-09	5.23E-10
<i>a</i> <sub>5,CO<sub>2</sub></sub>	-1.44E-13	-4.72E-14
<i>a</i> <sub>6,CO<sub>2</sub></sub>	-4.84E+ 04	-4.88E+ 04
<i>a</i> <sub>7,CO<sub>2</sub></sub>	9.90E+ 00	2.27E+ 00
Polynomial factors for H <sub>2</sub>	200K ≤ T < 1000	1000K ≤ T < 3500
<i>a</i> <sub>1,H<sub>2</sub></sub>	2.34E+ 00	3.34E+ 00
<i>a</i> <sub>2,H<sub>2</sub></sub>	7.98E-03	-4.94E-05
<i>a</i> <sub>3,H<sub>2</sub></sub>	-1.95E-05	4.99E-07
<i>a</i> <sub>4,H<sub>2</sub></sub>	2.02E-08	-1.80E-10
<i>a</i> <sub>5,H<sub>2</sub></sub>	-7.38E-12	2.00E-14
<i>a</i> <sub>6,H<sub>2</sub></sub>	-9.18E+ 02	-9.50E+ 02
<i>a</i> <sub>7,H<sub>2</sub></sub>	6.83E-01	-3.21E+ 00

The three gas transport property values for each of the gas species are taken from literature [39,46,47] and are listed in Table A.2.

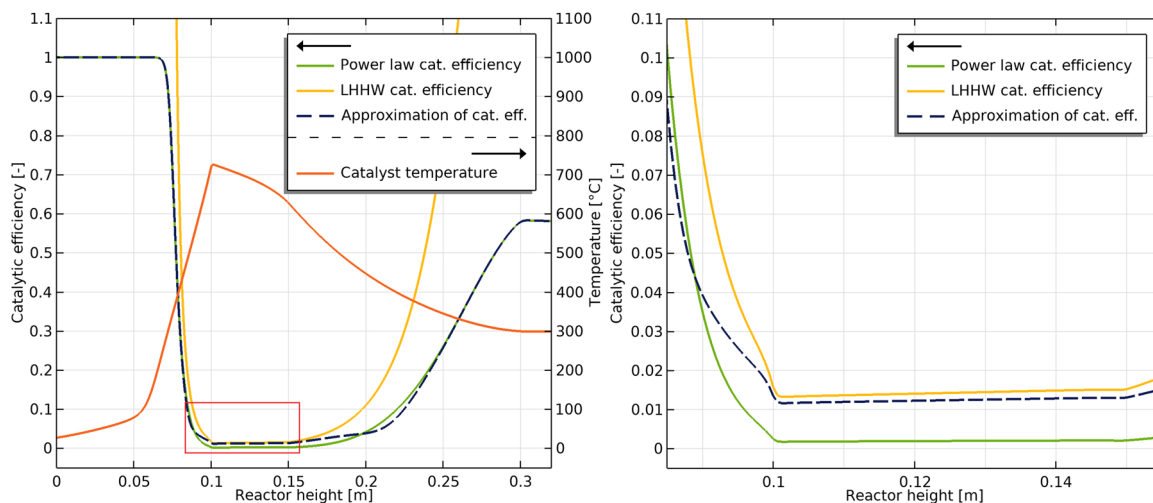
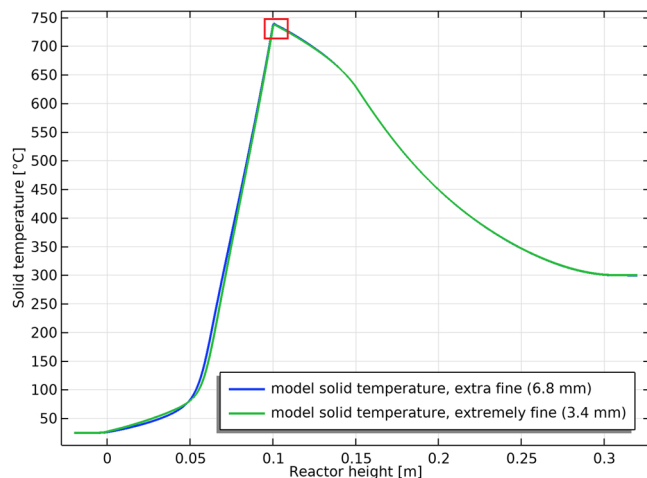


Fig. 12. Catalytic efficiency (left ordinate) from power law, LHHW and new approximation approaches along with catalyst temperature (right ordinate) over the reactor height in the central reactor axis at 4000 h<sup>-1</sup> and 8 bar including a closer look (red frame) with higher resolution of the catalyst zone in the right diagram.

**Table A.2**  
Transport properties values [39,47].

Species	Potential characteristic length of the Lennard-Jones/Stockmeyer potential [angstrom]	Potential energy minimum of the Lennard-Jones/Stockmeyer potential [K]	Dipole moment [C*m]
CH <sub>4</sub>	3.758	148.6	0
H <sub>2</sub> O	2.641	809.1	$1.8546 \cdot 3.34 \cdot 10^{-30}$
CO	3.690	91.7	$0.1098 \cdot 3.344 \cdot 10^{-30}$
CO <sub>2</sub>	3.941	195.2	0
H <sub>2</sub>	2.827	59.7	0



**Fig. C.1.** Comparison of central axial temperature profile at 10.07 bar and 4000 h<sup>-1</sup> with extra fine mesh at 6.8 mm maximum element size and extremely fine mesh at 3.4 mm maximum element size including red box marking the zoomed in area shown in Figure C.2.

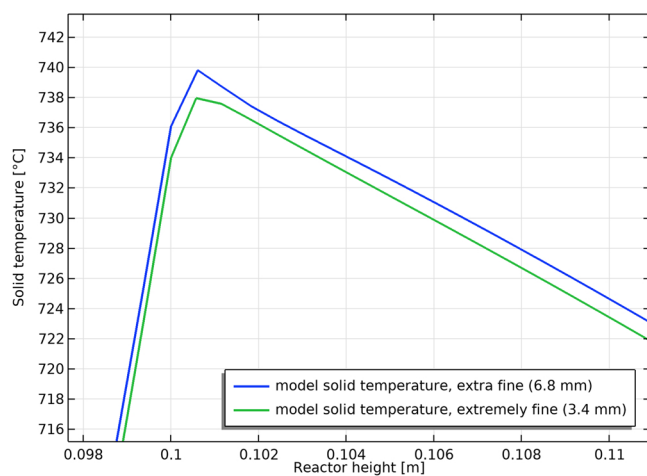


**Fig. C.2.** Zoomed in temperature peak central axial temperature profile at 10.07 bar and 4000 h<sup>-1</sup> with extra fine mesh at 6.8 mm maximum element size and extremely fine mesh at 3.4 mm maximum element size.

expected, the CO<sub>x</sub> conversion generally rises with increasing pressure and decreasing GHSV. This effect is predicted by the model as well as by the experiments. The deviation in CO<sub>x</sub> conversion between model and experiment range from 9.1% underestimation of CO<sub>x</sub> conversion at 2000 h<sup>-1</sup> and 1.2 bar to 4.9% points higher prediction of CO<sub>x</sub> conversion

than experimentally determined at 8000 h<sup>-1</sup> and 8.0 bar. Hence, there is a clear offset tendency with GHSV and pressure.

An analogous picture can obviously be drawn from the molar fraction comparison diagram in Fig. 9. The higher the pressure and the lower the GHSV, the more methane is formed. Again, model and experiment both represent this trend similarly. Moreover, the prediction of the absolute concentration value by the model is accurate for GHSV of 4000 h<sup>-1</sup> and higher. In terms of methane mole fraction the absolute deviation between model and experiment is only 0.2–3.7% points for 4000 h<sup>-1</sup>, 6000 h<sup>-1</sup> and 8000 h<sup>-1</sup>. At 2000 h<sup>-1</sup> the methane concentration were less accurately predicted with an error of up to 15.6% points at 1.2 bar pressure. The CO deviation ranges for all GHSV values from 0.11% to 2.7% points and for CO<sub>2</sub> between 0.05% and 0.76% points but on a lower absolute level. For the gas analysis results of the experimental investigation a significant error must be considered for higher pressures and higher GHSV. Less methane was measured in the product for example at 8000 h<sup>-1</sup> and 8 bar in comparison the CO and CO<sub>2</sub> amounts. This can be a result of carbon deposition within the reactor or an systematic error of the gas analysis.

The significance of considering two dimensions instead of a 1D model for an 80 mm methanation reactor in the model can be validated by the results shown in Fig. 10 and Fig. 11. In Fig. 10 the calculated radial temperature profiles at the inlet, centre and outlet of the catalyst zone and additionally in the centre of the lower inert bed are exemplarily given for a pressure of 8 bar.

As the axial profiles already indicated, at the inlet of the catalyst zone the temperature is higher than at the outlet. The radial profiles at the centre and the outlet have a similar shape but on a different temperature level. The radial profiles at the centre and outlet of the catalyst bed peak in the central axis and decrease in temperature in radial direction towards the reactor wall by roughly 80 K. The assumption of a constant radial temperature in a 1D model would be a significant loss of model accuracy. The temperature difference between gas and solid phase is only about 10 K at the catalyst zone inlet and almost zero further downstream. The radial temperature profile at the catalyst inlet is almost constant with a peak close to the wall. Due to very low gas velocities at the wall the temperature peaks almost immediately compared to a few millimetres downstream in the multi-thermocouple axis (Fig. 4), as explained earlier. Hence, this unexpected radial profile at the catalyst inert interface is a result of different axial gas velocities at different radial positions. The temperature within the wall varies only slightly by less than 20 K at the different axial positions. But the jump in temperature between the reactor bed and the reactor wall is significant, with more than 350 K at the catalyst zone inlet. This shows clearly that an important limiting factor of the effective radial heat transport is the heat transfer from the reactor bed to the reactor wall. For the example case of 8 bar and 4000 h<sup>-1</sup> the calculated solid-wall heat transfer coefficient  $\alpha_{solid-wall}$  (Eq. 37) ranges from 28 W/m<sup>2</sup>K to 65 W/m<sup>2</sup>K along the whole reactor.

Moreover, the two-dimensional model allows solving for a gas velocity distribution in axial and radial direction, which for the used reactor geometry seems to be crucial (Fig. 11). The small diameter of the inlet nozzle leads to very high axial flow in the centre of the lower inert bed. Significant gas velocity gradients occur in radial direction within the lower inert bed. The gas flow homogenise only within the catalyst zone. High transport of reactive gas in the axial centre of the catalyst bed and lower gas velocities at the reactor wall are modelled, which have a strong effect on the overall reactor performance. These specific flow characteristics would be completely omitted in a 1D model.

The model revealed the importance of implementing the intra-particle and particle-bulk-interface mass transfer limitations on the effective catalyst performance. The intrinsic catalytic activity is reduced by an efficiency factor to an effective, transfer-limited reaction rate value (Eq. 47). As displayed in Fig. 12, the catalytic efficiency for the example case of 8 bar and 4000 h<sup>-1</sup> was found to be in the range of 0.013–0.016 in the central axis of the catalytic bed. Therefore, only a

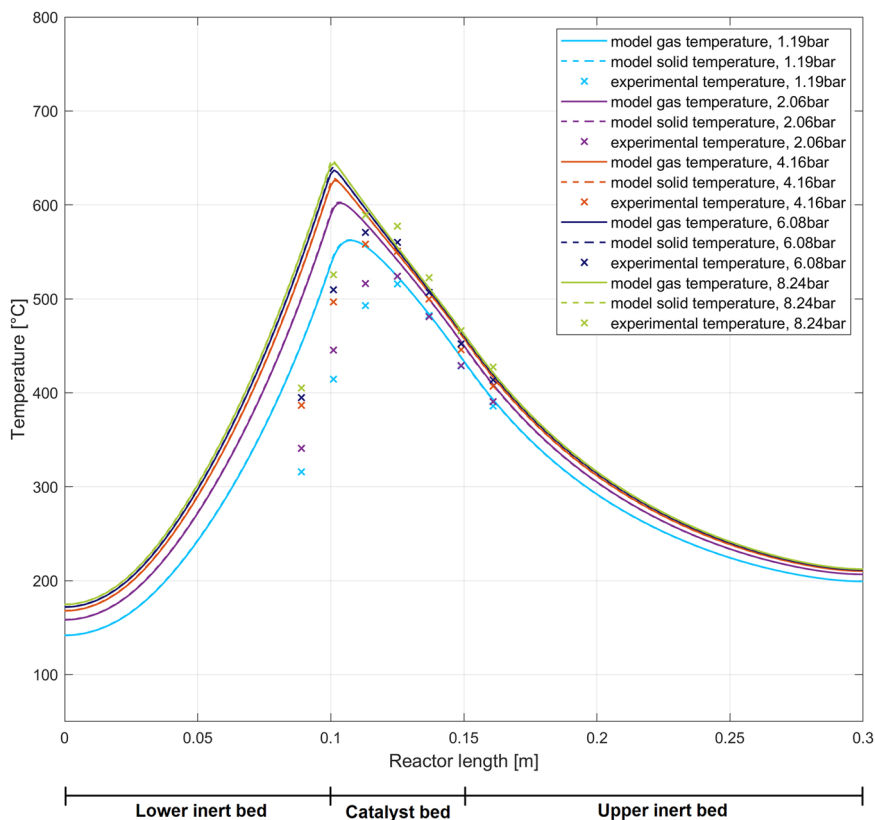


Fig. D.1. Experiment-model-comparison of axial temperature profiles at a radial offset of 25 mm from the central reactor axis for a laboratory packed bed methanation reactor at 2000 h<sup>-1</sup> GHSV and Co-SOEC syngas feed.

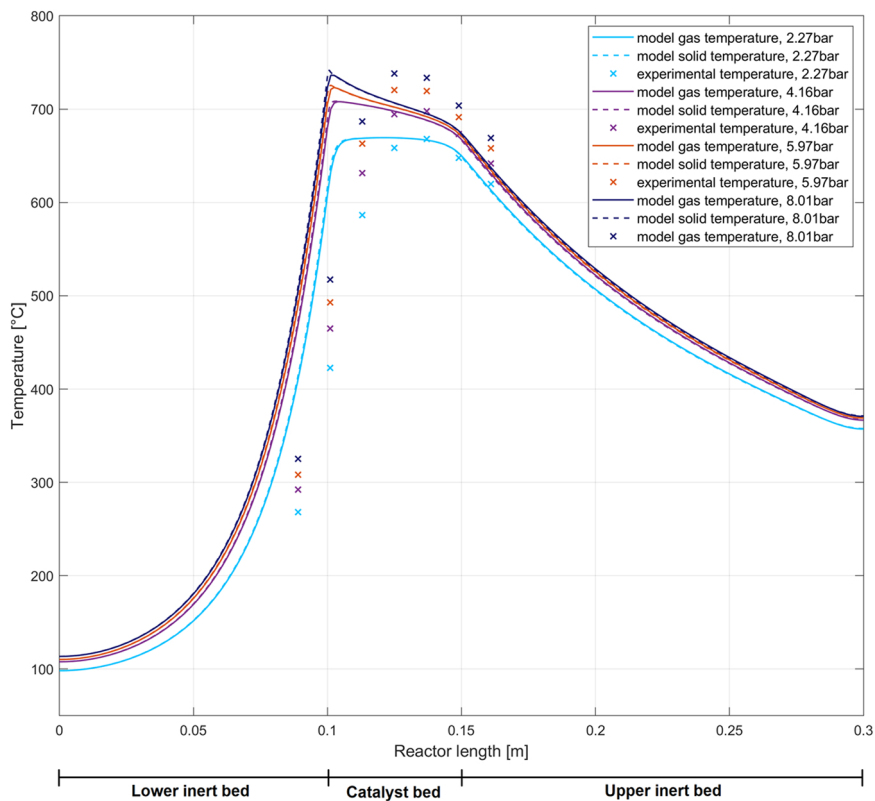


Fig. D.2. Experiment-model-comparison of axial temperature profiles at a radial offset of 25 mm from the central reactor axis for a laboratory packed bed methanation reactor at 8000 h<sup>-1</sup> GHSV and Co-SOEC syngas feed.



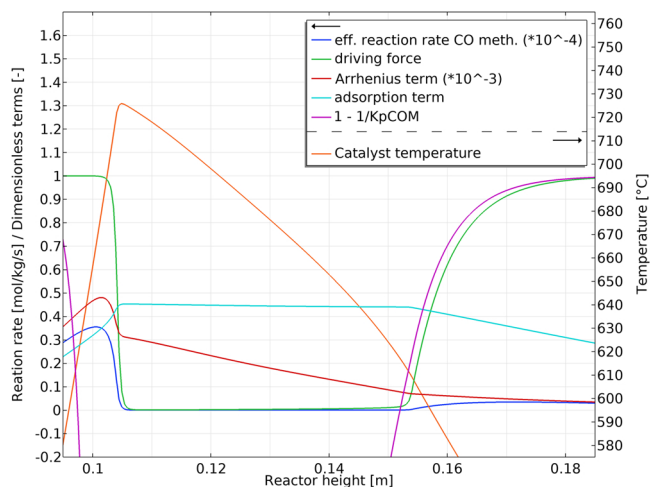


Fig. E.1. Modelled effective reaction rate of CO methanation including its fractional mathematical terms and the solid temperature over reactor height.

small amount of less than 2% of the intrinsic catalytic potential of the catalyst can actually be utilized for the example case. The catalytic efficiency outside of the catalyst bed (0.1–0.15 m) was also calculated and is therefore displayed in Fig. 12, but did of course not come into use because reaction rate was set to zero in the inert bed zones.

Moreover, it can be seen in the diagrams that the approximation between power law and LHHW approach for the catalytic efficiency was necessary for such small values. For low values the power law approach was not accurate enough predicting smaller values by approximately a factor of 10. However, the LHHW approach by Roberts and Satterfield [23] was designed in particular for small numbers and would lead to impossibly high values far above one as can be seen in the lower and upper inert bed area in Fig. 12. Unlimited reaction rates close to the catalytic interface would make computation of such a system highly instable and unpractical. The novel approach approximates between the two mentioned models and therefore combines the benefits of both allowing stability for higher numbers and accuracy at lower numbers at the same time.

## 5. Conclusions and Outlook

A detailed, stable and accurate model of a polytropic 80 mm diameter packed bed methanation reactor system was established. The 2D model shows good correlation with experimental results over a wide variety of GHSV (2000 – 8000 h<sup>-1</sup>) and pressure (1 – 10 bar) for the methanation of Co-SOEC syngas, which was managed without any fitting of model parameters to experimental data. A parity plot (Fig. 7) was implemented to demonstrate the good reflection of the experimentally found temperature values by the model. Deviations between model and experiment indicate potential for improvement in terms of temperature measurement sensitivity, incorrect axial positioning of the catalyst bed and fuzzy inert bed interface in the experiments. Small deviations in axial alignment of catalyst bed or temperature measurements result in high quantitative differences between model and experiment because of high temperature gradients in axial direction. Furthermore, very good agreement of output concentration and CO<sub>x</sub> conversion between model and experiments was determined. Model and experiments both approve already found pressure and GHSV dependencies in methanation. [3] Existing methanation reactor models in literature have mostly included significant heat removal by active

cooling which has a stabilizing effect to an exothermic system. The implementation of mass transfer limitation at the catalyst gas interface was a key step to correctly reduce extreme intrinsic values to effective reaction rates of the polytropic system with limited heat removal. This was managed through an approximation between a power law and LHHW based reaction efficiency calculation. This novel approach allows to accurately calculate reactor efficiency values not only for high values close to 1 but also for very low values smaller than 0.01. Existing modelling studies in literature found reaction efficiency values in a similar single digit percentage magnitude. Lower gas velocities and large catalyst particles in the underlying study explain efficiency values even beneath those found in current literature. In comparison to existing modelling approaches CO containing feed gas could be successfully realized by a two-step kinetic. As a consequence of the low reactor cooling rate, reaction heat removal by radial heat transport in the used setup is limiting, especially at the packed bed-to-wall interface. The reaction rate was found to decrease dramatically in the initial Millimetres of the catalyst zone as a consequence of almost immediate thermodynamic limitation. Certainly, there is potential of performance improvement in the limited cooling rate of this reactor, especially as a first reactor stage for Co-SOEC syngas. However, a naturally cooled polytropic system still has high technical relevance for simplified industrial implementation as second and third reactor stages and for less reactive gas mixtures such as steel gases or biogas. In consequence of the modelling findings the inlet geometry adaptations to improve evenly distributed gas velocity would be beneficial. Moreover, an increase in gas turbulence by reduction of the reactor diameter is expected to improve radial heat transport and decrease diffusion limitation. Secondly, active cooling can reduce thermodynamic limitation and lead to higher CO<sub>x</sub> conversion especially with increasing GHSV. It is for this reason that a subsequent reactor generation of 14 mm inner diameter with and without thermal oil cooling is planned to be tested in experiments as well as with this existing model approach. In addition different feed gas concentrations such as mixtures of biogas, blast furnace gas or pure CO<sub>2</sub> with hydrogen are planned to be tested.

## CRedit authorship contribution statement

**Andreas Krammer:** Conceptualization, Methodology, Formal analysis, Investigation, Data curation, Validation, Writing – original draft. **Martin Peham:** Conceptualization, Methodology. **Markus Lehner:** Supervision, Conceptualization, Funding acquisition, Writing – review & editing.

## Declaration of Competing Interest

The authors declare that they have no known competing financial interests or personal relationships that could have appeared to influence the work reported in this paper.

## Acknowledgment

The project HydroMetha is to a large extent financed by the research program “Energieforschungsprogramm 2016” funded by the Austrian “Klima- und Energiefonds” and the AVL List GmbH (grant no. 864578). The project consortium is formed by AVL List GmbH, Fraunhofer Institute for Ceramic Technologies and Systems, Chairs of Physical Chemistry and Process Technology of the Montanuniversitaet Leoben, Prozess Optimal CAP GmbH, Energieinstitut an der JKU Linz and AICHERNIG Engineering GmbH.

## Appendix

See Table. A.1, A.2.

See Fig. C.1, C.2, D.1, D.2, E.1.

A - Thermodynamic gas property.

Polynomial factors to calculate the thermodynamic properties for each species are listed below in Table A.1. Factors appropriate for a lower and higher temperature range were taken from literature [48].

B - Brinkman equation

$$\nabla \bullet (\rho u) = 0 \quad (\text{B.1})$$

$$\frac{\rho}{\epsilon_{bed}} (u \bullet \nabla) u \frac{1}{\epsilon_{bed}} = -\nabla p + \nabla \bullet \left[ \mu \frac{1}{\epsilon_{bed}} (\nabla u + (\nabla u)^T) - \frac{2}{3} \mu \frac{1}{\epsilon_{bed}} (\nabla \bullet u) I \right] - \frac{\mu}{\kappa} u \quad (\text{B.2})$$

The individual influences cumulated in the momentum equation (Eq. 5) are the terms.

$\frac{\rho}{\epsilon_{bed}} (u \bullet \nabla) u \frac{1}{\epsilon_{bed}}$  representing the inertial forces of the fluid,

$-\nabla p$  representing the pressure forces,

$\nabla \bullet \left[ \mu \frac{1}{\epsilon_{bed}} (\nabla u + (\nabla u)^T) - \frac{2}{3} \mu \frac{1}{\epsilon_{bed}} (\nabla \bullet u) I \right]$  corresponding to the viscous forces of the fluid.

and  $-\frac{\mu}{\kappa} u$  representing the resistance forces caused by the porous medium. [26–28].

C – Figures of mesh test based on solid temperature.

D – Figures of experiment-model-comparison.

E – Figure of effective reaction rate and fractional terms.

## References

- [1] M. Lehner, P. Biegger, A.R. Medved, Power-to-gas: Die Rolle der chemischen Speicherung in einem Energiesystem mit hohen Anteilen an erneuerbarer Energie, *Elektrotech. Inftech.* 134 (2017) 246–251, <https://doi.org/10.1007/s00502-017-0502-6>.
- [2] M. Gruber, Detaillierte Untersuchung des Wärme- und Stofftransports in einem Festbett-Methanisierungsreaktor für Power-to-Gas Anwendungen. Dissertation, Karlsruhe, 2020.
- [3] S. Rönisch, J. Schneider, S. Matthischke, M. Schlüter, M. Götz, J. Lefebvre, P. Prabhakaran, S. Bajohr, Review on methanation – from fundamentals to current projects, *Fuel* 166 (2016) 276–296, <https://doi.org/10.1016/j.fuel.2015.10.111>.
- [4] A. Krammer, A. Medved, M. Peham, P. Wolf-Zöllner, K. Salbrechter, M. Lehner, Dual pressure level methanation of Co-SOEC syngas, *Energy Technol.* 202 (2020) 2000746, <https://doi.org/10.1002/ente.202000746>.
- [5] M. Gruber, D. Wiedmann, M. Haas, S. Harth, A. Loukou, D. Trimis, Insights into the catalytic CO<sub>2</sub> methanation of a boiling water cooled fixed-bed reactor: simulation-based analysis, *Chem. Eng. J.* 406 (2021), 126788, <https://doi.org/10.1016/j.cej.2020.126788>.
- [6] F. Koschany, D. Schlereth, O. Hinrichsen, On the kinetics of the methanation of carbon dioxide on coprecipitated NiAl(O)<sub>x</sub>, *Appl. Catal. B: Environ.* 181 (2016) 504–516, <https://doi.org/10.1016/j.apcatb.2015.07.026>.
- [7] J. Lefebvre, S. Bajohr, T. Kolb, Modeling of the transient behavior of a slurry bubble column reactor for CO<sub>2</sub> methanation, and comparison with a tube bundle reactor, *Renew. Energy* 151 (2020) 118–136, <https://doi.org/10.1016/j.renene.2019.11.008>.
- [8] J. Lefebvre, S. Bajohr, T. Kolb, A comparison of two-phase and three-phase CO<sub>2</sub> methanation reaction kinetics, *Fuel* 239 (2019) 896–904, <https://doi.org/10.1016/j.fuel.2018.11.051>.
- [9] V. Vidal Vázquez, J. Kihlman, A. Mylvaganam, P. Simell, M.-L. Koskinen-Soivi, V. Alopaeus, Modeling of nickel-based hydrotalcite catalyst coated on heat exchanger reactors for CO<sub>2</sub> methanation, *Chem. Eng. J.* 349 (2018) 694–707, <https://doi.org/10.1016/j.cej.2018.05.119>.
- [10] J. Xu, G.F. Froment, Methane steam reforming, methanation and water-gas shift: I. Intrinsic kinetics, *AIChE J.* 35 (1989) 88–96, <https://doi.org/10.1002/aic.690350109>.
- [11] R. Try, A. Bengaouer, P. Baurens, C. Jallut, Dynamic modeling and simulations of the behavior of a fixed-bed reactor-exchanger used for CO<sub>2</sub> methanation, *AIChE J.* 64 (2018) 468–480, <https://doi.org/10.1002/aic.15874>.
- [12] D. Schlereth, O. Hinrichsen, A fixed-bed reactor modeling study on the methanation of CO<sub>2</sub>, *Chem. Eng. Res. Des.* 92 (2014) 702–712, <https://doi.org/10.1016/j.cherd.2013.11.014>.
- [13] D. Sun, D.S. Simakov, Thermal management of a Sabatier reactor for CO<sub>2</sub> conversion into CH<sub>4</sub>: Simulation-based analysis, *J. CO<sub>2</sub> Util.* 21 (2017) 368–382, <https://doi.org/10.1016/j.jcou.2017.07.015>.
- [14] J. Ducamp, A. Bengaouer, P. Baurens, Modelling and experimental validation of a CO<sub>2</sub> methanation annular cooled fixed-bed reactor exchanger, *Can. J. Chem. Eng.* 95 (2017) 241–252, <https://doi.org/10.1002/cjce.22706>.
- [15] L. Kiewidt, J. Thöming, Predicting optimal temperature profiles in single-stage fixed-bed reactors for CO<sub>2</sub>-methanation, *Chem. Eng. Sci.* 132 (2015) 59–71, <https://doi.org/10.1016/j.ces.2015.03.068>.
- [16] T.J. Schildhauer, S.M.A. Biollaz, Reactors for catalytic methanation in the conversion of biomass to synthetic natural gas (SNG) *Chim.* 69, 2015, pp. 603–607 doi: 10.2533/chimia.2015.603.
- [17] H. Thunman, M. Seemann, *The GoBiGas Plant in Substitute Natural Gas from Waste*, Elsevier, 2019, pp. 455–474.
- [18] S. Rönisch, J. Köcher, J. Schneider, S. Matthischke, Global reaction kinetics of CO and CO<sub>2</sub> methanation for dynamic process modeling, *Chem. Eng. Technol.* 39 (2016) 208–218, <https://doi.org/10.1002/ceat.201500327>.
- [19] P.J. Lunde, F.L. Kester, Carbon dioxide methanation on a ruthenium catalyst, *Ind. Eng. Chem. Proc. Des. Dev.* 13 (1974) 27–33, <https://doi.org/10.1021/i260049a005>.
- [20] B. Kreitz, G. Wehinger, T. Turek, Dynamic simulation of the CO<sub>2</sub> methanation in a micro-structured fixed-bed reactor, *Chem. Eng. Sci.* 195 (2019) 541–552, <https://doi.org/10.1016/j.ces.2018.09.053>.
- [21] J. Skrzypek, M. Grzesik, R. Szopa, Theoretical analysis of two parallel and consecutive reactions in isothermal symmetrical catalyst pellets using the dusty-gas model, *Chem. Eng. Sci.* 39 (1984) 515–521, [https://doi.org/10.1016/0009-2509\(84\)80049-4](https://doi.org/10.1016/0009-2509(84)80049-4).
- [22] K. Ghaib, 3D CFD simulation of reaction cells, cooling cells, and manifolds of a flatbed reactor for CO<sub>2</sub> methanation, *Chem. Eng. Technol.* 43 (2020) 1994–2006, <https://doi.org/10.1002/ceat.202000254>.
- [23] G.W. Roberts, C.N. Satterfield, Effectiveness factor for porous catalysts. langmuir-hinshelwood kinetic expressions, *Ind. Eng. Chem. Fund.* 4 (1965) 288–293, <https://doi.org/10.1021/i160015a009>.
- [24] VDI-Wärmeatlas, Springer Berlin Heidelberg, Berlin, Heidelberg, 2013.
- [25] M. Winterberg, E. Tsotsas, A. Kruschke, D. Vortmeyer, A simple and coherent set of coefficients for modelling of heat and mass transport with and without chemical reaction in tubes filled with spheres, *Chem. Eng. Sci.* 55 (2000) 967–979, [https://doi.org/10.1016/S0009-2509\(99\)00379-6](https://doi.org/10.1016/S0009-2509(99)00379-6).
- [26] C.F.D. COMSOL Inc, Module User's Guide, Version.: COMSOL 5 (2019) 5.
- [27] A. Kumar, S. Pramanik, M. Mishra, COMSOL Multiphysics® Modeling in Darcian and Non-Darcian Porous Media, in: Proceedings of the 2016 COMSOL Conference, Bangalore, India, 20–21 October 2016.
- [28] D.A. Nield, A. Bejan, *Convection in Porous Media*, Springer International Publishing, Cham, 2017.
- [29] M.F. Edwards, J.F. Richardson, Gas dispersion in packed beds, *Chem. Eng. Sci.* 23 (1968) 109–123, [https://doi.org/10.1016/0009-2509\(68\)87056-3](https://doi.org/10.1016/0009-2509(68)87056-3).
- [30] D.J. Gunn, Axial and radial dispersion in fixed beds, *Chem. Eng. Sci.* 42 (1987) 363–373, [https://doi.org/10.1016/0009-2509\(87\)85066-2](https://doi.org/10.1016/0009-2509(87)85066-2).
- [31] R.S. Brokaw, Predicting transport properties of dilute gases, *Ind. Eng. Chem. Proc. Des. Dev.* 8 (1969) 240–253, <https://doi.org/10.1021/i260030a015>.
- [32] COMSOL Inc., Chemical Reaction Engineering Module User's Guide. Version: COMSOL 5.5, 2019.
- [33] H. Janssen, Thermal diffusion of water vapour in porous materials: Fact or fiction? *Int. J. Heat. Mass Transf.* 54 (2011) 1548–1562, <https://doi.org/10.1016/j.jheatmasstransfer.2010.11.034>.
- [34] R. Bauer, E.U. Schlünder, Effective radial thermal conductivity of packings in gas flow. Part II. Thermal conductivity of the packing fraction without gas flow, *International Chemical Engineering* 189–204.
- [35] R. Bauer, E.U. Schlünder, Effective radial thermal conductivity of packings in gas flow. Part I. Convective transport coefficient, *Int. Chem. Eng.* (1978) 181–188.
- [36] P. Zehner, E.U. Schlünder, Einfluß der Wärmestrahlung und des Druckes auf den Wärmetransport in nicht durchströmten Schüttungen, *Chem.-Ing.-Tech.* 44 (1972) 1303–1308, <https://doi.org/10.1002/cite.330442305>.
- [37] P. Zehner, E.U. Schlünder, Wärmeleitfähigkeit von Schüttungen bei mäßigen Temperaturen, *Chem. Ing. Tech.* 42 (1970) 933–941, <https://doi.org/10.1002/cite.330421408>.



- [38] V. Specchia, G. Baldi, S. Sicardi, Heat transfer in packed bed reactors with one phase flow, *Chem. Eng. Commun.* 4 (1980) 361–380, <https://doi.org/10.1080/00986448008935916>.
- [39] R.H. Perry, D.W. Green. *Perry's Chemical Engineers' Handbook*, seventh ed., McGraw-Hill, New York, NY, 1999.
- [40] G.F. Froment, K.B. Bischoff, J. de Wilde, *Chemical Reactor Analysis and Design*, third ed., Wiley, Hoboken, NJ, 2011.
- [41] D. Papadias, L. Edsberg, P. Björnbo, Simplified method for effectiveness factor calculations in irregular geometries of washcoats, *Chem. Eng. Sci.* 55 (2000) 1447–1459, [https://doi.org/10.1016/S0009-2509\(99\)00375-9](https://doi.org/10.1016/S0009-2509(99)00375-9).
- [42] A. Jess, P. Wasserscheid. *Chemical Technology: From Principles to Products*, Second ed., Wiley-VCH, Weinheim, 2020.
- [43] S. Elnashaie, S.S. Elshishini, *Modelling, Simulation and Optimization of Industrial Fixed Bed Catalytic Reactors*, Gordon and Breach, Philadelphia, Pa, 1993.
- [44] Philip D. Neufeld, A.R. Janzen, R.A. Aziz, Empirical equations to calculate 16 of the transport collision integrals  $\Omega(l, s)^*$  for the Lennard-Jones (12–6) potential, *J. Chem. Phys.* 57 (2003) 1100, <https://doi.org/10.1063/1.1678363>.
- [45] L.I. Stiel, G. Thodos, The viscosity of polar substances in the dense gaseous and liquid regions, *AIChE J.* 10 (1964) 275–277, <https://doi.org/10.1002/aic.690100229>.
- [46] B. Todd, J.B. Young, Thermodynamic and transport properties of gases for use in solid oxide fuel cell modelling, *J. Power Sources* 110 (2002) 186–200, [https://doi.org/10.1016/S0378-7753\(02\)00277-X](https://doi.org/10.1016/S0378-7753(02)00277-X).
- [47] B.E. Poling, J.M. Prausnitz, J.P. O'Connell, *The Properties of Gases and Liquids*, fifth ed., internat. ed, McGraw-Hill, New York, NY, 2001.
- [48] B.J. McBride, *Coefficients for Calculating Thermodynamic and Transport Properties of Individual Species*, NASA Langley Research Center, 1993.
- [49] A.R. Medved, M. Lehner, D.C. Rosenfeld, J. Lindorfer, K. Rechberger, Enrichment of integrated steel plant process gases with implementation of renewable energy, *Johns Matthey Technol. Rev.* (2021), <https://doi.org/10.1595/205651321X16161444481140>.

## 3.2 Experimental and modelling investigation of Co-SOEC syngas methanation in low diameter ratio cooled and uncooled reactors

### Scientific article II – “High-capacity CO/CO<sub>2</sub> methanation reactor design strategy based on 1D PFR modelling and experimental investigation”

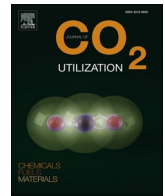
A. Krammer, K. Salbrechter, M. Lehner, High-capacity CO/CO<sub>2</sub> methanation reactor design strategy based on 1D PFR modelling and experimental investigation, Journal of CO<sub>2</sub> Utilization 80 (2024) 102661. <https://doi.org/10.1016/j.jcou.2023.102661>.

#### Contribution according to stated CRediT authorship contribution statement:

Andreas Krammer: Conceptualization, Data curation, Formal analysis, Investigation, Methodology, Project administration, Software, Validation, Visualization, Writing – original draft, Writing – review & editing.

Katrin Salbrechter: Data curation, Formal analysis, Investigation, Project administration.

Markus Lehner: Conceptualization, Funding acquisition, Project administration, Resources, Supervision, Writing – review & editing.



# High-capacity CO/CO<sub>2</sub> methanation reactor design strategy based on 1D PFR modelling and experimental investigation

Andreas Krammer<sup>\*</sup>, Katrin Salbrechter, Markus Lehner

Chair of Process Technology and Industrial Environmental Protection, Montanuniversität Leoben, Austria

## ARTICLE INFO

### Keywords:

Plug flow model  
CO/CO<sub>2</sub> methanation  
Co-SOEC syngas methanation  
Reactor design  
Tube-bundle reactor

## ABSTRACT

An in-depth analysis of oil-cooled and naturally ambient air-cooled fixed bed reactors for catalytic methanation of a feedgas containing CO and CO<sub>2</sub> has been performed. Combined investigation of modelling and experiments showed, that small tube-to-pellet diameters ratios and optimized reactor cooling are beneficial for high-capacity CO/CO<sub>2</sub> methanation. Very good model accuracy was proven with a 1D approach for small diameter reactor pipes. It is shown that the reactor design sweet spot under consideration of input gas capacity, methane output concentration, catalyst degradation and pressure loss can be assessed by the experimentally validated reactor model. The study reveals insights to the mechanism of combined CO and CO<sub>2</sub> methanation showing that initial CO methanation is kinetically limited, while subsequent CO<sub>2</sub> methanation is ruled by the kinetics of the reverse water gas shift reaction. Finally, this works aim is to provide a design strategy for effective and cheap high-capacity CO/CO<sub>2</sub> methanation reactors for industrial scale using commercial pellet catalysts in oil-cooled tube-bundle-reactors.

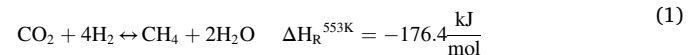
## 1. Introduction

Methanation of carbon oxides using renewably produced hydrogen plays a pivotal role in catalyzing the transition from fossil-based to green and decentralized energy generation. Enormous amounts of volatile green electric energy will need to be stored on a seasonal basis and transported in a multi-gigawatt scale, comparable to the capacity of today's fossil energy carriers. [1] Long-term energy storage and high-capacity energy distribution is already possible with the existing infrastructure of natural gas grids and underground gas storage facilities in the form of synthetic methane potentially containing also shares of green hydrogen. [2,3] In addition, certain carbon dioxide sources are emitted from hard-to-abate-industries, such as from waste incineration plants, refractory production or calcination of lime in cement plants, and thereof rely on CO<sub>2</sub> utilization. Furthermore, in a transitional period the natural gas demand of industrial processes can be satisfied without depending on unreliable fossil energy sources from instable regions. However, as the prior step an adequate electrolysis capacity is needed to produce hydrogen from green electricity. The high-temperature solid oxide electrolysis cell (SOEC), which can also be used to co-reduce CO<sub>2</sub> to CO (Co-SOEC), is known for its exceptional efficiencies [4]. With an SOEC excess heat e.g. from oil-cooled methanation reactors can be

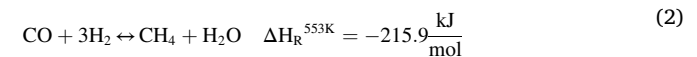
recycled to decrease the electric energy demand which allows for highest electric efficiencies [4]. However, lower TRL of 6–7 [5] and lower proven lifetime (<20,000 h) [6] were reported compared to alternative electrolysis technologies. In this paper, we will mainly address Co-SOEC syngas as methanation feed. However, other syngas sources with similar compositions, such as from biomass gasification, are also viable and can be treated similarly.

Methane is formed with hydrogen from carbon monoxide or carbon dioxide according to the Sabatier reactions shown in Eq. 1 and Eq. 2. [7, 8] The reverse water gas shift reaction couples both Sabatier reactions according to Eq. 3. In packed bed reactors, nickel has emerged as the most promising catalytically active material for catalytic methanation. It offers a compelling combination of low cost, excellent catalytic activity, and high selectivity [8].

CO<sub>2</sub> methanation :



CO methanation :



<sup>\*</sup> Correspondence to: Montanuniversität Leoben, Franz Josef-Straße 18, 8700 Leoben, Austria.

E-mail address: [andreas.krammer@unileoben.ac.at](mailto:andreas.krammer@unileoben.ac.at) (A. Krammer).

**Nomenclature***Abbreviations*

COM	CO methanation
GHSV	Gas hourly space velocity
PFR	Plug-flow reactor
rWGS	Reverse water gas shift reaction
WGS	Water gas shift reaction

*Symbols*

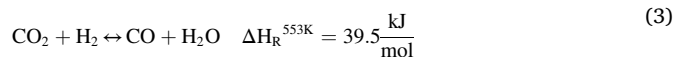
$c_i$	Concentration of component $i$ , $mol\ m^{-3}$
$c_p$	Heat capacity, $J\ kg^{-1}\ K^{-1}$
$D_i$	Diffusion coefficient of component $i$ , $m^2\ s^{-1}$
$d_{r,i}$	Inside diameter of the reactor pipe, $m$
$d_{r,o}$	Outside diameter of the reactor pipe, $m$
$d_{particle}$	Particle diameter of catalyst, $m$
$E_{A,j}$	Activation energy of reaction $j$ , $J\ mol^{-1}$
$\Delta G_{r,j}$	Free reaction enthalpy of reaction $j$ , $J\ kmol^{-1}$
$\Delta H_{ads,i}$	Adsorption enthalpy of component $i$ , $J\ mol^{-1}$
$\Delta H_R$	Enthalpy of reaction, $J\ mol^{-1}$
$k_b$	Stefan Boltzmann constant, $W\ m^{-2}\ K^{-4}$
$K_i$	Adsorption constant of component $i$ , differs
$K_i^0$	Pre-exponential factor of adsorption constant, differs
$k_j$	Reaction rate coefficient of reaction $j$ , differs
$k_j^0$	Pre-exponential factor of reaction rate coefficient, differs
$K_{p,COM}$	Equilibrium constant (pressure based) CO methanation, $Pa^{-2}$
$K_{p,rWGS}$	Equilibrium constant (pressure based) for reverse WGS, –
$k_w^{eff}$	Effective wall heat transfer coefficient, $W\ m^{-2}\ K^{-1}$
$L$	Reactor Length, $m$
$M$	Molar mass, $kg\ mol^{-1}$
$\dot{n}_i$	Molar flow of species $i$ , $mol\ s^{-1}$
$n_j$	Reaction order of reaction $j$ , –
$p$	Pressure, $Pa$ .
$r$	Reaction rate, $mol\ kg_{cat}^{-1}\ s^{-1}$
$r_r$	Control variable of reactor radius, $m$
$r_v$	Volumetric reaction rate, $mol\ m_{cat}^{-3}\ s^{-1}$
$R$	Ideal gas constant, $J\ mol^{-1}\ K^{-1}$
$R_r$	Radius of reactor, $m$
$Re_{0,p}$	Particle Reynolds number with superficial velocity, –
$Re_p$	Particle Reynolds number with “operating” velocity, –
$Sc$	Schmidt number, –
$Se$	Semenov number, –
$Sh$	Sherwood number, –
$T$	Temperature, $K$

$v$	Velocity, $m\ s^{-1}$
$\dot{V}_{in}$	Input volume flow, $m^3\ s^{-1}$
$V_{reactor}$	Reactor volume, $m^3$
$q$	Heat flow density, $W\ m^{-2}$
$\epsilon$	Porosity, –
$\epsilon_{rad}$	Emissivity coefficient, –
$\alpha$	Heat transfer coefficient, $W\ m^{-2}\ K^{-1}$
$\eta$	Dynamic viscosity / effectiveness factor, $Pa\ s /$ –
$\lambda$	Heat conductivity, $W\ m^{-1}\ K^{-1}$
$\mu_i$	Chemical potential of component $i$ , $J\ kmol^{-1}$
$\nu_{ij}$	Stoichiometric factor of component $i$ of reaction $j$ , –
$\rho$	Density, $kg\ m^{-3}$
$\tau_{cat}$	Tortuosity of catalyst, –
$\Phi$	Thiele modulus, –

*Subscripts and superscripts*

<i>air</i>	Ambient air
<i>adapted</i>	Adapted within this study
<i>bed</i>	Packed bed
<i>bed – wall</i>	From packed bed to pipe wall
<i>cat</i>	Catalyst
<i>cool</i>	Cooling
<i>eff</i>	Effective
<i>gas</i>	Gas
<i>i</i>	Index of gas component
<i>in</i>	Input
<i>inside</i>	At the inside of the pipe
<i>intr</i>	Intrinsic
<i>j</i>	Index of reaction
<i>knu</i>	Knudson (diffusion)
<i>mix</i>	Mixture (diffusion coefficient of component $i$ in gas mixture)
<i>outside</i>	At the outside of the pipe
<i>steel</i>	Steel
<i>STP</i>	Standard temperature and pressure conditions
<i>op.</i>	Operation condition
<i>out</i>	Output
<i>p</i>	Particle
<i>pore</i>	Pore
<i>rad</i>	Radiation
<i>radial</i>	Radial direction
<i>reactor</i>	Reactor
<i>solid</i>	Solid fraction without pores
<i>sup</i>	Superficial (velocity)
<i>V</i>	Volumetric
<i>wall – air</i>	From piping wall to ambient air
$\infty$	Of extended packed beds (bed porosity)

Reverse water gas shift :



The overall aim of this study is to highlight the most important factors to design efficient and cost effective CO/CO<sub>2</sub> methanation reactors. Effective and cheap tubular reactor design needs to ensure compliance with maximum catalyst temperature, low pressure drop at high gas input capacity and high conversion rates. For capacity comparison of different reactor systems the “gas hourly space velocity” (GHSV), which can also be referred to as catalyst load, is calculated by the standard volume flow per reactor volume (Eq. 4).

$$GHSV = \frac{\dot{V}_{in,op.}}{V_{reactor}} \frac{T_{in}}{T_{STP}} \frac{p_{STP}}{p_{in}} \quad (4)$$

The first reactor stage with high exothermic heat release is the most challenging step of a methanation system and therefore is the focus of most papers, as well as in this work. It has been shown by modelling and experiments in Krammer [9,10], that highly reactive Co-SOEC product gas consisting of mainly CO, H<sub>2</sub> and little amounts of CO<sub>2</sub> can be methanized in naturally cooled 80 mm reactors at up to 8000 h<sup>-1</sup> capacity with moderate conversion of 60% in the first reactor. Stoichiometric CO<sub>2</sub> methanation in oil-cooled packed bed reactors was investigated based on experimentally validated models at up to 38,000 h<sup>-1</sup> by Gruber [7], at up to approximately 15,000 h<sup>-1</sup> by Ducamp [11], Try [12] and Kiewidt [13] and at up to 4400 h<sup>-1</sup> by Vazquez [14]. Lefebvre [15], Schlereth and Hinrichsen [16], Sun and Simakov [17] and Kreitz [18] conducted CO<sub>2</sub> methanation modelling at up to 60,000 h<sup>-1</sup> but without experimental validation. Microchannel reactors for

methanation were investigated by Engelbrecht [19], Vazquez [14] and Kreitz [18] for CO<sub>2</sub> methanation at channel sizes between 0.45 and 2 mm. Reddy [20] investigated CO/CO<sub>2</sub> methanation on a ppm basis over Ru/ $\gamma$ -Al<sub>2</sub>O<sub>3</sub> catalysts. A proven and valid strategy to control fixed bed methanation reactor temperatures is product gas recycling. However, this approach requires additional equipment in terms of recycling compressors, more piping and larger reactor volumes contradicting the focus on developing the most cost-effective solution for stable methanation. [21] To our knowledge strategies for effective methanation reactor design, applicable for industrial scale CO-rich feed gases, are not sufficiently covered in literature. High reactivity of CO methanation results in extremely dense reaction heat production, which easily leads to undesired temperature peaks in the catalyst bed.

This work aims to close the research gap in CO/CO<sub>2</sub> methanation based on a combined experimental and modelling approach, with a focus on optimized heat management of fixed bed reactors, avoidance of hot spots, industrial applicability in large scale, high capacity reactors, and thus contribution to low-cost renewable SNG production. Therefore, commercial nickel-based catalyst pellets were used. A 1D PFR model

under different process conditions and for a low diameter ratio ( $d_{r,i}/d_p = 4.7$ ) is developed and its high accuracy is demonstrated. Process parameters (pressure, GHSV) and reactor design parameters (diameter, length, cooling) are addressed and its effects on important performance parameters (methane output concentration/CO<sub>x</sub> conversion, pressure drop, temperature profile) are derived.

## 2. Method

Three tubular reactors with the same inner diameter of 14 mm and varying catalyst lengths and cooling designs were used for the experimental investigations. Reactor 1 with a 840 mm catalyst zone and without active cooling, reactor 2 with 700 mm catalyst zone and with active cooling, and reactor 3 with 600 mm catalyst zone also with active cooling (Fig. 2). Reactor 2 and reactor 3 are cooled by thermal-oil in a shell-tube reactor. Reactor 3 differs from reactor 2 by a 100 mm pre-heating zone at the expense of catalyst height. The reactors were mounted into an existing lab-scale methanation plant, which was described in greater detail in Medved [22] and Krammer [10].

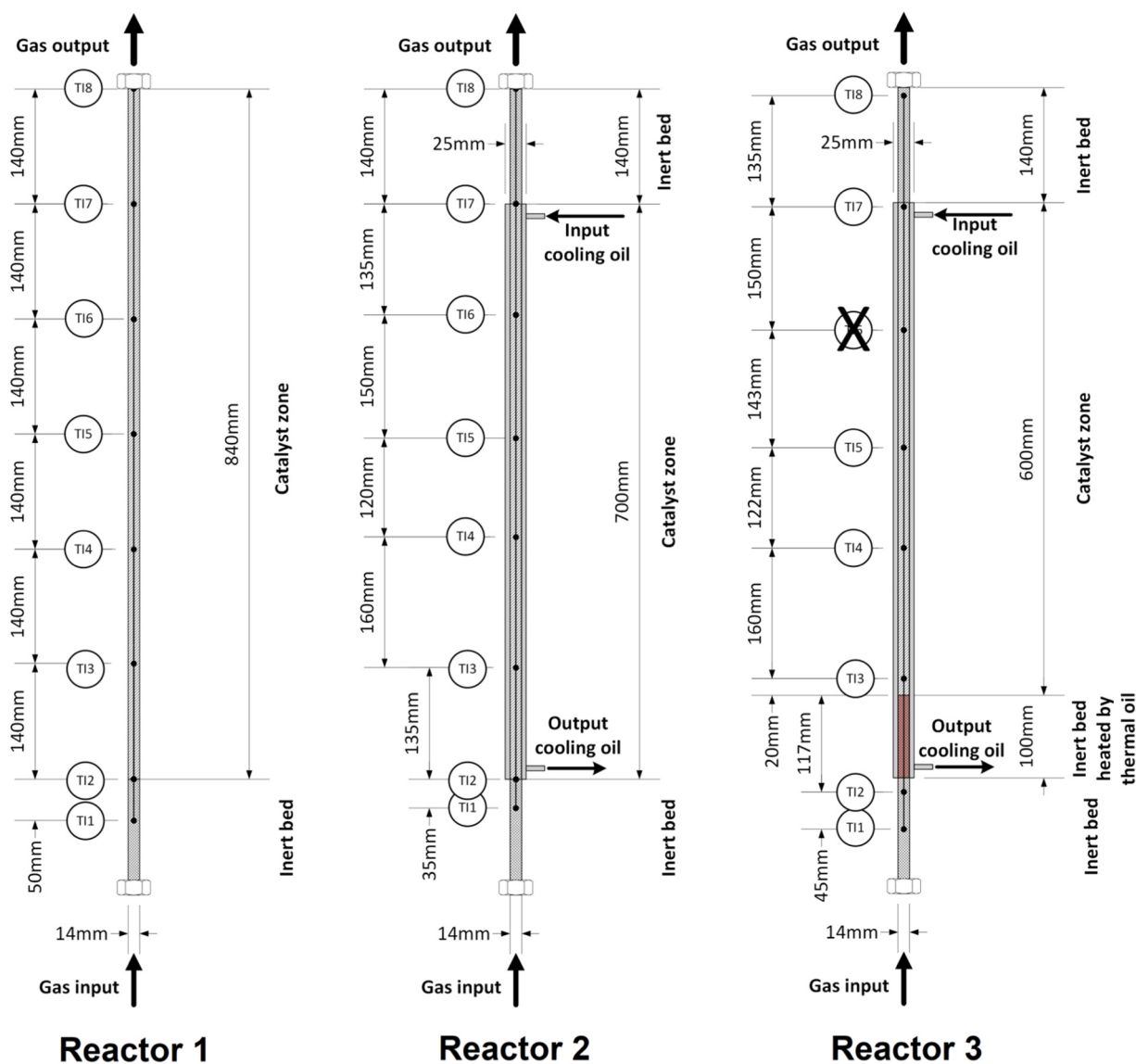


Fig. 1. Schematic scaled drawing of all three used types of 14 mm diameter tubular packed bed reactors with 840 mm (naturally cooled reactor 1), 700 mm (oil-cooled reactor 2) and 600 mm (oil-cooled reactor 3) catalyst bed length including eight temperature measurement points.

Reactor diameters in the range of 10 mm to 15 mm were suggested for tubular CO<sub>2</sub> methanation reactors. [13,23] Considering the higher exothermic heat release of CO methanation (Eq. 2), a high radial heat transport in the catalyst bed to the reactor wall is important, which can be achieved by reactor diameter minimization under consideration of industrial catalyst pellet dimensions. Based on a 1D model for CO<sub>2</sub> methanation, El-Sibai [23] found the optimum reactor diameter at the lower bound of 10 mm, since the small reactor diameter enhances heat transfer to the cooling medium and increases the area-to-volume ratio. Furthermore, the authors postulated a tube-particle diameter ratio  $\geq 10$ . According to Sie [24] the traditional rule of thumb of a tube-particle diameter ratio of at least 10 [25] for packed beds is not necessarily applicable, because the beneficial effects of radial dispersion of gas in a packed bed reduces the formation of a distinct radial velocity profile. Andriago [26] argues, that extremely low diameter ratios of 4 or 5 are viable to increase radial heat transfer and counter hot spot formation in packed beds. For simplified but sufficient experimental representation of industrial catalytic packed beds even single pellet string reactors are used with the extreme diameter ratio slightly above 1. [24,27,28] Also industrial applications with very low reactor diameters of 20–25 mm and low pellet-pipe-diameter-ratios around 3 have been realized for catalytic reactions in multitubular packed bed reactors [29–31]. Further information of low diameter ratios in packed bed reactors and related consequences for gas and porosity distribution are presented in the appendix.

Each reactor used for the experiments is equipped with eight single temperature measurement points with 1 mm diameter type K thermocouples (TI1 – TI8 in Fig. 1) within the reactor for measuring the axial temperature profile in order to facilitate a detailed model validation. Practical applicability of the experimental setup, such as implementation of eight thermocouples, resulted in 14 mm of inner reactor diameter as the possible lower limit. During experiments with the 600 mm long reactor the 6th thermocouple broke, resulting in a loss of temperature data.

The commercial nickel-based catalyst Meth134 was used with an original particle diameter largely between 2.8 and 6.3 mm. However, the catalyst spheres were sieved with a mesh size of 4 mm for easier reactor filling. The maximum operation temperature without activity loss of Meth134 is specified with 510 °C, and 700 °C for short periods.

The existing lab-scale plant was amended by an oil-thermostat LAUDA Integral IN 4 XTW to allow cooling temperatures precisely controlled up to 320 °C at the reactor cooling inlet. The cooling oil flows countercurrently to the gas flow direction. The counter current oil flow enables lowest cooling temperatures at the reactor output of about 320 °C, and consequently equilibrium composition at this temperature level is achieved. In contrast, at the input side of the reactor, higher cooling oil temperatures are beneficial for preheating the gas to the reaction kick-off temperature. In the hot spot zone the driving force between peak temperature (about 600 °C) and oil (323 °C +/- 3 K) is not significantly affected by single-digit lower cooling temperatures. Experiments showed that the maximum temperature increase of thermal oil over the reactor length is at its maximum about 6 K (from 320 °C to 326 °C). For simplification a constant mean value of 323 °C for thermal oil cooling temperature in the model was chosen. As feed gas synthetic Co-SOEC syngas of 76.8 vol.-% H<sub>2</sub>, 18.3 vol.-% CO and 4.9 vol.-% CO<sub>2</sub> [9] was mixed from bottle gases via mass flow controllers. The dry product gas concentration was measured behind a condensation trap with the gas analysis system ABB Advanced Optima AO2000. Reactor pressure was measured with a pressure transmitter downstream the reactor outlet. Reactor design and experimental parameters are summarized in Table 1.

**Table 1**

Experimental parameters, methanation reactor dimensions and packed bed parameters.

Inner reactor diameter	14 mm
Reactor wall thickness	2 mm
Inner cooling tube diameter	23 mm
Catalyst bed height	840 mm, 700 mm, 600 mm
Catalyst pellet diameter	mainly 3–4 mm
Catalyst bed porosity (centre)	0.395
Catalyst intra-particle porosity	0.67
Catalyst composition	Alumina (72.2 wt.-%), Calcium Oxide (5.6 wt.-%), Nickel (22.2 wt.-%)
Feed gas composition	H <sub>2</sub> : 76.8 vol.-%, CO: 18.3 vol.-%, CO <sub>2</sub> : 4.9 vol.-%
Cooling temperature	323 °C
Reactor pressure	1–6 bar
GHSV	4000–29,000 h <sup>-1</sup>

### 3. Model

The 1D stationary homogenous packed bed methanation reactor model was realized in MATLAB® using the numerical ODE23 solver. The Gierman criterion [32] as well as a criterion given by Sie [24] support the plug-flow assumption, whereas flow quality and radial porosity distribution of the packed bed are discussed in greater detail in the appendix. [24,33] Schlereth and Hinrichsen [16] compared 2D and 1D modelling for CO<sub>2</sub> methanation in 10 mm, 20 mm and 30 mm diameter reactors at 5000 h<sup>-1</sup> (reference case) and found, that for basic understanding of the process characteristics a 1D model was sufficient. However, the authors found the radial temperature gradients may lead to an underestimation of temperature peaks.

For the homogenous 1D model following assumptions in addition to steady-state plug-flow were made:

- Axial mass transport only by convection, dispersion was neglected
- Axial heat transport only by convection, heat transport by dispersion or effective bed heat conduction was neglected
- No significant concentration and temperature gradients between packed bed and gas (homogenous model)
- Ideal gas
- Constant cooling oil temperature and velocity

The exact same 1D plug-flow model was used to simulate all three, the naturally ambient air-cooled and the two actively oil-cooled reactor systems. As initial gas temperature for the model, experimentally determined values at the beginning of the catalyst zone were used for the 840 mm and 700 mm reactors. For the initial temperature of the 600 mm long reactor 3 the temperature values of the measurement points TI2 and TI3 (Fig. 2) were interpolated, since the exact interface between inert balls and catalyst bed cannot be determined. In the real reactor setup there is no explicit boundary layer between inert bed and catalyst as is considered in the model. The inert balls and catalyst balls mix at the interface during reactor filling and installation. As a consequence, there is a bed section with diluted catalyst between the inert and catalyst bed and the exact initial catalyst temperature can hardly be determined.

The mass balance for every gas species  $i$  and the energy balance are described in Eq. 5 and Eq. 6.

$$\frac{\delta}{\delta z}(v \cdot c_i) = \rho_{bed}(v_{i,COM} \cdot r_{COM} + v_{i,RWGS} \cdot r_{RWGS}) \quad (5)$$



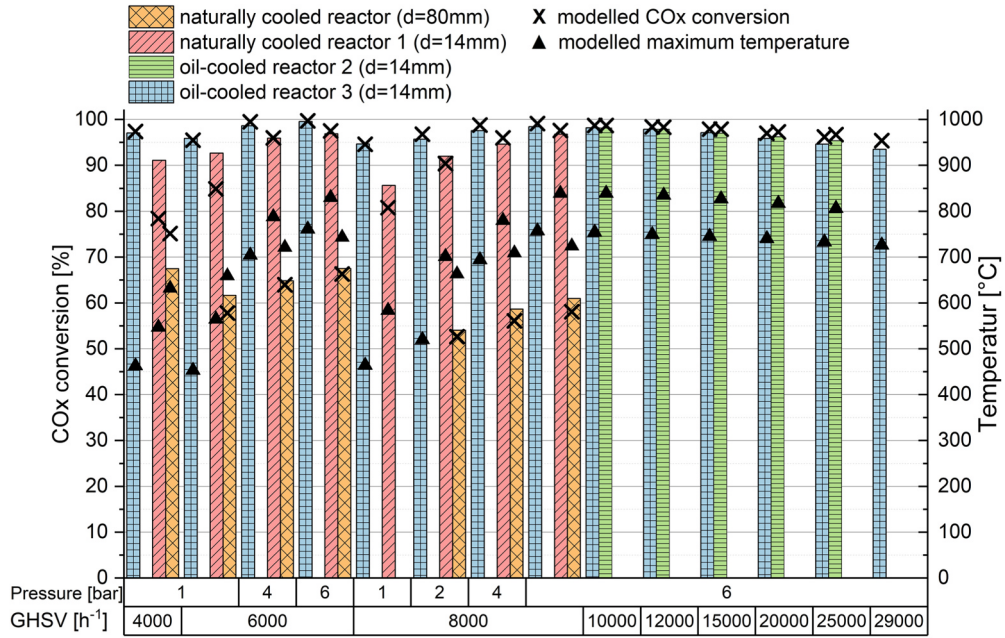


**Fig. 2.** Performance comparison based on experimentally found (bars) and modelled ('x'-markings) CO<sub>x</sub> conversion and modelled maximum temperature ('▲'-markings) of three reactors with 14 mm diameter (840 mm naturally cooled, 700 mm oil-cooled and 600 mm oil-cooled catalyst zone) and a reactor with 80 mm diameter (50 mm naturally cooled catalyst zone) [9] in dependency of GHSV and pressure.

$$\frac{\delta}{\delta z} (T \rho_{\text{gas}} c_p v) = \rho_{\text{bed}} (r_{\text{eff},\text{COM}} (-\Delta H_{\text{COM}}) + r_{\text{eff},\text{WGS}} (-\Delta H_{\text{WGS}})) - \frac{4}{d_{r,i}} k_w^{\text{eff}} (T - T_{\text{cool}}) - q_{\text{radiation}} \quad (6)$$

The effective reaction rate for CO methanation  $r_{\text{COM}}$  and the reverse water gas shift reaction  $r_{\text{WGS}}$  is calculated based on an adapted version of the intrinsic kinetic from Rönisch [34], which is extensively discussed in the appendix (Eq. 26 to Eq. 42). The effectiveness factor as presented in Gruber [7] is given in Eq. 7 to Eq. 18.

$$r_{j,\text{eff}} = r_{j,\text{intr}} \eta_{\text{cat},j} \quad (7)$$

$$\eta_{\text{cat},j} = \eta_{\text{ext},j} \eta_{\text{pore},j} \quad (8)$$

$$\eta_{\text{pore},j} = \frac{1}{\Phi_j} \left( \frac{1}{\tanh(3 \cdot \Phi_j)} - \frac{1}{3 \cdot \Phi_j} \right) \quad (9)$$

$$k_{\text{COM},V} = k_{\text{COM},m} \cdot \frac{R \cdot T}{p^2} \left[ \frac{\text{m}^3}{\text{kg}_{\text{cat}} \text{ s}} \right] \quad (12)$$

$$k_{\text{WGS},V} = k_{\text{WGS},m} \cdot R \cdot T \left[ \frac{\text{m}^3}{\text{kg}_{\text{cat}} \text{ s}} \right] \quad (13)$$

$$D_{\text{eff},\text{CO}} = \frac{\varepsilon_{\text{cat}}}{\tau_{\text{cat}}} \cdot \frac{1}{\frac{1}{D_{\text{CO}}^{\text{max}}} + D_{\text{knu},\text{CO}}} \quad (14)$$

$$D_{\text{knu},\text{CO}} = \frac{d_{\text{pore}}}{3} \cdot \sqrt{\frac{8R}{\pi} \frac{T}{M_{\text{CO}}}} \quad (15)$$

$$Sh = \left( 2 + \sqrt{(0.664 \text{Re}_p^{0.5} \text{Sc}^{\frac{1}{3}})^2 + \frac{0.037 \text{Re}_p^{0.8} \text{Sc}}{1 + 2.443 \text{Re}_p^{-0.1} (\text{Sc}^{\frac{2}{3}} - 1)}} \right) (1 + 1.5(1 - \varepsilon_p)) \quad (16)$$

$$\eta_{\text{ext},j} = \frac{1}{1 + \frac{0.6}{Sh} \Phi_j \tanh(\Phi_j)} \quad (10)$$

$$\Phi_j = \frac{d_{\text{particle}}}{6} \cdot \sqrt{\frac{n_j + 1}{2} \cdot \frac{k_{j,V}}{D_{\text{eff},\text{CO}}} \cdot \frac{\rho_{\text{particle}}}{\rho_{\text{gas}}} \cdot c_{\text{CO}}^{n_j - 1}} \quad (11)$$

$$\text{Re}_p = \frac{d_{\text{particle}} v \rho_{\text{gas}}}{\eta_{\text{gas}}} \quad (17)$$

$$\text{Sc} = \frac{\eta_{\text{gas}} \rho_{\text{gas}}}{D_{\text{eff},\text{CO}}} \quad (18)$$



Radial heat flux according to Eq. 19 shows that lower reactor diameters ensure higher radial heat transfer in tubular systems.

$$q_{\text{radial}} = -\frac{4}{d_{r,i}} k_w^{\text{eff}} (T - T_{\text{cool}}) \quad (19)$$

The overall wall heat transfer coefficient through a reactor wall is mainly defined by the inner and outer heat transfer coefficient and to a lesser extent by the wall heat conduction (Eq. 20).

$$k_w^{\text{eff}} = \left( \frac{1}{\alpha_{\text{bed-wall}}} + \frac{s_{\text{wall}}}{\lambda_{\text{steel}}} + \frac{1}{\alpha_{\text{outside}}} \right)^{-1} \quad (20)$$

The heat transfer coefficient between packed bed and wall  $\alpha_{\text{bed-wall}}$  is given in Eq. 21 as formulated by Specchia [35].

$$\alpha_{\text{bed-wall}} = \frac{\lambda_{\text{gas}}}{d_{\text{particle}}} \left( 0.0835 \text{Re}_{0,p}^{0.91} + 2\epsilon_{\text{bed}} + \frac{1 - \epsilon_{\text{bed}}}{\frac{\lambda_{\text{gas}}}{\lambda_{\text{solid}}} + 1} \right) \quad (21)$$

For an oil-cooled reactor the outside wall heat transfer coefficient to the cooling oil  $\alpha_{\text{outside,wall-oil}}$  is based on a Nusselt-correlation as described in Gnielinski [36]. For the naturally cooled system the outer heat transfer coefficient  $\alpha_{\text{outside,wall-air}}$  is considered based on free convective flow at the outside of the reactor pipe (Eq. 22) [37].

$$\alpha_{\text{outside,wall-air}} = 1.32 \sqrt[4]{\frac{T_{\text{wall}} - T_{\text{air}}}{d_{r,o}}} \quad (22)$$

The pressure loss in a packed bed can be calculated by the Ergun equation (Eq. 23).

$$\frac{\Delta p}{\Delta L} = 150 \frac{(1 - \epsilon_{\text{bed}})^2}{\epsilon_{\text{bed}}^3} \frac{\eta_{\text{gas}} v_{\text{sup}}}{d_{\text{particle}}^2} + 1.75 \frac{(1 - \epsilon_{\text{bed}})}{\epsilon_{\text{bed}}^3} \frac{\rho_{\text{gas}} v_{\text{sup}}^2}{d_{\text{particle}}} \quad (23)$$

Furthermore, radiation at the outside of the reactor pipe is taken into account as shown in Eq. 24. Since radiation in the oil-cooled system to ambient does not occur due to insulation it can be neglected for these reactor set-ups.

$$q_{\text{radiation}} = \frac{4}{d_{r,o}} \epsilon_{\text{rad}} k_b (T_{\text{wall}}^4 - T_{\text{air}}^4) \quad (24)$$

The CO/CO<sub>2</sub> methanation performance parameter CO<sub>x</sub> conversion is a combination of CO<sub>2</sub> and CO conversion as explained in Eq. 25.

$$\text{CO}_x \text{ conversion} = \frac{(\dot{n}_{\text{CO},\text{in}} - \dot{n}_{\text{CO},\text{out}}) + (\dot{n}_{\text{CO}_2,\text{in}} - \dot{n}_{\text{CO}_2,\text{out}})}{\dot{n}_{\text{CO},\text{in}} + \dot{n}_{\text{CO}_2,\text{in}}} \quad (25)$$

Calculation of physical properties such as gas viscosity, heat capacity, heat conductivity and diffusion coefficients are based on empirical polynomial functions found in VDI Wärmeatlas [38].

#### 4. Results and discussion

While the outer heat transfer coefficient can independently be tuned by active cooling properties, the inner bed-wall heat transfer is a function of gas turbulence ( $\text{Re}_{0,p}$ ), particle diameter, porosity and gas and solid heat conductivity. In conclusion of Eq. 19 and Eq. 21 as given in Specchia [35], the inner heat transfer coefficient can be practically mainly influenced by the gas velocity. A reduction of particle diameter has only limited beneficial effect on the coefficient, but it directly affects the radial transport distance.

However, an increase of gas velocity not only enhances radial heat transport but also increases the pressure loss according to the Ergun equation (Eq. 24) as discussed in [39]. In order to maintain a constant

pipe-to-pellet diameter ratio and avoid excessive pressure loss, it is not possible to reduce the particle size to the same extent as the tube diameter. Decreasing the particle size to match the tube diameter would result in even higher pressure losses. [40].

Improved heat removal allows more heat to be produced at higher reaction rates or higher GHSV without a temperature increase. As a result, improved temperature control can be achieved by higher gas velocity (Eq. 18 and Eq. 22), lower reactor diameter (Eq. 20) and enhanced active cooling at the outer reactor wall (Eq. 21).

Fig. 2 is an accumulation of experimental and model-based findings for 4 different reactor designs. The CO<sub>x</sub> conversion and the related maximum temperatures are shown in dependency of reactor design, pressure and GHSV.

Fig. 2 shows that the conversion of all the 14 mm reactors is significantly better than with the 80 mm naturally cooled system [9]. The reactor diameter reduction from 80 mm to 14 mm (both naturally cooled) resulted in a significant improvement of CO<sub>x</sub> conversion, for example from 67.5% to 97.5% at 6000 h<sup>-1</sup> and 6 bar. The radial heat transport within the packed bed was enhanced by lower radial distance (Eq. 20) and higher gas velocity (Eq. 18 and Eq. 22).

Comparison of actively oil-cooled reactor 1 and naturally cooled reactor 2 both with 14 mm diameter shows an improvement of performance by cooling. At 6 bar and 6000 h<sup>-1</sup> almost full conversion of 99.6% was achieved with cooling, compared to 97.5% without cooling. At the same time the maximum temperature could be reduced from 830 °C to 761 °C.

For the oil-cooled 14 mm reactors with and without preheating zone very similar results were found. Almost the same conversions can be detected. However, the maximum temperature increases as a result of preheating. At the one hand lower gas velocities occurred in reactor 3 (lower catalyst volume at the same GHSV), and additionally higher starting temperatures caused the peak temperature to increase.

In each of the oil-cooled 14 mm reactors the peak temperature decreases with increasing GHSV. This is again caused by an increase of radial heat transport due to higher gas velocities (Eq. 18 and Eq. 22). On the other hand, in the naturally cooled 14 mm reactor the peak temperatures increase with increasing GHSV. Without cooling the overall heat transfer is limited at the outer wall-air interface, not (only) at the inside. As a result, an increase of gas velocity has no significant beneficial effect on the overall radial heat transfer (Eq. 21) in the naturally cooled 14 mm reactor.

Furthermore, it can be seen that 'X'-markings and bars closely match, which indicates, that the model very accurately represents the experimental findings in terms of CO<sub>x</sub> conversion.

Finally, this diagram illustrates that peak temperatures are way too high at high capacities and high pressures, even in oil-cooled 14 mm reactors. Such extreme temperatures exceed not only the long term maximum temperature of 510 °C by far for the used catalyst, but also the the short term specification of 700 °C. Since no loss of activity could be detected throughout all the experiments, slightly higher temperatures around 550 °C may be feasible for long term methanation with this specific catalyst. A maximum temperature of 531 °C was achieved based on model and experimental data with the oil-cooled 14 mm reactor 2 at 6000 h<sup>-1</sup> and 1.4 bar, resulting in 95.5% CO<sub>x</sub> conversion. The dry product gas concentration in this case was 75.7 vol.-% CH<sub>4</sub>, 21 vol.-% H<sub>2</sub>, 3.3 vol.-% CO<sub>2</sub>, which would require a second reactor stage or gas processing to achieve recent natural gas injection requirements of Austria [41] and most European countries [2,3] of maximum 10 vol.-% H<sub>2</sub>. At equal conditions (1.5 bar, 6000 h<sup>-1</sup>) the 80 mm reactor achieved only 61.5% CO<sub>x</sub> conversion.

The experiment-model consistency is presented in greater detail in

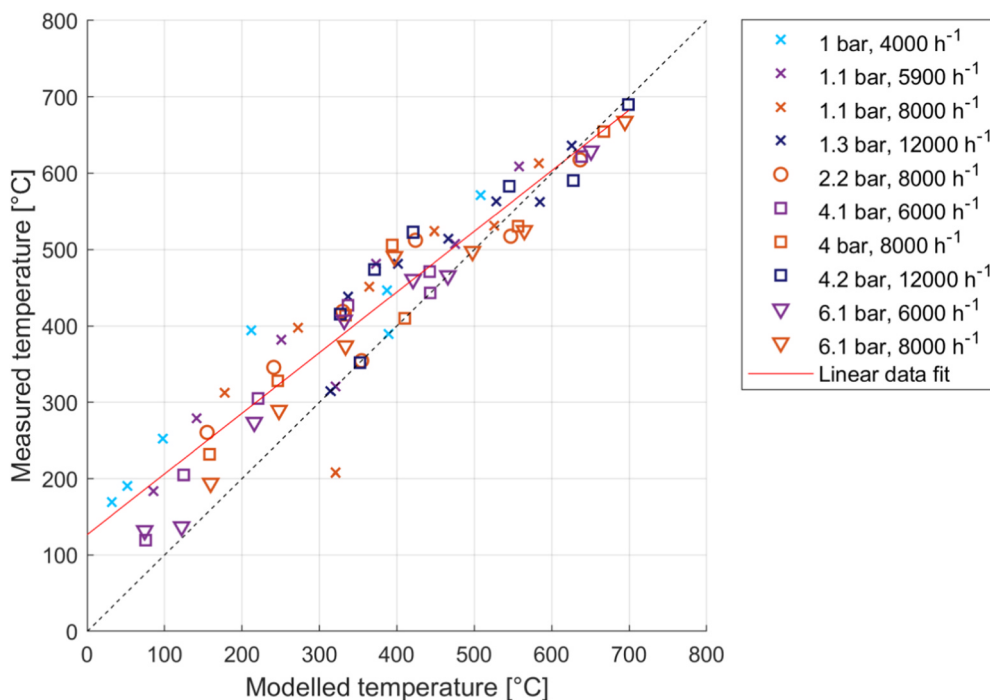


Fig. 3. Parity plot of modelled and experimentally found reactor temperatures in the 14 mm diameter and 840 mm length naturally cooled reactor for different pressures and GHSV (same symbols represent quasi-axial temperature profile).

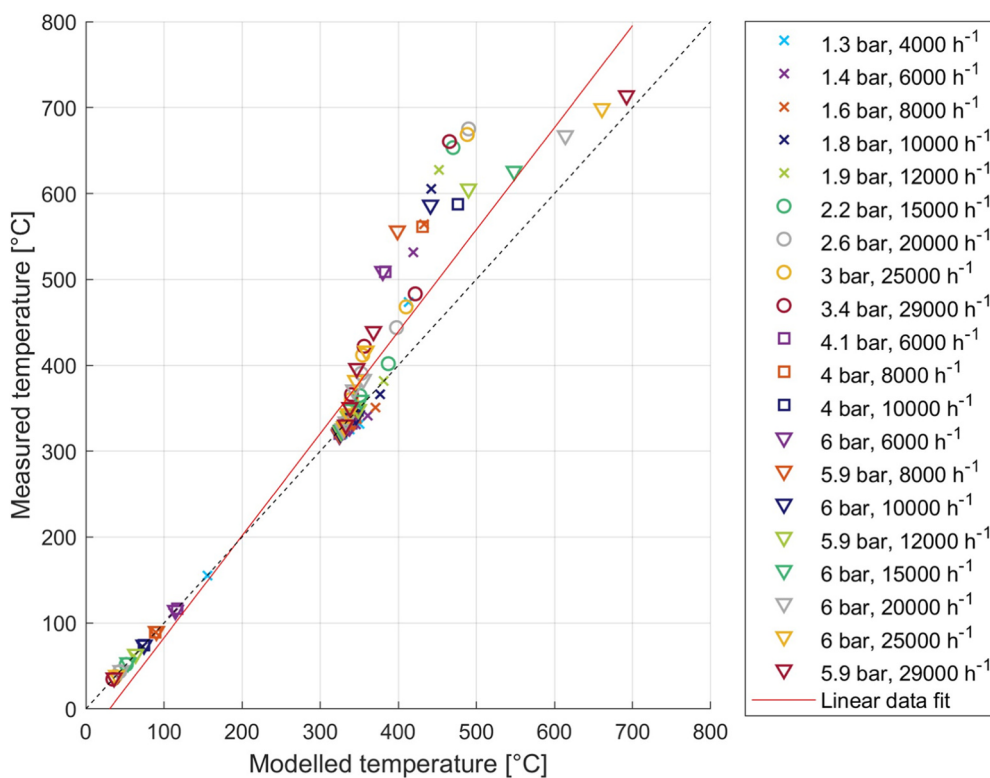


Fig. 4. Parity plot of modelled and experimentally found reactor temperatures in the 14 mm diameter and 700 mm length oil-cooled reactor for different pressures and GHSV (same symbols represent quasi-axial temperature profile).

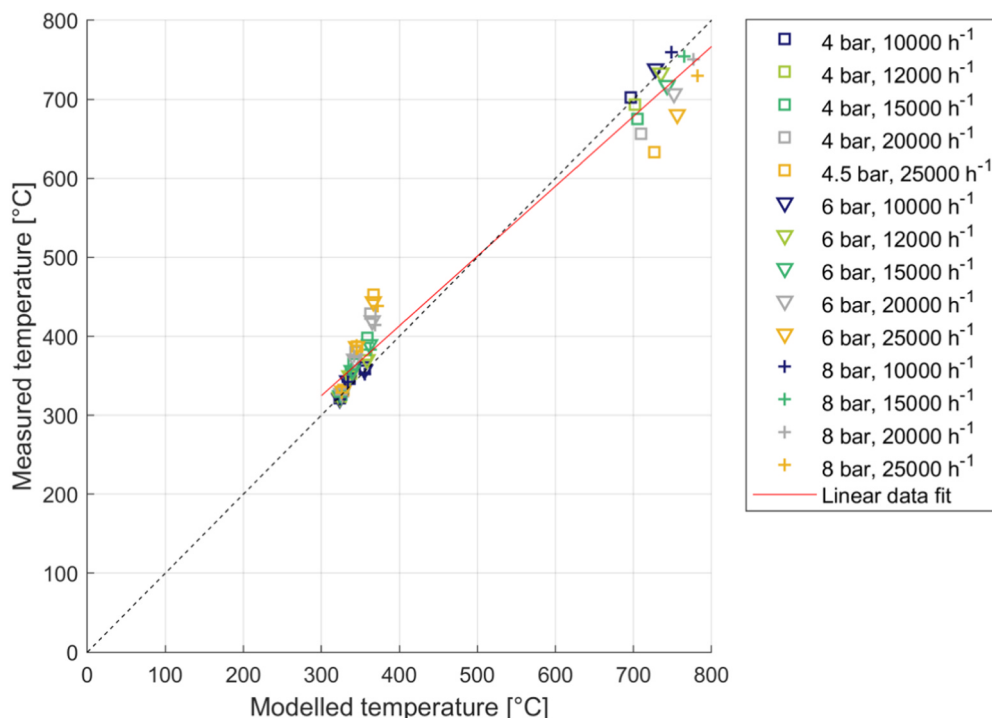


Fig. 5. Parity plot of modelled and experimentally found reactor temperatures in the 14 mm diameter and 600 mm length oil-cooled reactor for different pressures and GHSV (same symbols represent quasi-axial temperature profile).

Figs. 3–5, which present parity plots of measured and modelled temperature data for each of the three reactor types.

As Fig. 3 illustrates, for the naturally cooled 14 mm reactor at higher temperatures above 500 °C the model accuracy is very good, as the markings align closely with the 45° line. However, at cooler zones the model tends to underestimate the reactor temperatures roughly by about 100 K at 100 °C and about 50 K at 400 °C in regard to the linear data fit. In addition, tests at lower reactor pressure at around 1 bar (‘x’-markings) show the highest deviation, while higher reactor pressures (4 bar: ‘□’-markings, 6 bar: ‘▽’-markings) are more accurate.

The overall model accuracy for the oil-cooled 700 mm long 14 mm diameter reactor is very good. However, in contrast to the naturally cooled system the maximum temperature values are overestimated by about 120 K throughout all pressure values, while measured and modelled temperatures below 400 °C are almost identical.

For the 14 mm reactor with preheating and 600 mm catalyst zone, GHSV between 10,000 h<sup>-1</sup> and 25,000 h<sup>-1</sup> was investigated. The overall model accuracy is again very good, whereas maximum temperature values are slightly overestimated and moderate temperatures slightly underestimated by the model. Deviation tends to be higher for higher GHSV values, while low GHSV values have almost no deviation in measured and modelled temperature. An increasing trend in error almost perpendicular to the 45° line with increasing GHSV can be seen in Fig. 5. This trend in error implies the relations implemented in the model should be reconsidered for further investigations at higher gas velocities.

The parity plots give a good collective overview of the model-experiment consistency and allow to derive certain tendencies with pressure or GHSV as discussed above. However, axial temperature and mole fraction profiles enable a deeper insight in the reasons for the identified model inaccuracies. Therefore, in Figs. 6 and 7 axial

temperature and mole fraction profiles for selected cases are presented.

As exemplarily shown for three GHSV and pressure pairs in Fig. 6, the overall model-experiment alignment in terms of the axial temperature profile is extremely good. The information gained from the 1D model in terms of maximum temperatures is substantial, since extreme temperature gradients found by the model could hardly be identified accurately by punctual experimental measurement with thermocouples (Fig. 6c and Fig. 6e). Small errors in axial thermocouple alignment would result in a significant temperature measurement deviation due to the extreme axial temperature gradients.

A slightly higher model-experiment deviation in temperature at low pressures can be seen in Fig. 6a compared to Fig. 6c and Fig. 6e, which is likely caused by a lower accuracy of the kinetic model at low pressures as also shown for the naturally cooled reactor in Fig. 3. Although the temperature is initially rising at the catalyst bed inlet, the exponential increase of temperature is not high enough in Fig. 6a. This indicates too low reaction rate coefficients and therefore too low pre-exponential factors or too high activation energy for this low pressure range (Eq. 27 to Eq. 43) as similarly discussed by Gruber [7]. As a result, the achieved water and methane concentration shown in Fig. 6b is too low, while H<sub>2</sub>, CO and CO<sub>2</sub> remain at too high levels compared to the experiments. Hence, these deviations in modelled and measured concentration and temperature results are likely connected to reaction kinetics of the reverse water gas shift reaction (Eq. 28) and of the CO methanation reaction (Eq. 27), which may require further improvement of the intrinsic kinetic model at low pressures.

In Fig. 6c at 6 bar and 6000 h<sup>-1</sup> the temperature profile shows a sharp increase to 827 °C as a consequence of significantly higher reaction rates predicted by the kinetic model at elevated pressure. Downstream the maximum temperature value, the profile almost linearly decreases as the system cools down by natural convective cooling against atmospheric

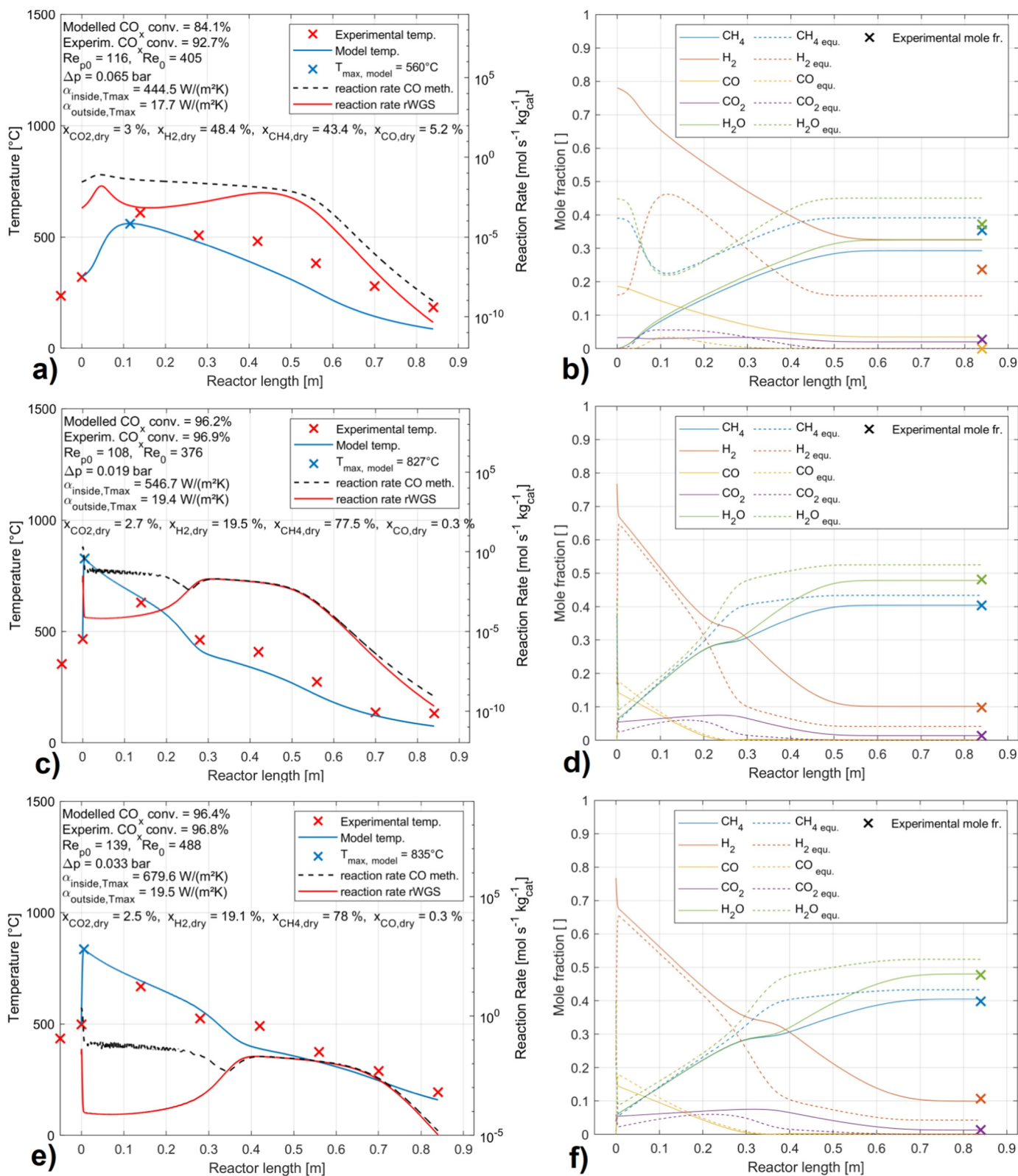


**Fig. 6.** Axial profiles of modelled (lines) and experimentally determined ('x'-markings) temperature and molar fractions of the 14 mm diameter and 840 mm long naturally cooled reactor at 6000 h<sup>-1</sup> and 1 bar (a and b), 6000 h<sup>-1</sup> and 6 bar (c and d) and 8000 h<sup>-1</sup> and 6 bar (e and f) (CO<sub>x</sub> conversions, Reynolds numbers, heat transfer coefficients and maximum temperature (blue 'x'-marking) included).



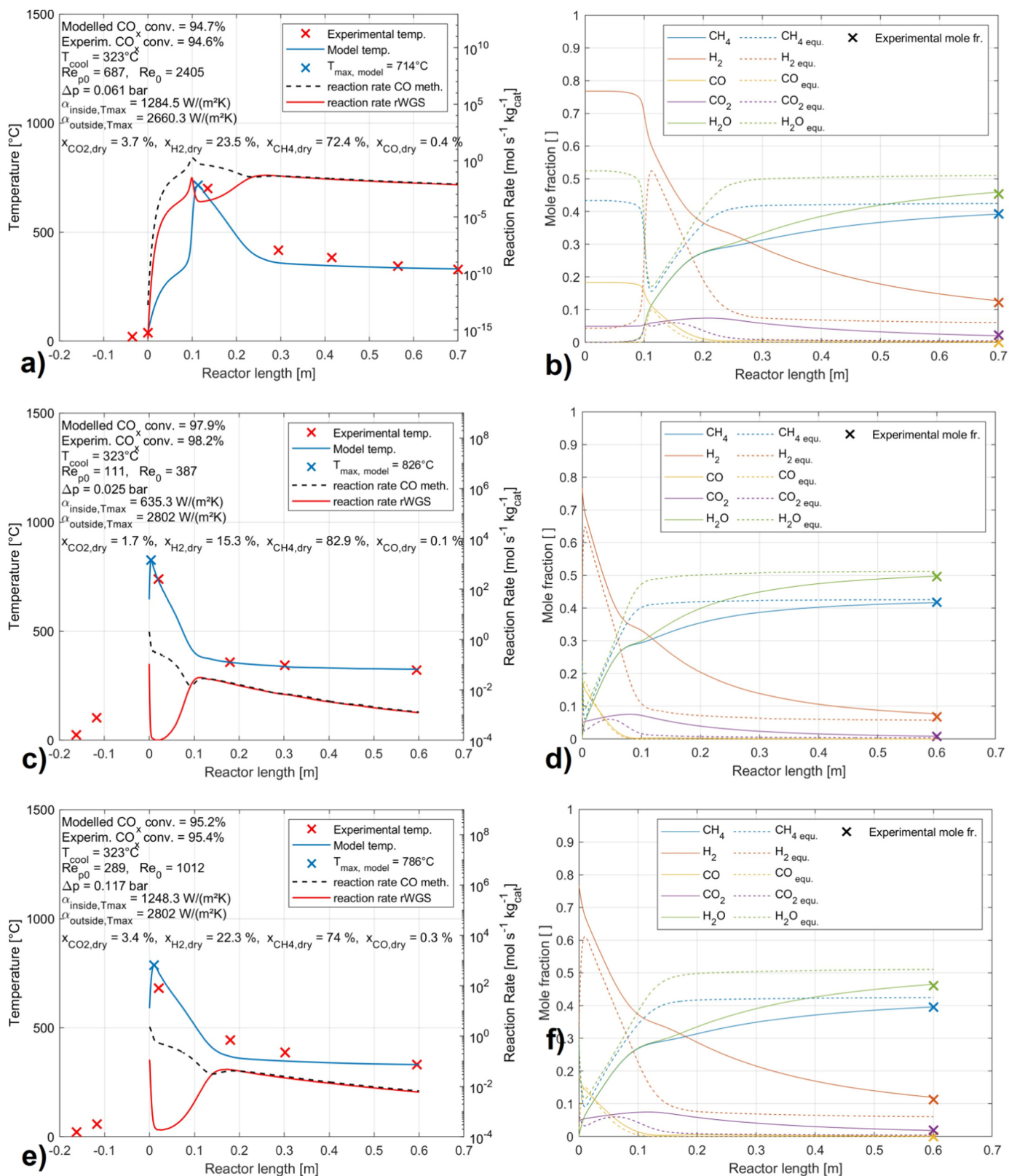


Fig. 7. Axial profiles of modelled (lines) and experimentally determined ('x'-markings) temperature and molar fractions, equilibrium composition (dashed line) and reaction rates for the 14 mm diameter, 700 mm long reactor 2 at 25,000 h<sup>-1</sup> and 6 bar (a and b), 600 mm long reactor 3 at 10,000 h<sup>-1</sup> and 6 bar (c and d) and 25,000 h<sup>-1</sup> and 6 bar (e and f) (CO<sub>x</sub> conversions, cooling temperature, Reynolds numbers, heat transfer coefficients, dry output concentration and maximum temperature (blue 'x'-marking) included).

temperature. A slight dip in the linear temperature decrease is given around 0.3 m length, which is aligned with the full consumption of CO (Fig. 6d). Downstream of this point CO<sub>2</sub> is consumed at a significantly higher rate. Upstream of this point in Fig. 6d and f, a CO<sub>2</sub> formation may be assumed, but the mole fraction only increases because the total number of moles decreases due to the ongoing chemical reactions. However, the mole fraction of CO downstream of 0.3 m in Fig. 6d does not increase, because it is immediately converted to CH<sub>4</sub>. Interestingly, the mentioned dip in temperature calculated from the 1D model can be seen as well in the experimentally found data at the almost same position.

In Fig. 6e an increase in GHSV value of 8000 h<sup>-1</sup> compared to 6000 h<sup>-1</sup> in Fig. 6c leads to generally higher temperatures in the naturally cooled system (the opposite tendency was found for oil-cooled reactors). The linear temperature decrease downstream the temperature peak is less steep with higher GHSV, which is a result of a heat transfer limitation. While the inner heat transfer coefficient at 6000 h<sup>-1</sup> and 6 bar with approximately 547 W m<sup>-2</sup> K<sup>-1</sup> increases due to an increase in Reynolds number to 680 W m<sup>-2</sup> K<sup>-1</sup> at 8000 h<sup>-1</sup> the outer heat transfer coefficient stays constant with 19.5 W m<sup>-2</sup> K<sup>-1</sup> (each value calculated at the point of maximum temperature). Therefore, the naturally cooled systems radial heat transfer rate is limited by the outer pipe-to-air heat transfer. As a result, an increase in feed gas flow at almost the same conversion leads to more produced reaction heat, which results in higher reactor temperatures because the heat cannot be adequately removed in radial direction. These findings show, that the extreme temperature values and outer heat transfer limitation have to be addressed by active cooling, e.g. with thermal oil. A detailed discussion of the oil-cooled 14 mm diameter methanation results based on axial profiles derived from model and experiments is conducted in Fig. 7.

As in Fig. 6, also in Fig. 7 the alignment of modelled and experimental temperatures and gas composition is very accurate.

It can be seen that the starting temperature at the catalyst bed entrance of the preheated reactor 3 is with 646 °C (Fig. 7c) and 590 °C (Fig. 7e) significantly higher, than for the 700 m long reactor without preheating given in Fig. 7a (39 °C). The reason for the high initial temperature is the above mentioned 100 mm long preheating zone in reactor 3, which is missing in reactor 2. In this preheating zone the hot thermal oil at around 323 °C significantly heats up the inert packed bed, and consequently the incoming gas. As a result, the reactor temperature quickly spikes to 826 °C only a few millimetres downstream the catalyst bed entrance (Fig. 7c and e), due to higher initial kinetics. In contrast, in reactor 2 without preheating the incoming gas needs to be heated to the kick-off temperature within the catalyst bed until it spikes roughly 100 mm downstream of the inlet (Fig. 7e). The maximum temperature in reactor 2 is lower compared to reactor 3 at the same GHSV of 25,000 h<sup>-1</sup>, because part of the gas is already converted upstream of the spike leading to lower maximum reaction rates. The maximum temperature decreases in the oil-cooled reactor with increasing GHSV (both reactor 3) from 826 °C at 10,000 h<sup>-1</sup> to 786 °C at 25,000 h<sup>-1</sup> due to higher inner heat transfer coefficients according to Eq. 18 and Eq. 22 as already discussed.

In all presented cases with reactor cooling subsequently to the temperature peak a rapid decrease can be observed which finally approaches the cooling temperature of 323 °C. Analogously to the temperature spike in the first 8 mm of the catalyst zone in Fig. 7c, a steep decrease in reactant gas concentration within 8 mm can be seen in Fig. 7d due to the high reaction rates at 10,000 h<sup>-1</sup> and 6 bar. Within this length of 8 mm CO is almost fully converted to CH<sub>4</sub>, similar to the findings of the naturally cooled reactor (Fig. 6). However, only 8 mm of reactor length are necessary for complete CO consumption with the oil-

cooled system compared to around 30 mm of reaction length at the naturally cooled set-up with comparable operation conditions of 8000 h<sup>-1</sup> and 6 bar (Fig. 6e). In conclusion, the capacity limiting pipe-to-air heat transfer of the naturally cooled 14 mm reactor was significantly reduced by oil cooling, resulting in less necessary reactor volume for the same conversion. Correspondingly, the outside heat transfer coefficient was increased from roughly 20 W m<sup>-2</sup> K (pipe-to-air) to 2800 W m<sup>-2</sup> K (pipe-to-oil). Therefore, the naturally cooled reaction is limited by the resulting packed bed temperature which indicates thermodynamic limitation between catalyst bed inlet and point of full CO conversion. By active oil-cooling, this thermodynamic limitation could be reduced.

The section of the temperature curve close to the reactor outlet (second half of catalyst zone) is characterized by a more flat form, slowly approaching the cooling temperature in all cases in Fig. 7a, c and e. Similar to the naturally cooled reactor discussed above, the turning point of the temperature curves corresponds to the points of full CO conversion (Fig. 7b, d, f). From this point on, CO<sub>2</sub> is converted to CO, which again immediately reacts to CH<sub>4</sub>.

In Fig. 11 in the appendix the deviation to the thermodynamic equilibrium at each point of the oil-cooled reactor length is presented. In accordance to Fig. 7b and d (as well as Fig. 11 in the appendix) the catalyst zone of the oil-cooled reactors can be divided into two zones with different limitations. First, a short initial zone of kinetic limitation of the CO methanation reaction of about 8 mm to the point of full CO consumption can be derived. The CO methanation kinetic limited zone is followed by a limitation of the reverse water gas shift reaction in the larger rest of the catalytic bed. This is also reflected by the reaction rates of CO methanation and rWGS. The reaction rate of CO methanation is limited to the rate of rWGS, which almost perfectly align in this section. Hence, a further increase in rWGS reaction rate would speed up the overall process. This could be achieved by blending the nickel catalyst in the second half of the reactor with rWGS specific catalyst, such as iron-chromium or copper-zinc based catalysts [42,43].

In Fig. 7e the temperature values of the experiment are not as well aligned as in Fig. 7c. Inaccurate estimation of the initial temperature at the reactor inlet or deviation due to a significant radial temperature profile are two possible explanations for model-experiment misalignment. A higher starting temperature leads to an increase in peak temperature and a horizontal shift of the curve to the right of the diagram, which becomes apparent when Fig. 7a and Fig. 7e are compared. On the other hand, experimental determination of extreme temperature gradients with 1 mm thick thermocouples, including a deviation in their exact axial and radial position in the catalyst bed, is a relevant source of error. Furthermore, the neglect of effective heat conduction within the catalyst bed may have resulted in model inaccuracy.

## 5. Design strategy for high-capacity methanation systems

As Böhm [44] suggested, the CAPEX costs are the second most important cost factor after electrical energy costs for SNG production of a combined Co-SOEC and methanation PtG plant. In order to considerably reduce methanation costs, the reactor size and complexity for a given volume flow should be minimized. Tube-bundle reactors are simple, easily scalable to industrial capacities, suitable for commercially available catalyst and thermal oil cooling. Furthermore, it is inevitable to keep the reactor temperature below catalyst deactivation temperature (510 °C long-term stability temperature for Meth134). Low pressure loss contributes to moderate operation costs.

In this regard, the PFR reactor model was used to investigate the effects of reactor design and operation parameters for industrial application outside its validation range. At first temperature reduction by

**Table 2**  
Comparison of performance results of different reactor dimensions.

	GHSV	Volume flow per reactor (STP)	Pressure	CO <sub>x</sub> -conv.	Max. Temp.	Pressure loss
$d_{r,i}=80$ mm	6000 h <sup>-1</sup>	25 L min <sup>-1</sup>	1.3 bar**	61.7%	613 °C	< 0.1 bar
L=50 mm	6000 h <sup>-1</sup>	25 L min <sup>-1</sup>	4 bar	64.8%	721 °C	< 0.1 bar
$d_{r,i}=14$ mm	6000 h <sup>-1</sup>	10.7 L min <sup>-1</sup>	1.4 bar**	95.5%	~531 °C*	0.03 bar
L=700 mm						
$d_{r,i}=14$ mm	10,000 h <sup>-1</sup>	15.4 L min <sup>-1</sup>	4 bar	97.2%	756 °C	0.05 bar
L=600 mm	25,000 h <sup>-1</sup>	38.5 L min <sup>-1</sup>	4.5 bar	94.1%	741 °C	0.2 bar
	100,000 h <sup>-1</sup>	153.9 L min <sup>-1</sup>	4 bar	83.9%	608 °C	2.2 bar
$d_{r,i}=10$ mm	100,000 h <sup>-1</sup>	56.1 L min <sup>-1</sup>	4 bar	80.7%	503 °C	0.84 bar
L=429 mm						
$d_{r,i}=10$ mm	100,000 h <sup>-1</sup>	39.3 L min <sup>-1</sup>	4 bar	80.4%	513 °C	0.3 bar
L=300 mm						

\* maximum temperature was derived by experiments

\*\* pressure < 4 bar may lead to carbon deposition with Co-SOEC syngas [10]

high gas velocities at high GHSV values were tested. At 100,000 h<sup>-1</sup> and 4 bar outlet pressure the temperature of the 14 mm diameter and 600 mm long reactor is calculated to peak at 608 °C (83.9% conversion), which is significantly lower compared to 25,000 h<sup>-1</sup> and 741 °C (Fig. 7c). However, with increasing gas velocity also the pressure loss increases ten-fold from 0.2 bar to 2.2 bar for the given example, leading to a significant increase in compression effort and overall inefficiency. Additionally, higher pressure loss contradicts efforts for temperature reduction, as higher absolute input pressures are necessary to maintain the outlet pressure.

Secondly, the maximum temperatures can be reduced by applying lower reaction pressures, but only on the expense of less favourable thermodynamic and kinetic conditions. In addition, the pressure for Co-SOEC syngas methanation should be kept above 4 bar to reduce the risk of carbon deposition as shown in an earlier study [10]. In consequence, moderate pressures between 4 bar and 6 bar for Co-SOEC syngas methanation should be aimed at.

If volume flow and pressure tuning is limited to achieve acceptable packed bed temperatures, the reduction of reactor diameter is the remaining tuning parameter in high-capacity reactors. As has been already suggested by El-Sibai [23] and Sie [24], the reactor diameter was further reduced to 10 mm for increased heat removal without the drawback of pressure loss. A reactor length of 429 mm at constant diameter-to-length ratio and constant particle diameter of 3 mm for low pressure loss was defined. On the downside, the low diameter ratio of 3.3 likely leads to more inhomogeneous bed porosity and velocity maldistribution compared to larger reactors, which was thoroughly addressed in detail in the appendix. Model-based testing resulted in 503 °C maximum temperature, 80.7% conversion and 0.84 bar pressure loss. Furthermore, it was found that with 10 mm diameter a catalyst bed length of 300 mm is sufficient to achieve almost equal 80.4% CO<sub>x</sub> conversion with only 0.3 bar pressure loss and 513 °C temperature peak in the 10 mm reactor. Such small reactor dimensions would lead to an enormous number of reactor pipes in tube bundle reactors built for industrial scale volume flows, if the relative capacity was not adequately increased. For the presented design examples, 14 mm diameter, 600 mm length, 25,000 h<sup>-1</sup> vs. 10 mm diameter, 300 mm length, 100,000 h<sup>-1</sup>, the absolute capacity per reactor pipe remains constant with about 2.3 Nm<sup>3</sup> h<sup>-1</sup>, while the avoidance of hot spots in the catalyst bed can only be achieved in the latter case. As a result of the suggested design adaption from 14 mm to 10 mm diameter the absolute number of pipes would stay the same for a given volume flow, whereas with 10 mm reactor pipes, only half of the total reactor pipe length and one quarter of the amount of catalyst would be necessary. In Table 2 an overview of the

performance at several reactor dimensions and operation parameters are summarized.

The only reactor design, other than the 10 mm reactor, that was found to be capable of meeting moderate maximum temperature around 550 °C is the 14 mm reactor at only 1.4 bar and 6000 h<sup>-1</sup> GHSV including high probability of carbon deposition due to low pressure. Obviously, the reactor diameter cannot be reduced infinitely due to practical installation and catalyst filling issues. Catalysts with high temperature tolerance [45] would benefit CO methanation at multiple levels, as higher reactor diameters and higher kinetics would be possible. A reduction of catalyst pellet size for higher diameter ratio would lead again to higher pressure loss. Further investigation of the proposed 10 mm reactor design is necessary with a focus on adverse impacts by flow and porosity maldistribution. However, industrial applications of catalytic packed bed reactors with 20 mm diameter and a diameter ratio of 3 have been successfully realized. [29–31] The benefits of maximum catalyst temperature compliance may outweigh adverse flow characteristics. Moreover, the presented example shows that model-based reactor dimension optimization with simple 1D models can lead to highly-optimized methanation systems as the main characteristics of the process can be sufficiently represented. A design strategy for highly reactive syngas methanation feed to maximize capacity can be summarized in the following points:

- <600 °C peak temperature is necessary to avoid catalyst sintering
- Active cooling is necessary to omit outer heat transfer limitation
- >4 bar pressure is necessary for Co-SOEC syngas to avoid carbon deposition
- Pressure reduction (max. to the 4 bar limit) reduces peak temperatures (at the expense of conversion)
- GHSV/volume flow increase reduces inner heat transfer limitation, leads to lower peak temperatures (only in oil-cooled systems) but is limited by maximum pressure loss
- Further temperature peak decrease can only be achieved by a reduction of reactor diameter (at the expense of bed maldistribution or practical applicability)

## 6. Conclusion

A combined experimental and modelling investigation of a packed bed methanation reactor with and without cooling for Co-SOEC syngas methanation was conducted. A 1D PFR model including an adapted two-step kinetic approach by Rönsch [34] was established. Generally good, and partially very good accuracy in terms of temperature and product



gas concentration between model and experiments in the range of 4000 h<sup>-1</sup> to 29,000 h<sup>-1</sup> and 1 bar to 6 bar was proven. However, for cooled reactor 3 more measurement points and a higher density of temperature measurements in the temperature peak section would improve model experimental data for validation of the model and is therefore aimed at for future investigations. In addition, the initial catalytic bed temperature has a significant impact on the exact temperature profile but. The results of 14 mm diameter reactors (840 mm, 700 mm, 600 mm catalyst bed length) were compared to a similar investigation of a 80 mm packed bed reactor [9]. As models and experiments confirmed, a decrease in diameter from 80 mm to 14 mm and active cooling with thermal oil increased the performance from 8000 h<sup>-1</sup> GHSV and 61% CO<sub>x</sub> (80 mm diameter, naturally cooled reactor) conversion to 93.5% at 29,000 h<sup>-1</sup> both at 6 bar (14 mm diameter, oil-cooled reactor). In addition, it was shown that the thermodynamic limitation and maximum temperatures of a 14 mm naturally cooled reactor could be reduced by active oil-cooling. The rate limitation in the actively cooled reactor is the reverse water gas shift reaction, which could be enhanced by catalyst blending. Despite cooling and improved radial heat transfer at high gas velocities, the modelled packed bed peak temperatures mostly exceeded the tolerable maximum catalyst temperature (510 °C) by far (720 °C at 29,000 h<sup>-1</sup> and 6 bar). Acceptable bed temperatures below 550 °C were proven by model and experiments for the 14 mm oil-cooled reactor only at low pressures of 1.4 bar and 6000 h<sup>-1</sup> reaching 95.5% of CO<sub>x</sub> conversion. Since carbon deposition below 4 bar for the investigated gas mixture likely occurs [10], further reactor designs for increased radial heat transfer were tested with the established model. A sweet spot of reactor dimension and operation parameters was found for Co-SOEC syngas methanation at 10 mm diameter with 3 mm catalyst pellets at a length of 300 mm, 4 bar pressure and a capacity of 100,000 h<sup>-1</sup>, which resulted in 80.4% CO<sub>x</sub> conversion, only 513 °C temperature peak and a pressure loss of 0.3 bar. With this 10 mm design for a first reactor stage for Co-SOEC syngas methanation all boundary conditions are met and due to the extreme capacity the total reactor length and catalyst volume can be minimized at constant total volume flow. An adequately designed second reactor stage for complete methanation would be necessary in any viable case, especially at such high capacities and this requires further investigation. A general design strategy for high-capacity syngas methanation reactors suitable for industrial scale tube-bundle systems

including most important boundary conditions and possible tuning parameters was presented. However, further steps to avoid catalyst bed hot spots such as a reduction in cooling temperature should be analysed. Lower cooling temperatures can have a positive effect on the maximum temperatures at the tolerable expense of conversion in a first reactor stage. High temperature resistant catalysts [45] would allow higher conversions and capacities without the drawback of catalyst deactivation.

### CRediT authorship contribution statement

**Krammer Andreas:** Conceptualization, Data curation, Formal analysis, Investigation, Methodology, Project administration, Software, Validation, Visualization, Writing – original draft, Writing – review & editing. **Salbrechter Katrin:** Data curation, Formal analysis, Investigation, Project administration. **Lehner Markus:** Conceptualization, Funding acquisition, Project administration, Resources, Supervision, Writing – review & editing.

### Declaration of Competing Interest

The authors declare that they have no known competing financial interests or personal relationships that could have appeared to influence the work reported in this paper.

### Data availability

Data will be made available on request.

### Acknowledgement

This study was performed within the project HydroMetha, which is to a large extent financed by the research program “Energieforschungsprogramm 2016” funded by the Austrian “Klima- und Energiefonds” and the AVL List GmbH (grant no. 864578). The project consortium is formed by AVL List GmbH, Fraunhofer Institute for Ceramic Technologies and Systems, Chairs of Physical Chemistry and Process Technology of the Montanuniversitaet Leoben, Prozess Optimal CAP GmbH, Energieinstitut an der JKU Linz and AICHERNIG Engineering GmbH.

## Appendix

### A – Adaption of kinetic model by Rönsch [34]

In Eq. 26 and Eq. 27 the reaction rates of CO methanation and rWGS reaction based on the two-step kinetic approach by Rönsch [34] in the form presented in Gruber [7] are listed. In Eq. 28 and Eq. 29 the principle approach to calculate the kinetic rate coefficients via an Arrhenius type equation and the adsorption constants via the Van't Hoff type relation are given. Furthermore, the explicit formal kinetic rate coefficients (Eq. 30 to Eq. 32) and adsorption constants (Eq. 33 to Eq. 38) according to Rönsch [34] are listed. Two different kinetic rate coefficients for the CO methanation were given, one valid for a catalyst with 18% nickel (Eq. 30) and one with 50% nickel (Eq. 31).

$$r_{COM, intr} = \frac{-k_{COM} K_C K_H^2 p_{CO}^{0.5} p_{H_2} \left(1 - \frac{p_{CH_4} p_{H_2O}}{p_{CO} p_{H_2} K_{p, COM}}\right)}{(1 + K_C p_{CO}^{0.5} + K_H p_{H_2}^{0.5})^3} \left[ \frac{mol}{kg_{cat} s} \right] \quad (26)$$

$$r_{rWGS, intr} = \frac{\frac{k_{rWGS}}{p_{H_2}} p_{CO} p_{H_2} \left(1 - \frac{p_{H_2} p_{CO_2}}{p_{CO} p_{H_2O} K_{p, rWGS}}\right)}{(1 + K_{CO} p_{CO} + K_{H_2} p_{H_2} + K_{CH_4} p_{CH_4} + K_{H_2O} \frac{p_{H_2O}}{p_{H_2}})^2} \left[ \frac{mol}{kg_{cat} s} \right] \quad (27)$$

$$k_j = k_j^0 \cdot \exp\left(-\frac{E_{A,j}}{R T}\right) \quad (28)$$

$$K_i = K_i^0 \cdot \exp\left(-\frac{\Delta H_{ads,i}}{R T}\right) \quad (29)$$

$$k_{COM,18\%Ni} = \frac{35}{18} \cdot 10^{10} \cdot \exp\left(-\frac{10300[J mol^{-1}]}{R T}\right) \left[ mol kg_{cat}^{-1} s^{-1} \right] \quad (30)$$

$$k_{COM,50\%Ni} = \frac{4.8}{3.6} \cdot 10^9 \cdot \exp\left(-\frac{10300[J mol^{-1}]}{R T}\right) \left[ mol kg_{cat}^{-1} s^{-1} \right] \quad (31)$$

$$k_{rWGS} = \frac{87}{40} \cdot 10^6 \cdot \exp\left(-\frac{62000[J mol^{-1}]}{R T}\right) \left[ mol kg_{cat}^{-1} s^{-1} \right] \quad (32)$$

$$K_C = 5.8 \cdot 10^{-4} \cdot \exp\left(\frac{42000[J mol^{-1}]}{R T}\right) \left[ bar^{-0.5} \right] \quad (33)$$

$$K_H = 1.6 \cdot 10^{-2} \cdot \exp\left(\frac{16000[J mol^{-1}]}{R T}\right) \left[ bar^{-0.5} \right] \quad (34)$$

$$K_{CO} = 8.23 \cdot 10^{-5} \cdot \exp\left(\frac{70650[J mol^{-1}]}{R T}\right) \left[ bar^{-1} \right] \quad (35)$$

$$K_{H_2} = 6.12 \cdot 10^{-9} \cdot \exp\left(\frac{82900[J mol^{-1}]}{R T}\right) \left[ bar^{-1} \right] \quad (36)$$

$$K_{CH_4} = 6.65 \cdot 10^{-4} \cdot \exp\left(\frac{38280[J mol^{-1}]}{R T}\right) \left[ bar^{-1} \right] \quad (37)$$

$$K_{H_2O} = 1.77 \cdot 10^5 \cdot \exp\left(-\frac{88680[J mol^{-1}]}{R T}\right) \left[ - \right] \quad (38)$$

In Eq. 39 and Eq. 40 the used approximations for the partial pressure based equilibrium constants for CO methanation and rWGS according to Elnashaie and Elshishini [46] are given.

$$K_{p,COM} = \frac{1}{1.026676 \cdot 10^{10}} \cdot \exp\left(-\frac{26830}{T - 30.11}\right) \quad (39)$$

$$K_{p,rWGS} = \exp\left(-\frac{4400}{T - 4.063}\right) \quad (40)$$

For the PFR model used in this study the calculation of the kinetic rate coefficient of the CO methanation  $k_{COM}$  (Eq. 41) and the adsorption constant for  $H_2O$  of the rWGS reaction  $K_{H_2O}$  (Eq. 42) were adapted.

$$k_{COM,adapted} = 4.1632 \cdot 10^9 \cdot \exp\left(-\frac{10300[J mol^{-1}]}{R T}\right) \left[ mol kg_{cat}^{-1} s^{-1} \right] \quad (41)$$

$$K_{H_2O,adapted} = 1.77 \cdot 10^5 \cdot \exp\left(-\frac{88680 \cdot 0.63[J mol^{-1}]}{R T}\right) \left[ - \right] \quad (42)$$

For the calculation of  $k_{COM}$  the pre-exponential factor  $k_{COM}^0$  was interpolated between the provided value for 18% (Eqs. 30) and 50% Nickel (Eq. 31). This adaption was performed to correct the amount of available catalytically active sites in a proportional manner for the used Meth134 catalyst with about 22% Nickel (in an activated state) (Eq. 41).

The aim of the adaption of  $K_{H_2O}$  through adjusting the adsorption enthalpy  $\Delta H_{ads,H_2O}$  from 88,680 kJ mol<sup>-1</sup> K<sup>-1</sup> to 55,868 kJ mol<sup>-1</sup> K<sup>-1</sup> was to increase the inhibition by formed water of the reverse water gas shift reaction. A similar strategy was pursued by Gruber [7], who also fitted the formal adaption constant for water of a CO<sub>2</sub> methanation kinetic given by Koschany [47] to the experimental data. A significant inhibition by formed water was also found by Hubble [48] and Yang Lim [49]. Hubble [48] shows that a single LHHW kinetic approach, representing one limiting reaction step, is likely not sufficient to describe the methanation reaction over a wide range of conversion. He states that a LHHW approach might be a mathematical simplification of the complex reaction process. With regard to these literature findings, the exact description of methanation reaction rates appears far from completed. Therefore, with the conducted numerical adaptions we aimed to contribute to an improvement of the existing empirically found formal methanation kinetics based on the broad experimental results of this study. In Fig. 8 for the example case of 10,000 h<sup>-1</sup> and 6 bar the temperature and mole fractions profiles are shown with and without adapted H<sub>2</sub>O adsorption constant equation.

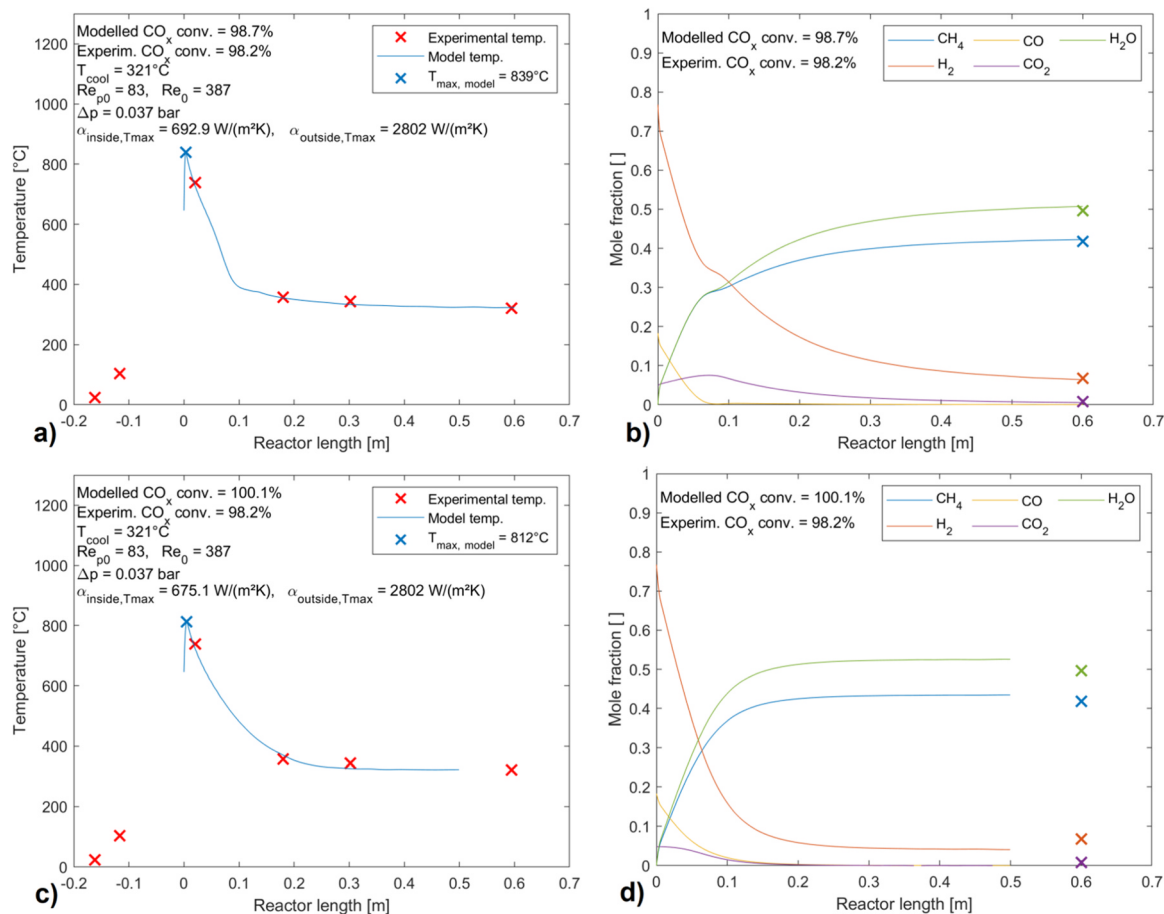


**Fig. 8.** Axial profiles of modelled (lines) and experimentally determined ('x'-markings) temperature and molar fractions of the 14 mm in diameter, 600 mm long reactor at 10000 h<sup>-1</sup> and 6 bar with (a and b) and without (c and d) kinetic model adaption (CO<sub>x</sub> conversions, Reynolds numbers, heat transfer coefficients and maximum temperature (blue 'x'-marking) included).

From the mole fraction profiles in Fig. 8d can be drawn, if the original kinetic coefficients of Rönsch [34] are used, the reverse water gas shift reaction consuming CO<sub>2</sub> is active at any point of the reactor. CO<sub>2</sub> is fully consumed at about 0.5 m upstream of the end of the reaction zone. As a result, at this point the modelling algorithm stopped and no further data was calculated. On the other hand, in Fig. 8b the mole fraction curves obtained with adapted kinetics show different reaction behaviour. As discussed in chapter "Results and Discussion", in the first 8 mm of the reaction zone the water gas shift reaction is dominating, subsequently the reaction direction is changed to the reverse water gas shift reaction transforming CO<sub>2</sub> to CO. The remaining amounts of CO<sub>2</sub> and accordingly higher fractions H<sub>2</sub> left in the product gas throughout all examined cases with varying parameter settings are well confirmed by the experimental results. With the naturally cooled reactor at low pressure of 1.3 bar at 12,000 h<sup>-1</sup> even more CO<sub>2</sub> was found in the product (6.9 vol.-%) than was injected in the educt (4.9 vol.-%), proving that in this case the CO<sub>2</sub> producing water gas shift reaction was active. In conclusion, the chosen adaption of the rWGS kinetic is supported by the experimental findings, however further examinations of dependencies based on the experimental findings would be necessary to confirm or further improve the given LHHW kinetic approach.

#### B – Comparison of 14 mm and 10 mm diameter reactors at 100,000 h<sup>-1</sup> and 4 bar

As already discussed, the model and experiments show that an increase in GHSV can be used to tune the maximum reactor temperature. However, GHSV increase also results in a severe increase of pressure loss. Therefore, a reduction in diameter is an alternative approach to achieve higher radial cooling. The axial temperature and mole fraction profiles for 14 mm and 10 mm reactors at equal process conditions are shown in Fig. 9. The cooling oil volume flow was increased to further reduce heat transfer limitation at the outer reactor surface in this investigation.

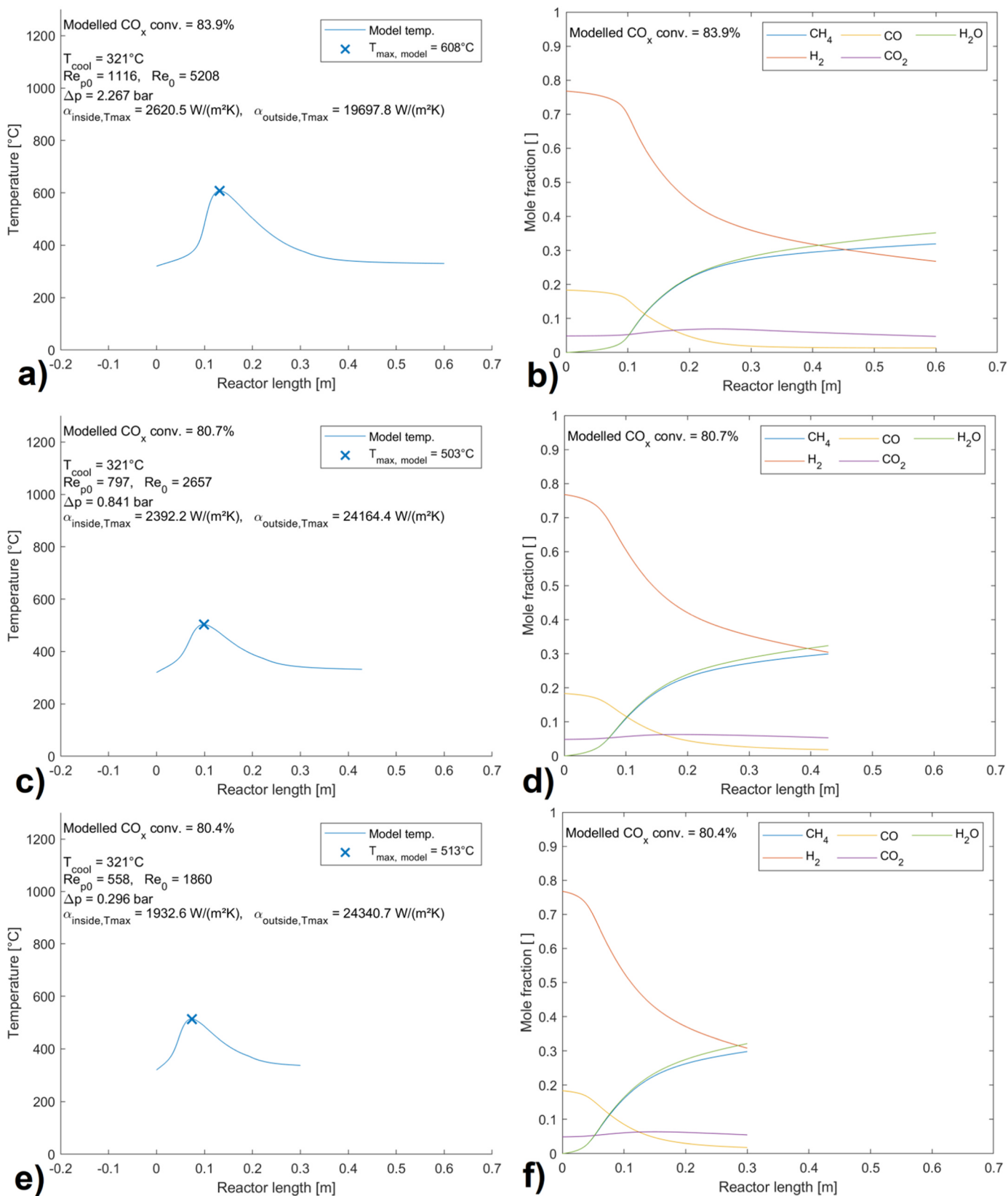


Fig. 9. Axial profiles of modelled temperature and molar fractions of the 14 mm diameter, 600 mm long reactor at 100.000 h<sup>-1</sup> and 4 bar (a and b) in comparison to a 10 mm diameter reactor with 429 mm (c and d) and 300 mm (e and f) length at the same GHSV and pressure (CO<sub>x</sub> conversions, Reynolds numbers, heat transfer coefficients and maximum temperature (blue 'x'-marking) included).

A reduction in diameter increases radial heat transfer at constant GHSV. At the same time the necessary reactor length can be reduced to achieve similar conversion at a constant diameter-length ratio consistent with geometric similarity [50], which results in lower absolute gas velocities and

therefore less pressure loss (at a constant catalyst particle diameter of 3 mm as in this case). In Fig. 9c and Fig. 9 d the reactor diameter reduction from 14 mm to 10 mm at a constant GHSV of 100,000 h<sup>-1</sup>, constant diameter/length ratio and 4 bar results in a lower maximum temperature (503 °C vs. 608 °C) and almost the same CO<sub>x</sub> conversions (80.7% vs. 83.9%). The reactor length at 10 mm diameter was further reduced to 300 mm length for even lower pressure loss, without a significant decrease of performance (Fig. 9 e and Fig. 9 f). Due to a lower absolute volume flow in the shorter reactor at constant GHSV the maximum temperature is slightly higher (513 °C) and the conversion almost equal (80.4%). The pressure loss could be reduced from 0.84 to 0.3 bar in the shorter 10 mm reactor.

### C – Packed bed quality and flow characteristics assessment in 14 mm tubular reactors

A catalytic fixed bed reactor must follow fundamental bed-scale quality principles to ensure relevance for industrial application. The strong exothermic behaviour of the CO/CO<sub>2</sub> methanation requires very small reactor diameters and relatively large catalyst particles, to enable highest radial heat transport rates at acceptable pressure loss. Therefore, the deviation from ideal plug-flow will be estimated to assess the quality of the packed bed characteristics in regard to industrial application. High radial gradients in porosity can result in near-wall gas channelling. Axial dispersion can lead to a spread in residence time at low gas velocities. For radial uniformity in bed porosity and therefore gas velocity the  $d_{r,i}/d_p$  ratio is determining. To prevent axial dispersion the  $L/d_{r,i}$  ratio is relevant. [24–26,33].

According to Andriago [26] the  $d_{r,i}/d_p$  ratio of packed beds should be 8 to 50, however to reduce the hot spot tendency through high radial heat transfer extreme values of 4 to 5 are possible. Sie [24] argues, that the traditional rule of thumb of at least 10 [25] for the  $d_{r,i}/d_p$  ratio is not valid, because the beneficial effects of radial dispersion of gas in a packed bed reduces the effect of a radial velocity profile. As a result, tube-to-particle ratios of 5 or smaller may still meet plug-flow conditions due to nullification of wall-effects by radial dispersion. For the presented reactor system with 14 mm diameter and estimated 3 mm pellet diameter used for modelling the tube-particle ratio is 4.7. The suggested reduction in reactor diameter to 10 mm at a constant pellet size for improved process performance results in a  $d_{r,i}/d_p$  ratio of 3.3.

The porosity of extended packed beds of monodisperse spheres is between 0.36 and 0.42, the porosity of polydisperse beds is lower and can be calculated according to Eq. 43 and Eq. 44 [38].

$$\varepsilon_{pd \text{ bed}} = \varepsilon_{bed,\infty} (-0.112\zeta^3 + 0.017\zeta^2 - 0.259\zeta + 1) \quad (43)$$

$$\zeta = \left( \frac{\sum Q_k/d_k^2}{(\sum Q_k/d_k)^2} - 1 \right)^{0.5} \quad (44)$$

A simple size distribution investigation of the sieved catalyst material was conducted by manual measurement with a slide gauge. The results of the size distribution measurement of a sample of 100 pellets revealed, that about 90 w.-% of the material is between 3.5 mm and 4 mm, and 10 w.-% is between 3 mm and 4 mm. Based on Eq. 44 and Eq. 45 a global polydisperse porosity of 0.395 with an estimated monodisperse porosity of 0.4 was computed. As a result, a significant polydispersity cannot be derived.

Giese [51] investigated the radial distribution of monodisperse sphericals in pipes, which was found to be similar for non-spherical and polydisperse pellet beds in cylindrical pipes. According to findings of Giese [51] the radial porosity distribution can be estimated based on the empirical exponential method shown in Eq. 45 with limited influence of non-sphericity or polydispersity.

$$\varepsilon_{bed(r)} = \varepsilon_{bed,\infty} \left( 1 + 1.36 \exp \left( -5 \frac{R_r - r_r}{d_p} \right) \right) \quad (45)$$

Contrary to Gieses findings, Schulze [52] investigated the porosity and flow distribution in polydisperse packed bed via the discrete elements method and found the gas velocity close to the tube wall increases by roughly 25% for polydisperse beds (largest-to-smallest pellet diameter ratio 2, 5 and 10) in comparison to monodisperse beds. In addition, the sinusoidal behaviour, which can be found in monodisperse beds, is significantly suppressed with increasing polydispersity. [38,52].

In a more recent CFD-based study Eppinger [53] investigated random packed beds generated by DEM-code with low diameter ratios ( $3 < d_{r,i}/d_p < 10$ ). The author showed that the existing empirical method for the global porosity by Dixon [54] (Eq. 46) and the local porosity calculation by de Klerk [55] for low diameter-ratio reactors are in very good accordance to the DEM-based data. De Klerk established two correlations in dependence of the normalized wall distance (Eq. 49), one for  $z \leq 0.367$  (Eq. 47) and one for  $z > 0.367$  (Eq. 48).

$$\varepsilon_{bed,\infty} = 0.4 + 0.05 \left( \frac{d_p}{d_{r,i}} \right) + 0.412 \left( \frac{d_p}{d_{r,i}} \right)^2 \quad (46)$$

$$\varepsilon_{bed(r),z \leq 0.637} = 2.14z^2 - 2.53z + 1 \quad (47)$$

$$\varepsilon_{bed(r),z > 0.637} = \varepsilon_{bed,\infty} + 0.29 \exp(-0.6z) \cdot [\cos(2.3\pi(z - 0.16))] + 0.15 \exp(-0.9z) \quad (48)$$

$$z = \frac{R_r - r_r}{d_p} \quad (49)$$

In Fig. 10 the radial porosity profiles for the 14 mm and 10 mm packed bed with 3 mm particle diameter according to methods by Giese [51] and de Klerk [55] are presented.

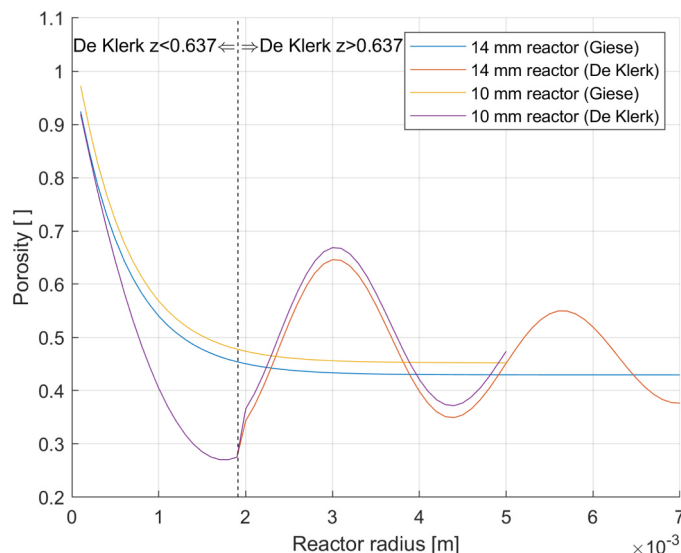


Fig. 10. Radial porosity distribution of 14 mm and 10 mm diameter reactors based on empirical methods by Giese [51] and de Klerk [55] (reactor radius is 0 at the reactor wall).

Eppinger [53] reported very good accordance of Eq. 49 with the data acquired by the DEM method with the exception, that for a very low  $d_{r,i}/d_p$  ratio of 4 the porosity rises to roughly 0.8 at about two pellet diameters distance from the tube wall. As a result, a channel is formed in the central axis of the packed bed. This effect likely occurs in the analysed 10 mm and also 14 mm reactors.

Eppinger [53] found gas channelling behaviour for all investigated diameter ratios between 4 and 10. For example, he found that the gas velocity locally increases to a factor of 11 compared to the average inlet velocity for  $Re_p = 100$  and  $d_{r,i}/d_p = 7$ . On the other hand, in dense areas within the packed bed the velocity can tend to zero or even backflow occurs. The backflow effect increases with increasing Reynolds number. For laminar flow ( $Re=1$ ), transitional flow ( $Re=100$ ) and turbulent flow ( $Re=1000$ ) the area with axial velocity equal to or smaller than zero accounts for 1%, 11% and 12.5% ( $d_{r,i}/d_p = 6$ ).

In conclusion, perfect plug-flow did most certainly not occur under the used experimental condition in the 14 mm reactors. Considering the 8 thermocouples of different length gas channelling likely occurred. Furthermore, a strong indication for high fluctuation of porosity is given. However, also at higher reactor diameter and reactor-pellet diameter ratios similar problems, such as porosity distribution and backflow were reported. Small reactor diameters (and small diameter ratios of approximately 3 or lower) in industrial [29,31,40] and experimental [27,28] applications were successfully realized. The strong need for temperature reduction by a reduced reactor diameter still may outweigh the decreasing conformity to ideal plug-flow. The presented good accordance of the modelled and experimental results speaks for sufficient representation by ideal plug-flow. For very exact results including back-flow and detailed porosity distribution, at least a 2D model based on DEM would be necessary.

#### D – Thermodynamic limitation analysis based on driving force

The ‘driving force’ as given in Eq. 50 is a term of the CO methanation reaction rate formulation (Eq. 26) and represents the deviation from thermodynamic equilibrium. The driving force term is a function of partial pressures and equilibrium constant (Eq. 39).

$$\left(1 - \frac{p_{CH_4} p_{H_2O}}{p_{CO} p_{H_2}^3 K_{p,COM}}\right) \quad (50)$$

The thermodynamic equilibrium is reached if the driving force equals 1. With higher deviation from 1, the gap from equilibrium concentration increases for the given gas mixture. The driving force of the CO methanation reaction was calculated along with the axial mole fraction profiles at 6 bar and  $10,000 \text{ h}^{-1}$  in the 14 mm diameter and 600 mm long oil-cooled reactor in Fig. 11. While the driving force within the initial 8 mm of reactor length indicates no thermodynamic limitation, it tends to 1 as the CO concentration approaches full consumption. However, the limiting factor for the CO methanation step most likely is the lack of CO. As a result, the overall process is limited in a short initial section by CO methanation kinetics, followed by a limitation of CO production by the rWGS reaction starting from the point of full CO consumption.

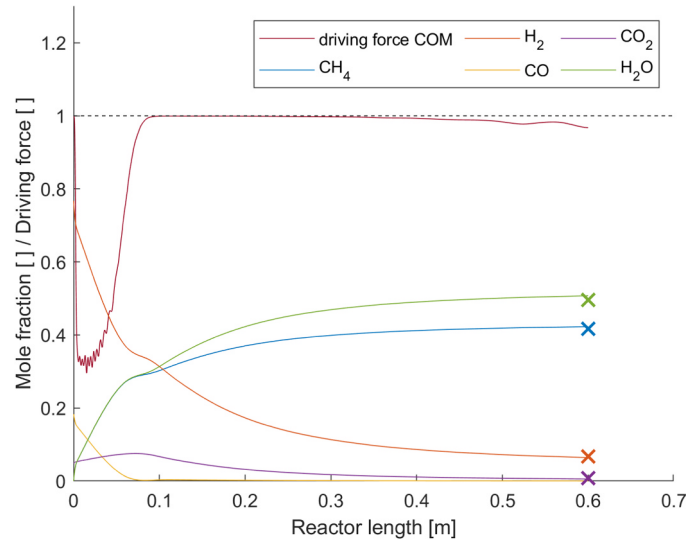


Fig. 11. Axial mole fraction profiles of the 14 mm diameter, 600 mm long reactor including driving force of CO methanation reaction at 6 bar and 10000 h<sup>-1</sup>.

### E – Equilibrium condition assessment at reactor outlet

To verify if the equilibrium was reached at the outlet of the reactors the free reaction enthalpy at the outlet was calculated based on Eqs. 51–57 for the given outlet temperature, pressure and mole fractions for the CO<sub>2</sub> methanation reaction, the CO methanation reaction and the water gas shift reaction as shown in Table 3. The molar chemical potential  $\mu_i$  for each species  $i$  and the equilibrium composition was calculated with the “Cantera” toolbox in MATLAB. [56] For  $\Delta G_R = 0$  thermodynamic equilibrium is reached. For  $\Delta G_R < 0$  the reaction runs spontaneously from thermodynamic perspective. For  $\Delta G_R > 0$  the reverse reaction runs spontaneously at the given temperature, pressure and concentration. [57].

$$\Delta G_R = \left( \frac{dG}{d\xi} \right)_{p,T} \quad (51)$$

$$dG = \mu_{educt} dn_{educt} + \mu_{product} dn_{product} = -\mu_{educt} d\xi_{educt} + \mu_{product} d\xi_{product} \quad (52)$$

$$dG = (\mu_{product} - \mu_{educt}) d\xi_{product} \quad (53)$$

$$\left( \frac{dG}{d\xi} \right)_{p,T} = \mu_{product} - \mu_{educt} \quad (54)$$

$$\Delta G_{R,CO2M} = \mu_{CH_4} + 2\mu_{H_2O} - \mu_{CO_2} - 4\mu_{CO} \quad (55)$$

$$\Delta G_{R,COM} = \mu_{CH_4} + \mu_{H_2O} - \mu_{CO} - 3\mu_{CO_2} \quad (56)$$

$$\Delta G_{R,rWGS} = \mu_{H_2O} + \mu_{CO} - \mu_{CO_2} - \mu_{H_2} \quad (57)$$

In addition, the difference between gas concentration as measured at the outlet and its corresponding equilibrium concentration is included in Table 3. Smaller than 1 vol.-% difference between the measured and thermodynamic equilibrium was reached at higher pressures and lower GHSV, such as in reactor 2 at 6000 h<sup>-1</sup> and 6 bar and in reactor 3 at 1000 h<sup>-1</sup> and 8 bar.

**Table 3**

Gas concentration difference between measured output concentration and its chemical equilibrium and the free reaction enthalpy  $\Delta G_R$  for the CO<sub>2</sub> methanation (“CO<sub>2</sub>M”), the CO methanation (COM) and the reverse water gas shift reaction (“rWGS”) for every experimental case including the used reactor, GHSV, outlet pressure and outlet temperature value.

	GHSV [h <sup>-1</sup> ]	outlet pressure [bar]	outlet temp. [°C]	Difference of product gas concentration to equilibrium concentration [vol.-%]					$\Delta G_{R, CO2M}$ [J/kmol]	$\Delta G_{R, COM}$ [J/kmol]	$\Delta G_{R, rWGS}$ [J/kmol]
				CH <sub>4</sub>	H <sub>2</sub>	CO	CO <sub>2</sub>	H <sub>2</sub> O			
<b>Reactor 1, 840 mm length, 14 mm diameter, air-cooled</b>	4000	1.0	34	6.73	-14.14	0.00	-3.61	11.02	-1.24E+ 08	8.08E+ 08	-9.32E+ 08
	6000	1.3	87	5.00	-10.26	0.00	-2.75	8.02	-1.23E+ 08	8.92E+ 08	-1.01E+ 09
	8000	1.1	45	10.83	-22.36	-0.08	-5.52	17.14	-9.63E+ 07	-1.15E+ 08	1.84E+ 07
	6000	1.3	101	14.66	-29.65	-0.75	-6.86	22.62	-7.52E+ 07	-8.99E+ 07	1.48E+ 07
	4000	2.2	29	6.19	-12.92	0.00	-3.27	10.00	-1.05E+ 08	1.35E+ 09	-1.46E+ 09
	6000	4.1	76	3.22	-6.76	0.00	-1.72	5.25	-1.33E+ 08	5.12E+ 08	-6.45E+ 08
	8000	4.0	156	4.22	-8.83	0.00	-2.25	6.86	-1.11E+ 08	1.18E+ 09	-1.29E+ 09

(continued on next page)



Table 3 (continued)

	GHSV [h <sup>-1</sup> ]	outlet pressure [bar]	outlet temp. [°C]	Difference of product gas concentration to equilibrium concentration [vol.-%]					$\Delta G_{R, CO2M}$ [J/kmol]	$\Delta G_{R, COM}$ [J/kmol]	$\Delta G_{R, rWS}$ [J/kmol]
				CH <sub>4</sub>	H <sub>2</sub>	CO	CO <sub>2</sub>	H <sub>2</sub> O			
Reactor 2, 700 mm length, 14 mm diameter, oil-cooled, no preheating zone	12,000	4.2	322	7.40	-15.30	-0.14	-3.77	11.82	-7.64E+07	-9.15E+07	1.52E+07
	6000	6.1	75	2.47	-5.18	0.00	-1.33	4.04	-1.31E+08	5.86E+08	-7.17E+08
	8000	6.1	159	2.52	-5.30	0.00	-1.36	4.14	-1.19E+08	9.53E+08	-1.07E+09
	4000	1.3	329	2.32	-4.86	0.00	-1.25	3.79	-8.12E+07	1.71E+09	-1.79E+09
	6000	1.4	332	3.25	-6.80	0.00	-1.74	5.29	-8.29E+07	1.73E+09	-1.81E+09
	8000	1.6	333	4.22	-8.79	0.00	-2.23	6.80	-8.45E+07	1.74E+09	-1.82E+09
	10,000	1.8	334	4.65	-9.71	0.00	-2.47	7.52	-8.63E+07	1.74E+09	-1.82E+09
	12,000	1.9	334	5.03	-10.51	0.00	-2.67	8.16	-8.74E+07	1.75E+09	-1.83E+09
	15,000	2.2	335	5.81	-12.12	-0.01	-3.06	9.38	-8.90E+07	-1.02E+08	1.32E+07
	20,000	2.6	335	6.68	-13.93	-0.02	-3.52	10.79	-9.10E+07	-1.06E+08	1.51E+07
	25,000	3.0	335	7.30	-15.22	-0.02	-3.83	11.77	-9.24E+07	-1.08E+08	1.53E+07
	29,000	3.4	336	7.75	-16.15	-0.03	-4.06	12.48	-9.32E+07	-1.09E+08	1.55E+07
	6000	4.1	325	1.10	-2.30	0.00	-0.59	1.80	-8.36E+07	1.71E+09	-1.79E+09
	8000	4.0	326	1.97	-4.12	0.00	-1.05	3.20	-8.29E+07	1.72E+09	-1.81E+09
	10,000	4.0	327	2.32	-4.86	0.00	-1.24	3.78	-8.44E+07	1.73E+09	-1.81E+09
6000	6.0	325	0.37	-0.77	0.00	-0.20	0.60	-8.18E+07	1.70E+09	-1.78E+09	
8000	5.9	325	1.30	-2.73	0.00	-0.69	2.12	-8.26E+07	1.71E+09	-1.79E+09	
10,000	6.0	326	1.47	-3.08	0.00	-0.79	2.40	-8.43E+07	1.71E+09	-1.80E+09	
12,000	5.9	327	1.71	-3.58	0.00	-0.92	2.79	-8.53E+07	1.72E+09	-1.81E+09	
15,000	6.0	328	2.28	-4.79	0.00	-1.22	3.73	-8.70E+07	1.73E+09	-1.82E+09	
20,000	6.0	330	3.25	-6.81	0.00	-1.74	5.30	-8.97E+07	1.74E+09	-1.83E+09	
25,000	6.0	331	4.20	-8.80	0.00	-2.24	6.84	-9.13E+07	1.75E+09	-1.84E+09	
29,000	5.9	333	5.07	-10.59	0.00	-2.69	8.21	-9.25E+07	1.77E+09	-1.86E+09	
Reactor 3, 600 mm length, 14 mm diameter, oil-cooled, 100 mm preheating zone	10,000	4.0	327	2.309	-4.829	0.000	-1.227	3.747	-8.39E+07	1.72E+09	-1.8E+09
	12,000	4.0	328	2.610	-5.464	0.000	-1.390	4.244	-8.51E+07	1.73E+09	-1.81E+09
	15,000	4.0	329	3.217	-6.736	0.000	-1.712	5.231	-8.64E+07	1.743E+09	-1.83E+09
	20,000	4.0	331	4.185	-8.756	0.000	-2.224	6.795	-8.84E+07	1.764E+09	-1.85E+09
	25,000	4.5	331	4.624	-9.669	0.000	-2.457	7.502	-8.97E+07	1.777E+09	-1.87E+09
	10,000	6.0	326	1.498	-3.140	0.000	-0.800	2.441	-8.33E+07	1.715E+09	-1.8E+09
	12,000	6.0	327	1.719	-3.605	0.000	-0.920	2.806	-8.45E+07	1.723E+09	-1.81E+09
	15,000	6.0	328	2.408	-5.039	0.000	-1.280	3.912	-8.58E+07	1.736E+09	-1.82E+09
	20,000	6.0	329	2.969	-6.222	0.000	-1.585	4.838	-8.79E+07	1.751E+09	-1.84E+09
	25,000	6.0	331	3.617	-7.576	0.000	-1.931	5.890	-8.93E+07	1.768E+09	-1.86E+09
	10,000	8.0	324	0.888	-1.866	0.000	-0.478	1.457	-8.35E+07	1.709E+09	-1.79E+09
	15,000	8.0	328	1.566	-3.287	0.000	-0.840	2.561	-8.54E+07	1.728E+09	-1.81E+09
	20,000	8.0	329	2.377	-4.979	0.000	-1.267	3.870	-8.73E+07	1.743E+09	-1.83E+09
	25,000	8.0	330	3.049	-6.378	0.000	-1.622	4.951	-8.90E+07	1.756E+09	-1.85E+09

## References

- [1] M. Lehner, R. Tichler, H. Steinmüller, M. Koppe, Storage options for renewable energy, in: M. Lehner, R. Tichler, H. Steinmüller, M. Koppe (Eds.), *Power-to-Gas: Technology and Business Models*, Springer International Publishing, Cham, s.l., 2014, pp. 1–6.
- [2] ENTSOG, Gas Infrastructure Europe, Hydrogen Europe, HOW TO TRANSPORT AND STORE HYDROGEN - FACTS AND FIGURES.
- [3] G.R. Tgaz, GRDF, elenegy, Geomethane, Teregea, REGAZ Bordeaux, Stroengy, R-GDS, Technical and economic conditions for injecting hydrogen into natural gas networks: Final report June 2019, 2019.
- [4] L.R. Clausen, G. Butera, S.H. Jensen, High efficiency SNG production from biomass and electricity by integrating gasification with pressurized solid oxide electrolysis cells, *Energy* 172 (2019) 1117–1131, <https://doi.org/10.1016/j.energy.2019.02.039>.
- [5] M.E. Ivanova, R. Peters, M. Müller, S. Haas, M.F. Seidler, G. Mutschke, K. Eckert, P. Röse, S. Calnan, R. Bagacki, R. Schlatmann, C. Grosseindemann, L.-A. Schäfer, N.H. Menzler, A. Weber, R. van de Krol, F. Liang, F.F. Abdi, S. Brendelberger, N. Neumann, J. Grobbel, M. Roeb, C. Sattler, I. Duran, B. Dietrich, M.E. C. Hofberger, L. Stoppel, N. Uhlenbruck, T. Wetzel, D. Rauner, A. Hecimovic, U. Fantz, N. Kulyk, J. Harting, O. Guillon, Technologische Pfade für die Herstellung von komprimiertem und hochreinem Wasserstoff mit Hilfe von Sonnenenergie, *Angew. Chem.* 135 (2023) e202218850, <https://doi.org/10.1002/ange.202218850#ange202218850-bib-0104>.
- [6] Q. Fang, C.E. Frey, N.H. Menzler, L. Blum, Electrochemical performance and preliminary post-mortem analysis of a solid oxide cell stack with 20,000h of operation, *J. Electrochem. Soc.* 165 (2018) F38–F45, <https://doi.org/10.1149/2.0541802jes>.
- [7] M. Gruber, Detailed analysis of heat and mass transfer in a packed bed methanation reactor for power to gas applications: Dissertation, Karlsruhe, 2020.
- [8] S. Rönch, J. Schneider, S. Matthischke, M. Schlüter, M. Götz, J. Lefebvre, P. Prabhakaran, S. Bajohr, Review on methanation – from fundamentals to current projects, *Fuel* 166 (2016) 276–296, <https://doi.org/10.1016/j.fuel.2015.10.111>.
- [9] A. Krammer, M. Peham, M. Lehner, 2D heterogeneous model of a polytropic methanation reactor, *J. CO<sub>2</sub> Util.* 62 (2022) 102059, <https://doi.org/10.1016/j.jcou.2022.102059>.
- [10] A. Krammer, A. Medved, M. Peham, P. Wolf-Zöllner, K. Salbrechter, M. Lehner, Dual pressure level methanation of Co-SOEC Syngas, *Energy Technol.* 202 (2020) 2000746, <https://doi.org/10.1002/ente.202000746>.
- [11] J. Ducamp, A. Bengaouer, P. Baurens, Modelling and experimental validation of a CO<sub>2</sub> methanation annular cooled fixed-bed reactor exchanger, *Can. J. Chem. Eng.* 95 (2017) 241–252, <https://doi.org/10.1002/cjce.22706>.
- [12] R. Try, A. Bengaouer, P. Baurens, C. Jallut, Dynamic modeling and simulations of the behavior of a fixed-bed reactor-exchanger used for CO<sub>2</sub> methanation, *AIChE J.* 64 (2018) 468–480, <https://doi.org/10.1002/aic.15874>.
- [13] L. Kiewidt, J. Thöming, Predicting optimal temperature profiles in single-stage fixed-bed reactors for CO<sub>2</sub>-methanation, *Chem. Eng. Sci.* 132 (2015) 59–71, <https://doi.org/10.1016/j.ces.2015.03.068>.
- [14] F. Vidal Vázquez, J. Kihlman, A. Mylvaganam, P. Simell, M.-L. Koskinen-Soivi, V. Alopaeus, Modeling of nickel-based hydroxalcalite catalyst coated on heat exchanger reactors for CO<sub>2</sub> methanation, *Chem. Eng. J.* 349 (2018) 694–707, <https://doi.org/10.1016/j.cej.2018.05.119>.
- [15] J. Lefebvre, S. Bajohr, T. Kolb, Modeling of the transient behavior of a slurry bubble column reactor for CO<sub>2</sub> methanation, and comparison with a tube bundle reactor, *Renew. Energy* 151 (2020) 118–136, <https://doi.org/10.1016/j.renene.2019.11.008>.
- [16] D. Schlereth, O. Hinrichsen, A fixed-bed reactor modeling study on the methanation of CO<sub>2</sub>, *Chem. Eng. Res. Des.* 92 (2014) 702–712, <https://doi.org/10.1016/j.chemd.2013.11.014>.
- [17] D. Sun, D.S. Simakov, Thermal management of a Sabatier reactor for CO<sub>2</sub> conversion into CH<sub>4</sub>: Simulation-based analysis, *J. CO<sub>2</sub> Util.* 21 (2017) 368–382, <https://doi.org/10.1016/j.jcou.2017.07.015>.
- [18] B. Kreitz, G. Wehinger, T. Turek, Dynamic simulation of the CO<sub>2</sub> methanation in a micro-structured fixed-bed reactor, *Chem. Eng. Sci.* 195 (2019) 541–552, <https://doi.org/10.1016/j.ces.2018.09.053>.
- [19] N. Engelbrecht, S. Chiuta, R.C. Everson, H.W. Neomagus, D.G. Bessarabov, Experimentation and CFD modelling of a microchannel reactor for carbon dioxide methanation, *Chem. Eng. J.* 313 (2017) 847–857, <https://doi.org/10.1016/j.cej.2016.10.131>.

- [20] D.L. Reddy, D. Lokhat, H. Siddiqi, B.C. Meikap, Modelling and simulating CO and CO<sub>2</sub> methanation over Ru/ $\gamma$ -Al<sub>2</sub>O<sub>3</sub> catalyst: An integrated approach from carbon capture to renewable energy generation, *Fuel* 314 (2022) 123095, <https://doi.org/10.1016/j.fuel.2021.123095>.
- [21] S. Matthischke, S. Roensch, R. Güttel, Start-up time and load range for the methanation of carbon dioxide in a fixed-bed recycle reactor, *Ind. Eng. Chem. Res.* 57 (2018) 6391–6400, <https://doi.org/10.1021/acs.iecr.8b00755>.
- [22] A.R. Medved, M. Lehner, D.C. Rosenfeld, J. Lindorfer, K. Rechberger, Enrichment of integrated steel plant process gases with implementation of renewable energy, *Johns. Matthey Technol. Rev.* (2021), <https://doi.org/10.1595/205651321X16161444481140>.
- [23] A. El Sibai, L.K. Rihko Struckmann, K. Sundmacher, Model-based optimal sabatier reactor design for power-to-gas applications, *Energy Technol.* 5 (2017) 911–921, <https://doi.org/10.1002/ente.201600600>.
- [24] S.T. Sie, Advantages, possibilities, and limitations of small-scale testing of catalysts for fixed-bed processes, in: P. O'Connor, T. Takatsuka, G.L. Woolery (Eds.), *Deactivation and Testing of Hydrocarbon-Processing Catalysts*, American Chemical Society, Washington, DC, 1996, pp. 6–41.
- [25] A. Jess, P. Wasserscheid. *Chemical Technology: From Principles to Products*, Second ed., Wiley-VCH, Weinheim, 2020.
- [26] P. Andriago, Fixed bed reactors, *Catal. Today* 52 (1999) 197–221, [https://doi.org/10.1016/S0920-5861\(99\)00076-0](https://doi.org/10.1016/S0920-5861(99)00076-0).
- [27] Johanna Fernengel, From Packing Generation to Single Pellet String Reactor Characteristics: A Numerical Approach to Fixed-Bed Reactors. Dissertation, München, 2022.
- [28] H.M. Bui, P.F. Großmann, T. Gros, M. Blum, A. Berger, R. Fischer, N. Szesni, M. Tonigold, O. Hinrichsen, 3D printed co-precipitated Ni-Al CO<sub>2</sub> methanation catalysts by Binder Jetting: Fabrication, characterization and test in a single pellet string reactor, *Appl. Catal. A: Gen.* 643 (2022) 118760, <https://doi.org/10.1016/j.apcata.2022.118760>.
- [29] L.S. Kershenbaum, F. Lopez-Isunza, Dynamic behavior of an industrial scale fixed-bed catalytic reactor, in: P. O'Connor, T. Takatsuka, G.L. Woolery (Eds.), *Deactivation and Testing of Hydrocarbon-Processing Catalysts*, American Chemical Society, Washington, DC, 1996, pp. 109–120.
- [30] M. Müller, M. Kutscherauer, S. Böcklein, G.D. Wehinger, T. Turek, G. Mestl, Modeling the selective oxidation of n-butane to maleic anhydride: From active site to industrial reactor, *Catal. Today* 387 (2022) 82–106, <https://doi.org/10.1016/j.cattod.2021.04.009>.
- [31] G. Che-Galicia, R.S. Ruiz-Martínez, F. López-Isunza, C.O. Castillo-Araiza, Modeling of oxidative dehydrogenation of ethane to ethylene on a MoVTeNbO/TiO<sub>2</sub> catalyst in an industrial-scale packed bed catalytic reactor, *Chem. Eng. J.* 280 (2015) 682–694, <https://doi.org/10.1016/j.cej.2015.05.128>.
- [32] H. Gierman, Design of laboratory hydrotreating reactors, *Appl. Catal.* 43 (1988) 277–286, [https://doi.org/10.1016/S0166-9834\(00\)82732-3](https://doi.org/10.1016/S0166-9834(00)82732-3).
- [33] D.A. Hickman, J.C. Degenstein, F.H. Ribeiro, Fundamental principles of laboratory fixed bed reactor design, *Curr. Opin. Chem. Eng.* 13 (2016) 1–9, <https://doi.org/10.1016/j.coche.2016.07.002>.
- [34] S. Rönisch, J. Köchermann, J. Schneider, S. Matthischke, Global reaction kinetics of CO and CO<sub>2</sub> methanation for dynamic process modeling, *Chem. Eng. Technol.* 39 (2016) 208–218, <https://doi.org/10.1002/ceat.201500327>.
- [35] V. Specchia, G. Baldi, S. Sicardi, Heat transfer in packed bed reactors with one phase flow, *Chem. Eng. Commun.* 4 (1980) 361–380, <https://doi.org/10.1080/00986448008935916>.
- [36] V. Gnielinski, Heat transfer coefficients for turbulent flow in concentric annular ducts, *Heat. Transf. Eng.* 30 (2009) 431–436, <https://doi.org/10.1080/01457630802528661>.
- [37] ISO International Organization for Standardization, *Thermal insulation for building equipment and industrial installations — Calculation rules*, 2nd ed. 91.120.10, 2008.
- [38] VDI-Wärmeatlas, 11th ed., Springer Berlin Heidelberg, Berlin, Heidelberg, 2013.
- [39] Karl-Ernst Wirth, *Druckverlust in durchströmten Schüttungen (eleventh)*, VDI-Wärmeatlas, Springer Berlin Heidelberg, Berlin, Heidelberg, 2013, pp. 1275–1279 (eleventh).
- [40] G.F. Froment, K.B. Bischoff, J. de Wilde, *Chemical reactor analysis and design (third. ed.)*, Wiley, Hoboken, NJ, 2011.
- [41] ÖVGW, Richtlin. G B210: Gasbeschaffenheit 75 (2021) 060.
- [42] D.B. Pal, R. Chand, S.N. Upadhyay, P.K. Mishra, Performance of water gas shift reaction catalysts: A review, *Renew. Sustain. Energy Rev.* 93 (2018) 549–565, <https://doi.org/10.1016/j.rser.2018.05.003>.
- [43] C. Ratnasamy, J.P. Wagner, Water Gas Shift Catalysis, *Catal. Rev.* 51 (2009) 325–440, <https://doi.org/10.1080/01614940903048661>.
- [44] H. Böhm, M. Lehner, T. Kienberger, Techno-economic assessment of thermally integrated co-electrolysis and methanation for industrial closed carbon cycles, *Front. Sustain.* 2 (2021) 726332, <https://doi.org/10.3389/frsus.2021.726332>.
- [45] T. Nguyen, L. Wissing, M.S. Skjøth-Rasmussen, High temperature methanation: catalyst considerations, *Catal. Today* 215 (2013) 233–238, <https://doi.org/10.1016/j.cattod.2013.03.035>.
- [46] S. Elnashaie, S.S. Elshishini, Modelling, simulation and optimization of industrial fixed bed catalytic reactors, Gordon and Breach, Philadelphia, Pa., 1993.
- [47] F. Koschany, D. Schlereth, O. Hinrichsen, On the kinetics of the methanation of carbon dioxide on coprecipitated NiAl(O)<sub>x</sub>, *Appl. Catal. B: Environ.* 181 (2016) 504–516, <https://doi.org/10.1016/j.apcatb.2015.07.026>.
- [48] R. Hubble, *Studies of Carbon Dioxide Methanation and Related Phenomena in Porous Catalysts*, 2019.
- [49] J. Yang Lim, J. McGregor, A.J. Sederman, J.S. Dennis, Kinetic studies of CO<sub>2</sub> methanation over a Ni/ $\gamma$ -Al<sub>2</sub>O<sub>3</sub> catalyst using a batch reactor, *Chem. Eng. Sci.* 141 (2016) 28–45, <https://doi.org/10.1016/j.ces.2015.10.026>.
- [50] M. Zlokarnik, *Scale-up in chemical engineering, first. ed.*, Wiley-VCH, Weinheim, 2002.
- [51] M. Giese, K. Rottschäfer, D. Vortmeyer, Measured and modeled superficial flow profiles in packed beds with liquid flow, *AIChE J.* 44 (1998) 484–490, <https://doi.org/10.1002/aic.690440225>.
- [52] S. Schulze, P.A. Nikrityuk, B. Meyer, Porosity distribution in monodisperse and polydisperse fixed beds and its impact on the fluid flow, *Part. Sci. Technol.* 33 (2015) 23–33, <https://doi.org/10.1080/02726351.2014.923960>.
- [53] T. Eppinger, K. Seidler, M. Kraume, DEM-CFD simulations of fixed bed reactors with small tube to particle diameter ratios, *Chem. Eng. J.* 166 (2011) 324–331, <https://doi.org/10.1016/j.cej.2010.10.053>.
- [54] A.G. Dixon, Correlations for wall and particle shape effects on fixed bed bulk voidage, *Can. J. Chem. Eng.* 66 (1988) 705–708, <https://doi.org/10.1002/cjce.5450660501>.
- [55] A. de Klerk, Voidage variation in packed beds at small column to particle diameter ratio, *AIChE J.* 49 (2003) 2022–2029, <https://doi.org/10.1002/aic.690490812>.
- [56] D.G. Goodwin, H.K. Moffat, I. Schoegl, R.L. Speth, B.W. Weber, *Cantera: an object-oriented software toolkit for chemical kinetics, Thermodyn., Transp. Process., Zenodo* (2023).
- [57] P.W. Atkins, J. de Paula, J.J. Keeler, *Physikalische Chemie, sixth ed., Auflage* Wiley-VCH, Weinheim, 2022.

### 3.3 Plant level optimization concept for the methanation of Co-SOEC syngas for higher overall efficiency

#### Scientific article III – “Dual Pressure Level Methanation of Co-SOEC Syngas”

A. Krammer, A. Medved, M. Peham, P. Wolf-Zöllner, K. Salbrechter, M. Lehner, Dual Pressure Level Methanation of Co-SOEC Syngas, Energy Technol. 202 (2020) 2000746. <https://doi.org/10.1002/ente.202000746>.

#### Personal contribution statement:

The personal contribution to this scientific work account for the vast effort including the idea formulation, methodology, mass and energy balance calculation, experimental analysis, the validation of data and writing of the original draft. Markus Lehner supervised this work, provided resources including funding provision and reviewed and edited the written paper. The remaining authors contributed to the experimental tasks and provided assistance in reviewing the paper.

# Dual Pressure Level Methanation of Co-SOEC Syngas

Andreas Krammer,\* Ana Medved, Martin Peham, Philipp Wolf-Zöllner, Katrin Salbrechter, and Markus Lehner

The objective of this article is to demonstrate significant efficiency and performance improvements by simple process modifications of a power to gas plant consisting of high-temperature coelectrolysis and catalytic methanation. For the advanced process design dual step methanation with two different pressure levels including intermediate compression is proposed, leading to several advantages. By experimental investigations on a lab-scale methanation test plant higher turnovers (increase of up to 7.1 percentage points) and lower temperature peaks (decrease by up to 130 K) can be proven. Basic energy balance calculations reveal furthermore a reduction in compressor power by 42% for this proposed system.

Characteristics and functionality of available electrolysis technologies have been extensively discussed in literature.<sup>[1,2]</sup> The electrolytically sourced hydrogen can be combined with subsequent synthesis technologies to produce gaseous or liquid energy carriers and chemical feedstocks.<sup>[1]</sup> By combining electrolysis and methanation hydrogen can be converted with carbon oxides (CO, CO<sub>2</sub>) to useful synthetic natural gas (SNG). One main advantage of this concept is the seamless integration of the energy carrier SNG into the existing natural gas infrastructure, enabling the coupling of energy sectors and the chemical storage of renewable energy.<sup>[3,4]</sup>

## 1. Introduction


Decarbonization by electrification of industrial processes plays a key role on the way to successful countermeasures against anthropogenic climate change. For a successful realization of an energy revolution, two interacting aspects have to be considered. On the one hand, enormous capacities of renewable energy have to be created very rapidly. On the other hand, these large amounts of electric energy need to be integrated economically viable into existing industrial infrastructure. The development of most effective power to gas (PtG) technologies is essential to promote the necessary rapid growth of renewables and enable industrial integration.

The key part of a PtG plant consists of a water electrolysis splitting water with electric energy to hydrogen and oxygen. While especially the most mature type, the alkaline electrolysis cell (AEC), and also the proton exchange membrane (PEM) electrolysis are available on a MW scale, the high temperature solid oxide electrolysis cell (SOEC) has still development potential.<sup>[1]</sup>

The methanation step of the power-to-gas process chain can be performed either catalytically or biologically, whereas latter is not in the focus of this work.<sup>[5]</sup> Catalytic methanation can again be differentiated on a catalyst, respectively, reactor domain (fixed bed reactor/bulk catalyst, structured catalyst, microstructured catalyst, fluidized bed reactor, three-phase reactor, membrane reactor).<sup>[2,5]</sup> Whereas bulk catalysts are commercially available, recently promising developments for structured and microstructured catalysts have been made.<sup>[6–8]</sup> Microstructured catalysts are mostly designed to properly manage the high exothermic reaction heat. Nevertheless, microstructured catalytic reactors have a drawback in terms of costs if large-scale applications with tremendous capacities are aimed at, as for most industrial processes. However, if manufacturing processes such as additive manufacturing improve, this situation may change.<sup>[9]</sup> For detailed characterization of the different types of reactors, several publications provide a comprehensive overview.<sup>[2,10]</sup> For the experimental examinations of this study, a common form of catalyst, a commercial nickel-based bulk catalyst in a fixed bed reactor was used, as the investigation focus lies on a process rather than on a catalyst level.

In addition, several process concepts for catalytic methanation can be distinguished. From uncooled adiabatic reactor cascades to product recycling concepts with intermediate cooling, a decent variety of methanation concepts has been developed. A large number of catalytic methanation plants have been built in pilot scale or laboratory scale in recent years, but it is often hard to determine what exact type of system is being used.<sup>[4]</sup> Only a few concepts are commercially available or have even been realized in industrial scale, all of them being fixed bed reactors.<sup>[11,12]</sup> Whereas the commercial processes “TREMPE,” “Lurgi methanation,” and “HICOM” use product gas recycling and intermediate cooling, “Vesta” and “TREMPE modified” aim at reducing the increased effort due to recycle gas compressors.<sup>[12]</sup>

A. Krammer, A. Medved, M. Peham, P. Wolf-Zöllner, K. Salbrechter, Prof. M. Lehner  
Chair of Process Technology and Industrial Environmental Protection  
Montanuniversität Leoben  
Franz-Josef Strasse, Leoben 8700, Austria  
E-mail: andreas.krammer@unileoben.ac.at

 The ORCID identification number(s) for the author(s) of this article can be found under <https://doi.org/10.1002/ente.202000746>.

© 2020 The Authors. Energy Technology published by Wiley-VCH GmbH. This is an open access article under the terms of the Creative Commons Attribution License, which permits use, distribution and reproduction in any medium, provided the original work is properly cited.

The copyright line for this article was changed on 21 December 2020 after original online publication.

DOI: 10.1002/ente.202000746

Koytsoumpa already showed that intermediate compression of syngas between serial connected, adiabatic syngas methanation reactors can lead to a significant decrease in required compressor power.<sup>[13]</sup> The authors found that by smart positioning of the compressor between a bulk methanation reactor at 18.9 bar and a trim methanation reactor at 77.9 bar reduction of compressor power by 72% can be achieved. Koytsoumpa used thermodynamic and kinetic modeling approaches for their findings, which is certainly sufficient to prove the main concept advantage of decreased compression power. Neubert et al.<sup>[14]</sup> correctly concluded, that intermediate compression is particularly useful if the hydrogen is generated at moderate pressures. The proposed PtG concept of combined Co-SOEC and methanation with intermediate compression represents an alternative to upstream syngas compression. Two options for the pressurization of syngas and hydrogen, respectively, are available: compression within a polytropic compressor or by pressurized electrolyzers. Whereas pressurized PEM electrolysis is already widely developed,<sup>[15–20]</sup> it is not yet state of the art for (Co-)SOEC although research has strongly gained momentum in recent years.<sup>[1,21]</sup> Brabandt and Posdziech successfully tested high-pressure SOEC operation at 15 bar. The authors argue that high-pressure steam integration from industrial processes saves part of the compression energy for hydrogen, and see potential in providing hydrogen at elevated pressures for downstream processes. Furthermore, they overcame mechanical issues at high differential pressure by placing the SOEC in a pressurized vessel. However, increasing pressure led to slightly higher temperatures and voltage as experiments showed. In conclusion, Brabandt and Posdziech found that high-pressure SOEC operation is feasible and leads to 5–7% less energy consumption by saving compression energy when steam is provided at a high-pressure level, but resulted in increased heat loss, for example, due to insulation performance decrease.<sup>[22,23]</sup> Bernadet et al. investigated pressurized high-temperature coelectrolysis and found improvement of cell-limiting current densities by a decrease in electrode gas diffusion resistance at increased pressure.<sup>[24,25]</sup> Clausen et al. tested a SNG production plant including Co-SOEC at 19 bar pressure and determined that 16% of the methane was formed within the Co-SOEC. The energetically optimal combination of exothermic methanation and endothermic reduction of water and carbon dioxide leads to very promising overall efficiencies of 84%.<sup>[26]</sup> For specific high-pressure-related processes pressurized electrolysis can be more efficient regarding the overall system as Bensmann et al.<sup>[16]</sup> found, although a higher energy demand for the electrolysis itself would be the result with increasing pressure.<sup>[1,16]</sup> Nevertheless, the main reason for high-pressure electrolysis is based on the necessity of integrating the hydrogen source into high-pressure applications, such as hydrogen drying, compressed storage, pressure swing adsorption, downstream catalytic conversions, or grid injection, rather than benefits for the electrolysis system itself.<sup>[16,17]</sup> This statement applies for several types of electrolyzers, as the open-circuit voltage increases with increasing pressure according to the Nernst equation.<sup>[21]</sup> Hansen showed that increased pressure lowers the overpotential due to improved kinetics at the electrodes and reduced diffusion limitation at higher operation voltage. He states that this effect, caused by elevated pressures, decreases SOEC performance at low current densities, but improves it at higher current densities.

In contrast to experimental findings by Brabandt and Posdziech,<sup>[23]</sup> Hansen sees an improvement in heat transfer by increased operation pressure in heat exchangers.<sup>[27]</sup> Also carbon deposition must be kept in mind for pressurized coelectrolysis, as will be discussed in greater detail later in this work. Additional drawbacks by high-pressure electrolysis were found, such as increased cross permeation of hydrogen.<sup>[1]</sup> In contrast, electrolysis at low or moderate pressure benefits from reduced complexity and therefore lower system costs. Especially for the high-temperature SOEC, the sealing effort for high-pressure levels is disproportionate and still under development, as recent studies show.<sup>[28–30]</sup> Due to aforementioned reasons, it is of paramount importance to develop downstream processes for electrolysis in a way to ensure simple and cost effective integration of electrolysis.

The aim of this work is the process optimization of a high temperature coelectrolysis coupled with a two-stage catalytic methanation in fixed bed reactors. To our very best knowledge, in addition to the theoretical work of Koytsoumpa based on thermodynamic considerations, so far no investigations on alternating pressure levels in downstream methanation and their influence on the process performance and energy efficiency have been published.<sup>[13]</sup> The concept presented in this article is the result of a holistic approach to overcome practical challenges and drawbacks when realizing highly efficient PtG systems. In contrast to the methods of Koytsoumpa, in the underlying study both thermodynamic considerations as well as experimental investigations in laboratory scale are used. Only the combination of theoretical and practical methods enables to work out the additional advantages of the dual pressure level methanation concept.

The investigations for this work were conducted in the course of the project “HydroMetha”, in which a highly efficient power to gas system shall be demonstrated. The HydroMetha system consists of a high-temperature coelectrolyzer (Co-SOEC) coupled with a catalytic methanation unit (Figure 1). Renewable electric energy fuels the electrochemical transformation of pure CO<sub>2</sub> captured from industrial or biological off-gases and water into valuable syngas.

The main advantage of the high-temperature electrolysis, compared with other electrolysis technologies such as polymer

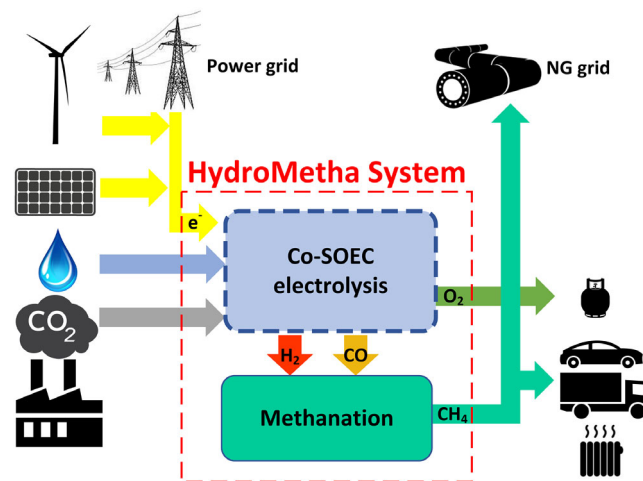


**Figure 1.** Functional scheme of a HydroMetha system.

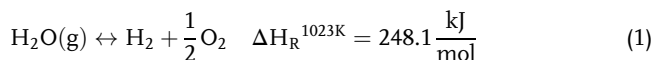


electrolyte membrane (PEM), is its capability to be cofueled by heat. Hence, part of the energy for hydrogen production can be introduced by surplus heat of industrial processes reducing the electric energy demand. Furthermore, the HydroMetha system allows integration of excess heat generated by the exothermal reactions of the methanation unit into the Co-SOEC. Due to the different operating temperature levels of the methanation (200–600 °C) and the Co-SOEC process ( $\approx 800$  °C), only preheating of the Co-SOEC feed is possible. The mentioned aspects of heat integration make an overall efficiency of >90% for the conversion of electric energy to hydrogen possible.

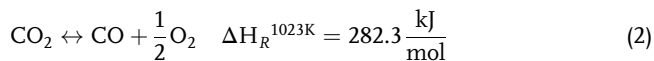
While the Co-SOEC operates well at atmospheric pressure, the methanation reactions can be generally enhanced by increasing pressures (2–10 bar) and reduced temperatures. At higher pressures, the thermodynamic equilibrium of the methanation reactions can be shifted toward products, as is shown in **Figure 2**, whereby the data are created with Matlab including the open source tool “Cantera” for thermodynamic data. The compression of process gas before the methanation is therefore generally beneficial, whereas the arrangement of multistep methanation and compression significantly influences the energy efficiency of the process.

The basic chemical reactions within the coelectrolysis process are the electrochemical splitting of water and the prereduction of CO<sub>2</sub> to CO.<sup>[31]</sup>

Splitting of H<sub>2</sub>O



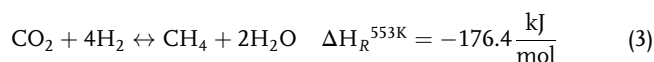
Prereduction of CO<sub>2</sub>



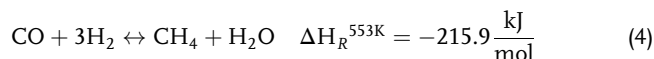
Due to incomplete reduction of CO<sub>2</sub> in the Co-SOEC small amounts of CO<sub>2</sub> remain in the syngas.

Subsequently to syngas production within the second part of the HydroMetha concept this syngas will be processed to a gas consisting largely of methane and small amounts of hydrogen, due to overstoichiometric hydrogen excess in the feed.<sup>[32,33]</sup> The methanation process is described by the Sabatier reactions. The methanation reaction of CO<sub>2</sub> is a combination of the CO methanation reaction and the reverse water gas shift reaction.<sup>[34]</sup>

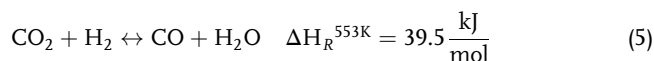
CO<sub>2</sub> methanation reaction



CO methanation reaction



Reverse water gas shift reaction



Feeding excess H<sub>2</sub> to the methanation reactor reduces the risk of carbon deposition.<sup>[35]</sup> Moreover, excess H<sub>2</sub> is beneficial for methanation performance and potentially enables full CO/CO<sub>2</sub> conversion.<sup>[33]</sup> In contrast, additional H<sub>2</sub> in the feed will subsequently remain in the product gas stream. Due to mole-reducing reactions and removal of water, 3% H<sub>2</sub>-surplus over the stoichiometric ratio at the input results in a H<sub>2</sub> volume fraction of about 10% in the product stream. Without a further downstream H<sub>2</sub> removal, the current legal restrictions for natural gas grid injection would not be met but it is expected that in near future 10 vol% hydrogen will be permitted in the natural gas grid.

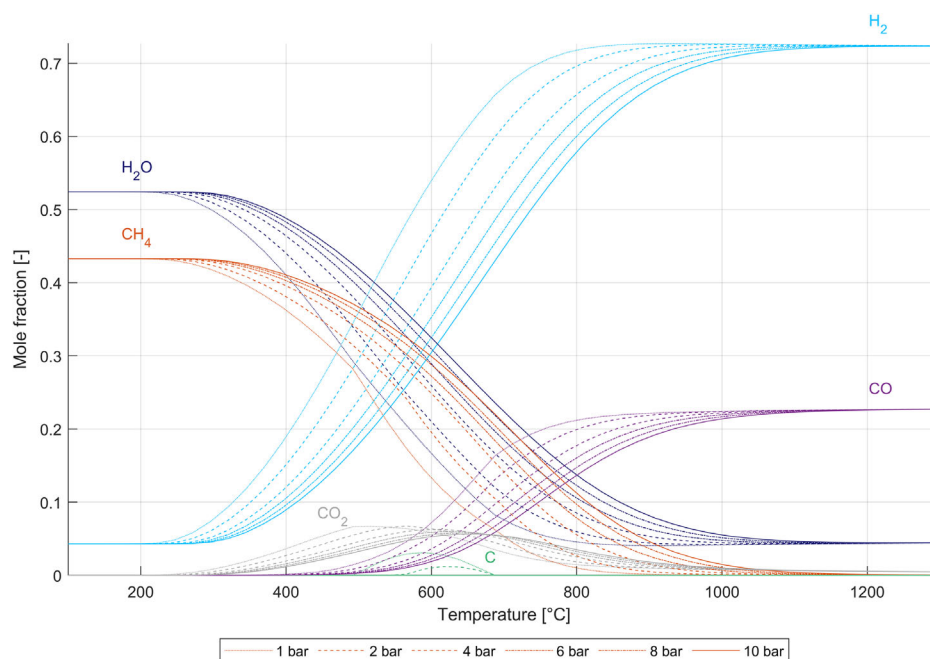


**Figure 2.** Equilibrium composition of Co-SOEC syngas in dependence of temperature and pressure.



The dynamic operability of a combined Co-SOEC and methanation plant is of major importance for power grid balancing applications. For the proposed process concept of a PtG system with intermediate compression, there is no indication of a decrease in dynamic operability, hence it can be expected to be similarly dynamic as its single components. Only for the SOEC part promising results were reported based on experiments. Posdziech et al. achieved very good load variation ability at stack level.<sup>[22]</sup> From literature addressing the methanation system, it can be concluded that load dynamics is not expected to be the limiting factor, as it affects mainly the methanation bed temperature.<sup>[36]</sup> Dynamic experiments have also been conducted by our working group which basically confirm the knowledge from literature. These results will be published separately.

Reactor pressure, temperature level, gas composition, and catalyst are the key performance influences in terms of CO/CO<sub>2</sub> methanation. Some boundary conditions such as input composition (Co-SOEC syngas) or output pressure (natural gas grid injection) are predefined based on the specific application. Nevertheless, other major performance factors fall within the field of the process design. Temperature level and distribution as well as reactor pressures are defined to a large extend by the selected process arrangement and reactor design. This work illustrates an overall performance improvement of a combined Co-SOEC and methanation power-to-gas concept by minor process arrangement adaptations. Within this article, two process paths are compared by energy and mass balance considerations validated by experiments. In the following section, the basic process and the advantages of the proposed adaptations is outlined. Subsequently, the experimental tests are described and the results discussed.

## 2. Process Design

Two different process scenarios shall be compared within this article. The basis process scheme consists of the Co-SOEC followed by a compressor unit ensuring higher pressures at the

same level in both methanation reactors (**Figure 3**). In contrast, the compressor of the adapted process scheme is placed not upstream the methanation unit but in-between methanation reactors 1 and 2 (**Figure 4**), and thus the first reactor is operated at the same low-pressure level (atmospheric pressure) as the Co-SOEC but the second reactor is affected by the pressure increase in the compressor. Preprocessing of off-gases to achieve clean CO<sub>2</sub> as well as potential postprocessing of product gas (drying) can be considered as equal in both process cases. Increasing reaction pressure within the range of 2–10 bar leads generally to an improvement in syngas methanation performance, as experimental investigations have shown.<sup>[33]</sup> However, operating the methanation reactors in the proposed dual pressure level mode are supposed to lead to several advantages. 1) Reduction of required compressor power; 2) Reduction of temperature peaks in reactor 1; and 3) Improvement of overall methanation performance (CO/CO<sub>2</sub> turnover).

Advantage 1) The required electric power of a compressor is linearly dependent on the volume flow of the compressed gas. The Sabatier reactions are mole consuming by a factor of 0.5 and 0.6 for CO methanation and CO<sub>2</sub> methanation, respectively. The set of balance equations for the reactions according to Equation (3) and (4) are given by Equation (6)–(13).

$$\text{conversion}_{\text{CO}} = \frac{\dot{n}_{\text{CO,in}} - \dot{n}_{\text{CO,out}}}{\dot{n}_{\text{CO,in}}} \quad (6)$$

$$\text{conversion}_{\text{CO}_2} = \frac{\dot{n}_{\text{CO}_2,\text{in}} - \dot{n}_{\text{CO}_2,\text{out}}}{\dot{n}_{2,\text{in}}} \quad (7)$$

$$\text{conversion}_{\text{CO/CO}_2} = \frac{(\dot{n}_{\text{CO,in}} + \dot{n}_{\text{CO}_2,\text{in}}) - (\dot{n}_{\text{CO,out}} + \dot{n}_{\text{CO}_2,\text{out}})}{\dot{n}_{\text{CO,in}} + \dot{n}_{\text{CO}_2,\text{in}}} \quad (8)$$

$$\dot{n}_{\text{H}_2,\text{R1out}} = \dot{n}_{\text{H}_2,\text{in}} - \dot{n}_{\text{CO,in}} * \text{con.}_{\text{CO}} * 3 - \dot{n}_{\text{CO}_2,\text{in}} * \text{con.}_{\text{CO}_2} * 4 \quad (9)$$

$$\dot{n}_{\text{CH}_4,\text{R1out}} = \dot{n}_{\text{CH}_4,\text{in}} + \dot{n}_{\text{CO,in}} * \text{con.}_{\text{CO}} + \dot{n}_{\text{CO}_2,\text{in}} * \text{con.}_{\text{CO}_2} \quad (10)$$

$$\dot{n}_{\text{CO},\text{R1out}} = \dot{n}_{\text{CO,in}} - \dot{n}_{\text{CO,in}} * \text{con.}_{\text{CO}} \quad (11)$$

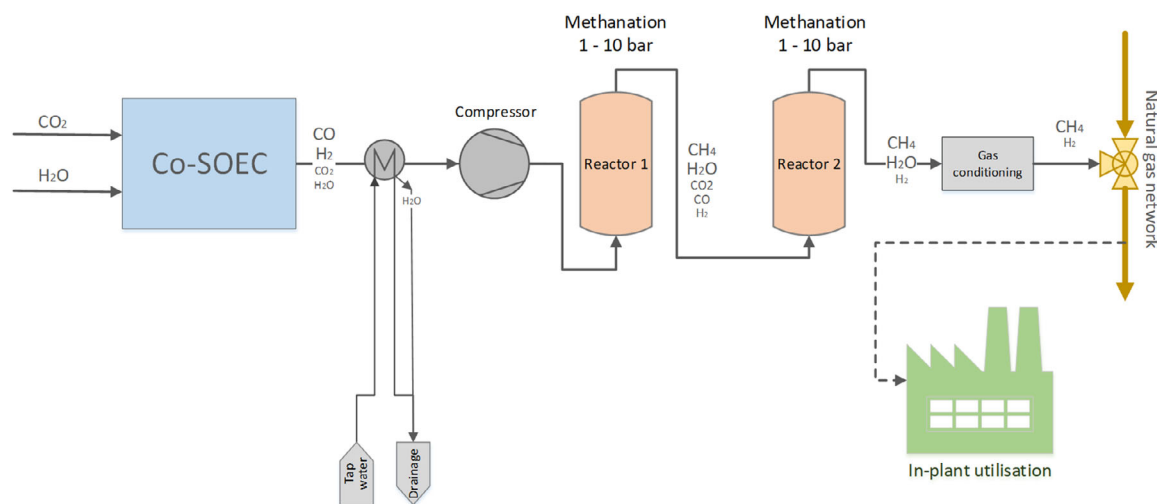


**Figure 3.** Basis process flow diagram of high-temperature coelectrolysis and catalytic methanation with compression upstream the methanation unit.

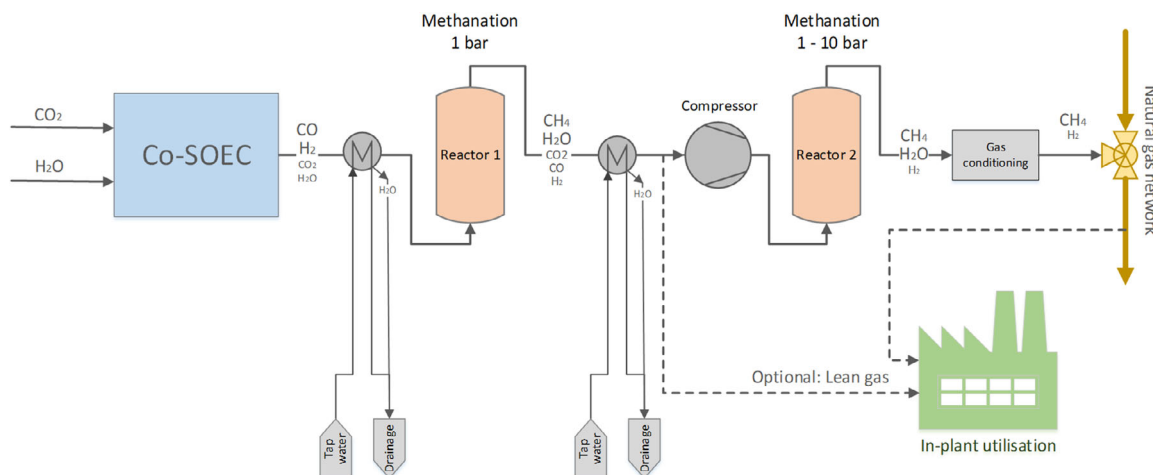


**Figure 4.** Adapted process flow diagram of high-temperature coelectrolysis and methanation with intermediate compression.

$$\dot{n}_{\text{CO}_2, R1\text{out}} = \dot{n}_{\text{CO}_2, \text{in}} - \dot{n}_{\text{CO}_2, \text{in}} * \text{con-}\text{CO}_2 \quad (12)$$

$$\dot{n}_{\text{tot., R1out}} = \sum_{i=1}^n \dot{n}_{i, R1\text{out}} \quad (13)$$

For example, considering 67.5% CO/CO<sub>2</sub> conversion (83.4% CO conversion and 8.3% CO<sub>2</sub> conversion) for the methanation of Co-SOEC syngas in the first reactor step, the standard volume flow decreases by 31% due to the reaction according to Equation (6)–(13).

In addition, water is needed to be removed in front of the compressor to prevent compressor damage. This leads to a further reduction of standard volume flow. In total, the standard volume flow of the process gas would be reduced by 40% due to partial conversion by the methanation reaction in the first reactor and water removal for the given example. By these proposed adaptations, a reduction of 42% in compressor power was calculated via isentropic compression and a compressor efficiency of 65%.

$$T_{\text{comp, out}} = T_{\text{comp, in}} * e^{\frac{\dot{Q}}{c_p} \ln \left( \frac{p_{\text{comp, out}}}{p_{\text{comp, in}}} \right)} \quad (14)$$

$$P_{\text{comp}} = \dot{n}_{\text{tot, R2in}} * c_p * (T_{\text{comp, out}} - T_{\text{comp, in}}) \quad (15)$$

Advantage 2.) As extensively explained by Kiewidt and Thöming, the exothermic Sabatier reactions can lead to thermodynamic limitations, especially in uncooled reactor systems.<sup>[37]</sup> For thermodynamically limited reactors, a correlation of pressure and temperature can be assumed. Accordingly, in the case of thermodynamic limitation, the output concentration is bound to its equilibrium at a certain temperature and pressure. For higher pressures, the equilibrium will be shifted toward more products, whereas higher turnovers produce more reaction heat and therefore higher temperatures (Figure 2). On the opposite, at lower pressures fewer products would be formed until the thermodynamic equilibrium is reached leading to less reaction heat and lower temperatures in the reactor. In other words, pressure control is a key influence to limit catalyst temperature peaks in highly reactive and therefore often thermodynamically

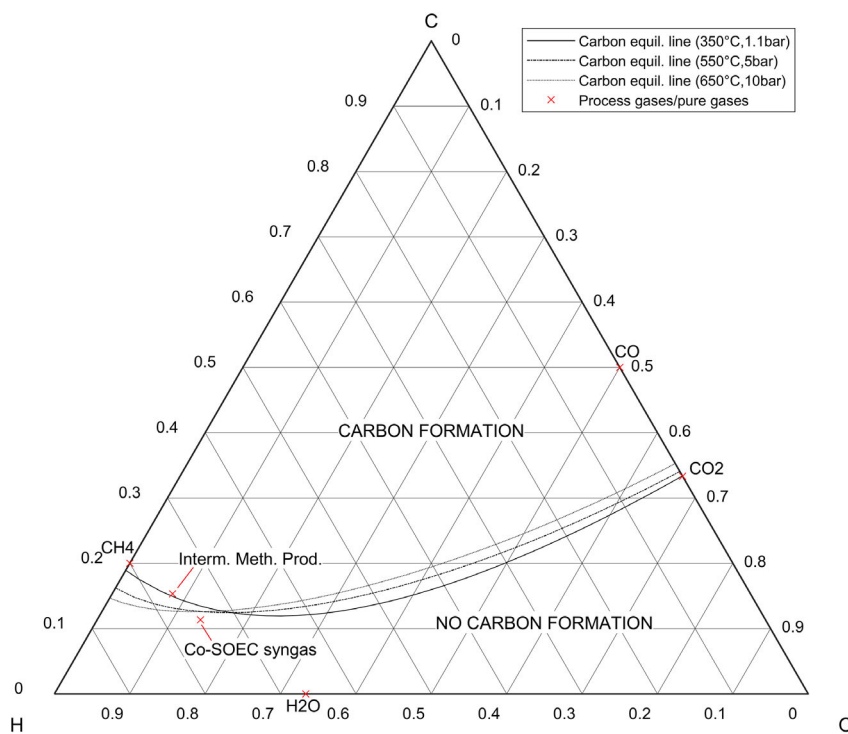
limited reaction systems, such as upstream methanation reactor stages.

Advantage 3.) As comprehensively shown by El-Sibai intermediate condensation leads to a significant improvement of the space–time yield.<sup>[38]</sup> The authors described that removal of the methanation byproduct water downstream the first reactor step leads to an increase in overall performance. This effect applies also for the proposed process scenario because a significant amount of water must be condensed and removed before the compressor.

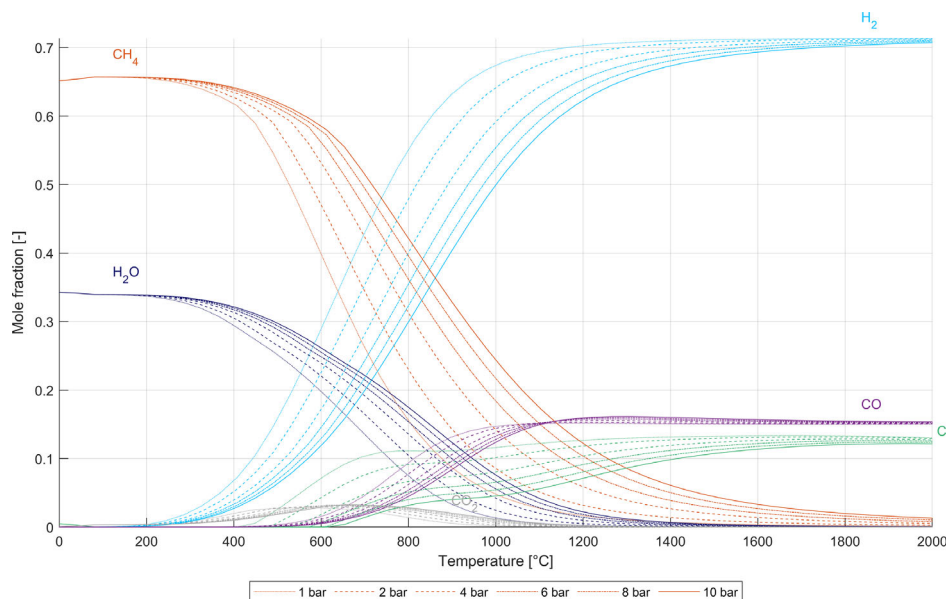
Unfortunately, intermediate water removal increases the risk of carbon deposition, as **Figure 5** and **6** show.

Figure 5 show a ternary diagram including the three process relevant atoms, namely carbon, hydrogen, and oxygen. Within this diagram, several gas compositions can be displayed by its C–O–H ratio, such as the Co-SOEC syngas and the intermediate methanation product gas determined downstream reactor 1 at 4000 h<sup>-1</sup> and 1.2 bar pressure. Furthermore, the carbon deposition equilibrium lines have been drawn in this diagram, dividing the areas where carbon deposition is thermodynamically possible (area above lines), or not (area beneath lines). As the thermodynamic behavior is not only dependent on composition but also on temperature and pressure, three lines for critical temperature–pressure pairs were drawn. This diagram shows that Co-SOEC syngas is thermodynamically not likely to form solid carbon, as the C–O–H ratio of this concentration (lower red cross) is positioned beneath all three carbon equilibrium lines. Nevertheless, the composition of the intermediate methanation process gas after removal of water is critical, because it is positioned within the area of carbon deposition (upper red cross). Further detailed information of ternary C–O–H diagrams can be found in the study by Neubert.<sup>[9]</sup>

Figure 6 shows the equilibrium mole fraction lines of all relevant gas molecules (CH<sub>4</sub>, H<sub>2</sub>O, H<sub>2</sub>, CO, CO<sub>2</sub>) and carbon (C) for only one composition (ordinate), in this case, the intermediate methanation product after water removal. On the abscissa, the temperature is visualized, whereas different line styles represent different pressures. The risk of carbon deposition is present for carbon mole fractions (green lines) above zero. From Figure 6, it can be concluded that carbon shares



**Figure 5.** Ternary carbon–hydrogen–oxygen–proportion diagram including solid carbon equilibrium lines at three different temperature–pressure pairs (marked by lines) and the position of process gases (marked by red crosses) representing the thermodynamic carbon formation property due to C–O–H ratio.



**Figure 6.** Temperature and pressure dependence of the equilibrium composition for the intermediate dual pressure stage methanation product after H<sub>2</sub>O removal.

(green lines) tend to zero for low temperatures and higher pressures (e.g., <350 °C at 1 bar, <550 °C at 10 bar).

As a result reactor temperature and pressure are essential to prevent carbon deposition after intermediate water removal

as proposed within 3). Higher risks of carbon deposition by water removal can be countered by lower temperatures and higher pressures (e.g., <350 °C at 1 bar) for the second reactor.

### 3. Experimental Section

The experimental work comprised in this article refers only to the optimization of the catalytic methanation, but not of the whole system coupled with a Co-SOEC. The aim of the experimental work was to substantiate the theoretically estimated benefits of converting Co-SOEC syngas via two pressure levels by intermediate compression. Therefore, synthetic Co-SOEC syngas was generated from bottle gases and fed to a laboratory methanation plant at different pressures. The Co-SOEC syngas concentration containing of 76.8 vol% H<sub>2</sub>, 18.3 vol% CO, and 4.9 vol% CO<sub>2</sub> included a H<sub>2</sub> excess of 3% above methanation stoichiometry level. It had been expected that this composition allows achieving good methanation results, staying on a reduced carbon formation risk level and having an attractive SNG composition at full methanation of CO<sub>x</sub>. Due to volume decrease and water condensation throughout the process (see Equation (3) and (4)) SNG containing 90 vol% CH<sub>4</sub> with an acceptable share of 10 vol% H<sub>2</sub> can be obtained at full methanation. This SNG quality is likely to find broad industrial application and therefore makes expensive H<sub>2</sub> separation or major infrastructure modifications obsolete. The feed gas composition from Co-SOEC for the methanation was suggested and approved by partners within the project HydroMetha based on their experience and test results of Co-SOEC operation. In addition to gas flow, the important parameter “gas hourly space velocity” (GHSV) is used as a tantamount to catalyst load. It is calculated by the standard input volume flow divided by the catalyst volume.

$$\text{GHSV} = \frac{\dot{V}_{N,\text{in}}}{V_{\text{cat}}} [\text{h}^{-1}] \quad (16)$$

The base and the adapted design were validated at values of 4000 h<sup>-1</sup> (Figure 8) and 6000 h<sup>-1</sup> (Figure 9) equaling a volume flow input for reactor 1 of 16.8 and 25.1 Nl min<sup>-1</sup>, respectively.

The laboratory test plant for methanation used for the experiments consists of up to three fixed-bed reactors in series each filled with 0.25 L of commercial bulk catalyst, whereas also bypassing of reactors is possible. Details of the experimental set-up can be found in the studies by Kirchbacher et al.<sup>[33,34]</sup> A wide range of gas concentrations and total gas flows could be adjusted via five Bronkhorst mass-flow controllers for CH<sub>4</sub>, H<sub>2</sub>, CO, CO<sub>2</sub>, and N<sub>2</sub>. The feed gas as well as the (intermediate) products after each of the three reactors could be analyzed by a gas analysis system (ABB Advanced Optima AO2000). Several pressure measurements along with a pressure reduction valve ensured pressure regulation up to 20 bar. A multithermocouple including seven temperature measurement points along the reactor axis made precise temperature recording along catalyst bed depth for each reactor possible. In Figure 7a, schematic drawing of one reactor is shown.

The inner diameter of the reactor was 80 mm. The commercial Ni-based catalyst (Meth134) was used with a bulk height of 50 mm. Above and below the catalyst zone, inert stoneware balls were positioned for homogenization of the incoming gas flow. Five measurement points of the multithermocouple were located within the catalyst bulk material, one closely beneath and one above the catalyst zone, respectively. Measurement point 6 (TI6) was defined as the catalyst zone outlet temperature,

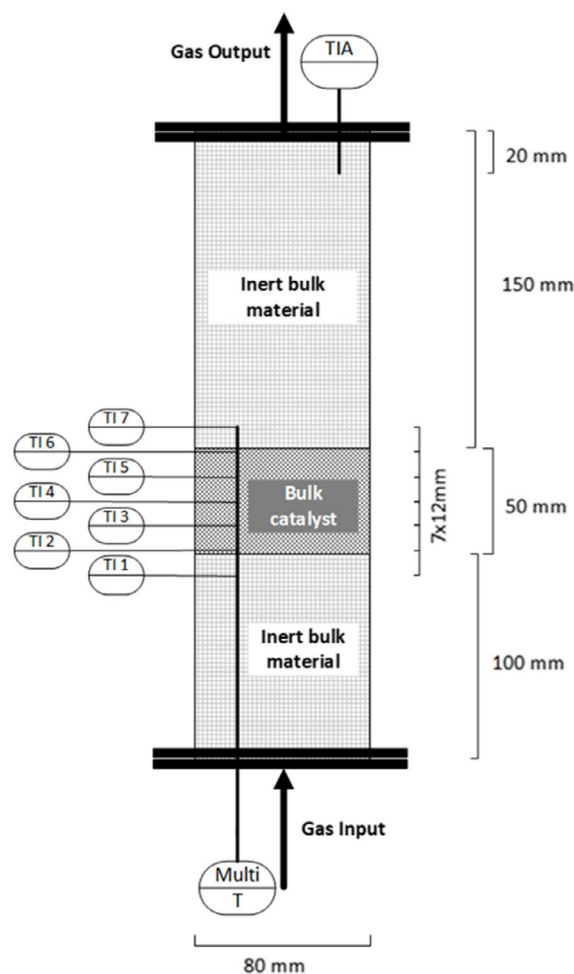


**Figure 7.** Schematic drawing including multithermocouple of one of three identical methanation reactors of the laboratory test plant.

for example, used within Figure 10. Furthermore, the reactor could be heated by infrared heaters, which was especially necessary for heat up and catalyst activation phases. For experiments causing low reaction heat, the heaters could be used to compensate partly for cooling by natural convection, and keep reaction temperature above 200 °C to prevent toxic nickel tetracarbonyl formation.<sup>[39]</sup> Consequently, the reactor system could be considered as polytropic. To increase cooling by natural convection and simplify reactor removal for modification, the heaters could be folded to the sides.

The methanation experiments aimed on demonstrating the methanation performance of single pressure level methanation versus a dual pressure level process design. The single pressure level scenario served as base case (Figure 4). Therefore, methanation at 1.2, 2, 4, 6, 8, and 10 bar in two serial reactors both operated at the same pressure was carried out with synthetic Co-SOEC syngas.

In a second step, the dual pressure level methanation performance was examined for comparison. Therefore, the second reactor was fed with the product gas of reactor 1 operated at 1.2 bar pressure whereby the steam content of the product gas

of reactor 1 was assumed to be fully condensed. The resulting feed gas composition for reactor 2 was experimentally determined as 31.3 vol% CH<sub>4</sub>, 53.6 vol% H<sub>2</sub>, 5.9 vol% CO, 9.2 vol% CO<sub>2</sub>. This feed gas for reactor 2, again synthetically mixed from bottles, was inserted to reactor 2 at pressures of 1.4, 2, 4, 6, 8, and 10 bar. Reactor 2 had the same configuration as reactor 1, as shown in Figure 7. This procedure was repeated for 6000 h<sup>-1</sup> or 25.1 Nl min<sup>-1</sup> under the same feed gas composition.

## 4. Results

### 4.1. Single Pressure Level Scenario at 4000 h<sup>-1</sup>

Starting with the base case scenario of methanation in a single pressure level for 4000 h<sup>-1</sup> (Figure 8 on the right) shows CO/CO<sub>2</sub> total conversions of 87.1%, 93.6%, and 95.1% at 1.2, 2, and 4 bar pressure, respectively. At 6 bar pressure, 97.3% conversion could be achieved, slightly increasing to 97.8% and 98.2% when the pressure is increased to 8 and 10 bar. The conversion generally increases in reactor 1 as well as in reactor 2 with higher pressures in both reactors.

The maximum temperatures in reactor 1 are always higher than in reactor 2. While the maximum temperatures in reactor 1 steadily rise from 624 °C at 1.2 bar to 700 °C at 10 bar, the temperatures of reactor 2 barely increase from 434 °C (1.4 bar) to 438 °C (4 bar) but decrease significantly to 394 °C at 10 bar. Therefore, the differences of the maximum temperatures of reactor 1 and reactor 2 increases from 190 K at 1.2 bar to 305 K at 10 bar.

### 4.2. Dual Pressure Level Scenario at 4000 h<sup>-1</sup>

The settings of the first pressure stage within the dual pressure level scenario were kept at the same level of 1.2 bar throughout

this scenario. The dual pressure level results (Figure 8 on the left) reveal that the total conversions downstream the pressurized reactor 2 are higher (or almost equal at 10 bar) compared with the single pressure version. The better overall conversion and higher methane concentrations are achieved howbeit reactor 1 has lower conversions due to its continuous operation under atmospheric pressure. At 4 bar 97.5% and at 6 bar 98.3%, conversion can be reached compared with 95.1% and 97.3%, respectively, under equal pressure operation of both methanation stages. To reach a conversion value of 98.7% in the single pressure level scenario 10 bar are necessary, for the dual pressure operation only 6 bar. The methane concentration in the product gas follows the same trend and reaches after the second reactor at 8 bar 88.5% for the dual pressure levels scenario compared with 82.2% in the base case. These results show that in the dual pressure level scenario, the improved performance of the second reactor even overcompensates for the weak performance of reactor 1 at atmospheric pressure.

The temperatures in reactor 2 of the dual pressure level scenario are lower than in the single pressure level scenario, especially for 4000 h<sup>-1</sup>. The settings of reactor 1 in the dual pressure level scenario are identical to those at 1.2 bar for the base case and therefore equal temperatures and turnovers are the logical consequence.

### 4.3. Single Pressure Level Scenario at 6000 h<sup>-1</sup>

At a GHSV of 6000 h<sup>-1</sup> (Figure 9, on the right) a similar performance is observed as for 4000 h<sup>-1</sup>, except with slightly lower conversions and higher temperatures what is based on the thermodynamic limitation behavior of the methanation reactions. The conversion in the single pressure level scenario does not reach values above 94% at all, whereas at 4 bar, it even stays

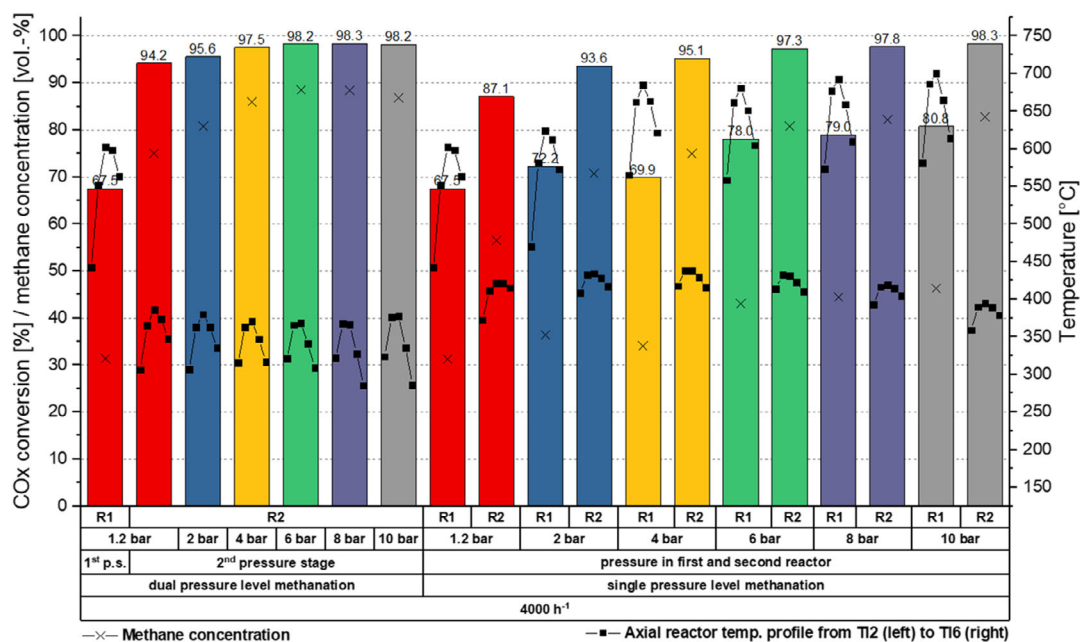


**Figure 8.** Experimental results of single and dual pressure level methanation at 4000 h<sup>-1</sup> (bars for COx conversion, black crosses for methane concentration, black squares for temperatures).



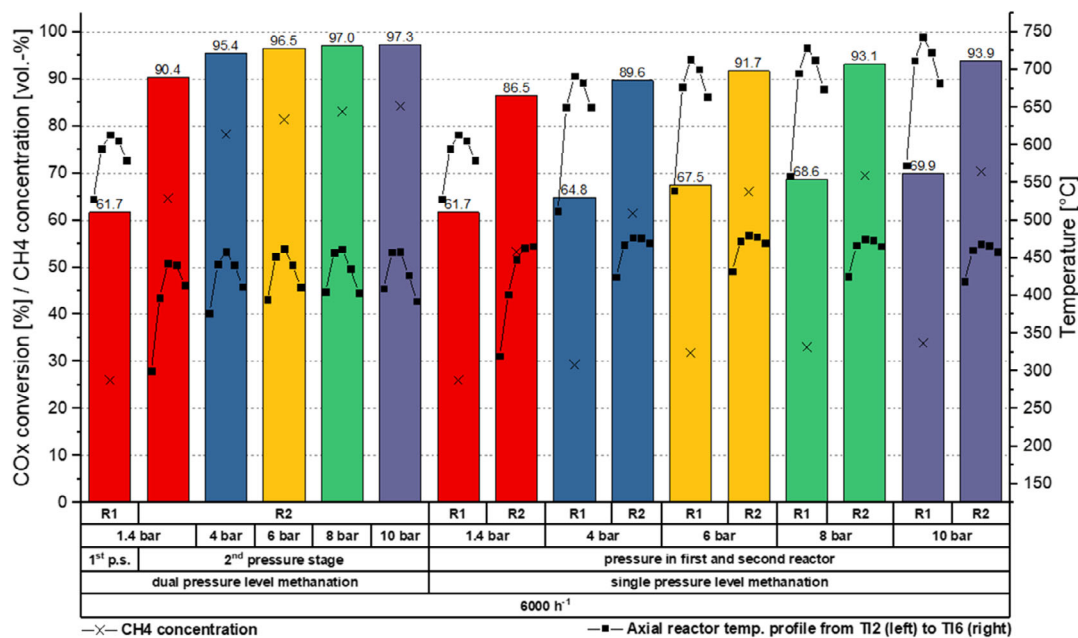


**Figure 9.** Experimental results of single and dual pressure levels methanation at  $6000\text{ h}^{-1}$  (bars for COx conversion, black crosses for methane concentration, black squares for temperatures).

below 90%, referring to a methane concentration of 70.3 and 61.4 vol%, respectively.

The maximum temperatures of reactor 1 again increase and in reactor 2 analogously decrease with higher pressures, just like for  $4000\text{ h}^{-1}$ . The differences between reactor 1 and reactor 2 in terms of temperature are smaller for the higher volume flow ( $6000\text{ h}^{-1}$ ).

#### 4.4. Dual Pressure Level Scenario at $6000\text{ h}^{-1}$

The dual pressure level results of  $6000\text{ h}^{-1}$  show a similar trend as for the same experiments at  $4000\text{ h}^{-1}$ . The conversions downstream the second reactor in the dual pressure level mode (90.4–97.3%) are again generally higher compared with the results of the single pressure level scenario at the same catalyst load of  $6000\text{ h}^{-1}$  (86.5–93.9%). Analogously behaves the concentration of methane reaching higher values at intermediate compression (64.64–84.22 vol%) compared with compression upstream of the methanation reactors (53.3–70.3 vol%).

Compared with the same dual pressure level scenario at  $4000\text{ h}^{-1}$ , the conversion for higher pressures (2–8 bar) downstream reactor 2 is only 1 to 1.2 percentage points lower with  $6000\text{ h}^{-1}$ , although the catalyst load was increased by 50%. Interestingly, at the lowest pressures (1.2/1.4 bar), the difference in turnover is four percentage points, about four times as much.

Temperatures of reactor 2 in the dual pressure level scenario are in a similar range as the temperatures in the single pressure level operation.

In **Figure 10a**, correlation of thermodynamic equilibrium with experimental and modeling results is presented. The experimentally determined  $\text{CH}_4$  mole fraction downstream reactor 1 was validated by a 2D CFD FEM reactor model elaborated in Comsol Multiphysics. A detailed description of this methanation

reactor model will be published in a follow-up publication. For the determination of the average temperature over the cross-sectional area at the catalyst zone outlet, the reactor model was indispensable. Other than the model, the experimental setup in terms of temperature measurement (Figure 7) gives only information on the axial temperature profile in the catalyst bed, but provides only the temperature at a single radial position at the catalyst bed outlet. The model-based radial temperature profile was averaged over the total cross-sectional area. The modeled and experimentally determined  $\text{CH}_4$  mole fractions and the averaged outlet temperatures indicate thermodynamic behavior, as the values clearly follow the respective thermodynamic equilibrium lines in Figure 10. With increasing pressure, the results shift to higher methane mole fractions, but also higher temperatures. To demonstrate comparability of experiment and model, also the  $\text{CH}_4$  mole fractions obtained by the model are shown in Figure 10, which only slightly differ from the experimentally determined. In total, a very good correlation between the experimental/modeling results and the thermodynamic equilibrium is shown in Figure 10.

## 5. Conclusions

Mass and energy balance calculations combined with experimental investigations were conducted to approve significant performance improvements of catalytic methanation operated under dual pressure levels.

As a general result of the methanation experiments with Co-SOEC syngas the achieved CO/CO<sub>2</sub> conversion under the defined input specification of 3% H<sub>2</sub> excess are promising. Nearly full conversion of >97% leading to methane and hydrogen shares of 84.2 and 13.2 vol%, respectively, was achieved



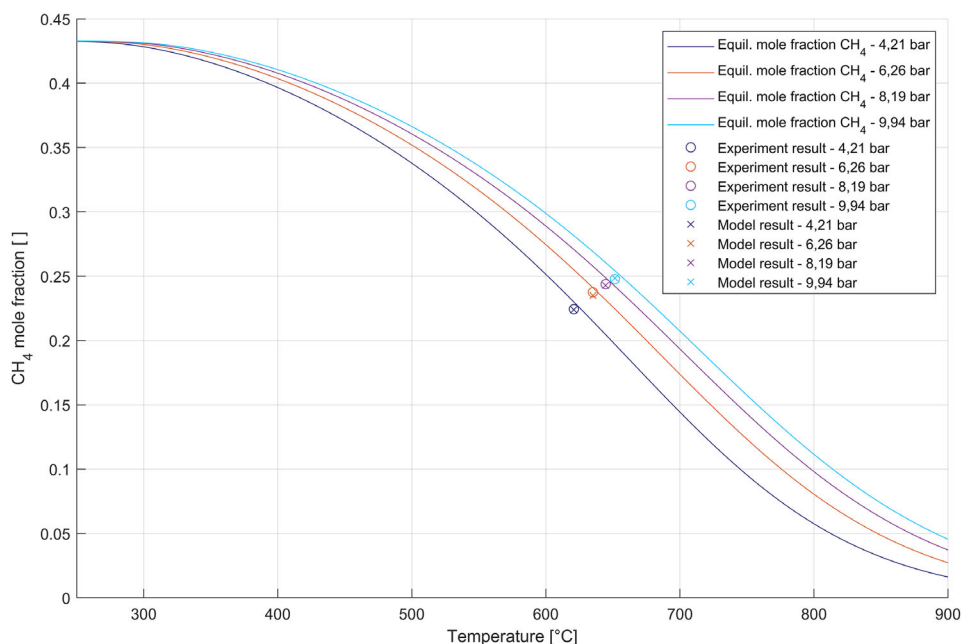


**Figure 10.** Thermodynamic equilibrium concentration of methane over temperature at different pressures in comparison to methane concentrations determined by experiment as well as by model (only reactor 1,  $6000 \text{ h}^{-1}$ ) over cross-sectional averaged temperatures at the catalyst zone outlet obtained by a Comsol Multiphysics reactor model.

with the existing equipment for a wide range of process parameters for GHSV values of up to  $6000 \text{ h}^{-1}$ . Furthermore, conversions of  $>98\%$  and methane concentrations of  $88.5 \text{ vol}\%$  including a rest share of  $9.1 \text{ vol}\%$  hydrogen were possible for GHSV values of  $4000 \text{ h}^{-1}$ .

The experimental results show that full methanation of Co-SOEC syngas is possible also with only a small  $\text{H}_2$  excess of  $3\%$ , demonstrating that  $\text{H}_2$ , costly produced by electric energy, can be used to a large extent for  $\text{CO}_2$  utilization. As a consequence, most of the PtG plant's  $\text{CO}_2$  recycling potential can be exploited. At the same time, the generation of an attractive product of mainly  $\text{CH}_4$ ,  $10\text{--}16\%$   $\text{H}_2$  and amounts of  $\text{CO}_2$  smaller than  $2\%$  could be demonstrated. The produced SNG is likely to find broad application in industrial infrastructure as well as for natural gas grid injection.<sup>[40–42]</sup>

Moreover, it could be shown that methanation in two pressure levels has significant advantages compared to methanation in a single pressure level scenario. The benefit of significantly less necessary compression power by changing the process flow arrangement (thesis no. 1), similar to the findings of Koytsoumpa,<sup>[13]</sup> was confirmed by simple mass flow calculations.  $42\%$  compressor power reduction was calculated for an experimentally validated example case ( $67.5\%$  conversion at  $1.2 \text{ bar}$  behind reactor 1, see Figure 8) by the proposed process rearrangement.

To substantiate the findings from energy- and mass balance calculations also experimental tests series were conducted. Initially, reactors 1 and 2 were operated at the same pressures ( $1.2\text{--}10 \text{ bar}$ ) for the single pressure level tests. In comparison, in the dual pressure level scenario, the pressure was kept around atmospheric in reactor 1, and has been increased only in reactor 2 ( $1.2\text{--}10 \text{ bar}$ ). The stated reduction in reactor peak temperatures

by the advanced process scheme (thesis no. 2) could be confirmed by experimental results. At  $6000 \text{ h}^{-1}$ , the peak temperatures in reactor 1 could be reduced from  $691$  to  $743 \text{ }^\circ\text{C}$  in the single pressure level scenario to  $613 \text{ }^\circ\text{C}$  in the dual pressure mode. The peak temperatures of reactor 1 at  $4000 \text{ h}^{-1}$  could be also lowered from  $621$  to  $700 \text{ }^\circ\text{C}$  by  $21\text{--}98 \text{ K}$ . The reason of lower temperature peaks with lower pressure is the thermodynamic limitation of the methanation reactor 1. The general thermodynamics of methanation reactions are widely described.<sup>[10,43]</sup> Thermodynamically dominated behavior in reactor 1 for the used setup was shown by comparing the experimental results to its corresponding thermodynamic equilibrium under the same conditions. In Figure 10, the measured methane concentrations for reactor 1 correlate with the thermodynamic equilibrium concentrations at the detected temperatures and pressures. For the determination of the corresponding average temperatures at the catalyst bed outlet, a Comsol Multiphysics model has been elaborated which accurately predicts the measured  $\text{CH}_4$  mole concentrations. The proven thermodynamic limitation characteristic of reactor 1 leads to a temperature-pressure-dependency. For higher pressures, the thermodynamic equilibrium will be reached at higher temperatures. On the other side, low, almost atmospheric pressure in reactor 1 ( $\approx 1.2 \text{ bar}$ ) leads to lower reactor temperatures (Figure 10).

In conclusion, keeping the pressures in reactor 1 low (dual pressure level scenario) prevents from temperature peaks. In contrast, increased pressure in reactor 1, (single pressure level scenario, reactors 1 and 2 at the same pressure level) leads to temperature peaks in the catalyst bed of reactor 1 with consequent limitations in the conversion performance. In other words, pressure control is a key influence to limit catalyst temperature

peaks in highly reactive exothermic, and therefore often thermodynamically limited, reaction systems, such as upstream methanation reactor stages.

As a consequence, the demonstrated temperature decrease by pressure reduction could result in a significant benefit in catalyst lifetime. High temperatures of 700 °C and higher can lead to sintering and deactivation phenomena of nickel-based methanation catalysts.<sup>[44]</sup> Therefore, the proven temperature reduction in reactor 1 could save elaborate cooling or recirculation process steps for an industrial plant.

In terms of reactor performance improvement (thesis no. 3), the experimental results show that by methanation in two pressure levels, the conversion can be increased by 3.4–7.1 percentage points at 4000 h<sup>-1</sup> and 0.5–3.9 percentage points at 6000 h<sup>-1</sup>, whereas the largest improvements occurred at low pressure operation. This performance increase from single-to-dual pressure level design is assumed to be caused mainly by water condensation of the intermediate feed. It can be concluded that removal of the side product water from the intermediate feed enhances thermodynamics as well as kinetics within reactor 2, which can also be derived from studies by El-Sibai et al.<sup>[38]</sup>

The intermediate output compositions of reactor 1 at almost atmospheric pressures (1.2 bar at 4000 h<sup>-1</sup> and 1.4 at 6000 h<sup>-1</sup>) are equal for both scenarios, dual and single pressure levels. At higher pressures (2–10 bar), the intermediate output compositions of reactor 1 vary between single and dual pressure scenarios. While the conversion downstream reactor 1 increases with every pressure step for the single pressure scenario; for the dual pressure scenario in reactor 1, steady conditions result in steady output composition. This means that for higher pressures, the process gas entering reactor 2 is less converted in the dual pressure level scenario compared with the single pressure mode. In conclusion, the positive influence of reduction in water vapor outweighs the negative effect that the intermediate process gas entering reactor 2 is less converted (higher CO + CO<sub>2</sub> to H<sub>2</sub> ratio) in the dual pressure level scenario.

From Figure 5 and 6, it can be drawn that carbon deposition could have appeared in reactor 2 for lower pressures. For pressures of 1.2–4 bar, the reactor temperature was not low enough to have certainly prevented carbon formation. Nevertheless, at higher pressures of 6–10 bar measured temperatures of <480 °C exclude carbon formation thermodynamically.

In summary, it can be confirmed that methanation with intermediate compression including water condensation leads to higher conversions of CO/CO<sub>2</sub> in comparison with operating a compressor before both methanation reactors.

This article intends to emphasize the benefits of intermediate process gas compression independent of the exact number of the lower and higher pressure level. Similar benefits may occur for a different pair of pressure stages, which should certainly be chosen according to available upstream steam pressure and the required downstream SNG pressure available at a potential industrial application. The pressurized electrolysis operation has been accomplished and recent studies show the high efficiency potential due to direct high pressure steam integration, parallel exothermic methanation reaction, if CO<sub>2</sub> is cofed, and reduced diffusion limitations.<sup>[22–24,26]</sup> Therefore, it can be assumed as an attractive alternative to or even a potential technology to be combined with the proposed dual pressure level methanation

process. The most efficient strategy must be determined according to the existing boundary conditions. Nevertheless, the process proposed in this work offers experimentally proven and energy efficient process path to generate SNG at a high downstream pressure, while allowing to keep electrolyzers at moderate pressure. Benefits considering the electrolyzer can be expected from reduced complexity and investment costs. Similar benefits can be expected, if a SOEC is used instead of a Co-SOEC system, as the findings of this article apply for both systems. Which solution is the most energy efficient, depends on the specific PtG application.

In further works, a full picture of the temperature behavior of the reactors shall be achieved by pursuing different temperature measurement strategies. This includes temperature measurement at several radial and axial positions within the catalyst bed in upcoming experimental campaigns.

Furthermore, biogas plants are expected to be an attractive application for PtG technologies based on high-temperature electrolysis combined with catalytic methanation plants. Temperature peak issues and performance optimization is also fundamental in biogas methanation applications. Therefore, the dual pressure level approach shall be extended to process gases from biogas plants.

## Acknowledgements

The open source tools of ‘Cantera’ originally developed at the California Institute of Technology was enormously helpful for investigating thermodynamic behavior of methanation reactions. This work was to a large extent funded by the Austrian Research Promotion Agency and the AVL List GmbH within the project HydroMetha (grant no. 864578). The project’s success relies on the essential contributions of its consortium leader (AVL List GmbH) and all project partners (Fraunhofer Institute for Ceramic Technologies and Systems, Chair of Physical Chemistry of the Montanuniversitaet Leoben, Prozess Optimal CAP GmbH, Energieinstitut an der JKU Linz).

## Conflict of Interest

The authors declare no conflict of interest.

## Keywords

CO methanation, Co-SOEC coupling, Co-SOEC syngas methanation, intermediate compression

Received: August 24, 2020

Revised: October 16, 2020

Published online: November 10, 2020

- [1] A. Buttler, H. Spliethoff, *Renewable Sustainable Energy Rev.* **2018**, *82*, 2440.
- [2] K. Ghaib, F.-Z. Ben-Fares, *Renewable Sustainable Energy Rev.* **2018**, *81*, 433.
- [3] M. Lehner, *Technology and Business Models*, Springer, Cham, Heidelberg **2014**.
- [4] M. Thema, F. Bauer, M. Sterner, *Renewable Sustainable Energy Rev.* **2019**, *112*, 775.

- [5] M. Götz, J. Lefebvre, F. Mörs, A. McDaniel Koch, F. Graf, S. Bajohr, R. Reimert, T. Kolb, *Renewable Energy* **2016**, *85*, 1371.
- [6] A. Vita, C. Italiano, L. Pino, M. Laganà, M. Ferraro, V. Antonucci, *Fuel Process. Technol.* **2020**, *202*, 106365.
- [7] S. Ratchahat, M. Sudoh, Y. Suzuki, W. Kawasaki, R. Watanabe, C. Fukuhara, *J. Util.* **2018**, *24*, 210.
- [8] Y. Li, Q. Zhang, R. Chai, G. Zhao, F. Cao, Y. Liu, Y. Lu, *Appl. Catal., A* **2016**, *510*, 216.
- [9] M. Neubert, *Catalytic Methanation for Small- and Mid-Scale SNG Production*, Friedrich-Alexander-Universität Erlangen-Nürnberg (FAU), Erlangen **2019**.
- [10] W. J. Lee, C. Li, H. Prajitno, J. Yoo, J. Patel, Y. Yang, S. Lim, *Catal. Today* **2020**.
- [11] J. Kopyscinski, T. J. Schildhauer, S. M. A. Biollaz, *Fuel* **2010**, *89*, 1763.
- [12] S. Rönsch, J. Schneider, S. Matthischke, M. Schlüter, M. Götz, J. Lefebvre, P. Prabhakaran, S. Bajohr, *Fuel* **2016**, *166*, 276.
- [13] E. I. Koytsoumpa, C. Bergins, E. Kakaras, *J. Supercrit. Fluids* **2018**, *132*, 3.
- [14] M. Neubert, A. Hauser, B. Pourhossein, M. Dillig, J. Karl, *Appl. Energy* **2018**, *229*, 289.
- [15] M. Sánchez, E. Amores, L. Rodríguez, C. Clemente-Jul, *Int. J. Hydrogen Energy* **2018**, *43*, 20332.
- [16] B. Bensmann, R. Hanke-Rauschenbach, G. Müller-Syring, M. Henel, K. Sundmacher, *Appl. Energy* **2016**, *167*, 107.
- [17] G. Tjarks, A. Gibelhaus, F. Lanzerath, M. Müller, A. Bardow, D. Stolten, *Appl. Energy* **2018**, *218*, 192.
- [18] H.-W. Wu, *Appl. Energy* **2016**, *165*, 81.
- [19] M. Carmo, D. L. Fritz, J. Mergel, D. Stolten, *Int. J. Hydrogen Energy* **2013**, *38*, 4901.
- [20] V. Mehta, J. S. Cooper, *J. Power Sources* **2003**, *114*, 32.
- [21] D. M. A. Dueñas, M. Riedel, M. Riegraf, R. Costa, K. A. Friedrich, *Chem. Ing. Tech.* **2020**, *92*, 45.
- [22] O. Posdziech, K. Schwarze, J. Brabandt, *Int. J. Hydrogen Energy* **2019**, *44*, 19089.
- [23] J. Brabandt, O. Posdziech, *ECS Trans.* **2017**, *78*, 2987.
- [24] L. Bernadet, J. Laurencin, G. Roux, D. Montinaro, F. Mauvy, M. Reytier, *Electrochim. Acta* **2017**, *253*, 114.
- [25] L. Bernadet, G. Gousseau, A. Chatroux, J. Laurencin, F. Mauvy, M. Reytier, *Int. J. Hydrogen Energy* **2015**, *40*, 12918.
- [26] L. R. Clausen, G. Butera, S. H. Jensen, *Energy* **2019**, *172*, 1117.
- [27] J. B. Hansen, *Faraday Discuss.* **2015**, *182*, 9.
- [28] P. A. Lessing, *J. Mater. Sci.* **2007**, *42*, 3465.
- [29] M. Fakouri Hasanabadi, M. A. Faghihi-Sani, A. H. Kokabi, S. M. Groß-Barsnick, J. Malzbender, *Ceram. Int.* **2019**, *45*, 733.
- [30] H. Javed, A. G. Sabato, I. Dlouhy, M. Halasova, E. Bernardo, M. Salvo, K. Herbrig, C. Walter, F. Smeacetto, *Materials* **2019**, *12*, 298.
- [31] N. Trofimenko, M. Kusnezoff, A. Michaelis, *ECS Trans.* **2017**, *78*, 3025.
- [32] G. A. Mills, F. W. Steffgen, *Catal. Rev.* **1974**, *8*, 159.
- [33] F. Kirchbacher, P. Biegger, M. Miltner, M. Lehner, M. Harasek, *Energy* **2018**, *146*, 34.
- [34] P. Biegger, F. Kirchbacher, A. Medved, M. Miltner, M. Lehner, M. Harasek, *Energies* **2018**, *11*, 1679.
- [35] D. C. Gardner, C. H. Bartholomew, *Ind. Eng. Chem. Prod. Res. Dev.* **1981**, *20*, 80.
- [36] M. Gruber, P. Weinbrecht, L. Biffar, S. Harth, D. Trimis, J. Brabandt, O. Posdziech, R. Blumentritt **2018**.
- [37] L. Kiewidt, J. Thöming, *Chem. Eng. Sci.* **2015**, *132*, 59.
- [38] A. El Sibai, L. K. Rihko Struckmann, K. Sundmacher, *Energy Technol.* **2017**, *5*, 911.
- [39] M. Goetz, *Dissertationsschrift*, Karlsruher Institut für Technologie (Karlsruhe) **2014**.
- [40] J. Ogden, A. M. Jaffe, D. Scheitrum, Z. McDonald, M. Miller, *Energy Policy* **2018**, *115*, 317.
- [41] Y. Zhao, V. McDonell, S. Samuelsen, *Int. J. Hydrogen Energy* **2019**, *44*, 12239.
- [42] K. Altfeld, D. Pinchbeck, *Admissible Hydrogen Conc. Nat. Gas Syst.* **2013**, [https://www.gerg.eu/wp-content/uploads/2019/10/HIPS\\_Final-Report.pdf](https://www.gerg.eu/wp-content/uploads/2019/10/HIPS_Final-Report.pdf).
- [43] J. Gao, Y. Wang, Y. Ping, D. Hu, G. Xu, F. Gu, F. Su, *RSC Adv.* **2012**, *2*, 2358.
- [44] T. T. M. Nguyen, L. Wissing, M. S. Skjøth-Rasmussen, *Catal. Today* **2013**, *215*, 233.

## 4 Summary and Discussion

The pathway to optimum CO/CO<sub>2</sub> methanation reactors can be summarized based on set of five research questions including their answers. At first the limiting factors of fixed bed methanation reactors and the set of operation and design parameters which are relevant for optimization in order to reduce the found limitations need to be determined (research question 1). The exact influence and interdependencies of the operation and design parameters on the methanation performance have to be understood in a second step (research question 2 and 3). Finally, an optimization strategy and process design rules for high CO/CO<sub>2</sub> methanation performance were derived (research question 4). In addition, potential efficiency enhancements for CO/CO<sub>2</sub> methanation on the process level for a combined Co-SOEC and methanation plant were elaborated (research question 5).

### 4.1 Answer to research question 1: What are the limiting factors of fixed bed methanation of CO/CO<sub>2</sub> feed gas and what are the relevant design and operation parameters to reduce these limiting effects?

The methanation of CO and CO<sub>2</sub> is a process consisting of a sequence of interlinked process steps including mass transport, heat transport and chemical reaction (Figure 3). All of these steps interfere with each other and with any design or operation parameter. No transport or transformation phenomena can be influenced independently. For example, the reaction kinetics is a function of pressure and temperature and determines the amount of reaction heat formed in the catalyst bed. Higher pressure in the reactor triggers more reaction heat to be released. Consequently, higher bed temperatures occur, which affects the effective gas velocity, which influences mass and heat transfer, which again relates to temperature and therefore kinetics. For a given process condition setting one of these physical or chemical phenomena is the limiting factor, because the overall process rate marches to the beat of the slowest step. The limiting or process dominating factor can differ in different sections within the reactor bed. For example, the process can be initially kinetically limited, followed by a thermodynamically limited zone in the latter section of the fixed bed.

In Figure 6 the performance of a variety of reactor dimensions for Co-SOEC syngas at several “gas hourly space velocity” (GHSV) and pressure values is presented. For capacity comparison of different reactor systems, the GHSV, which can also be referred to as catalyst load, is calculated by the standard volume flow per reactor volume (Equation 44).

$$GHSV = \frac{\dot{V}_{in,op.} \cdot T_{in} \cdot p_{STP}}{V_{reactor} \cdot T_{STP} \cdot p_{in}} \quad (\text{Equation 44})$$

The essential performance parameter CO<sub>x</sub> conversion is defined by Equation 45.

$$CO_x \text{ conversion} = \frac{(\dot{n}_{CO,in} - \dot{n}_{CO,out}) + (\dot{n}_{CO_2,in} - \dot{n}_{CO_2,out})}{\dot{n}_{CO,in} + \dot{n}_{CO_2,in}} \quad (\text{Equation 45})$$

With increasing pressure, the CO<sub>x</sub> conversion but also the temperature peaks increase. Furthermore, increasing GHSV leads to lower conversion rates. For only naturally air-cooled reactors with increasing GHSV also the peak temperatures increase at constant pressure.



However, in oil-cooled reactors the maximum temperature decreases with higher GHSV at constant pressure. The reactor performance generally increases with smaller diameters or enhanced cooling (80 mm diameter naturally cooled < 14 mm naturally cooled < 14 mm actively cooled) as shown in Figure 6. The performance could be significantly increased by improving the limiting factor for a given reactor design and operation condition.

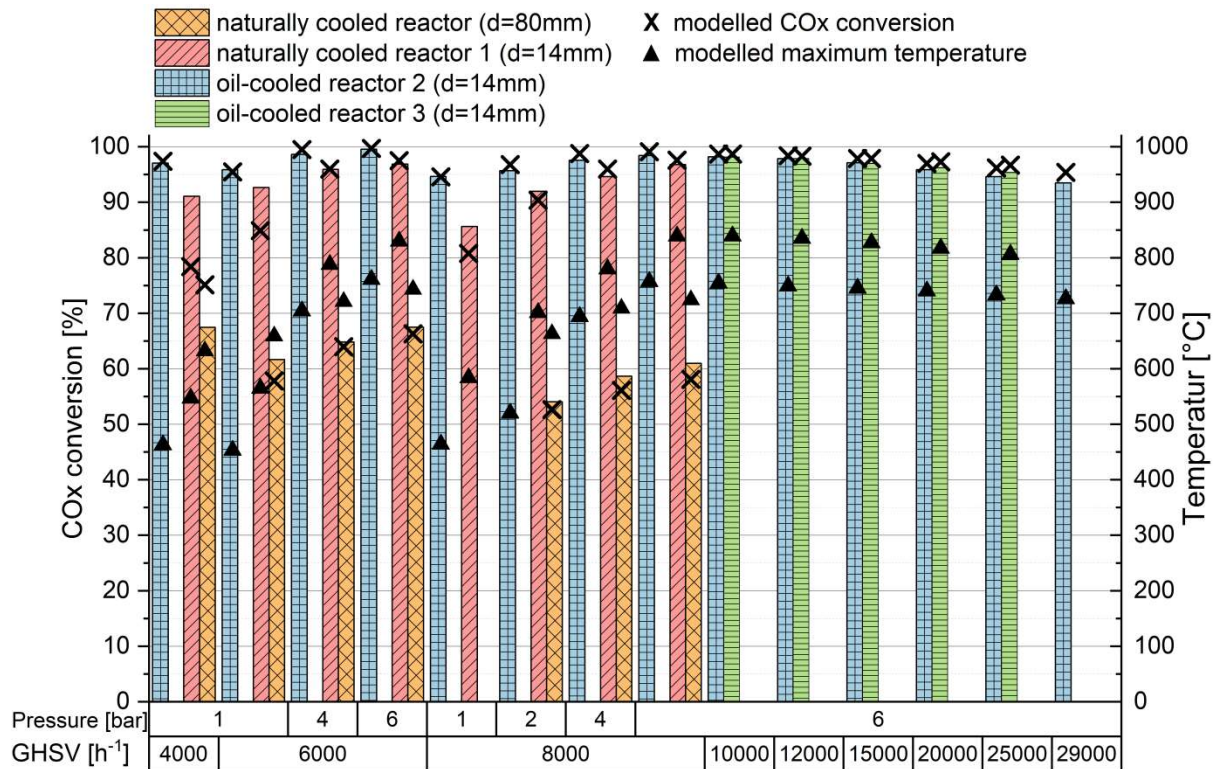


Figure 6: Performance comparison based on experimentally found (bars) and modelled ('x'-markings) CO<sub>x</sub> conversion and modelled maximum temperature ('▲'-markings) of three reactors with 14 mm diameter (840 mm naturally cooled reactor 1, 700 mm oil-cooled reactor 2 and 600 mm oil-cooled reactor 3) and a reactor with 80 mm diameter (50 mm naturally cooled catalyst zone) [8] in dependency of GHSV and pressure.

The chemical methanation reactions accelerated by nickel catalysts are in general intrinsically fast and highly exothermic. This means that the methanation reaction tends to initially generate a lot of heat in a small bed volume leading to a fast exponential increase in temperature. In Figure 7 the modelled axial temperature curves for an 80 mm reactor are presented.

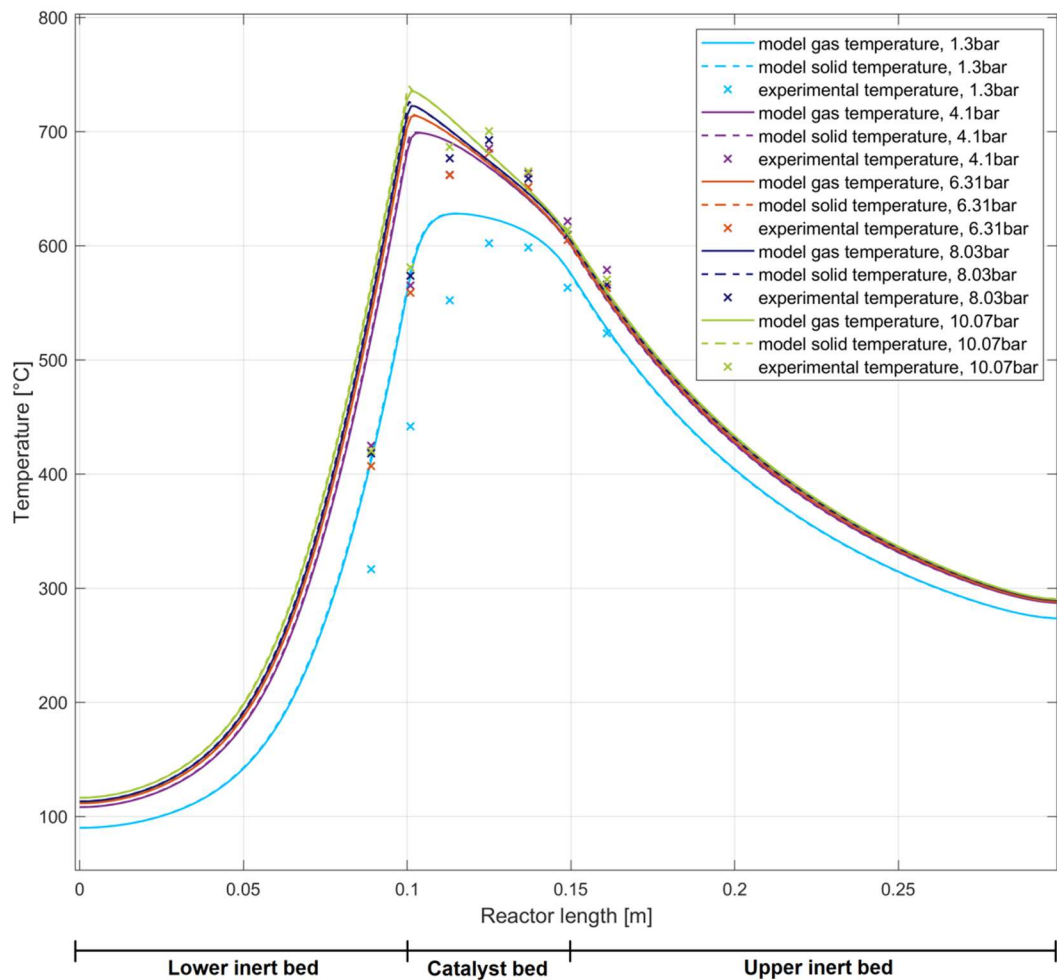


Figure 7: Experiment-model-comparison of axial temperature profiles for a lab-scale packed bed methanation reactor at  $4000 \text{ h}^{-1}$  GHSV and Co-SOEC syngas feed

The high rate of reaction heat in the initial section needs to be removed in the same magnitude as it is produced in order to be able to control the temperature profile. In a tubular system reaction heat can only be removed from the reactor system in radial direction. If this heat removal is not sufficiently done, the temperature rises until thermodynamic equilibrium conditions are reached and the reaction progress is thermodynamically hindered, which was the case in the 80 mm reactor. The three most relevant radial heat transport mechanisms are effective fixed bed heat conduction in radial direction, bed-wall heat transfer at the inner wall interface and wall-coolant heat transfer at the outer wall interface, which was also discussed in detail in paper II [55].

Heat transport by **effective fixed bed heat conduction** for catalytic fixed beds is mainly a function of gas velocity, pellet diameter (particle Reynolds number), pellet heat conduction and radial distance as thoroughly presented in chapter 2.2.6. The dependencies can be derived from the  $\Lambda_r(R)$ -model as shown in Equation 22. In practice, the tube diameter and the gas velocity are the most important tuning parameters to increase radial heat transport in terms of reactor design. Heat conductivity of fixed beds increases also with lower pellet diameter. However, the smallest pellet diameter is a question of the maximum acceptable pressure loss,



which is increasing with lower pellet diameters and therefore should not be significantly reduced.

**Bed-wall heat transfer** for a given gas quality is determined mainly by gas velocity, whereas the particle diameter has only limited influence as discussed in paper II, using the formulation of Specchia [57]. The significant performance limitation in the 80 mm diameter naturally cooled reactor is caused by limited radial heat transfer, especially at the inner bed-wall interface. This is indicated by the considerable temperature jump between bed and wall (at radius 0,04 m) in radial temperature profiles of Figure 8 at already moderate GHSV of 4000 h<sup>-1</sup>.

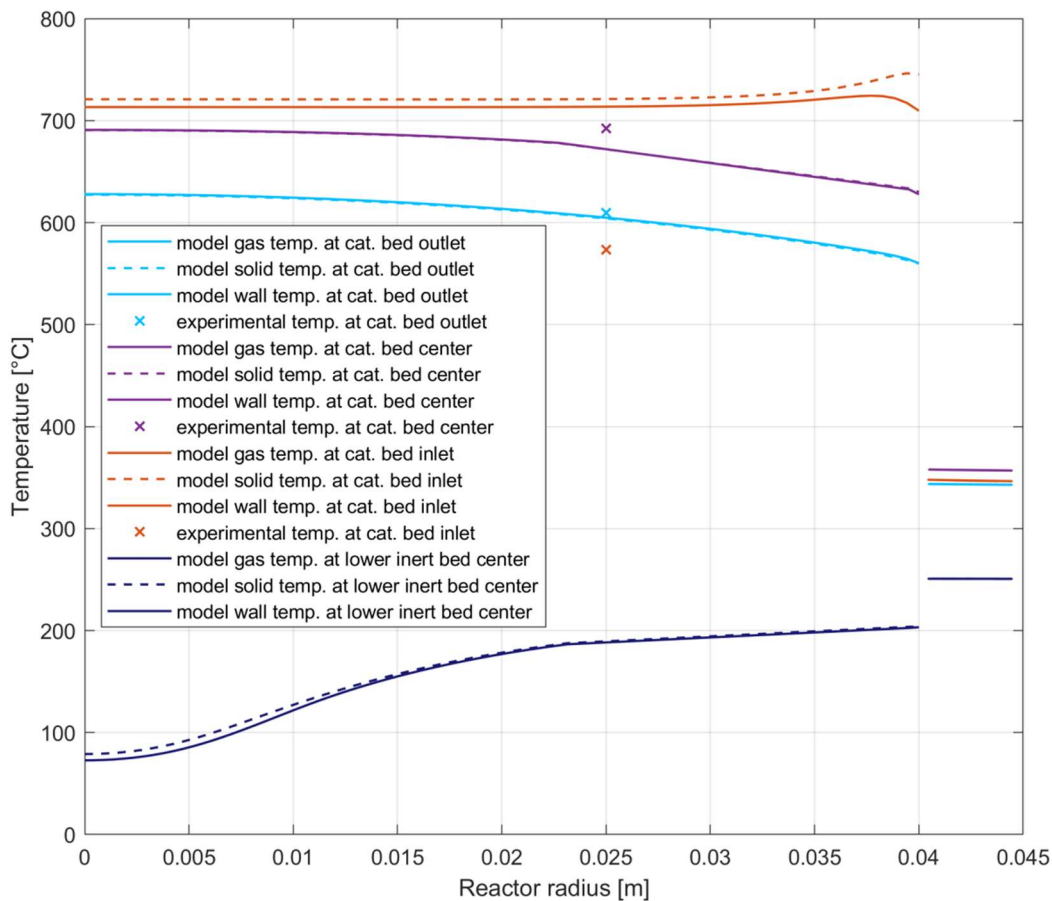


Figure 8: Radial temperature profiles of an 80 mm diameter fixed bed reactor at the catalyst zone inlet (0.1 m reactor height), center (0.125 m reactor height) and outlet (0.15 m reactor height) of solid, gas and wall based on the 2D reactor model for a pressure of 8.03 bar and GHSV of 4000 h<sup>-1</sup>

Through significant reduction of diameter from 80 mm to 14 mm, the velocity was increased and the inner heat transfer limitation reduced. However, in the naturally cooled 14 mm reactor still severe hotspots were found. As shown in Figure 6, the radial heat transfer limitation of the naturally cooled 14 mm diameter reactor causes higher peak temperatures (e.g. 839 °C at 8000 h<sup>-1</sup>, 6 bar) compared to a 14 mm reactor with oil-cooling (e.g. 757 °C at 8000 h<sup>-1</sup>, 6 bar) at equal process conditions despite lower reaction heat release due to lower conversion in the naturally cooled system. The 14 mm reactor with natural air-cooling is an example of radial heat transfer limitation at the outer wall interface, which was solved by active oil-cooling. **Wall-coolant heat transfer** of clearly superior oil-cooling can be further enhanced by increasing the

coolant Reynolds number. As a consequence, especially coolant velocity is the relevant influence factor as shown by Nusselt correlations according to Gnielinski [69] for thermal oil. Furthermore, the coolant temperature plays a decisive role because it affects not only wall-coolant heat transfer at the temperature peak, but also the catalyst temperature close to the input section and especially the product gas relevant output section of the reactor.

Limited radial heat transport leading to temperature increase within the reactor easily results in **thermodynamic limitation**. The thermodynamic equilibrium depends on the set of process conditions including gas concentration, pressure and temperature. As is presented in Figure 9, for Co-SOEC syngas an equilibrium composition with high methane concentration and CO<sub>2</sub> conversion can only be reached at temperatures below 350 °C and elevated pressures above 4 bar.

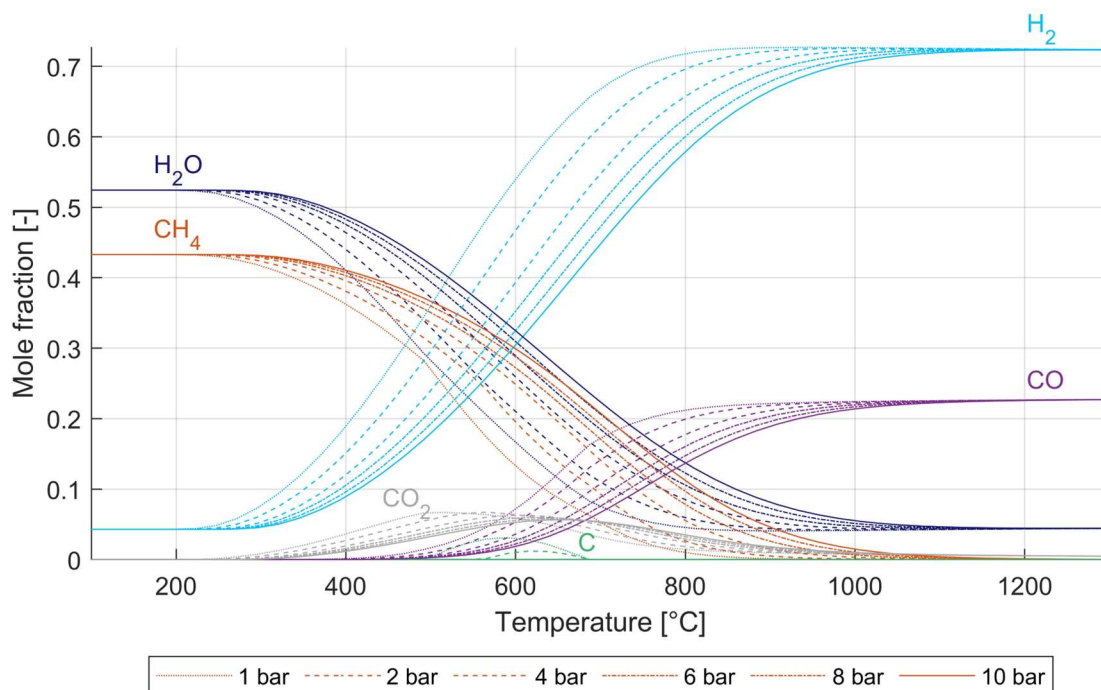


Figure 9: Equilibrium composition of Co-SOEC syngas in dependence of temperature and pressure based on Co-SOEC syngas composition with 3% hydrogen excess (76.8 vol.-% H<sub>2</sub>, 18.3 vol.-% CO and 4.9 vol.-% CO<sub>2</sub>)

The effective reaction rate is defined by the process conditions within the reactor and plays also a decisive role for the overall performance of Co-SOEC methanation in fixed beds. For the effective reaction rate it should be distinguished between intrinsic kinetics and mass transport limitation. The **intrinsic reaction** rate is a function of gas concentration, pressure and temperature, as mentioned before. Kinetics dependencies can be derived according to the intrinsic kinetic formulations by Rönsch [70] as used in paper I [8] and paper II [55]. Higher pressures, higher temperatures and higher educt concentrations lead to higher reactions rates.

**Mass transport between the bulk gas and the catalyst** can be limiting, especially for low gas turbulences, as shown in paper I. In Figure 10 extremely low catalyst efficiencies around 1 % were calculated for Co-SOEC methanation in the 80 mm reactor due to very low gas

velocities. Mass transport limitation between bulk gas and active sites on the catalyst surface depends on the pellet size and characteristics (pore diameter) as well as on the gas velocity.

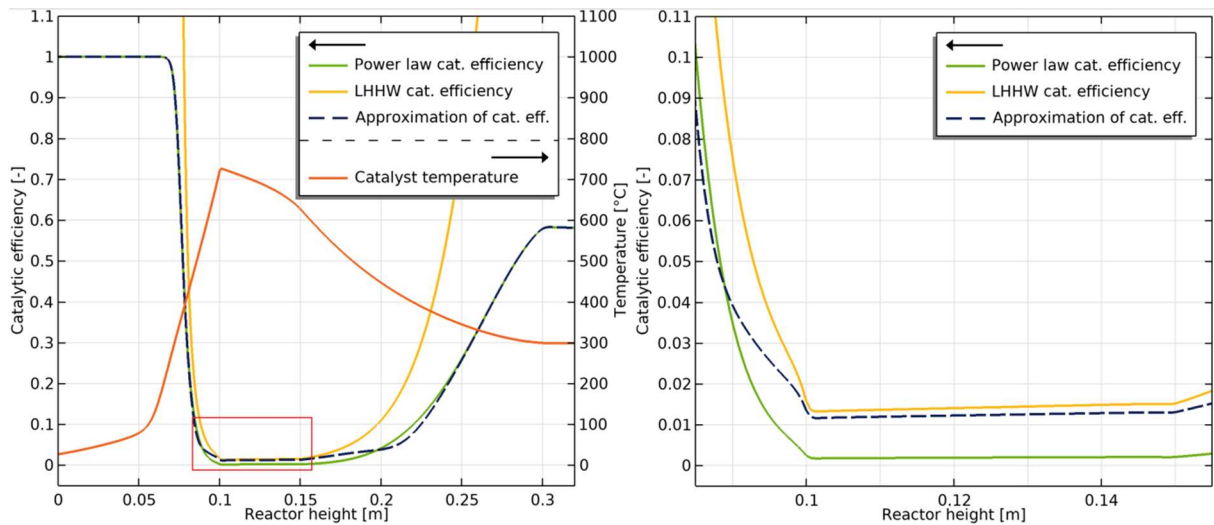


Figure 10: Catalytic efficiency (left ordinate) from a power law, a Langmuir-Hinshelwood-Hougen-Watson and new approximation approaches along with catalyst temperature (right ordinate) over the reactor height in the central reactor axis at  $4000 \text{ h}^{-1}$  and 8 bar in a 80 mm diameter 50 mm length reactors including a closer look (red frame) with higher resolution of the catalyst zone in the right diagram

In Figure 11 the catalytic efficiency for a 14 mm reactor is presented. High gas velocities in smaller reactor diameters generate high turbulences (high Reynolds numbers), which lead to high Sherwood numbers which consequently decreases mass transport limitation. [19] In the center and output section of the 14 mm reactor, which are due to lower reaction rates the essential zones for good reactor performance, the catalytic efficiency was roughly increased by an order of magnitude. In zones with highest temperatures and therefore already too high reaction rates catalytic efficiencies as low as 4 % were found in the 14 mm reactor at high GHSV values.

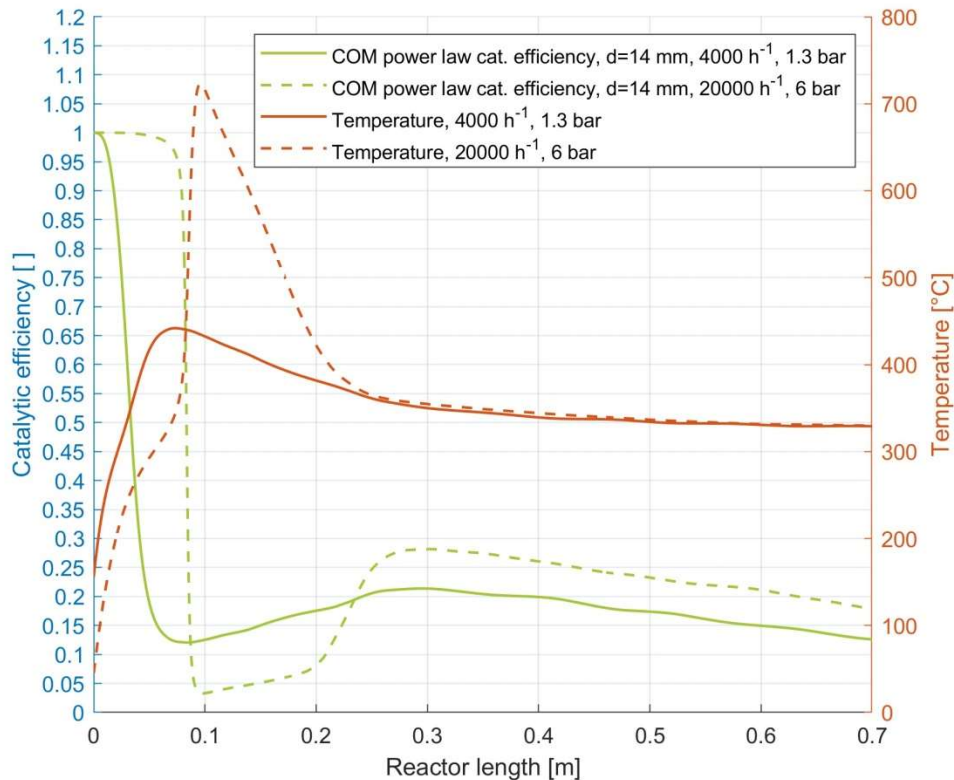


Figure 11: Catalytic efficiency (left ordinate) from a power law approach along with temperature (right ordinate) over the reactor length at  $4000 \text{ h}^{-1}$ , 1.3 bar and  $20000 \text{ h}^{-1}$ , 6 bar in a 14 mm diameter 700 mm length reactor

For stable operation certain boundary conditions in terms of temperature, pressure and concentration have to be met to exclude hindering side effects. The two most important performance hindering side effects are catalyst sintering and carbon deposition, which can lead to lower conversion over time or even complete system failure.

Hot spots caused by low radial heat transport and high kinetics can lead to **catalyst sintering**. Catalyst sintering can be avoided if the maximum reactor temperature is kept below the maximum allowed catalyst temperature stated by the supplier, such as  $510 \text{ }^\circ\text{C}$  maximum temperature for the catalyst Meth134 used in paper I, II, III.

**Carbon deposition** can be highly likely omitted, if explicit thermodynamic conditions for carbon formation are avoided. Thermodynamic carbon deposition is defined by the C-O-H ratio, temperature and pressure. Carbon deposition was discussed via ternary diagrams in paper III and is shown in Figure 12 [71]. In the ternary diagram is shown, that no carbon deposition is thermodynamically possible for the Co-SOEC syngas. However, if intermediate water removal is conducted between a first and second reactor stage, carbon deposition is thermodynamically possible. As a consequence, if a second reactor stage with intermediate water removal is used low temperature and high pressures should be aimed at to reduce carbon deposition ( $<400 \text{ }^\circ\text{C}$ ,  $>4 \text{ bar}$ ) as shown in paper III [71]. Ideally, single stage Co-SOEC

syngas methanation without intermediate water removal is possible based on an advanced reactor design, as shown in chapter 4.4.

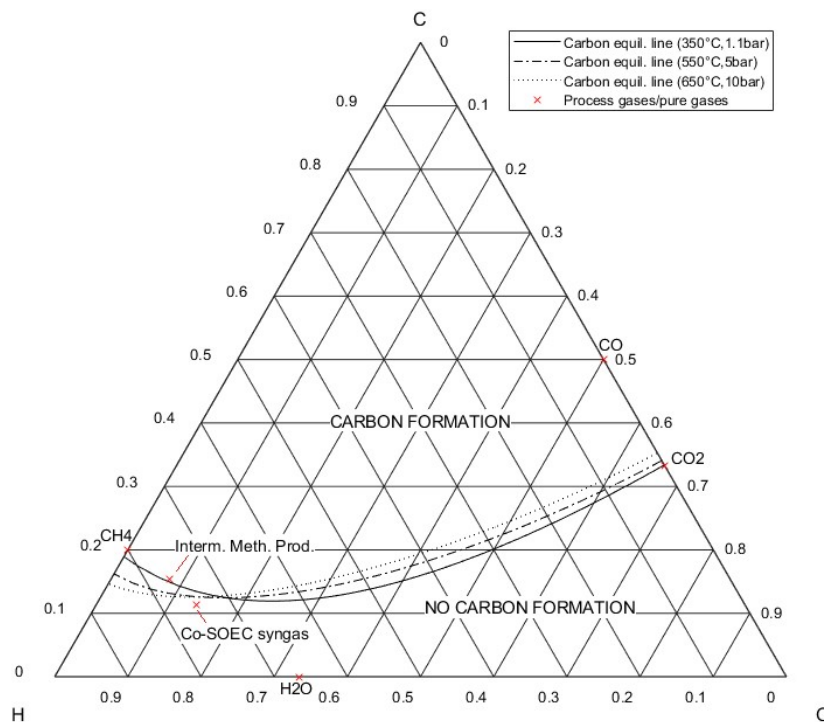


Figure 12: Ternary carbon-hydrogen-oxygen-proportion diagram including solid carbon equilibrium lines at three different temperature-pressure pairs (marked by lines) and the position of process gases (marked by red crosses) representing the thermodynamic carbon formation property of Co-SOEC syngas.

The most important rate and performance limiting factors can be summarized as:

- Radial heat transport
  - Effective radial heat conduction (Inter-bed heat transport)
  - Heat transfer between fixed bed and wall
  - Heat transfer between wall and coolant
- Thermodynamics
- Intrinsic kinetics
- Mass transfer between bulk gas and catalyst surface
- Carbon deposition
- Catalyst sintering

The understanding of these limiting factors was the most important finding drawn from the extensive experimental and modelling investigation with the 80 mm reactor presented in scientific paper I. In scientific paper II these limitations could be significantly reduced in the not actively cooled and especially the oil-cooled 14 mm reactors. The maximum conversion

increased from 8000 h<sup>-1</sup> GHSV and 61 % CO<sub>x</sub> (80 mm diameter, naturally cooled reactor) conversion to 93.5 % at 29000 h<sup>-1</sup> both at 6 bar (14 mm diameter, oil-cooled reactor).

In Figure 13 the most relevant limiting factors for the design of fixed bed CO/CO<sub>2</sub> methanation and its influential parameters are once again clustered in a graphic.

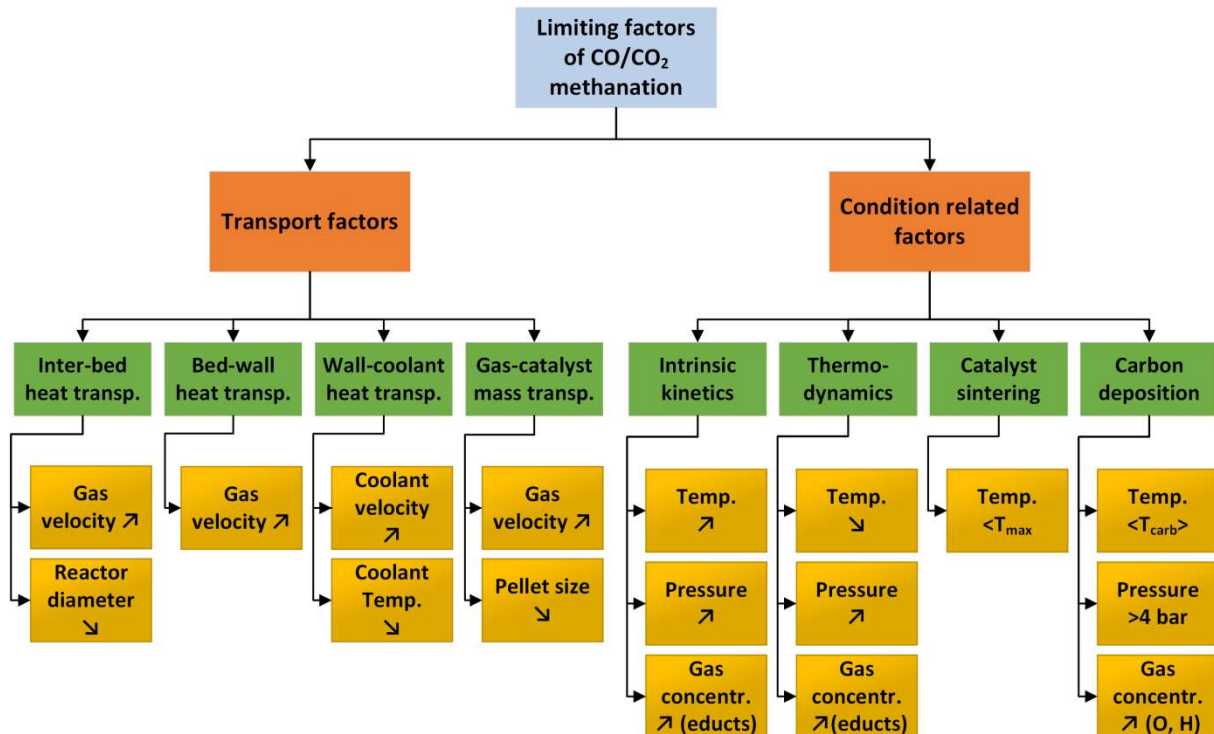


Figure 13: Overview of performance limiting factors (green) of fixed bed CO/CO<sub>2</sub> methanation and the influential design and operation parameters (yellow) including an indication of limitation how to reduce it by ↗ (increase to improve) and ↘ (decrease to improve).

Increasing the gas velocity enhances several transport limitations in a fixed bed. For methanation at very high gas velocities the pressure drop at some point becomes an additional limiting factor, which was set aside in this chapter due to insignificance under the used conditions.

In addition, the gas channelling effects as a consequence of uneven porosity distribution can be relevant as is shown in Figure 14. The porosity distribution in radial direction calculated from Giese [66] and de Klerk [67] shows significant variation, especially for low diameters. In contrast, small reactor diameters (and small diameter ratios of approximately 3 or lower) in industrial [72–74] and experimental [75, 76] applications were realized with success. The focus on temperature reduction by higher radial heat transfer in small diameter reactors still may outweigh the decreasing conformity to ideal plug-flow.



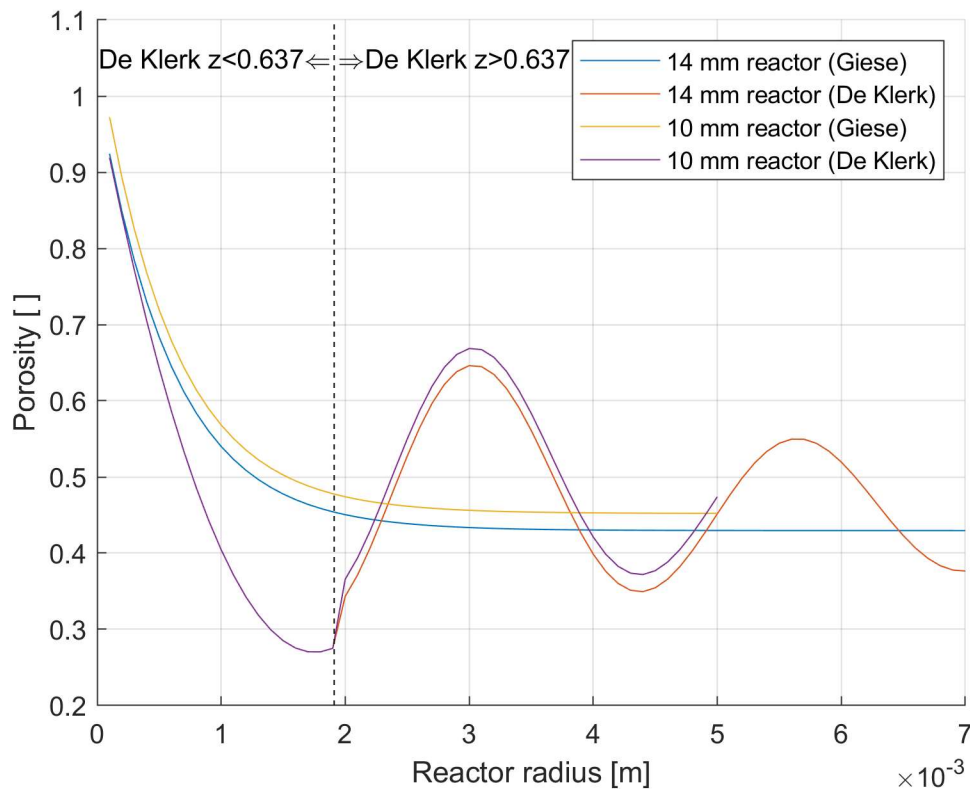


Figure 14: Radial porosity distribution of 14 mm and 10 mm diameter reactors based on empirical methods by Giese [66] and de Klerk [67] (reactor radius is 0 at the reactor wall)

## 4.2 Answer to research question 2: Is the CO/CO<sub>2</sub> methanation limited by thermodynamics or kinetics and what is the influence of reactor cooling?

It is of the essence for reactor optimization to investigate the kinetically and thermodynamically limited sections within a reactor at given process conditions for CO/CO<sub>2</sub> methanation. Thermodynamics and intrinsic kinetics are both related to process condition parameters temperature, pressure and gas concentrations. While increased pressure and higher educt gas concentration favor kinetics as well as thermodynamics, the temperature dependency is contrary. If the thermodynamic is limiting, a reduction of temperature would speed up the process. If the thermodynamic is not limiting, it can be considered kinetically limited and a temperature increase according to Arrhenius law is beneficial.

In Figure 15 temperature and mole fraction profiles of two reactors, one with natural air cooling and one with active cooling are compared at the same GHSV and pressure pair of 8000 h<sup>-1</sup> and 6 bar. This comparison reveals alternating kinetic and thermodynamic domination along the reactor axis highlighted via the background color, which also completely changes with the cooling method. Figure 15 and Figure 16 are based on the 1D PFR model and are presented in a very similar form in paper II. They were only supplemented in this thesis by a kinetic limitation analysis. This was achieved by simply checking within the model algorithm if a temperature increase (kinetic limitation) or a temperature decrease (thermodynamic limitation) leads to an increase of reaction rate of CO methanation and WGS reaction, as can also be described by Equation 46 and Equation 47.

Kinetic limitation:

$$\frac{dr_j}{dT} > 0$$

(Equation 46)

Thermodynamic limitation:

$$\frac{dr_j}{dT} < 0$$

(Equation 47)

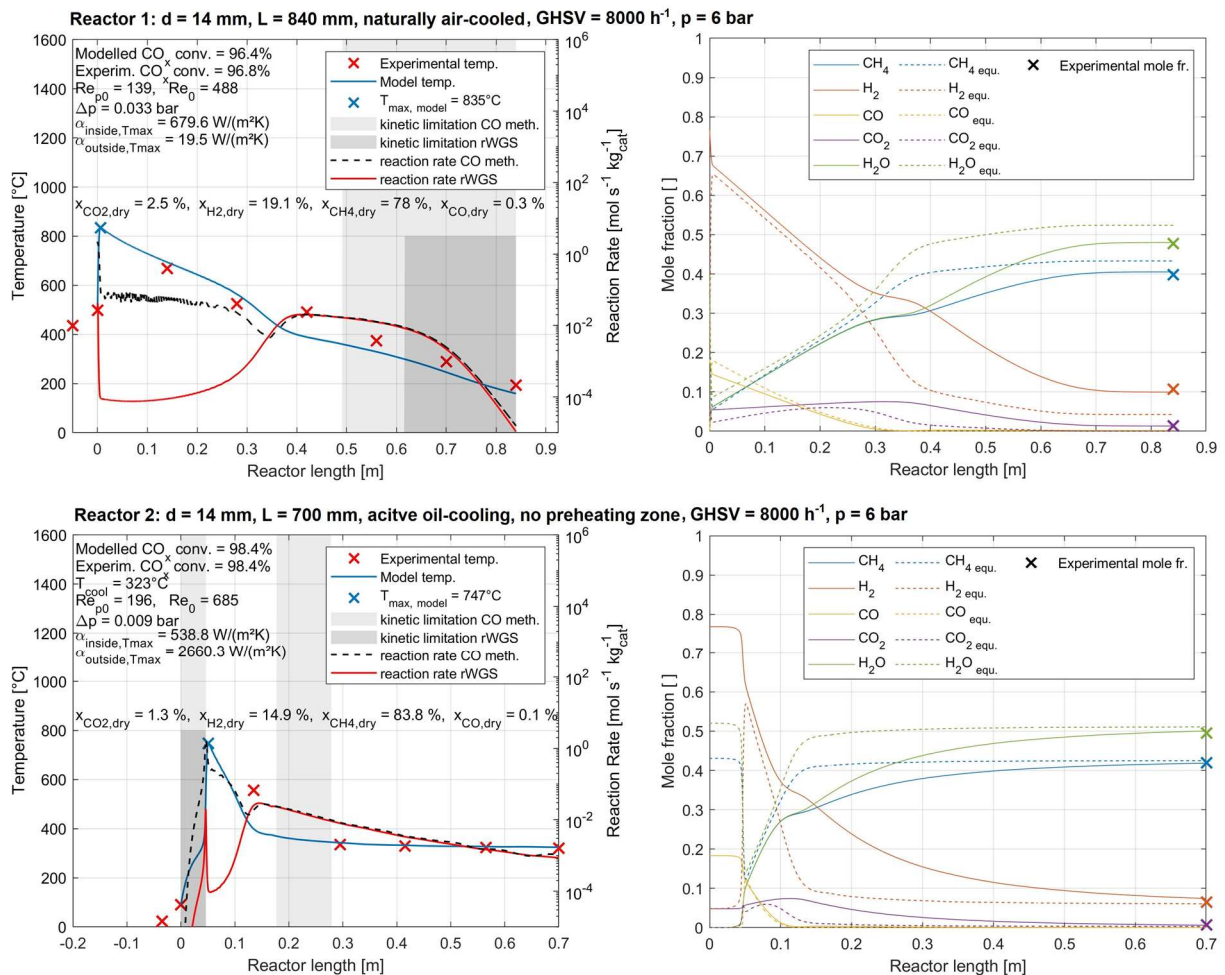


Figure 15: Axial profiles of modelled (lines) and experimentally determined ('x'-markings) temperature and molar fractions of the 14 mm diameter and 840 mm long naturally cooled compared to the 700 mm long actively oil-cooled reactor at 8000 h<sup>-1</sup> and 6 bar including indication of kinetic limitation for CO methanation and WGS reaction by grey background (CO<sub>x</sub> conversions, Reynolds numbers, heat transfer coefficients and maximum temperature (blue 'x'-marking) included).

The naturally with ambient air (~20 °C) cooled system is due to an immediate temperature jump initially dominated by thermodynamic limitation, which means a reduction in temperature would increase the reaction rate for the first 500 mm of catalyst length until the temperature hits about 370 °C. This is confirmed by the modelled mole fraction profiles, which show little deviation to the equilibrium mole fractions in the first third of the reactor, also indicating thermodynamic limitation. Downstream of 500 mm catalyst length the temperature continues to drop due to cooling to 20 °C ambient air. At lower temperatures <370 °C the system is

hindered at the given pressure by kinetics. At first only regarding the CO methanation and about 100 mm further downstream also kinetic limitation of the WGS reaction occurs. As a result, oil-cooling at elevated temperature around 280-320 °C can play an important role in two respects. Reducing the temperature in the first half of the reactor to reduce thermodynamic limitation and increase the temperature in the second half to reduce kinetic limitation.

In the oil-cooled reactor the temperature does not immediately spike but starts at low initial temperature around 90 °C, as no preheating of the gas was conducted in reactor 2. This leads to low initial kinetics for CO methanation and WGS reaction, but kinetic is rapidly increasing with increasing temperature. This zone between reactor input and temperature peak is a typical example of a kinetically limited section with an exponentially increasing temperature profile. Only 747 °C maximum temperature appears due to oil cooling, instead of 835 °C in the naturally cooled reactor. A faster decrease of temperature in the actively oil-cooled reactor shortens the reactor length with thermodynamic limitation compared to the air-cooled system until the reactor temperature approaches the oil-cooling temperature around 323 °C.

Furthermore, the mole fraction profiles reveal, that CO is fully consumed as it is transformed to methane at some point along the reactor axis. Consequently, further downstream from 300 mm reactor length in the naturally cooled and from 110 mm reactor length in the oil-cooled reactor, the water gas shift reaction becomes the limiting reaction. For both reactors, this is the greater part of the reactor length. A short zone of CO methanation kinetic limitation between 180 and 280 mm reactor length occurs in the oil-cooled reactor. However, considering the WGS reaction is the rate dominating reaction, the oil-cooled reactor is still thermodynamically limited to a great extent of its length (93%), starting from the temperature peak until the reactor outlet.

In Figure 16 the same temperature and mole fraction profiles are presented for two reactors with and without preheating zone both at higher GHSV of 25000 h<sup>-1</sup>. While reactor 2 has no preheating zone, in reactor 3 the incoming gas is heated up by the oil-cooling (~323°C) leading to significantly higher initial temperatures. Effective heat conduction in countercurrent direction leads to temperature increase above oil-temperature at the catalyst zone inlet of reactor 3.

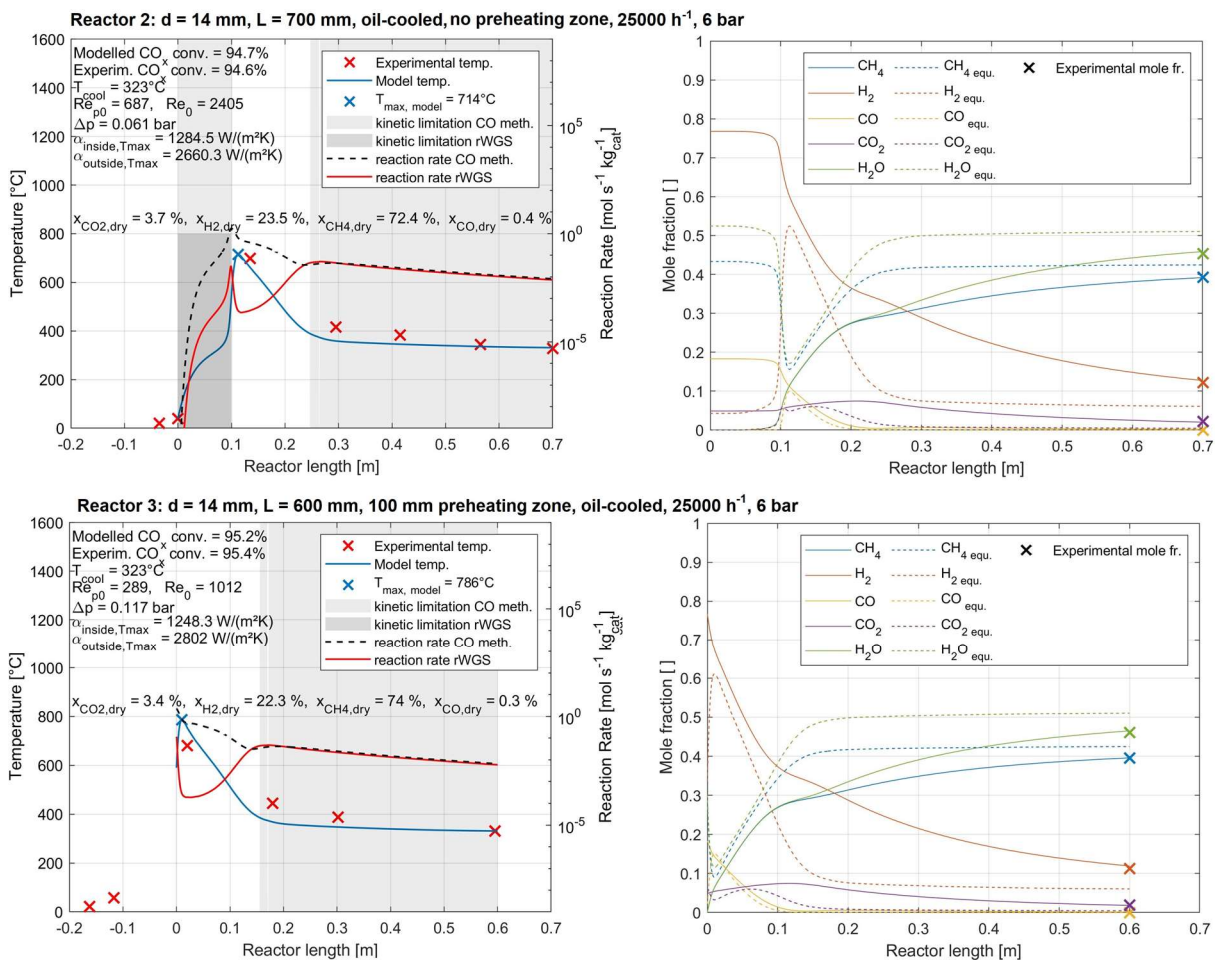


Figure 16: Axial profiles of modelled (lines) and experimentally determined ('x'-markings) temperature (left) and molar fractions (right) of the 14 mm diameter and 700 mm long oil-cooled reactor without preheating zone compared to the 600 mm long oil-cooled reactor with 100 mm preheating zone at 25000 h<sup>-1</sup> and 6 bar including indication of kinetic limitation for CO methanation and WGS reaction by grey background (CO<sub>x</sub> conversions, Reynolds numbers, heat transfer coefficients and maximum temperature (blue 'x'-marking) included).

The temperature profile of reactor 2 is characterized by a typical exponential increase in temperature in a kinetically limited zone, as discussed in Figure 15 for reactor 2. With higher GHSV this kinetically limited zone widens from 46 mm at 8000 h<sup>-1</sup> to 100 mm at 25000 h<sup>-1</sup>. Due to higher gas velocities and therefore higher radial heat transport the temperature peak decreases despite more reaction heat is released at more than 3 times higher mass flow. This is a strong indication, that the gas velocity and the radial heat transfer play a crucial role.

In comparison, in reactor 3 the initially rising temperature slope is almost completely omitted due to the preheating zone and very high initial kinetics. As a consequence, the preheating also leads to a higher temperature peak of 786 °C compared to 714 °C with no preheating. Without preheating some of the educts already react at a lower reaction rate in the kinetically dominated section. Therefore, the thermodynamic limitation is reached at a lower temperature since already less educts and more products are present at the peak.

Downstream of the temperature peak both reactor 2 and reactor 3 are predominantly thermodynamically limited. Again, CO is soon fully consumed making the WGS reaction the dominant reaction. Consequently, the kinetic limitation of the CO methanation reaction in the last, roughly 450 mm long section in reactor 2 and reactor 3 is not relevant, as shown in Figure 16.

The dominance of the WGS reaction can also be seen in the reaction rate curves. At first the CO methanation reaction rate spikes in accordance with temperature. Roughly 120 mm downstream of the temperature peak the CO methanation reaction rate approaches the significantly lower and rate determining WGS reaction rate.

In conclusion, the following list summarizes the essential points regarding thermodynamic vs. kinetic limitation and oil-cooling.

- Oil-cooling of fixed bed CO/CO<sub>2</sub> methanation reduces temperature peaks, reduces thermodynamic limitation in the first section of the catalyst bed and kinetic limitation in the latter section of the catalyst bed found in naturally air-cooled reactors.
- CO/CO<sub>2</sub> methanation is strongly dominated by the WGS reaction rate rather than the CO methanation reaction as CO is fully consumed.
- The reaction rate of CO/CO<sub>2</sub> methanation with oil-cooling at 320 °C cooling temperature can be still thermodynamically limited downstream of the temperature peak. Lower cooling temperatures can be favorable.
- Preheating the feed gas leads to shorter catalyst zone lengths at the cost of higher temperature peaks (and preheating length)
- Oil-cooled reactors and moderate GHSVs (8000 h<sup>-1</sup>) are limited by radial heat transfer inside the reactor (inter bed and bed-wall). However, an increase in GHSV (25000 h<sup>-1</sup>) and therefore higher gas velocity significantly reduces the temperature peak despite higher total reaction heat (similar conversion, 3-fold mass flow increase).

Two consequences and proposal for further research can be drawn by the found results:

- A reduction of oil-cooling temperature beneath 320 °C can improve process performance.
- Using catalyst suitable to accelerate the WGS reaction, for example by doping nickel-based catalyst, could have a decisive positive impact on CO/CO<sub>2</sub> methanation.

### **4.3 Answer to research question 3: What is the dependency of heat and mass transfer from operational and design parameters and what is the sensitivity to enhance methanation performance?**

Performance limitation can not only result from condition related thermodynamic and kinetic limitation (chapter 4.2) but also from heat and mass transport factors. To improve methanation reactor performance radial heat transport and gas-catalyst mass transfer needs to be enhanced through appropriate reactor dimension and operation parameters. Therefore, the dependencies of parameters influencing heat and mass transport were derived from the 1D PFR model in MATLAB. The relevant heat and mass transfer coefficients are listed below.



- Inner heat transfer coefficient (Equation 20)
- Effective heat conductivity (Equation 28)
- Catalytic efficiency (Equation 35-42)
- Radial heat flux equivalent (Equation 31 and Equation 33)
- CO<sub>x</sub> conversion (Equation 45)
- Maximum temperature

In Figure 17 the dependency of the heat transfer coefficient at the inner fixed bed-wall interface and the effective fixed bed heat conductivity from the superficial input velocity is presented.

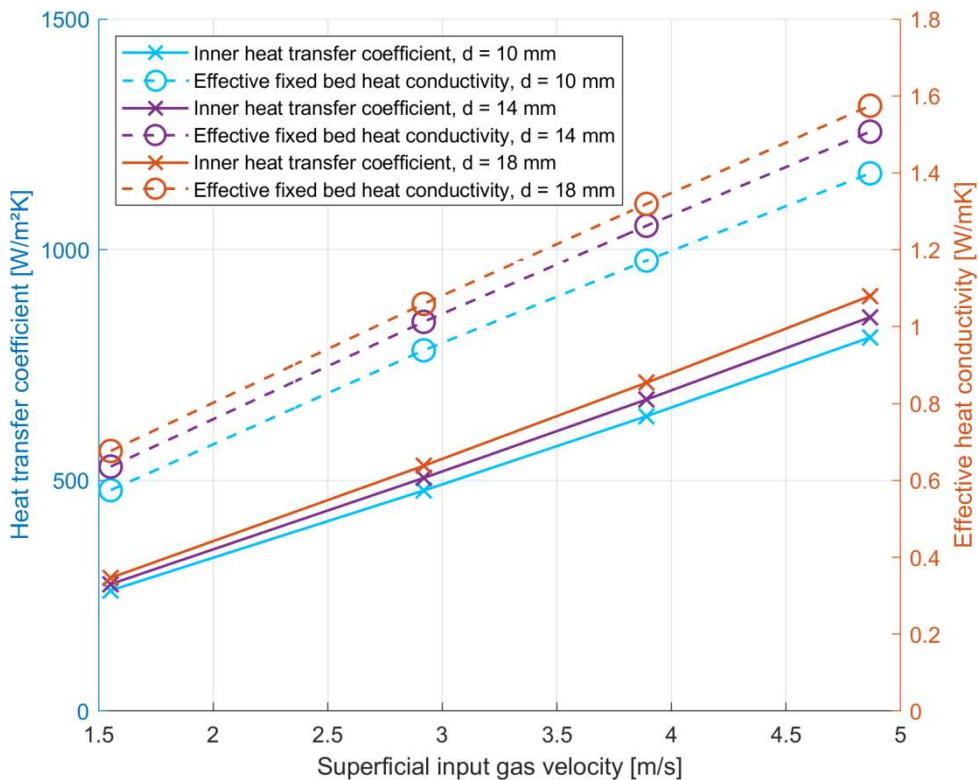


Figure 17: Inner bed-wall heat transfer coefficient and effective fixed bed heat conductivity over superficial input gas velocity for 8000 h<sup>-1</sup>, 15000 h<sup>-1</sup>, 20000 h<sup>-1</sup> and 25000 h<sup>-1</sup> at 6 bar and for 10 mm, 14 mm and 18 mm reactor diameter at 700 mm catalyst length.

It can be seen that the heat transfer coefficient increases almost linearly by 165-182 W m<sup>-2</sup> K<sup>-1</sup> and the heat conductivity by roughly 0.25-0.27 W m<sup>-1</sup> K<sup>-1</sup> per every 1 m s<sup>-1</sup> velocity increase. Through an increase of the GHSV from 8000 h<sup>-1</sup> to 25000 h<sup>-1</sup>, which is proportional to a velocity increase from 1.6 m s<sup>-1</sup> to 4.9 m s<sup>-1</sup> at constant reactor length, the bed-wall heat transfer coefficient could be increased by roughly 210 % and the effective bed conductivity on average by 138 % with only small deviations between the tested diameters. An increase in diameter from 10 mm to 18 mm leads to a maximum increase in bed wall heat transfer by 11 % and in bed conductivity by 13 % at 25000 h<sup>-1</sup>. The small enhancing effect of larger diameters on these heat transport coefficients is overcompensated when the complete diameter influence on the radial heat flux is considered making small diameters beneficial for radial heat transfer, as will be explained below.



Mass transport limitation within the porous catalyst pellet and between catalyst surface and bulk gas via gas diffusion can be obtained by the catalyst efficiency. In Figure 18 the catalyst efficiency over the superficial input velocity for the CO methanation reaction and the water gas shift reaction is presented.

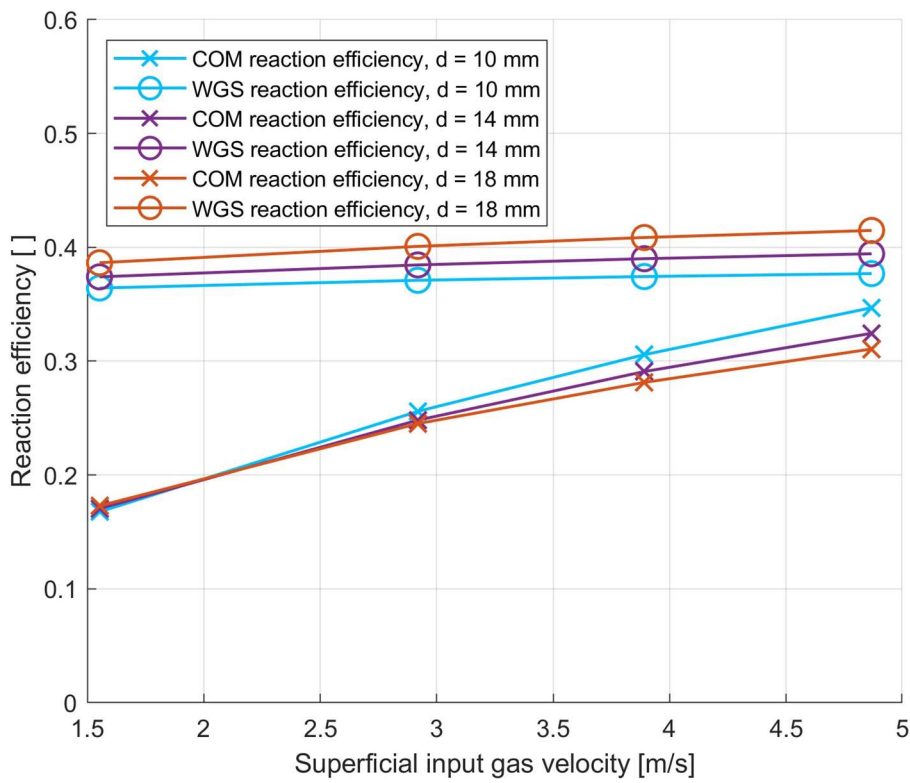


Figure 18: Catalyst efficiency for CO methanation (COM) and water gas shift reaction (WGS) over superficial input gas velocity for  $8000 \text{ h}^{-1}$ ,  $15000 \text{ h}^{-1}$ ,  $20000 \text{ h}^{-1}$  and  $25000 \text{ h}^{-1}$  at 6 bar and for 10 mm, 14 mm and 18 mm reactor diameter at 700 mm catalyst length.

Figure 18 proves that the reaction efficiency of the CO methanation reaction increases by 80-107 % due to an increase of gas velocity by 213 %, whereas the water gas shift reaction efficiency remains almost constant (3-7 % increase). The water gas shift reaction efficiency therefore could mainly result from low CO concentrations, consequently an increase in gas turbulence at higher velocities has almost no beneficial effect. Again, the diameter effect on the efficiency factor is limited with 10 % increase for the CO methanation and 12 % for the water gas shift reaction for  $25000 \text{ h}^{-1}$ .

As is explained in Equation 29 to Equation 33 the radial heat flux is a function of heat transfer coefficients, heat conductivity and diameter. The velocity and diameter dependency of the radial heat flux is presented in Figure 19. For a one dimensional approach the consideration of only the heat transfer coefficient between fixed bed and wall, the wall heat conduction and the wall-coolant heat transfer as in the heat flux  $q'_r$  is viable (Equation 31). However, the effective fixed bed heat conductivity taking into account dispersion also plays a crucial role for radial heat transport. As a consequence, an artificial mean radial heat flux equivalent  $q'_{r,bed-oil}$  (Equation 33) considering all heat transfer resistances including effective conduction within the

bed, transfer at the bed-wall interface, the wall conductivity and the outer wall-coolant interface is additionally presented in Figure 19.

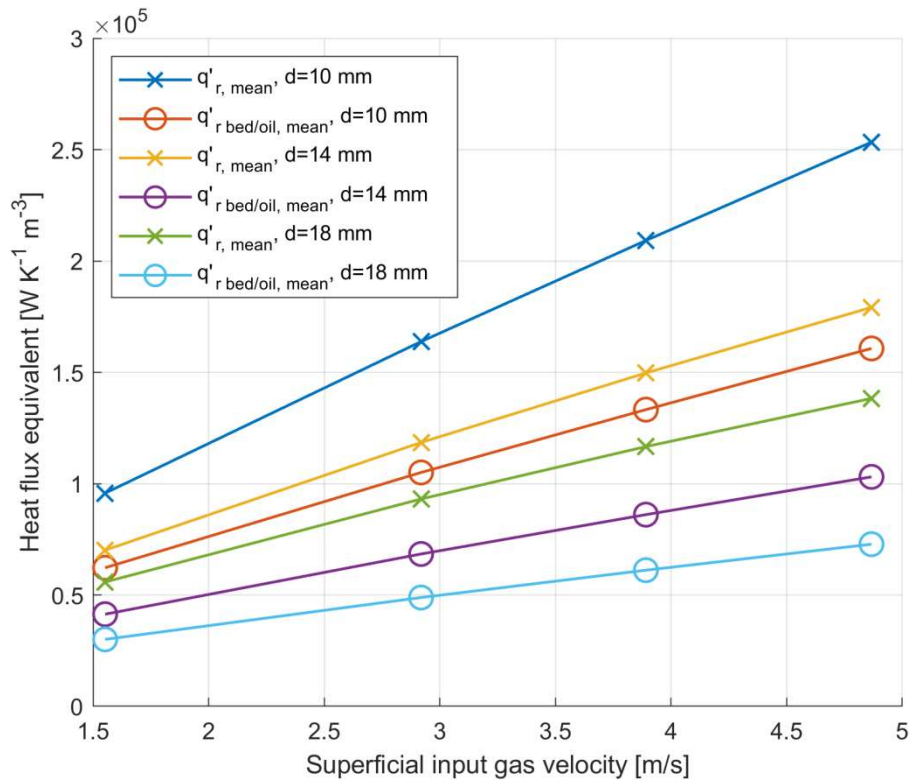


Figure 19: Mean radial heat flux equivalent without temperature difference influence (Equation 31 and Equation 33) over superficial input gas velocity for 8000 h<sup>-1</sup>, 15000 h<sup>-1</sup>, 20000 h<sup>-1</sup> and 25000 h<sup>-1</sup> at 6 bar and for 10 mm, 14 mm and 18 mm reactor diameter at 700 mm catalyst length.

The superficial gas velocity increase from 1.6 m s<sup>-1</sup> to 4.9 m s<sup>-1</sup> leads to an increase in temperature difference omitted heat flux for a 1D PFR approach  $q'_{r, \text{mean}}$  by 148-165 %. The radial heat flux equivalent including all radial heat resistances  $q'_{r, \text{bed-oil}}$  was increased by 142-158 % due to a 213 % velocity increase. For 25000 h<sup>-1</sup> the diameter increase from 10 mm to 14 mm led to an increase of heat flux  $q'_{r, \text{mean}}$  by 83 % and of heat flux  $q'_{r, \text{bed-oil}}$  by 121 %.

Figure 20 displays the dependency of COx conversion and maximum temperature from gas velocity and reactor diameter. The COx conversion and the maximum temperature are important indicators for methanation performance.

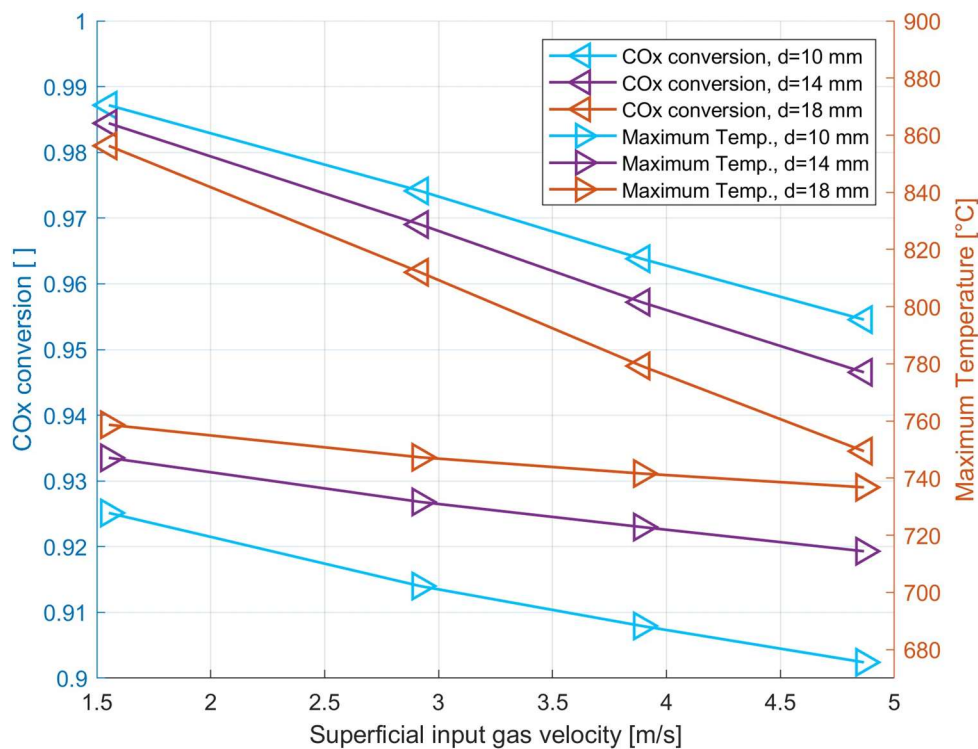


Figure 20: COx conversion and maximum temperature over superficial input gas velocity for  $8000 \text{ h}^{-1}$ ,  $15000 \text{ h}^{-1}$ ,  $20000 \text{ h}^{-1}$  and  $25000 \text{ h}^{-1}$  at 6 bar and for 10 mm, 14 mm and 18 mm reactor diameter at 700 mm catalyst length.

In Figure 20 it is shown, that smaller reactor diameters and higher gas velocities lead to lower peak temperatures, which is a consequence of higher radial heat transport. The decrease of temperature peaks with higher GHSV values comes at the cost of lower COx conversions. However, smaller reactor diameters can partially compensate for the loss of conversion resulting from higher GHSV.

In conclusion, the methanation performance is defined to a large extent by heat and mass transfer parameters, which are influenced by the reactor diameter and the gas velocity. The most important learnings from the analysis of the influence of transport factors are listed below:

- Higher gas velocities in fixed bed methanation reactors have a significantly beneficial effect on heat and mass transport properties (bed-wall, bed conductivity, catalytic efficiency).
- Higher diameters do not have a strong influence on these heat and mass transport properties.
- The radial heat flux, corrected by the influence of temperature difference, is highly influenced by both diameter (+121% from 18 mm to 10 mm diameter reduction) and gas velocity (+158% from  $1.6 \text{ m s}^{-1}$  to  $4.9 \text{ m s}^{-1}$  velocity increase).
- Temperature peaks can be significantly reduced by small reactor diameters and by higher gas velocities despite higher total reaction heat at higher loads.
- The COx conversion decreases from a high level (>98 % at  $1.6 \text{ m s}^{-1}$ ) with increasing velocity (>93% at  $4.9 \text{ m s}^{-1}$ ) but again increases with lower reactor diameter (+2 %-points).

As a consequence, one of the most hindering challenges for methanation of CO/CO<sub>2</sub> mixtures in oil-cooled fixed bed reactors, extremely high temperatures, can be substantially addressed by using small diameters to minimize heat and mass transport limitation. In combination with pressure adjustment to lower levels and high-temperature catalyst (~600 °C maximum temperature), this problem can be fully solved. However, higher gas velocities at lower diameters also lead to increasing pressure loss. Practical limitations during the filling procedure of small reactor tubes with catalyst and adverse bed distribution at low catalyst pellet-reactor diameter ratios have to be considered. In a following step, the reactor length and the thermodynamic conditions at the reactor output must be adjusted accordingly to enable sufficient COx conversion in a single reactor stage, as is thoroughly discussed in the next chapter.

#### **4.4 Answer to research question 4: What process and design strategies can be derived to overcome limiting effects and achieve maximum methanation performance?**

The findings of the first three research questions led to the formulation of design rules, which can be understood as design principles supporting design decisions for methanation reactors converting CO/CO<sub>2</sub> mixtures. The temperature curve is one of the most important performance indicators of a methanation reactor and is suitable to discuss the optimum design of methanation reactors. The temperature profile is influenced by all design and operation parameters, and it defines how much product gas per reactor volume and time (kinetics) in what quality (thermodynamics) can be produced. The axial temperature curve indicates what limitations occur in what zones of the reactor. This was elaborated in detail along the previous research questions.

A good reactor and cooling design is therefore crucial to “steer” the temperature curve. A proposal of six main rules for adequate reactor and cooling design of a catalytic methanation reactor is listed below and is illustrated based on the typical shape of temperature profiles of CO/CO<sub>2</sub> methanation reactors in Figure 21. Neubert [45] formulated 2 tasks of reactor cooling for fixed bed methanation reactors. These six rules are a further detailing of Neuberts proposal and are in particular meant for fixed bed methanation reactors especially for CO/CO<sub>2</sub> methanation with thermal oil cooling. In Figure 21 an illustration of the qualitatively optimal temperature curve including the 6 tasks of cooling are presented.

1. The input temperature should be kept above the reaction kick-off temperature, depending on the input concentration, pressure and catalyst type (appr. >250-300 °C).
2. The maximum catalyst temperature must be kept within the catalyst specification limits (usually 500–600 °C maximum temperature depending on catalyst) to avoid catalyst sintering. Without appropriate countermeasures such as active thermal oil-reactor cooling, almost the adiabatic maximum temperature would be reached, which is usually significantly above the maximum catalyst temperature (>700 °C depending on pressure and concentration).
3. However, it is favourable for higher conversion rates and reactor capacity to operate only slightly below the maximum catalyst temperature at the temperature peak, since the reaction rate increases exponentially with higher temperatures. In contrast, isothermal methanation

such as in fluidized beds without moderate hot-spots leads to low reactor capacities due to kinetic limitation.

4. Downstream of the temperature peak the reactor is highly likely thermodynamically limited for CO/CO<sub>2</sub> methanation without active cooling. Therefore, reactor cooling should ensure a significant reduction of temperature.

5. If the coolant temperature is too low (ambient air at 20 °C, water cooling at low pressure), kinetic limitation may occur in the rear section of the reactor. The theoretical optimum temperature profile can be reached if neither thermodynamic limitation, nor kinetic limitation occurs. The optimum cooling rate can be approximately met with thermal oil around 270-320 °C depending on exact conditions.

6. In addition, the output reactor temperature must be settled around 300 °C to ensure favourable thermodynamic conditions for high output methane concentrations. The thermodynamics of methanation of Co-SOEC was described in detail in paper I. The necessary output temperature depends on input concentration, pressure and aimed output concentration. For Co-SOEC syngas at 4 bar pressure at least 280 °C and at 6 bar 290 °C must be reached at the outlet to thermodynamically enable a dry output concentration of H<sub>2</sub> <10 vol.-% and CH<sub>4</sub> > 90 vol.-% necessary for direct grid injection.

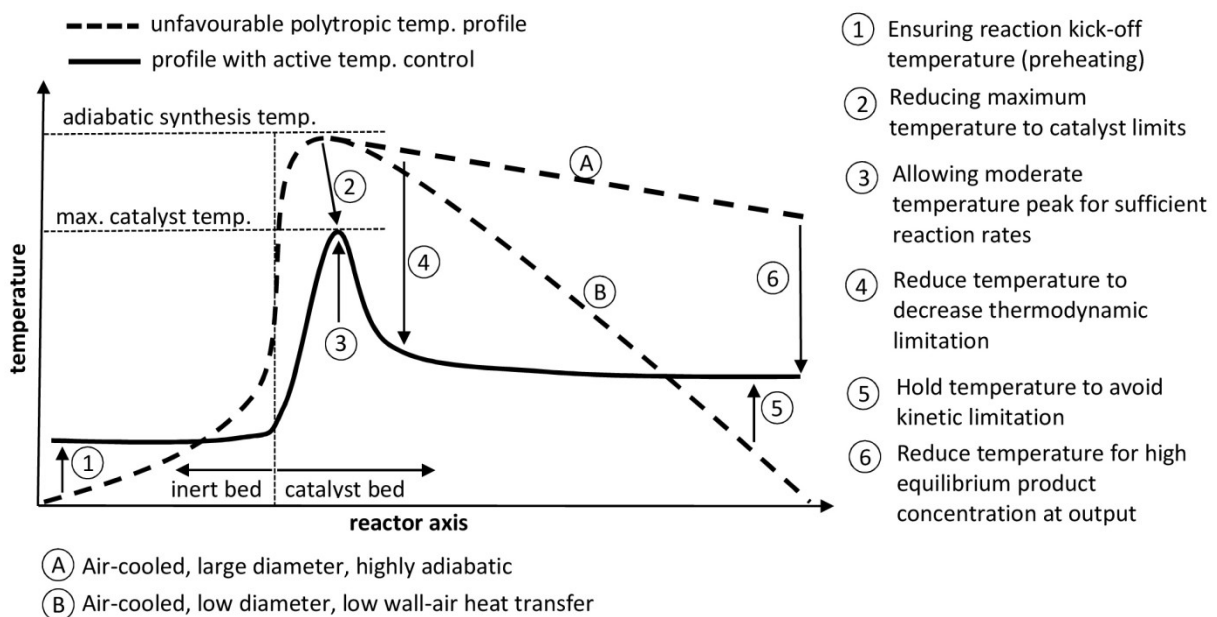


Figure 21: 6 main tasks of temperature control in a catalytic fixed bed methanation reactor (idea based on illustration from Neubert [45])

If these six design rules regarding the temperature profile are met, the methanation reactor will perform well, since the limitations are reduced as much as possible with low-complexity. The most important tuning parameters for tubular fixed bed methanation reactors to form this favourable temperature profile are:

1. the reactor diameter
2. the gas input capacity
3. the reactor pressure

4. the input gas temperature
5. the coolant temperature and velocity

Small reactor diameters increase radial heat transfer (Figure 17, Figure 19), enhance cooling and therefore especially reduce peak temperatures. At constant volume flow smaller diameters lead to an increase in conversion (Figure 20).

High gas input capacity can have a cooling effect (if the system is not limited by wall-coolant heat transfer e.g. in air-cooled systems), due to higher gas velocities, but also increases the absolute amount of heat produced due to higher absolute number of moles converted. On the downside, high volume flow at constant reactor diameter and length reduces the residence time, therefore in almost every case higher volume flow leads to lower conversions and higher pressure loss (Figure 20). The influence of higher gas volume flow can be described as almost a downstream shift of the temperature curve towards the reactor outlet and flattening of the temperature profile.

Higher reactor pressure reduces the kick-off temperature, increases the initial acceleration of the temperature increase (kinetics) and leads to higher temperature peaks. It mostly also leads to higher conversion rates and higher product concentrations since it is preferential in terms of thermodynamics, which is important especially at the outlet section. Pressure has no significant effect on the gas turbulence.

The input gas temperature has no severe influence, as long as it is above the kick-off temperature. The comparison of oil-cooled reactors with and without preheating zone shows, that no preheating with lower input temperatures leads to slightly lower peak temperatures (Figure 6). The total reactor length did not change, as 100 mm catalyst zone was traded with 100 mm preheating zone. However, preheating improves operation stability especially in flexibly operated systems as the kick-off temperature can be held no matter the pressure and volume flow.

Coolant temperature and velocity are important design parameters. The oil velocity should be chosen to match the necessary heat removal rate defined by the heat transfer at the wall-coolant interface under consideration of the chosen temperature value. As shown in Figure 15 and Figure 16, a wall-coolant heat transfer coefficient above  $2000 \text{ W m}^{-2} \text{ K}^{-1}$  should be aimed for. The cooling temperature should be chosen in the range of 250-350 °C, depending on the aimed output concentration, input concentration and pressure.

One important parameter, which was not changed in the course of this thesis, is the hydrogen excess, as its effect is quite clear. Higher  $\text{H}_2$  excess above the stoichiometric minimum amount has several beneficial effects to the methanation process. More hydrogen improves thermodynamics, kinetics, carbon deposition prevention and thermal management, as more ballast gas increases velocity and heat capacity flow leading to lower temperatures. However, already a small excess in the feed leads to a significant concentration in the dry product gas due to the volume reducing methanation reaction. From Co-SOEC syngas feed with about 3 % excess of  $\text{H}_2$  a dry product concentration of 9 vol.-%  $\text{H}_2$  and 91 vol.-%  $\text{CH}_4$  is formed at 100 % conversion. To enable direct grid injection without downstream  $\text{H}_2$  removal, the  $\text{H}_2$  feed



concentration should be chosen accordingly. In Austria and in most European countries the maximum H<sub>2</sub> concentration for grid injection is currently 10 vol.-%. [46,77–79]

Under consideration of the aforementioned design recommendations an example design for Co-SOEC syngas based on Meth134 catalyst and thermal-oil cooling was conducted. For the highly reactive feed gas a sweet spot at high gas input capacity of 100 000 h<sup>-1</sup> was found for a 10 mm reactor diameter, a reactor length of 300 mm and 4 bar pressure, as presented in paper I. The particular aim of keeping 510 °C of maximum catalyst temperature at maximum capacity was almost reached with 513 °C temperature peak in this design example. The input parameters led to 80.4 % conversion and a pressure loss of 0.3 bar. It is not possible to conduct single stage methanation with a fixed bed oil-cooled methanation reactor with applicable tube diameters if only 510 °C maximum temperature is allowed.

If a high-temperature compatible catalyst was used with a maximum temperature of 630 °C and the focus is not on high capacity but on single stage methanation of Co-SOEC the optimum reactor design looks different. It is possible to achieve 99.9 % CO<sub>x</sub> conversion in a single 14 mm diameter reactor at 2.5 m length for 4.4 bar pressure as shown in Figure 22. However, this equals only 5000 h<sup>-1</sup> catalyst load, hence 20 times more catalyst is necessary compared to the first reactor stage example at 100 000 h<sup>-1</sup>.

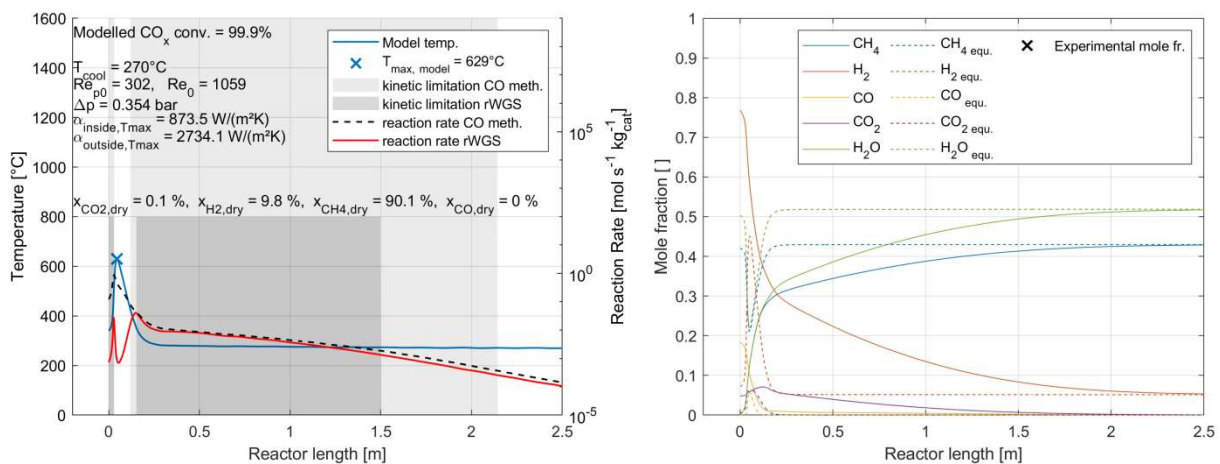


Figure 22: Axial profiles of modelled temperature (left) and molar fractions (right) of a single stage reactor with 14 mm diameter and 2500 mm length with oil-cooled reactor at 340 °C input temperature including indication of kinetic limitation for CO methanation and WGS reaction by grey background (left) and equilibrium concentration (right) (CO<sub>x</sub> conversions, Reynolds numbers, heat transfer coefficients and maximum temperature (blue 'x'-marking) included).

These results are based on modelling results of the developed 1D PFR model. For CO<sub>2</sub> methanation and especially biogas methanation the reactor diameter can be larger, because the feed gas is initially less reactive, meaning less heat is produced per catalyst volume and the radial heat transport can be lower. The 1D reactor model presented in Paper II is capable of simulating all kinds of feed gases, operation and design conditions. Therefore, it can be used as a reactor design tool, if the above rules are applied. Sweet-spot reactor designs over a wide field of parameter settings can be achieved by the model, however results should be experimentally verified for CO<sub>2</sub> methanation and Co-SOEC syngas. The design can be

optimized based on the feed gas or externally predefined pressure requirements of a methanation application, but also can prioritize capacity over high output concentration or vice versa. For Co-SOEC syngas methanation almost full conversion cannot be achieved with fixed beds in a single reactor within the boundary limits presented above, if the maximum catalyst temperature is 510 °C. For CO<sub>2</sub> methanation almost complete conversion of CO<sub>2</sub> to meet the grid injection requirements in Austria in one reactor stage is possible. Full conversion in the first reactor may be preferred in terms of investment and operational costs over high capacities, since this would completely spare the necessity of intermediate cooling and a second reactor stage.

#### **4.5 Answer to research question 5: What are potential efficiency enhancements of a combined Co-SOEC and methanation plant?**

After the discussion of how a reactor can be optimized based on operation parameters and dimensions to maximize specific performance goals, the aspect of combining several reactor stages and upstream electrolysis should be addressed too. The combination of an electrolyzer and a methanation system must be carefully coordinated to achieve the highest possible efficiencies of the overall plant. In particular, a (Co-)SOEC pairs very well with a methanation system because the excess heat generated during methanation can be utilized to preheat the feed for the (Co-)SOEC. The heat produced during methanation is sufficient to vaporize the water required for the Co-SOEC feed.

Furthermore, compressing the feed gases for methanation, such as CO and H<sub>2</sub>, to achieve higher methanation pressure can be expensive. One solution to reduce investment and operational costs for a combined electrolysis and methanation system is to use pressurized electrolyzers. Pressurized alkaline electrolyzers [80,81] and pressurized PEM (Proton Exchange Membrane) electrolyzers [82] allow for the compression of water (and CO<sub>2</sub>) instead of H<sub>2</sub> (and CO). Results for (Co-)SOEC in a pressurized environment have been promising. [83–86]

If an increase in pressure downstream of the electrolyzer is required, as is the case for state-of-the-art Co-SOEC, a dual pressure stage for the methanation process can be employed to minimize the overall energy consumption as shown in Figure 23.

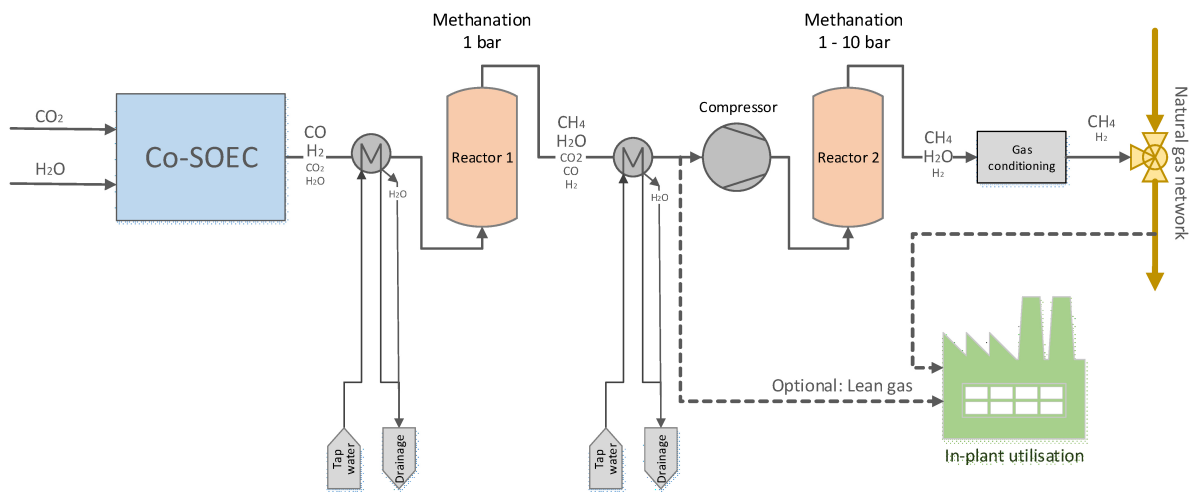


Figure 23: Optimized process flow diagram of high-temperature co-electrolysis and methanation with intermediate compression.

As discussed in paper III, a state-of-the-art Co-SOEC operates at approximately ambient pressure [71]. In the first methanation stage, also operating well at low pressure, a 67.5% conversion rate was achieved. However, in the second reactor stage, an increased pressure of 10 bar is necessary to achieve a 98.2 % conversion rate in the performed experimental investigation. Due to the volume-reducing nature of methanation reactions and the removal of water downstream of reactor 1, up to 42 % of the compression power can be saved through an intermediate compression configuration. Nonetheless, carbon deposition must be considered in the second reactor stage as a consequence of water removal.

## 5 Conclusion

Methanation is the sole technology capable of converting renewable electrical energy into a gaseous energy carrier that can be transported and stored within our current energy infrastructure. This thesis endeavours to make a meaningful contribution to the development of highly flexible, high-capacity and low-complexity methanation systems. These systems are essential for producing low-cost green synthetic natural gas (SNG), which is crucial for meeting our industrial CO<sub>2</sub> emission reduction goals.

The complexity of catalytic methanation was accurately described by Neubert [45] as the trilemma of methanation. Contradicting limitations by kinetics and thermodynamics have to be overcome in a simple and cost-effective reactor. With this thesis an approach is proposed on how multi-tubular methanation reactors can be designed to overcome this trilemma of methanation. The list of important design and operation parameters for methanation is long and their interdependencies are complicated. However, a parameter sweet spot leading to high performance in simple oil-cooled tubular fixed beds is possible. In this thesis the main questions on how to overcome most relevant limitations and design a very well performing catalytic methanation reactor were answered. The focus of this work lies on CO/CO<sub>2</sub> as methanation feed, such as syngas product from a Co-SOEC, but the outlined design rules are qualitatively also applicable to other carbon containing sources, such as concentrated CO<sub>2</sub> or biogas.

Based on an iterative method including a combination of reactor modelling and experimental investigation in a lab-scale test plant the limitations of methanation reactors were identified. The most crucial performance limitations relate from thermodynamics, effective kinetics (intrinsic kinetics, gas-catalyst mass transfer), heat removal properties (inter-bed, bed-wall and wall-coolant heat transport, cooling temperature and velocity), carbon deposition, catalyst sintering and at very high capacities also pressure loss.

Subsequently, all the interdependencies of design and process parameters with the identified limiting physical phenomena were determined. Most importantly, the turbulence, hence the gas velocity, within the catalyst bed affects any heat and mass transfer. High gas velocity has a beneficial effect for most physical phenomena, whereas it also decreases CO<sub>x</sub> conversion and increases pressure loss. In addition, catalyst and reactor design parameters combined with temperature, pressure and gas concentration are essential to steer the performance of the reactor.

The most important feedback of the reactor performance is the axial temperature curve formed during operation within the catalyst bed. The axial temperature profile can be easily measured and compared to modelling data. It allows assessing limitations of a given setup and enables to conclude what measure have to be taken to improve reactor performance.

Based on the axial temperature profile, six fundamental principles were derived to guide the design of an optimally performing reactor:

1. Input temperature: Appr. >250-300 °C to ensure reaction kick-off temperature

2. The maximum catalyst temperature should be kept approximately at 500-600 °C to avoid catalyst sintering, which necessitates active cooling.
3. Operate only slightly below the maximum catalyst temperature at the temperature peak to maximize reaction rates
4. Intensive cooling and temperature reduction downstream of the temperature peak are important to reduce highly probable thermodynamic limitation (inner and outer radial heat transfer relevant)
5. Cooling temperatures should be aimed at 270-320 °C to avoid kinetic limitation in the rear section of the reactor (optimum: neither thermodynamic limitation, nor kinetic limitation occurs)
6. Finally, the output reactor temperature must be settled around 300 °C to ensure favourable thermodynamic conditions for high output methane concentrations.

The exact values of the mentioned temperature ranges depend on input concentration, pressure, catalyst type and targeted output concentration. Adhering to these six principles enables the attainment of high reaction kinetics, prevention of catalyst degradation, mitigation of thermodynamic limitations, and the elimination of carbon deposition. Adjustment of the comprehensively discussed design and operational parameters allow the shaping of the temperature curve. Above all, varying the diameter of the reactor pipe remains the most effective method to enhance methanation performance and increase the specific reactor capacity. Additionally, factors such as the input gas volume flow and reactor pressure play a crucial role in shaping the ideal temperature profile.

Finally, the process arrangement and integration of a complete power to gas unit, consisting of electrolyzer, methanation, compressor and gas post-processing is crucial for high overall energy efficiency. The combination of (Co-)SOEC and methanation is highly beneficial, because excess heat from the methanation system can be reused to preheat the SOEC feed and reduce electric energy demand. Furthermore, the methanation reactor can be designed for low-pressure operation, which makes a combination with slightly pressurized electrolyzers very attractive. Alternatively, dual pressure levels with intermediate compression between first and second methanation reactor stage allows the reduction of the compression power by up to 42 %.

Nevertheless, there remains untapped potential in achieving cost-effective renewable SNG by leveraging high-capacity and flexible methanation reactors. Monolithic catalysts with high radial heat conductivity could enable the utilization of larger reactor diameters. Moreover, employing high-temperature sustaining catalysts could lead to increased reaction rates allowing single stage methanation with only downstream steam removal and direct grid injection. Both of these catalyst advancements have the potential to raise the specific capacity of reactors, subsequently reducing reactor costs. Furthermore, proper reactor dimensioning can also enable the full methanation of biogas or CO<sub>2</sub> methanation in fixed beds with thermal oil-cooling, including the direct injection of the methanation product into the gas grid. The developed 1D model can serve as a valuable tool for designing optimal reactor and cooling dimensions.

The goal of this thesis, which is to contribute to the decarbonization of the current energy system by designing cost-effective, high-capacity catalytic methanation reactors with an emphasis on CO/CO<sub>2</sub> containing feed gases, has been accomplished. Nevertheless, there is still much more to discover and understand in this field.



## 6 References

- [1] G. Thunberg (Ed.), *The climate book: The facts and the solutions*, Penguin Press, New York, 2023.
- [2] H. Diamond, *Yearly global surface temperature and atmospheric carbon dioxide (1850-2022)*.  
<https://www.climate.gov/media/13840>.
- [3] Fiona Harvey, *The Guardian* (18 July 2022).
- [4] H. Böhm, M. Lehner, T. Kienberger, 2021. *Techno-Economic Assessment of Thermally Integrated Co-Electrolysis and Methanation for Industrial Closed Carbon Cycles*. *Front. Sustain.* 2, 726332.  
<https://doi.org/10.3389/frsus.2021.726332>.
- [5] P. Sabatier, J.B. Senderens, *New methane synthesis (1902)* 333.
- [6] J. Kopyscinski, T.J. Schildhauer, S.M. Biollaz, *Production of synthetic natural gas (SNG) from coal and dry biomass – A technology review from 1950 to 2009*, *Fuel* 89 (2010) 1763–1783.  
<https://doi.org/10.1016/j.fuel.2010.01.027>.
- [7] S. Rönsch, J. Schneider, S. Matthischke, M. Schlüter, M. Götz, J. Lefebvre, P. Prabhakaran, S. Bajohr, *Review on methanation – From fundamentals to current projects*, *Fuel* 166 (2016) 276–296. <https://doi.org/10.1016/j.fuel.2015.10.111>.
- [8] A. Krammer, M. Peham, M. Lehner, *2D heterogeneous model of a polytropic methanation reactor*, *Journal of CO2 Utilization* 62 (2022) 102059.  
<https://doi.org/10.1016/j.jcou.2022.102059>.
- [9] J. Sehested, *Sintering of nickel steam-reforming catalysts: effects of temperature and steam and hydrogen pressures*, *Journal of Catalysis* 223 (2004) 432–443.  
<https://doi.org/10.1016/j.jcat.2004.01.026>.
- [10] J. Sehested, *Sintering of nickel steam-reforming catalysts*, *Journal of Catalysis* 217 (2003) 417–426. [https://doi.org/10.1016/S0021-9517\(03\)00075-7](https://doi.org/10.1016/S0021-9517(03)00075-7).
- [11] J. Barrientos, M. Lualdi, R. Suárez París, V. Montes, M. Boutonnet, S. Järås, *CO methanation over TiO<sub>2</sub>-supported nickel catalysts: A carbon formation study*, *Applied Catalysis A: General* 502 (2015) 276–286. <https://doi.org/10.1016/j.apcata.2015.06.029>.
- [12] T. Nguyen, L. Wissing, M.S. Skjøth-Rasmussen, *High temperature methanation: Catalyst considerations*, *Catalysis Today* 215 (2013) 233–238.  
<https://doi.org/10.1016/j.cattod.2013.03.035>.
- [13] M. Held, D. Schollenberger, S. Sauerschell, S. Bajohr, T. Kolb, *Power-to-Gas: CO<sub>2</sub> Methanation Concepts for SNG Production at the Engler-Bunte-Institut*, *Chemie-ingenieur-technik* 92 (2020) 595–602. <https://doi.org/10.1002/cite.201900181>.
- [14] M. Seemann, *Methanation of biosyngas in a fluidized bed reactor: development of a one-step synthesis process, featuring simultaneous methanation, watergas shift and low temperature tar reforming*, 2007.
- [15] M. Maheut, *GAYA: Production of SNG from dry biomass and waste pyrogasification in France*, 2022.
- [16] D. Schollenberger, S. Bajohr, M. Gruber, R. Reimert, T. Kolb, *Scale-Up of Innovative Honeycomb Reactors for Power-to-Gas Applications - The Project Store&Go*, *Chemie-ingenieur-technik* 90 (2018). <https://doi.org/10.1002/cite.201700139>.
- [17] G. Groppi, E. Tronconi, *Honeycomb supports with high thermal conductivity for gas/solid chemical processes*, *Catalysis Today* 105 (2005) 297–304.  
<https://doi.org/10.1016/j.cattod.2005.06.041>.
- [18] F. Vidal Vázquez, J. Kihlman, A. Mylvaganam, P. Simell, M.-L. Koskinen-Soivi, V. Alopaeus, *Modeling of nickel-based hydrotalcite catalyst coated on heat exchanger reactors for CO<sub>2</sub>*

- methanation, *Chemical Engineering Journal* 349 (2018) 694–707.  
<https://doi.org/10.1016/j.cej.2018.05.119>.
- [19] M. Gruber, Detailed analysis of heat and mass transfer in a packed bed methanation reactor for power to gas applications: Dissertation, Karlsruhe, 2020.
- [20] D. Schlereth, O. Hinrichsen, A fixed-bed reactor modeling study on the methanation of CO<sub>2</sub>, *Chemical Engineering Research and Design* 92 (2014) 702–712.  
<https://doi.org/10.1016/j.cherd.2013.11.014>.
- [21] R. Try, A. Bengaouer, P. Baurens, C. Jallut, Dynamic modeling and simulations of the behavior of a fixed-bed reactor-exchanger used for CO<sub>2</sub> methanation, *AIChE J.* 64 (2018) 468–480.  
<https://doi.org/10.1002/aic.15874>.
- [22] D. Sun, D.S. Simakov, Thermal management of a Sabatier reactor for CO<sub>2</sub> conversion into CH<sub>4</sub>: Simulation-based analysis, *Journal of CO<sub>2</sub> Utilization* 21 (2017) 368–382.  
<https://doi.org/10.1016/j.jcou.2017.07.015>.
- [23] J. Ducamp, A. Bengaouer, P. Baurens, Modelling and experimental validation of a CO<sub>2</sub> methanation annular cooled fixed-bed reactor exchanger, *The Canadian Journal of Chemical Engineering* 95 (2017) 241–252. <https://doi.org/10.1002/cjce.22706>.
- [24] L. Kiewidt, J. Thöming, Predicting optimal temperature profiles in single-stage fixed-bed reactors for CO<sub>2</sub>-methanation, *Chemical Engineering Science* 132 (2015) 59–71.  
<https://doi.org/10.1016/j.ces.2015.03.068>.
- [25] B. Kreitz, G. Wehinger, T. Turek, Dynamic simulation of the CO<sub>2</sub> methanation in a micro-structured fixed-bed reactor, *Chemical Engineering Science* 195 (2019) 541–552.  
<https://doi.org/10.1016/j.ces.2018.09.053>.
- [26] J. Lefebvre, S. Bajohr, T. Kolb, A comparison of two-phase and three-phase CO<sub>2</sub> methanation reaction kinetics, *Fuel* 239 (2019) 896–904. <https://doi.org/10.1016/j.fuel.2018.11.051>.
- [27] M. Gruber, D. Wiedmann, M. Haas, S. Harth, A. Loukou, D. Trimis, Insights into the catalytic CO<sub>2</sub> methanation of a boiling water cooled fixed-bed reactor: Simulation-based analysis, *Chemical Engineering Journal* 406 (2021) 126788. <https://doi.org/10.1016/j.cej.2020.126788>.
- [28] M. Hervy, J. Maistrello, L. Brito, M. Rizand, E. Basset, Y. Kara, M. Maheut, Power-to-gas: CO<sub>2</sub> methanation in a catalytic fluidized bed reactor at demonstration scale, experimental results and simulation, *Journal of CO<sub>2</sub> Utilization* 50 (2021) 101610.  
<https://doi.org/10.1016/j.jcou.2021.101610>.
- [29] J. Li, L. Zhou, P. Li, Q. Zhu, J. Gao, F. Gu, F. Su, Enhanced fluidized bed methanation over a Ni/Al<sub>2</sub>O<sub>3</sub> catalyst for production of synthetic natural gas, *Chemical Engineering Journal* 219 (2013) 183–189. <https://doi.org/10.1016/j.cej.2013.01.005>.
- [30] M.C. Seemann, T.J. Schildhauer, S.M.A. Biollaz, Fluidized Bed Methanation of Wood-Derived Producer Gas for the Production of Synthetic Natural Gas, *Ind. Eng. Chem. Res.* 49 (2010) 7034–7038. <https://doi.org/10.1021/ie100510m>.
- [31] M. Neubert, A. Hauser, B. Pourhossein, M. Dillig, J. Karl, Experimental evaluation of a heat pipe cooled structured reactor as part of a two-stage catalytic methanation process in power-to-gas applications, *Applied Energy* 229 (2018) 289–298.  
<https://doi.org/10.1016/j.apenergy.2018.08.002>.
- [32] A. Hauser, M. Neubert, A. Feldner, A. Horn, F. Grimm, J. Karl, Design and Implementation of an Additively Manufactured Reactor Concept for the Catalytic Methanation, *Applied Sciences* 12 (2022) 9393. <https://doi.org/10.3390/app12189393>.

- [33] A. Hauser, M. Weitzer, S. Gunsch, M. Neubert, J. Karl, Dynamic hydrogen-intensified methanation of synthetic by-product gases from steelworks, *Fuel Processing Technology* 217 (2021) 106701. <https://doi.org/10.1016/j.fuproc.2020.106701>.
- [34] V.A. Danilov, M. Wichert, G. Kolb, 2D model of the transfer processes for CO<sub>2</sub> methanation in a microchannel reactor, *Chemical Engineering Journal* 450 (2022) 137863. <https://doi.org/10.1016/j.cej.2022.137863>.
- [35] P. Frontera, A. Macario, M. Ferraro, P. Antonucci, Supported Catalysts for CO<sub>2</sub> Methanation: A Review, *Catalysts* 7 (2017) 59. <https://doi.org/10.3390/catal7020059>.
- [36] A.I. Tsiotsias, N.D. Charisiou, I.V. Yentekakis, M.A. Goula, Bimetallic Ni-Based Catalysts for CO<sub>2</sub> Methanation: A Review, *Nanomaterials (Basel)* 11 (2020). <https://doi.org/10.3390/nano11010028>.
- [37] I. Hussain, A.A. Jalil, N.S. Hassan, M. Farooq, M.A. Mujtaba, M. Hamid, H. Sharif, W. Nabgan, M. Aziz, A.H. Owgi, Contemporary thrust and emerging prospects of catalytic systems for substitute natural gas production by CO methanation, *Fuel* 311 (2022) 122604. <https://doi.org/10.1016/j.fuel.2021.122604>.
- [38] J. Li, P. Li, J. Li, Z. Tian, F. Yu, Highly-Dispersed Ni-NiO Nanoparticles Anchored on an SiO<sub>2</sub> Support for an Enhanced CO Methanation Performance, *Catalysts* 9 (2019) 506. <https://doi.org/10.3390/catal9060506>.
- [39] S. Chen, A.M. Abdel-Mageed, D. Li, J. Bansmann, S. Cisneros, J. Biskupek, W. Huang, R.J. Behm, Morphology-Engineered Highly Active and Stable Ru/TiO<sub>2</sub> Catalysts for Selective CO Methanation, *Angew. Chem. Int. Ed Engl.* 58 (2019) 10732–10736. <https://doi.org/10.1002/anie.201903882>.
- [40] T. Burger, P. Donaubaue, O. Hinrichsen, On the kinetics of the co-methanation of CO and CO<sub>2</sub> on a co-precipitated Ni-Al catalyst, *Applied Catalysis B: Environmental* 282 (2021) 119408. <https://doi.org/10.1016/j.apcatb.2020.119408>.
- [41] I. Hussain, A.A. Jalil, C.R. Mamat, T.J. Siang, A. Rahman, M.S. Azami, R.H. Adnan, New insights on the effect of the H<sub>2</sub>/CO ratio for enhancement of CO methanation over metal-free fibrous silica ZSM-5: Thermodynamic and mechanistic studies, *Energy Conversion and Management* 199 (2019) 112056. <https://doi.org/10.1016/j.enconman.2019.112056>.
- [42] D. Meyer, Effect of CO, CO<sub>2</sub> and CO/CO<sub>2</sub> Mixtures on the Steady- and Unsteady-State Methanation Reaction, 2022.
- [43] L. Gómez, I. Martínez, M.V. Navarro, T. García, R. Murillo, Sorption-enhanced CO and CO<sub>2</sub> methanation (SEM) for the production of high purity methane, *Chemical Engineering Journal* 440 (2022) 135842. <https://doi.org/10.1016/j.cej.2022.135842>.
- [44] Richard Schauerl, Manuel Tandl, Christoph Sams, Werner Sitte, Markus Lehner, Andreas Egger, Edith Bucher, Andreas Krammer, Stefan Megel, Günther Holzer, Fabian Zapf, Hans Böhm, Christian Aichernig, Endbericht HydroMetha: Development of a stationary electricity storage system via high temperature co-electrolysis and catalytic methanation, 2023.
- [45] M. Neubert, Catalytic methanation for small- and mid-scale SNG production, Friedrich-Alexander-Universität Erlangen-Nürnberg (FAU), Erlangen, 2019.
- [46] ÖVGW, Richtlinie G B210: Gasbeschaffenheit 75.060, 2021.
- [47] W. Sitte, R. Merkle (Eds.), High-Temperature Electrolysis, IOP Publishing, 2023.
- [48] K. Hertwig, L. Martens, Chemische Verfahrenstechnik: Berechnung, Auslegung und Betrieb chemischer Reaktoren, second., überarbeitete Auflage, Oldenbourg Verlag, München, 2012.

- [49] S.T. Sie, Advantages, Possibilities, and Limitations of Small-Scale Testing of Catalysts for Fixed-Bed Processes, in: P. O'Connor, T. Takatsuka, G.L. Woolery (Eds.), *Deactivation and Testing of Hydrocarbon-Processing Catalysts*, American Chemical Society, Washington, DC, 1996, pp. 6–41.
- [50] A.H. Cutler, M.J. Antal, M. Jones, A critical evaluation of the plug-flow idealization of tubular-flow reactor data, *Ind. Eng. Chem. Res.* 27 (1988) 691–697.  
<https://doi.org/10.1021/ie00076a027>.
- [51] A. Jess, P. Wasserscheid, *Chemical technology: From principles to products*, Second edition, Wiley-VCH, Weinheim, 2020.
- [52] D.E. Mears, The role of axial dispersion in trickle-flow laboratory reactors, *Chemical Engineering Science* 26 (1971) 1361–1366. [https://doi.org/10.1016/0009-2509\(71\)80056-8](https://doi.org/10.1016/0009-2509(71)80056-8).
- [53] H. Gierman, Design of laboratory hydrotreating reactors, *Applied Catalysis* 43 (1988) 277–286.  
[https://doi.org/10.1016/S0166-9834\(00\)82732-3](https://doi.org/10.1016/S0166-9834(00)82732-3).
- [54] S. Spatenka, M. Matzopoulos, Z. Urban, A. Cano, From Laboratory to Industrial Operation: Model-Based Digital Design and Optimization of Fixed-Bed Catalytic Reactors, *Ind. Eng. Chem. Res.* 58 (2019) 12571–12585. <https://doi.org/10.1021/acs.iecr.9b01314>.
- [55] A. Krammer, K. Salbrechter, M. Lehner, High-capacity CO/CO<sub>2</sub> methanation reactor design strategy based on 1D PFR modelling and experimental investigation, *Journal of CO<sub>2</sub> Utilization* 80 (2024) 102661. <https://doi.org/10.1016/j.jcou.2023.102661>.
- [56] M. Winterberg, E. Tsotsas, A. Krischke, D. Vortmeyer, A simple and coherent set of coefficients for modelling of heat and mass transport with and without chemical reaction in tubes filled with spheres, *Chemical Engineering Science* 55 (2000) 967–979. [https://doi.org/10.1016/S0009-2509\(99\)00379-6](https://doi.org/10.1016/S0009-2509(99)00379-6).
- [57] V. Specchia, G. Baldi, S. Sicardi, Heat transfer in packed bed reactors with one phase flow, *Chemical Engineering Communications* 4 (1980) 361–380.  
<https://doi.org/10.1080/00986448008935916>.
- [58] VDI-Wärmeatlas, 11th ed., Springer Berlin Heidelberg, Berlin, Heidelberg, 2013.
- [59] R. Bauer, E.U. Schlunder, Effective radial thermal conductivity of packings in gas flow. Part II. Thermal conductivity of the packing fraction without gas flow, *International Chemical Engineering* 189–204.
- [60] R. Bauer, E.U. Schlunder, Effective radial thermal conductivity of packings in gas flow. Part I. Convective transport coefficient, *International Chemical Engineering* (1978) 181–188.
- [61] E. Schlunder, Heat transfer to packed and stirred beds from the surface of immersed bodies, *Chemical Engineering and Processing: Process Intensification* 18 (1984) 31–53.  
[https://doi.org/10.1016/0255-2701\(84\)85007-2](https://doi.org/10.1016/0255-2701(84)85007-2).
- [62] M. Gruber, Detaillierte Untersuchung des Wärme- und Stofftransports in einem Festbett-Methanisierungsreaktor für Power-to-Gas Anwendungen. Dissertation, Karlsruhe, 2020.
- [63] Ed Fontes, *Modeling Approaches in Heterogeneous Catalysis*, 2015.  
<https://www.comsol.com/blogs/modeling-approaches-in-heterogeneous-catalysis/> (accessed 14 August 2023).
- [64] G.W. Roberts, C.N. Satterfield, Effectiveness Factor for Porous Catalysts. Langmuir-Hinshelwood Kinetic Expressions, *Ind. Eng. Chem. Fund.* 4 (1965) 288–293.  
<https://doi.org/10.1021/i160015a009>.
- [65] T. Eppinger, K. Seidler, M. Kraume, DEM-CFD simulations of fixed bed reactors with small tube to particle diameter ratios, *Chemical Engineering Journal* 166 (2011) 324–331.  
<https://doi.org/10.1016/j.cej.2010.10.053>.

- [66] M. Giese, K. Rottschäfer, D. Vortmeyer, Measured and modeled superficial flow profiles in packed beds with liquid flow, *AIChE J.* 44 (1998) 484–490. <https://doi.org/10.1002/aic.690440225>.
- [67] A. de Klerk, Voidage variation in packed beds at small column to particle diameter ratio, *AIChE J.* 49 (2003) 2022–2029. <https://doi.org/10.1002/aic.690490812>.
- [68] P. Andrigo, Fixed bed reactors, *Catalysis Today* 52 (1999) 197–221. [https://doi.org/10.1016/S0920-5861\(99\)00076-0](https://doi.org/10.1016/S0920-5861(99)00076-0).
- [69] V. Gnielinski, Heat Transfer Coefficients for Turbulent Flow in Concentric Annular Ducts, *Heat Transfer Engineering* 30 (2009) 431–436. <https://doi.org/10.1080/01457630802528661>.
- [70] S. Rönsch, J. Köchermann, J. Schneider, S. Matthischke, Global Reaction Kinetics of CO and CO<sub>2</sub> Methanation for Dynamic Process Modeling, *Chem. Eng. Technol.* 39 (2016) 208–218. <https://doi.org/10.1002/ceat.201500327>.
- [71] A. Krammer, A. Medved, M. Peham, P. Wolf-Zöllner, K. Salbrechter, M. Lehner, Dual Pressure Level Methanation of Co-SOEC Syngas, *Energy Technol.* 202 (2020) 2000746. <https://doi.org/10.1002/ente.202000746>.
- [72] G.F. Froment, K.B. Bischoff, J. de Wilde, *Chemical reactor analysis and design*, third. ed., Wiley, Hoboken, NJ, 2011.
- [73] G. Che-Galicia, R.S. Ruiz-Martínez, F. López-Isunza, C.O. Castillo-Araiza, Modeling of oxidative dehydrogenation of ethane to ethylene on a MoVTeNbO/TiO<sub>2</sub> catalyst in an industrial-scale packed bed catalytic reactor, *Chemical Engineering Journal* 280 (2015) 682–694. <https://doi.org/10.1016/j.cej.2015.05.128>.
- [74] L.S. Kershenbaum, F. Lopez-Isunza, Dynamic Behavior of an Industrial Scale Fixed-Bed Catalytic Reactor, in: P. O'Connor, T. Takatsuka, G.L. Woolery (Eds.), *Deactivation and Testing of Hydrocarbon-Processing Catalysts*, American Chemical Society, Washington, DC, 1996, pp. 109–120.
- [75] Johanna Fernengel, *From Packing Generation to Single Pellet String Reactor Characteristics: A Numerical Approach to Fixed-Bed Reactors*. Dissertation, München, 2022.
- [76] H.M. Bui, P.F. Großmann, T. Gros, M. Blum, A. Berger, R. Fischer, N. Szesni, M. Tonigold, O. Hinrichsen, 3D printed co-precipitated Ni-Al CO<sub>2</sub> methanation catalysts by Binder Jetting: Fabrication, characterization and test in a single pellet string reactor, *Applied Catalysis A: General* 643 (2022) 118760. <https://doi.org/10.1016/j.apcata.2022.118760>.
- [77] ENTSOG, Gas Infrastructure Europe, Hydrogen Europe, HOW TO TRANSPORT AND STORE HYDROGEN - FACTS AND FIGURES.
- [78] GRTgaz, GRDF, elenegy, Geomethane, Teregea, REGAZ Bordaux, Stroengy, R-GDS, Technical and economic conditions for injecting hydrogen into natural gas networks: Final report June 2019, 2019.
- [79] DVGW, G 260 Arbeitsblatt 09/2021: Gasbeschaffenheit, 2021.
- [80] E. Stamatakis, E. Perwög, E. Garyfallos, M.S. Millán, E. Zoulias, N. Chalkiadakis, Hydrogen in Grid Balancing: The European Market Potential for Pressurized Alkaline Electrolyzers, *Energies* 15 (2022) 637. <https://doi.org/10.3390/en15020637>.
- [81] Á. Iribarren, D. Elizondo, E.L. Barrios, H. Ibaiondo, A. Sanchez-Ruiz, J. Arza, P. Sanchis, A. Ursúa, Dynamic Modeling of a Pressurized Alkaline Water Electrolyzer: A Multiphysics Approach, *IEEE Trans. on Ind. Applicat.* 59 (2023) 3741–3753. <https://doi.org/10.1109/TIA.2023.3247405>.
- [82] G. Tjarks, A. Gibelhaus, F. Lanzerath, M. Müller, A. Bardow, D. Stolten, Energetically-optimal PEM electrolyzer pressure in power-to-gas plants, *Applied Energy* 218 (2018) 192–198. <https://doi.org/10.1016/j.apenergy.2018.02.155>.

- [83] J. Brabandt, O. Posdziech, System Approach of a Pressurized High-Temperature Electrolysis, *ECS Trans.* 78 (2017) 2987–2995. <https://doi.org/10.1149/07801.2987ecst>.
- [84] O. Posdziech, K. Schwarze, J. Brabandt, Efficient hydrogen production for industry and electricity storage via high-temperature electrolysis, *International Journal of Hydrogen Energy* 44 (2019) 19089–19101. <https://doi.org/10.1016/j.ijhydene.2018.05.169>.
- [85] L. Bernadet, G. Gousseau, A. Chatroux, J. Laurencin, F. Mauvy, M. Reytier, Influence of pressure on solid oxide electrolysis cells investigated by experimental and modeling approach, *International Journal of Hydrogen Energy* 40 (2015) 12918–12928. <https://doi.org/10.1016/j.ijhydene.2015.07.099>.
- [86] L. Bernadet, J. Laurencin, G. Roux, D. Montinaro, F. Mauvy, M. Reytier, Effects of Pressure on High Temperature Steam and Carbon Dioxide Co-electrolysis, *Electrochimica Acta* 253 (2017) 114–127. <https://doi.org/10.1016/j.electacta.2017.09.037>.



## Nomenclature

### Abbreviations

COM	CO methanation
CO2M	CO <sub>2</sub> methanation
GHSV	Gas hourly space velocity
PFR	Plug-flow reactor
rWGS	Reverse water gas shift reaction
WGS	Water gas shift reaction

### Symbols

$A$	Area	$m^2$
$c_i$	Concentration of component $i$	$mol\ m^{-3}$
$c_p$	Heat capacity	$J\ kg^{-1}\ K^{-1}$
$D_i$	Diffusion coefficient of component $i$	$m^2\ s^{-1}$
$d$	Diameter	$m$
$d_{particle}$	Particle diameter of catalyst	$m$
$\Delta H_R$	Enthalpy of reaction	$J\ mol^{-1}$
$j$	Mass or heat flow variable	$mol\ m^{-2}m^{-1}\ or\ W\ m^{-2}m^{-1}$
$K_1, K_2$	Coefficient of $\Lambda_r(r)$ -model	—
$K_i$	Adsorption constant of component $i$	differs
$k_j$	Reaction rate coefficient of reaction $j$	differs
$k$	Overall heat transfer coefficient	$W\ m^{-2}\ K^{-1}$
$L$	Reactor Length	$m$
$M$	Molar mass	$kg\ mol^{-1}$
$\dot{m}_i$	Mass flow of species $i$	$kg\ s^{-1}$
$\dot{n}_i$	Molar flow of species $i$	$mol\ s^{-1}$
$n_j$	Reaction order of reaction $j$	—

$p$	Pressure	$Pa$
$\dot{Q}$	Heat flow	$W$
$q$	Heat flow (volumetric) density	$W m^{-3}$
$r$	Control variable of reactor radius	$m$
$r_j$	Reaction rate of reaction $j$	$mol kg_{cat}^{-1} s^{-1}$
$r_V$	Volumetric reaction rate	$mol m_{cat}^{-3} s^{-1}$
$R$	Radius of reactor or ideal gas constant	$m$ or $J mol^{-1} K^{-1}$
$Re_{0,p}$	Particle Reynolds number with superficial velocity	—
$Re_p$	Particle Reynolds number with “operating” velocity	—
$Sc$	Schmidt number	—
$Sh$	Sherwood number	—
$T$	Temperature	$K$
$t$	Time	$s$
$\dot{V}$	Volume flow	$m^3 s^{-1}$
$V_{reactor}$	Reactor volume	$m^3$
$w$	Velocity	$m s^{-1}$
$\alpha$	Heat transfer coefficient	$W m^{-2} K^{-1}$
$\beta$	Mass transfer coefficient	$mol m^{-2} K^{-1}$
$\Gamma$	State variable	—
$\varepsilon$	Porosity	—
$\eta$	Dynamic viscosity / effectiveness factor	$Pa s$ or —
$\lambda$	Heat conductivity	$W m^{-1} K^{-1}$
$\Lambda_r(r)$	Effective fixed bed heat conductivity as function of radial position $r$	$W m^{-1} K^{-1}$
$\nu_{ij}$	Stoichiometric factor of component $i$ of reaction $j$	—
$\rho$	Density	$kg m^{-3}$
$\tau_{cat}$	Tortuosity of catalyst	—
$\Phi$	Thiele modulus	—

Subscripts and superscripts

<i>air</i>	Ambient air
<i>bed</i>	Fixed bed
<i>bed – oil</i>	From fixed bed to coolant oil
<i>bed – wall</i>	From fixed bed to pipe wall
<i>cat</i>	Catalyst
<i>conv</i>	Convection
<i>cond</i>	Conduction
<i>cool</i>	Cooling
<i>diff</i>	Diffusion
<i>eff</i>	Effective
<i>gas</i>	Gas
<i>heat conv</i>	Heat convection
<i>i</i>	Index of gas component or at the inside of the pipe
<i>in</i>	Input
<i>intr</i>	Intrinsic
<i>j</i>	Index of reaction
<i>knu</i>	Knudson (diffusion)
<i>lat</i>	Lateral
<i>lhw</i>	Langmuir Hinshelwood Hougen Watson
<i>long</i>	Longitudinal
<i>m</i>	Molecular or mean
<i>mix</i>	Mixture (diffusion coefficient of component <i>i</i> in gas mixture)
<i>mt</i>	Mass transfer
<i>o</i>	At the outside of the pipe
<i>op.</i>	Operation condition

---

<i>out</i>	Output
<i>oil</i>	Oil
<i>p</i>	Particle
<i>pore</i>	Pore
<i>r</i>	Reactor (pipe) or radial
<i>radiation</i>	Radiation
<i>solid</i>	Solid fraction without pores
<i>steel</i>	Steel
<i>STP</i>	Standard temperature and pressure conditions
<i>sup</i>	Superficial (velocity)
<i>V</i>	Volumetric
<i>wall (or w)</i>	Reactor wall
<i>wall – air</i>	From piping wall to ambient air

## Figures

Figure 1: Yearly global surface temperature (bars) and atmospheric carbon dioxide (grey line) (1850-2022) [2] .....	3
Figure 2: Trilemma of decentralized methanation by Neubert [45] .....	6
Figure 3: Heat and mass transfer phenomena in fixed beds taken from [54] .....	40
Figure 4: 7 steps of heterogeneous gas catalysis (reproduced based on [62]) .....	45
Figure 5: Reactant concentration profile as a consequence of rate determining phenomenon (reproduced based on [61]) .....	46
Figure 6: Performance comparison based on experimentally found (bars) and modelled ('x'-markings) CO <sub>x</sub> conversion and modelled maximum temperature ('▲'-markings) of three reactors with 14 mm diameter (840 mm naturally cooled reactor 1, 700 mm oil-cooled reactor 2 and 600 mm oil-cooled reactor 3) and a reactor with 80 mm diameter (50 mm naturally cooled catalyst zone) [8] in dependency of GHSV and pressure. ....	102
Figure 7: Experiment-model-comparison of axial temperature profiles for a lab-scale packed bed methanation reactor at 4000 h <sup>-1</sup> GHSV and Co-SOEC syngas feed .....	103
Figure 8: Radial temperature profiles of an 80 mm diameter fixed bed reactor at the catalyst zone inlet (0.1 m reactor height), center (0.125 m reactor height) and outlet (0.15 m reactor height) of solid, gas and wall based on the 2D reactor model for a pressure of 8.03 bar and GHSV of 4000 h <sup>-1</sup> .....	104
Figure 9: Equilibrium composition of Co-SOEC syngas in dependence of temperature and pressure based on Co-SOEC syngas composition with 3% hydrogen excess (76.8 vol.-% H <sub>2</sub> , 18.3 vol.-% CO and 4.9 vol.-% CO <sub>2</sub> ) .....	105
Figure 10: Catalytic efficiency (left ordinate) from a power law, a Langmuir-Hinshelwood-Hougen-Watson and new approximation approaches along with catalyst temperature (right ordinate) over the reactor height in the central reactor axis at 4000 h <sup>-1</sup> and 8 bar in a 80 mm diameter 50 mm length reactors including a closer look (red frame) with higher resolution of the catalyst zone in the right diagram .....	106
Figure 11: Catalytic efficiency (left ordinate) from a power law approach along with temperature (right ordinate) over the reactor length at 4000 h <sup>-1</sup> , 1.3 bar and 20000 h <sup>-1</sup> , 6 bar in a 14 mm diameter 700 mm length reactor .....	107
Figure 12: Ternary carbon-hydrogen-oxygen-proportion diagram including solid carbon equilibrium lines at three different temperature-pressure pairs (marked by lines) and the position of process gases (marked by red crosses) representing the thermodynamic carbon formation property of Co-SOEC syngas .....	108
Figure 13: Overview of performance limiting factors (green) of fixed bed CO/CO <sub>2</sub> methanation and the influential design and operation parameters (yellow) including an indication of limitation how to reduce it by ↗ (increase to improve) and ↘ (decrease to improve). ....	109

- Figure 14: Radial porosity distribution of 14 mm and 10 mm diameter reactors based on empirical methods by Giese [65] and de Klerk [66] (reactor radius is 0 at the reactor wall) ..... 110
- Figure 15: Axial profiles of modelled (lines) and experimentally determined ('x'-markings) temperature and molar fractions of the 14 mm diameter and 840 mm long naturally cooled compared to the 700 mm long actively oil-cooled reactor at 8000 h<sup>-1</sup> and 6 bar including indication of kinetic limitation for CO methanation and WGS reaction by grey background (CO<sub>x</sub> conversions, Reynolds numbers, heat transfer coefficients and maximum temperature (blue 'x'-marking) included). ..... 111
- Figure 16: Axial profiles of modelled (lines) and experimentally determined ('x'-markings) temperature (left) and molar fractions (right) of the 14 mm diameter and 700 mm long oil-cooled reactor without preheating zone compared to the 600 mm long oil-cooled reactor with 100 mm preheating zone at 25000 h<sup>-1</sup> and 6 bar including indication of kinetic limitation for CO methanation and WGS reaction by grey background (CO<sub>x</sub> conversions, Reynolds numbers, heat transfer coefficients and maximum temperature (blue 'x'-marking) included). ..... 113
- Figure 17: Inner bed-wall heat transfer coefficient and effective fixed bed heat conductivity over superficial input gas velocity for 8000 h<sup>-1</sup>, 15000 h<sup>-1</sup>, 20000 h<sup>-1</sup> and 25000 h<sup>-1</sup> at 6 bar and for 10 mm, 14 mm and 18 mm reactor diameter at 700 mm catalyst length.... 115
- Figure 18: Catalyst efficiency for CO methanation (COM) and water gas shift reaction (WGS) over superficial input gas velocity for 8000 h<sup>-1</sup>, 15000 h<sup>-1</sup>, 20000 h<sup>-1</sup> and 25000 h<sup>-1</sup> at 6 bar and for 10 mm, 14 mm and 18 mm reactor diameter at 700 mm catalyst length.... 116
- Figure 19: Mean radial heat flux equivalent without temperature difference influence (Equation 31 and Equation 33) over superficial input gas velocity for 8000 h<sup>-1</sup>, 15000 h<sup>-1</sup>, 20000 h<sup>-1</sup> and 25000 h<sup>-1</sup> at 6 bar and for 10 mm, 14 mm and 18 mm reactor diameter at 700 mm catalyst length. .... 117
- Figure 20: CO<sub>x</sub> conversion and maximum temperature over superficial input gas velocity for 8000 h<sup>-1</sup>, 15000 h<sup>-1</sup>, 20000 h<sup>-1</sup> and 25000 h<sup>-1</sup> at 6 bar and for 10 mm, 14 mm and 18 mm reactor diameter at 700 mm catalyst length. .... 118
- Figure 21: 6 main tasks of temperature control in a catalytic fixed bed methanation reactor (idea based on illustration from Neubert [45]) ..... 120
- Figure 22: Axial profiles of modelled temperature (left) and molar fractions (right) of a single stage reactor with 14 mm diameter and 2500 mm length with oil-cooled reactor at 340 °C input temperature including indication of kinetic limitation for CO methanation and WGS reaction by grey background (left) and equilibrium concentration (right) (CO<sub>x</sub> conversions, Reynolds numbers, heat transfer coefficients and maximum temperature (blue 'x'-marking) included). ..... 122
- Figure 23: Optimized process flow diagram of high-temperature co-electrolysis and methanation with intermediate compression. .... 124





## Tables

Table 1: Structure of the thesis including all publications.....	9
Table 2: Overview of heat and mass transport phenomena in chemical reactors.....	39

## Publications

### Articles in peer-reviewed journals

A. Krammer, A. Medved, M. Peham, P. Wolf-Zöllner, K. Salbrechter, M. Lehner, Dual Pressure Level Methanation of Co-SOEC Syngas, *Energy Technol.* 202 (2020) 2000746. <https://doi.org/10.1002/ente.202000746>.

A. Krammer, M. Peham, M. Lehner, 2D heterogeneous model of a polytropic methanation reactor, *Journal of CO<sub>2</sub> Utilization* 62 (2022) 102059. <https://doi.org/10.1016/j.jcou.2022.102059>.

A. Krammer, K. Salbrechter, M. Lehner, High-capacity CO/CO<sub>2</sub> methanation reactor design strategy based on 1D PFR modelling and experimental investigation, *Journal of CO<sub>2</sub> Utilization* 80 (2024) 102661. <https://doi.org/10.1016/j.jcou.2023.102661>.

### Book chapter

A. Krammer, M. Lehner, Co-solid oxide electrolysis and methanation, in: W. Sitte, R. Merkle (Eds.), *High-Temperature Electrolysis*, IOP Publishing, 2023, pp. 365–390.

### Conference contributions

A. Medved, A. Krammer, P. Wolf-Zöllner, M. Lehner, 2019. Methanisierung von Hochofengichtgas [Methanation of blast furnace gas], **oral contribution** in: Jahrestreffen der ProcessNet-Fachgruppe Energieverfahrenstechnik, Frankfurt, Germany, 07.03.2019.

A. Krammer, A. Medved, P. Wolf-Zöllner, M. Lehner, Methanation of Co-SOEC syngas - Presentation and first results of a novel power to gas concept, **oral and written contribution** in: Conference Proceedings of 15<sup>th</sup> Minisymposium Verfahrenstechnik and 6<sup>th</sup> Partikelforum, Montanuniversität Leoben, Austria, 29th-30th April 2019. p. 85, 15th Minisymposium Verfahrenstechnik and 6th Partikelforum, Leoben, Austria, 29/04/19.

A. Krammer, A. Medved, P. Wolf-Zöllner, S. Salbrechter, M. Lehner, 2020. Effizienzsteigerung einer katalytischen Methanisierung durch Zwischenverdichtung [Efficiency enhancement of catalytic methanation by intermediate compression], **oral contribution** in: Jahrestreffen der ProcessNet-Fachgruppe Energieverfahrenstechnik, Frankfurt, Germany, 04.03.2020.

P. Wolf-Zöllner, A. Krammer, A. Medved, S. Salbrechter, M. Lehner, 2020. Dynamische Methanisierung von Prozessgasen – reale Anwendungsfälle aus der Industrie [Dynamic methanation of process gas – real applications from industry], **oral contribution** in: Jahrestreffen der ProcessNet-Fachgruppe Energieverfahrenstechnik, Frankfurt, Germany, 04.03.2020.

A. Krammer, P. Wolf-Zöllner, S. Salbrechter, M. Lehner, 2021. Effizienzsteigerung einer katalytischen Methanisierung durch Zwischenverdichtung [Efficiency enhancement of catalytic methanation by intermediate compression], **oral contribution** in: NEFI - New Energy for Industry 2021, online, Austria, 2021.

A. Krammer, P. Wolf-Zöllner, S. Salbrechter, M. Lehner, 2021. Effizienzsteigerung einer katalytischen Methanisierung durch Zwischenverdichtung [Efficiency enhancement of catalytic methanation by intermediate compression], **oral contribution** in: 5th Nuremberg Workshop Methanation and 2nd Generation Fuels, Nuremberg, Austria, 28.5.2021.

A. Krammer, M. Lehner, 2023. Solution proposal for the “trilemma of methanation” by high-capacity tube-bundle reactors, **oral contribution** in: 6<sup>th</sup> Nuremberg Workshop Methanation and 2<sup>nd</sup> Generation Fuels, Nuremberg, Austria, 17.5.2023

A. Krammer, S. Salbrechter, M. Lehner, 2023. High-capacity multi-feedstock methanation – from model to 20 kW pilot plant (part 1), **oral contribution** in: 11<sup>th</sup> International Freiberg Conference on Circular Carbon Technologies, Rotterdam, Netherland, 25.9.2023

## **(Co-)Supervised Bachelor’s and Master’s Theses**

Peham M., 2019. Konstruktion einer Versuchsanlage zur katalytischen Reformierung [Design of a lab-scale test plant for catalytic reforming], **Master’s Thesis**.

Lindebner M., 2020. Reaktor-Temperaturvermessung zur verbesserten thermischen Analyse der katalytischen Methanisierung [Reactor temperature measurement for optimized thermal analysis of catalytic methanation], **Master’s Thesis**.

Zawodnik V., 2021. Herstellung und Testung von Wabenkatalysatoren für die Methanisierung von kohlenstoffhaltigen Prozessgasen im Labormaßstab [Production and testing of honeycomb catalysts for methanation of carbon based process gases in laboratory-scale], **Master’s Thesis**.

Khodier T., 2023. Modellierung der katalytischen Methanisierung mit einem Plug-Flow-Reaktormodell [Modelling of catalytic methanation in a plug-flow-reactor model], **Bachelor’s Thesis**.

Kienast P., 2023. Modellierung der Methanisierung von Co-SOEC-Synthesegas in einem Plug-Flow-Reaktor [Modelling of methanation of Co-SOEC syngas in a plug-flow reactor model], **Bachelor’s Thesis**.

Allgäuer R., 2023. Kinetische und thermodynamische Analyse des katalytischen Reformierungsprozesses mit Bezug auf eine Versuchsanlage [Kinetic and thermodynamic analysis of catalytic reforming], **Bachelor’s Thesis**.

Sorger G., 2023. Wärmetransportevaluierung eines elektrisch geheizten Reformingreaktors [Evaluation of an electrically heated reforming reactor], **Bachelor’s Thesis**.